

# **Oxide-Encapsulated Electrocatalysts for Solar Fuels Production**

Natalie Y. Labrador

Submitted in partial fulfillment of the  
requirements for the degree of  
Doctor of Philosophy  
in the Graduate School of Arts and Sciences

Columbia University

2018

© 2018

Natalie Labrador

All rights reserved

## ABSTRACT

### Oxide-Encapsulated Electrocatalysts for Solar Fuels Production

Natalie Labrador

As the cost of solar energy continues to drop, the major hurdle limiting the widespread use of intermittent renewable solar energy is the lack of efficient and cost-effective energy storage. Electrochemical technologies, such as electrolyzers, photoelectrochemical cells, and fuel cells, have the potential to compensate for solar energy intermittency on a large scale, by converting excess solar energy into storable solar fuels, such as hydrogen ( $H_2$ ), which can be converted back to electrical energy at a later time. However, improvements in the efficiency and lifetime of these technologies, in particular the electrocatalysts, are necessary for their commercialization. During operation, efficiency losses result from energetic penalties (overpotentials) associated with several processes occurring at or near the electrocatalyst/electrolyte (ohmic resistance, kinetic barriers, and mass transport limitations). These losses can be further exacerbated due to electrocatalyst durability issues such as dissolution, agglomeration, detachment, and poisoning. A major challenge in electrocatalysis field is developing methods to mitigate these losses without adversely affecting the electrocatalytic stability, selectivity, and/or activity.

One promising solution is an oxide-encapsulated electrocatalyst architecture, which has been shown to improve electrocatalyst durability and provide mechanisms for controlling reaction pathways. Previous studies on oxide-encapsulated electrocatalysts, in which metal catalysts are fully or partially covered by ultrathin layers of permeable oxide films, have mostly focused on supported nanoparticles because of their high electrochemically active surface area per catalyst loading. However, these nanoparticle-based architectures tend to have poorly defined and/or non-uniform structures which make it difficult to understand and elucidate structure-property-

relationships. This dissertation investigates well-defined oxide-coated electrocatalysts, which serve as model platforms for gaining a fundamental understanding of kinetic and transport phenomena that underlie their operation. This dissertation presents three studies which highlight the versatile functionalities of oxide-encapsulated electrocatalysts to improve the electrocatalyst stability, selectivity, and activity in different electrochemical systems. This dissertation demonstrates the ability of room temperature synthesized silicon oxide ( $\text{SiO}_x$ )-encapsulated Pt electrocatalysts to: i) stabilize nanoparticles and improve electron transfer, ii) mitigate catalyst poisoning and control reaction pathways through selective transport, and iii) alter reaction energetics associated with catalysis at the buried interface.

First, this dissertation establishes the ability of room temperature synthesized  $\text{SiO}_x$  coatings to stabilize nanoparticle electrocatalysts by mitigating electrocatalyst migration, coalescence, and detachment on metal-insulator-semiconductor (MIS) photoelectrodes for solar-driven water splitting. Metallic Pt nanoparticles are inherently unstable on the insulating support due to poor physical adhesion and electronic coupling between Pt and  $\text{SiO}_2$ . To overcome this issue, a room temperature UV ozone synthesis process was used to deposit 2-10 nm thick  $\text{SiO}_x$  overlayers on top of electrodeposited Pt nanoparticles to stabilize Pt on the electrode surface. The photoelectrodes containing oxide-encapsulated electrocatalysts exhibit superior durability and electron transfer (ohmic) properties compared to the photoelectrode that lacked the  $\text{SiO}_x$  encapsulation. While this study demonstrates that the oxide-encapsulated electrocatalyst architecture improves the stability of electrocatalytic nanoparticles deposited on insulating materials, it does not elucidate how reactants and products transport through the  $\text{SiO}_x$  barrier to reach the Pt surface.

In order to gain a better understanding of kinetic and transport phenomena that govern performance of oxide-encapsulated electrocatalysts, the following studies investigate model

electrodes consisting of continuous  $\text{SiO}_x$  overlayers of uniform thickness deposited onto smooth Pt thin films. This planar electrode geometry allows for simple and unambiguous characterization of structure-property relationships. The next study systematically evaluates the influence of  $\text{SiO}_x$  thickness on the HER performance to understand species transport through  $\text{SiO}_x$ . Through detailed characterization and electroanalytical tests, it is shown that proton and  $\text{H}_2$  transport occur primarily through the  $\text{SiO}_x$  coating such that the HER occurs at the buried Pt| $\text{SiO}_x$  interface. Importantly, the  $\text{SiO}_x$  nanomembranes were found to exhibit high selectivity for proton and  $\text{H}_2$  transport compared to  $\text{Cu}^{2+}$ , a model HER poison. Leveraging this property, it is shown that  $\text{SiO}_x$ -encapsulation can enable poison-resistant operation of Pt HER electrocatalysts. This oxide-encapsulated architecture offers a promising approach to enhancing electrocatalyst stability while incorporating advanced catalytic functionalities such as poison resistance or tunable reaction selectivity.

The final study demonstrates ability of  $\text{SiO}_x$  overlayers to alter reaction energetics associated with catalysis at the buried interface. Carbon monoxide (CO), methanol, and ethanol oxidation reactions are studied for their relevance in direct alcohol fuel cell applications. Oxide-supported catalysts have been shown to enhance alcohol oxidation by promoting CO oxidation at metal/oxide interfacial regions through the so-called bifunctional mechanism, in which hydroxyls on the oxide facilitate the removal of adsorbed CO-intermediates from active sites. A key advantage of the oxide-encapsulated electrocatalyst design compared to oxide-supported nanoparticles is that the former maximizes the density of metal/oxide interfacial sites. This study shows that the  $\text{SiO}_x$  overlayer provides proximal hydroxyls, in the form of silanol groups, which can enhance CO and alcohol oxidation through unique interactions at the buried Pt| $\text{SiO}_x$  interface. Overall, this dissertation highlights the potential of using oxide-encapsulated electrocatalysts for stable, selective, and efficient electrochemical production and use of solar fuels.

## TABLE OF CONTENTS

<b>List of Figures.....</b>	<b>x</b>
<b>List of Tables .....</b>	<b>xxv</b>
<b>Acknowledgements .....</b>	<b>xxvi</b>
<b>Chapter 1 Introduction .....</b>	<b>1</b>
1.1 Solar Energy Storage and Solar Fuels .....	1
1.2 Electrochemical Technologies for Solar Fuel Production and Conversion .....	2
1.2.1 Electrolyzers .....	3
1.2.2 Photoelectrochemical Cells .....	5
1.2.3 Fuel Cells .....	6
1.3 Electrolyzer, Photoelectrochemical Cell, and Fuel Cell Performance Metrics .....	8
1.4 Electrode Materials and Design .....	10
1.5 Photoelectrode Materials and Design .....	11
1.5.1 Light Absorption and Charge Carrier Generation .....	12
1.5.2 Charge Carrier Separation, Diffusion, Drift, and Collection.....	13
1.5.3 Challenges and Requirements.....	15
1.5.4 Metal-Insulator-Semiconductor Photoelectrode .....	18
1.6 Electrocatalyst Requirements.....	20
1.6.1 Stability.....	21
1.6.2 Selectivity .....	24
1.6.3 Activity .....	25
1.7 Oxide Encapsulated Electrocatalysts .....	26
1.7.1 Overview of Similar Electrocatalyst Architectures .....	27

1.7.2	Challenges with the Rational Design of Oxide-Encapsulated Electrocatalysts .....	29
1.8	Dissertation Overview .....	30
1.9	References .....	33
<b>Chapter 2</b>	<b>Experimental Methods .....</b>	<b>47</b>
2.1	Materials .....	47
2.1.1	Silicon .....	47
2.1.2	Silicon Oxide .....	49
2.1.3	Polydimethylsiloxane .....	50
2.1.4	Platinum .....	51
2.1.5	Nanoparticles versus Thin Films .....	52
2.2	Materials Synthesis Methods .....	53
2.2.1	Electrodeposition .....	53
2.2.2	Electron Beam Physical Vapor Deposition .....	54
2.2.3	Ultraviolet Ozone Photochemistry .....	55
2.3	Materials Characterization Techniques .....	56
2.3.1	Ellipsometry .....	56
2.3.2	Scanning Electron Microscopy .....	57
2.3.3	Atomic Force Microscopy .....	57
2.3.4	Ultraviolet-Visible Spectroscopy .....	58
2.3.5	X-ray Photoelectron Spectroscopy .....	59
2.3.5.1	Quantitative Data Analysis .....	61
2.4	Electrochemical Characterization .....	62

2.4.1	Three-Electrode Electrochemical Cell.....	62
2.4.1.1	Reference Electrode.....	63
2.4.2	Photoelectrochemical Test Cell.....	64
2.4.2.1	Light Source Calibration.....	65
2.4.3	Standard Electroanalytical Techniques.....	65
2.5	References.....	66

### **Chapter 3 Enhanced Performance of Silicon MIS Photocathodes Containing Oxide-Coated**

	<b>Nanoparticle Electrocatalysts .....</b>	<b>70</b>
3.1	Introduction.....	71
3.2	Experimental Methods.....	73
3.2.1	SiO <sub>x</sub>  Pt native SiO <sub>2</sub>  Si Fabrication .....	73
3.2.1.1	SiO <sub>2</sub>  Si Electrode Preparation.....	73
3.2.1.2	Platinum Photoelectrodeposition.....	73
3.2.1.3	SiO <sub>x</sub> Film Synthesis.....	75
3.2.1.4	Electron Beam Evaporated Metal Layers.....	76
3.2.2	Materials Characterization.....	76
3.2.2.1	Scanning Electron Microscopy.....	76
3.2.2.2	X-ray Photoelectron Spectroscopy .....	77
3.2.2.3	Scanning Transmission Electron Microscopy .....	78
3.2.2.4	Ultraviolet-Visible Spectroscopy.....	78
3.2.3	Electrochemical Characterization.....	78
3.2.3.1	Photoelectrochemical Characterization .....	78
3.2.3.2	Scanning Photocurrent Microscopy.....	79



3.2.3.3	Ferri/Ferrocyanide Cyclic Voltammograms .....	80
3.2.3.4	Variable Illumination Intensity .....	81
3.3	Results.....	81
3.3.1	Description of Insulator-Metal-Insulator-Semiconductor Photoelectrode ....	81
3.3.2	Characterization.....	82
3.3.2.1	Platinum Particle Analysis.....	82
3.3.2.2	Chemical and Physical Structure .....	84
3.3.3	Photoelectrochemical Performance .....	87
3.3.3.1	Control Electrodes: UV Ozone Treated Platinum and SiO <sub>x</sub> without Platinum.....	90
3.3.4	Photoelectrochemical Stability .....	91
3.3.4.1	Short-Term.....	91
3.3.4.2	Long-Term.....	93
3.4	Discussion .....	96
3.4.1	Understanding Origins of Poor Performance .....	96
3.4.1.1	Light Absorption and Catalysis .....	96
3.4.1.2	Charge Carrier Transport.....	97
3.4.1.3	Electron Tunneling .....	98
3.4.1.3.1	High Tunneling Current Density.....	98
3.4.1.3.2	Voltage Penalty .....	99
3.4.2	Hypothesis for Observed Improvement in Performance .....	101
3.4.2.1	Additional Carrier Transport Pathways .....	102
3.4.3	Understanding Origins of Instability during PEC Operation .....	104

3.4.3.1	Pt Nanoparticle Adhesion .....	104
3.4.3.2	Degradation Dependence on Operating Current Density .....	107
3.5	Conclusions.....	108
3.6	Appendix.....	109
3.6.1	Summary of Particle Characterization for Electrodes in Figures 3.10, 3.12, and 3.13.....	109
3.6.2	XPS Characterization of Pristine MIS, IMIS, and IIS Samples .....	110
3.6.3	Summary of Particle Characterization for Electrodes in Figure 3.14.....	111
3.6.4	Effective Carrier Diffusion Length.....	111
3.6.5	Summary of Particle Characterization for Electrodes in Figure 3.23.....	112
3.6.6	Cyclic Voltammetry Modelling for Device Series Resistance .....	114
3.7	Acknowledgements.....	115
3.8	References.....	115

<b>Chapter 4</b>	<b>Hydrogen Evolution at the Buried Interface between Platinum Thin Films and Silicon Oxide Nanomembranes.....</b>	<b>122</b>
4.1	Introduction.....	123
4.2	Experimental Section .....	127
4.2.1	SiO <sub>x</sub>  Pt Fabrication .....	127
4.2.1.1	Electrode Preparation.....	127
4.2.1.2	SiO <sub>x</sub> Film Synthesis .....	127
4.2.2	Structural Characterization .....	128
4.2.2.1	Ellipsometry and Ellipsometric Porosimetry .....	128
4.2.2.2	Scanning Electron and Atomic Force Microscopy .....	129

4.2.2.3	X-ray Photoelectron Spectroscopy .....	129
4.2.3	Electrochemical characterization .....	129
4.2.3.1	Series Resistance .....	130
4.2.3.2	Hydrogen and Copper Underpotential Deposition .....	130
4.3	Results .....	131
4.3.1	Description of SiO <sub>x</sub> -Encapsulated Pt MCEC Electrodes for HER Electrocatalysis .....	131
4.3.2	Characterization of SiO <sub>x</sub> Overlayers .....	132
4.3.2.1	SiO <sub>x</sub> Thickness and Surface Topology .....	132
4.3.2.2	SiO <sub>x</sub> Porosity .....	135
4.3.2.3	SiO <sub>x</sub> Composition .....	135
4.3.3	Electrochemically Active Surface Area of SiO <sub>x</sub> -Encapsulated Pt Thin Films .....	137
4.3.3.1	Hydrogen Underpotential Deposition.....	138
4.3.3.2	Copper Stripping.....	140
4.3.4	Hydrogen Evolution Reaction Performance .....	143
4.3.5	Evaluating the Contribution of Holes in SiO <sub>x</sub> Overlayers to HER Current	145
4.3.5.1	HER Performance for SiO <sub>x</sub> Bilayer Electrode.....	145
4.3.5.2	HER Performance in the Presence of a Poison.....	146
4.4	Discussion .....	149
4.4.1	SiO <sub>x</sub> Selectivity.....	149
4.4.2	SiO <sub>x</sub> Permeability .....	151
4.4.3	SiO <sub>x</sub> Impact on Concentration Overpotential .....	154

4.4.4	Inspire Future Studies .....	155
4.5	Conclusions .....	156
4.6	Appendix .....	157
4.6.1	Ellipsometric Porosimetry .....	157
4.6.2	Tafel Analysis .....	158
4.6.3	XPS Characterization of SiO <sub>x</sub> Film after Copper Poisoning Test .....	160
4.6.4	Electrochemical Activity on SiO <sub>x</sub> Only .....	161
4.6.5	Derivation of Concentration Overpotential for a 1D Permeable Overlayer .....	161
4.6.6	Fitting Procedure For Modeling HER LSV Curves .....	165
4.7	Acknowledgments .....	166
4.8	References .....	167

## **Chapter 5 Silicon Oxide-Encapsulated Platinum Thin Films as Highly Active**

	<b>Electrocatalysts for Carbon Monoxide and Alcohol Oxidation .....</b>	<b>176</b>
5.1	Introduction .....	177
5.2	Experimental Methods .....	182
5.2.1	Electrode Preparation .....	182
5.2.2	Structural Characterization .....	182
5.2.3	Electrochemical Characterization .....	183
5.3	Results .....	185
5.3.1	Characterization .....	185
	5.3.1.1 Physical and Chemical Characterization .....	185
	5.3.1.2 Electrochemically Active Surface Area .....	186
5.3.2	CO stripping voltammetry .....	187

5.3.3	Cyclic voltammetry in methanol, ethanol, and formic acid.....	190
5.3.3.1	Methanol Oxidation .....	190
5.3.3.2	Ethanol Oxidation .....	192
5.3.3.3	Formic Acid Oxidation .....	193
5.3.4	Role of Pt-OH <sub>ad</sub> and PtO <sub>x</sub> on methanol oxidation .....	194
5.3.5	Electrocatalyst stability .....	196
5.4	Discussion .....	199
5.4.1	Role of SiO <sub>x</sub> in Bifunctional Mechanism .....	199
5.4.2	Oxophilicity and Reactivation Efficiency .....	201
5.4.3	Role of Silanol Groups in CO and Methanol Oxidation.....	203
5.5	Conclusions .....	205
5.6	Appendix .....	206
5.6.1	CO Stripping on UV Ozone Treated Platinum .....	206
5.6.2	Methanol Oxidation Behavior for Varied CV Upper Vertex Potentials.....	207
5.6.3	AFM and XPS Characterization of SiO <sub>x</sub> Films Post Methanol CV Measurements .....	207
5.7	Acknowledgments .....	208
5.8	References .....	209
<b>Chapter 6 Conclusions and Future Directions .....</b>		<b>218</b>
6.1	Future Directions of Oxide-Encapsulated Electrocatalysts .....	219
6.1.1	Modification of Oxide Overlayers .....	219
6.1.1.1	Incorporate Dopants .....	220
6.1.1.2	Change Oxide Precursor .....	220

6.1.1.3	Alter Synthesis Technique .....	222
6.1.2	Preventing Dissolution of Electrocatalyst Materials .....	223
6.1.2.1	Apply to Overlayers to Smaller Nanoparticles .....	224
6.1.3	Extend Poison Resistance .....	226
6.1.3.1	Operation in Hudson River Water .....	226
6.1.3.2	Other Design Considerations that Influence Species Transport Through Overlayers .....	230
6.2	Integrating Oxide-Encapsulated Electrocatalysts into Electrochemical Technologies .....	232
6.3	References .....	233

## LIST OF FIGURES

Figure 1.1. Schematic of key technologies for a solar fuels-based energy system. a) PV solar cell, b) PEM electrolyzer, c) H <sub>2</sub> storage, d) PEM fuel cell, and e) photoelectrochemical (PEC) cell.....	3
Figure 1.2. Schematic of a direct alcohol fuel cell for converting alcohol fuels to electricity. ....	7
Figure 1.3. Energy band diagram of a semiconductor illustrating fundamental absorption. The photon energy is defined by $h\nu$ , where $h$ is Planck's constant and $\nu$ is the frequency of the photon. $E_g$ is the gap in energy between $E_v$ (highest occupied energy level) and $E_c$ (lowest unoccupied energy level). ....	13
Figure 1.4. Energy band diagrams for a) p-n junction in a solar PV cell and b) liquid junction in a photocathode used in a PEC. ....	14
Figure 1.5. Solar spectrum power density as a function of photon wavelength and energy/band gap energy to illustrate the tradeoffs between photovoltage, photocurrent, power density, and stability .....	17
Figure 1.6. a) Side view schematic of a metal-insulator-semiconductor (MIS) photoelectrode for stable and efficient solar water splitting. b) Energy band diagram illustrating operation of a MIS photocathode with the HER occurring at liquid interface. ....	19
Figure 1.7. Schematic of four common electrocatalyst degradation mechanisms: i) dissolution, ii) re-deposition and/or aggregation (particle migration and coalescence), iii) detachment, and iv) poisoning by an impurity species. ....	22
Figure 1.8. Side view schematic of an oxide coated electrocatalysts architecture in which an ultrathin oxide overlayer anchors catalyst (e.g. Pt) nanoparticles to the support surface	

to prevent migration and detachment and selectively allows the desired redox chemistry ( $O + n e^- \leftrightarrow R$ ) while suppressing undesirable poisoning and dissolution. ....	26
Figure 1.9. Side view schematics of silicon oxide ( $SiO_x$ )-encapsulated Pt electrocatalyst a) nanoparticles (Chapter 3) and b) thin films (Chapters 4 and 5) investigated in this dissertation. The substrate in (a) is a p-type Si (p-Si) semiconductor with an ultrathin native oxide layer (not labeled for clarity), whereas the substrate in (b) is the Pt film itself, which creates a well-defined, planar structure that removes complexities associated with semiconductors and non-uniformly coated nanoparticles. ....	31
Figure 2.1. Polydimethylsiloxane (PDMS) polymer structure. ....	50
Figure 2.2. a) Front view image of the photoelectrochemical (PEC) test cell used in this dissertation. Shown is a photoelectrode working electrode (WE) and reference electrode (RE). b) Side view image of PEC cell under illumination (light source originating from the left side of the image). A Pt counter electrode is shown in a separate compartment from the WE and RE.....	64
Figure 3.1. Nanoparticle-based MIS and IMIS photoelectrodes. Schematic side views of a metal- insulator-semiconductor (MIS) photoelectrode decorated with electrodeposited Pt nanoparticles and an insulator-metal-insulator-semiconductor (IMIS) photoelectrode containing an additional $SiO_x$ overlayer. ....	73
Figure 3.2. CV and LSV in electrodeposition solution. Current-potential curves for $SiO_2/p-Si$ (100) in 3 mmol $L^{-1}$ potassium tetrachloroplatinate. CV scan between -50 mV to -450 mV vs. Ag AgCl at 50 $mV s^{-1}$ scan rate for a) 5, b) 10, and c) 20 cycles. d) CV scan between +450 mV to -800 mV Ag AgCl at 50 $mV s^{-1}$ scan rate to determine potential range for	



electrodeposition. Inset zooms in on the onset potentials for Pt deposition in scans 1 and 2.....	75
Figure 3.3. Side-view schematic of SPCM measurement set-up used for determining the effective diffusion length in MIS and IMIS control samples in which the metal component, or collector, consisted of e-beam deposited 500 $\mu\text{m}$ bilayer islands with 3 nm Pt on top of 2 nm of Ti.....	80
Figure 3.4. Schematic side-view illustrating the basic operating processes occurring in an IMIS photoelectrode.....	82
Figure 3.5. Top view SEM images. Representative SEM images of MIS photoelectrodes with Pt loadings of 1, 5, and 20 $\mu\text{g cm}^{-2}$ .....	83
Figure 3.6. MIS and IMIS side-view. Representative cross sectional FE-SEM images of a) MIS and b) IMIS samples generally reveal smoother Pt nanoparticle features on the IMIS surface than compared to the MIS surface. The smooth features indicate the $\text{SiO}_2$ overlayer coating over and around most of the spikey Pt nanoparticles as suggested by the schematics in Figure 3.1 and 3.4.....	83
Figure 3.7. Cross sectional HAADF-STEM image of a $\text{SiO}_x \text{Pt} \text{native SiO}_2 \text{p-Si}$ IMIS nanojunction based on a 10 nm thick $\text{SiO}_x$ overlayer with Pt protection layer. ....	84
Figure 3.8. Cross section of the IMIS photoelectrodes revealed by HAADF-STEM. a) Low magnification STEM images of a 10 nm $\text{SiO}_x \text{Pt} \text{native SiO}_2 \text{p-Si}$ IMIS sample showing the $\text{SiO}_x$ overlayer on native $\text{SiO}_2 \text{Si}$ substrate. b) High resolution HAADF-STEM showing the structure details of an IMIS photoelectrode. c) Atomic resolved HAADF-STEM illustrates that the Pt cluster consists of small Pt particles oriented differently. The Pt area marked by the blue arrow in coincidentally laid in the zone axis to show	

clear 2D atomic column distribution, while in neighboring areas marked by black arrows the Pt particles are disoriented with different lattice. d) Additional STEM image revealing some larger particles protrude out of the SiO <sub>x</sub> shell. ....	85
Figure 3.9. STEM-XEDS mapping of an IMIS photoelectrode. a) The Pt map showing a cluster of Pt on top of SiO <sub>2</sub> layer. b) The Si map shows a weak shell structure on the top surface of Pt cluster. c) The overlay of Pt (red) and Si (green) maps show the relative distribution of those two elements. d) The XEDS spectra from 3 representative sites showing the different presence of Si and Pt signal. ....	87
Figure 3.10. MIS and IMIS performance. LSV measurements for  Pt native SiO <sub>2</sub>  p-Si(100) MIS (red) and  2 nm SiO <sub>x</sub>  Pt native SiO <sub>2</sub>  p-Si(100) IMIS (blue) photoelectrodes for a.) 1 μg cm <sup>-2</sup> Pt, b.) 5 μg cm <sup>-2</sup> Pt, and c.) 20 μg cm <sup>-2</sup> Pt. d.) LSV measurements for  ‘x’ nm SiO <sub>x</sub>  5 μg cm <sup>-2</sup> Pt native SiO <sub>2</sub>  p-Si(100) for various SiO <sub>x</sub> thicknesses from 0 nm to 10 nm. All LSV measurements were performed at 20 mV s <sup>-1</sup> in 0.5 mole L <sup>-1</sup> H <sub>2</sub> SO <sub>4</sub> under AM 1.5 G illumination. Current densities are normalized with respect to the geometric area of the exposed photoelectrode. ....	88
Figure 3.11. PEC performance of UV ozone treated MIS and bare SiO <sub>2</sub> control samples. LSV measurements in 0.5 mol L <sup>-1</sup> H <sub>2</sub> SO <sub>4</sub> under 1 sun of AM 1.5G illumination for a) UV ozone treated MIS 5 μg cm <sup>-2</sup> Pt native SiO <sub>2</sub>  p-Si(100) and b) ‘x’ nm SiO <sub>x</sub>  native SiO <sub>2</sub>  p-Si(100) control samples. ....	91
Figure 3.12. Short-term stability. LSV measurements in 0.5 mol L <sup>-1</sup> H <sub>2</sub> SO <sub>4</sub> under 1 sun of AM 1.5 G illumination for ‘x’ nm SiO <sub>x</sub>  ‘y’ μg cm <sup>-2</sup> Pt native SiO <sub>2</sub>  p-Si(100) for various SiO <sub>x</sub> thicknesses (x) from 0 nm to 10 nm and various amounts of Pt loading (y) from 1 to 20 μg cm <sup>-2</sup> and. Dark LSVs and LSV’s 1, 2, and 3 are shown. a-c) 1, 5, and 20 μg cm <sup>-2</sup> Pt	

with 0 nm SiO <sub>x</sub> , d-f) with 2 nm SiO <sub>x</sub> , and g-h) 5 μg cm <sup>-2</sup> Pt with 5 and 10 nm SiO <sub>x</sub> . The LSV scan rate was 20 mV s <sup>-1</sup> .....	92
Figure 3.13. 1 hour stability tests. Chronopotentiometry stability measurements in 0.5 mol L <sup>-1</sup> H <sub>2</sub> SO <sub>4</sub> for a) MIS Pt native SiO <sub>2</sub>  p-Si(100) and b) IMIS 2 nm SiO <sub>x</sub>   Pt native SiO <sub>2</sub>  p-Si(100) for various amounts of Pt loading, and for c) ‘x’ nm SiO <sub>x</sub>  5 μg cm <sup>-2</sup> Pt native SiO <sub>2</sub>  p-Si(100) for various SiO <sub>x</sub> thicknesses from 0 to 10 nm operating at -10 mA cm <sup>-2</sup> for 1 hr under 1 sun of AM 1.5G illumination. Open-circuit potentials were measured twice for 1 minute during the study. The larger fluctuations in potential for the MIS photoelectrode are caused by differences in bubble growth and detachment. d) LSV measurements for MIS (red) and IMIS (black) samples with 5 μg cm <sup>-2</sup> Pt loading before (solid lines) and after (dashed lines) the 1 hr CP stability test conducted at -10 mA cm <sup>-2</sup> for 1 hr. Measurements performed in 0.5 mole L <sup>-1</sup> H <sub>2</sub> SO <sub>4</sub> under simulated AM 1.5 G illumination. ....	94
Figure 3.14. Long-term stability. CP stability measurements for MIS (red) and IMIS (black) samples with 12 μg cm <sup>-2</sup> Pt loading operating at -10 mA cm <sup>-2</sup> for 12 hrs. Measurements performed in 0.5 mole L <sup>-1</sup> H <sub>2</sub> SO <sub>4</sub> under simulated AM 1.5 G illumination. ....	95
Figure 3.15. Light transmittance and catalytic activity of electrodeposited Pt particles. a) UV-Vis on Pt transparent indium tin oxide (ITO) and b) LSV measurements in 0.5 mol L <sup>-1</sup> H <sub>2</sub> SO <sub>4</sub> for 5 μg cm <sup>-2</sup> Pt ITO glass sample. LSV scan rate was 20 mV s <sup>-1</sup> . c) SEM image of Pt ITO glass.....	97
Figure 3.16. Current densities normalized to net particle area. a) LSV measurements from Figure 3.10a for MIS Pt native SiO <sub>2</sub>  p-Si(100) for various amounts of Pt loading normalized by illuminated and junction area and b) a zoomed in plot. ....	99

Figure 3.17. Voltage penalty at large tunneling current densities. a) Normalized I-V measurements in air for a 45  $\mu\text{m}$  diameter 20 nm Pt|30 nm Ti circular contact, that was e-beam deposited onto 2 nm RTO  $\text{SiO}_2$ |p-Si, under varying intensities of 532 nm laser illumination. The listed current densities are normalized to the junction area, taken to be the area of the e-beam deposited metal contact. b) Optical image of a tungsten probe in contact with a metal contact. I-V curves were measured at a scan rate of 100  $\text{mV s}^{-1}$ . ..... 100

Figure 3.18. Alternative carrier transport pathways. Schematic side-view of IMIS photoelectrode illustrating possible charge transfer pathways between the Si substrate and Pt nanoparticles. Pathways include (1) conventional tunneling through MIS nano-junction and (2),(3) alternative charge transfer routes involving conduction through the  $\text{SiO}_x$ . ..... 101

Figure 3.19. Analyzing carrier transport pathways. a.) CV measurements in 10  $\text{mmol L}^{-1}$  ferri/ferrocyanide, 1  $\text{mole L}^{-1}$  KCl solution for 3 nm Pt|2 nm Ti|‘x’ nm  $\text{SiO}_x$ |native  $\text{SiO}_2$ |p-Si(100) for various  $\text{SiO}_x$  thicknesses from 0 nm to 10 nm. The CV sweep rate was 100  $\text{mV s}^{-1}$ . b.) Peak-to-peak splitting voltage (circles) and corresponding charge transfer resistances (squares) associated with the CV curves in a.). ..... 103

Figure 3.20. SEM images of MIS photoelectrode before and after PEC LSVs. SEM images of a 5  $\mu\text{g cm}^{-2}$  Pt|native  $\text{SiO}_2$ |p-Si(100) a) before and b) after 3 LSVs in 0.5  $\text{mol L}^{-1}$   $\text{H}_2\text{SO}_4$ . c) First (solid) and third (dashed) LSV measurements in 0.5  $\text{mol L}^{-1}$   $\text{H}_2\text{SO}_4$  under 1 sun of AM 1.5G illumination for 5  $\mu\text{g cm}^{-2}$  Pt|native  $\text{SiO}_2$ |p-Si(100). ..... 105

Figure 3.21. Low resolution SEM images of c.) MIS and d.) IMIS samples after the 12 hr CP stability test in Figure 3.14. .... 106

- Figure 3.22. Effect of light intensity and tunneling current density on MIS stability. CV measurements in  $0.5 \text{ mol L}^{-1} \text{ H}_2\text{SO}_4$  for low and high Pt loaded MIS samples under a) 0.25 sun and b) 1 sun intensity. CV scan rate was  $20 \text{ mV s}^{-1}$  for 5 cycles. Grey curves: low Pt loading. Black curves: high Pt loading. .... 108
- Figure 3.23. XPS results. X-ray photoelectron spectra of 10 nm  $\text{SiO}_x$ |native  $\text{SiO}_2$ |p-Si(100) a) Survey, b) Si 2p, c) C 1s, d) O 1s, and e) Pt 4f. The PDMS was converted into  $\text{SiO}_2$  with trace amounts of carbon remaining. The  $\text{SiO}_x$ | $\text{SiO}_2$ |Si (IIS) contained 50% higher C 1s signal compared to samples containing native  $\text{SiO}_2$  (IS) where the carbon only arises from adventitious carbon compounds. .... 110
- Figure 3.24.  $L_e$  measurements on MIS and 10 nm IMIS. a) Side-view schematic of SPCM measurement set-up used for determining the effective diffusion length in MIS and IMIS control samples in which the metal component, or collector, consisted of e-beam deposited  $500 \text{ }\mu\text{m}$  bilayer islands with 3 nm Pt on top of 2 nm of Ti. b) Plots of  $\ln(J_N)$  versus  $D_L$ , measured with a 532 nm laser focused to a beam diameter of  $\approx 3 \text{ }\mu\text{m}$  and with incident power of  $13.3 \text{ }\mu\text{W}$ . .... 112
- Figure 3.25. LSV before and after stability test. LSV measurements in  $0.5 \text{ mol L}^{-1} \text{ H}_2\text{SO}_4$  under 1 sun of AM 1.5G illumination for 'x' nm  $\text{SiO}_x$ |'y'  $\mu\text{g cm}^{-2}$  Pt|native  $\text{SiO}_2$ |p-Si(100) for various amounts of Pt loading from 1 to  $20 \mu\text{g cm}^{-2}$  and various  $\text{SiO}_x$  thicknesses from 0 to 10 nm. a-c) 1, 5, and  $20 \mu\text{g cm}^{-2}$  Pt with 0 nm  $\text{SiO}_x$ , d-f) with 2 nm  $\text{SiO}_x$ , and g-h)  $5 \mu\text{g cm}^{-2}$  Pt with 5 and 10 nm  $\text{SiO}_x$ . The LSV scan rate was  $20 \text{ mV s}^{-1}$ . .... 113
- Figure 3.26. Simulated cyclic voltammograms for total series resistance. CV of a) 3 nm Pt|2 nm Ti|1.5 nm  $\text{SiO}_2$ |p-Si and b) 3 nm Pt|2 nm Ti|2 nm  $\text{SiO}_x$ |1.5 nm  $\text{SiO}_2$ |p-Si in

ferri/ferrocyanide solution compared to a simulated fit using EC-lab software. CV scan rate was 100 mV s <sup>-1</sup> .....	115
Figure 4.1. a.) Planar electrode platform for studying membrane-coated electrocatalysts (MCECs) in which a thin, permeable SiO <sub>x</sub> overlayer uniformly coats an electroactive catalyst. b.) Schematic side view illustrating the basic operating process of hydrogen evolution at a planar metallic electrocatalyst (Pt) covered by an ultrathin SiO <sub>x</sub> overlayer of thickness t <sub>SiO<sub>x</sub></sub> that (i) enables facile transport of reactants and products to and from the electrocatalyst surface. Also shown is a (ii) macroscopic opening in the SiO <sub>x</sub> through which reactants and products may transport to the electrocatalyst interface unimpeded by the SiO <sub>x</sub> and (iii) a non-penetrating hole or crack in the SiO <sub>x</sub> in which a barrier film remains at the bottom of the holes. ....	132
Figure 4.2. Top view SEM images. Representative SEM images of SiO <sub>x</sub>  Pt electrodes containing: a.) t <sub>SiO<sub>x</sub></sub> =0 nm, b.) t <sub>SiO<sub>x</sub></sub> =1.9 nm , c.) t <sub>SiO<sub>x</sub></sub> =4.6 nm, d.) t <sub>SiO<sub>x</sub></sub> =9.4 nm, and e.) t <sub>SiO<sub>x</sub></sub> =19.8 nm SiO <sub>x</sub> films. Brightness and contrast were increased to see features more clearly. ....	133
Figure 4.3. Surface topology characterization of SiO <sub>x</sub> coated Pt thin films. AFM images of as-made SiO <sub>x</sub>  Pt electrodes and corresponding depth profiles over holes for: a.) t <sub>SiO<sub>x</sub></sub> =0 nm, b.) t <sub>SiO<sub>x</sub></sub> =1.9 nm, c.) t <sub>SiO<sub>x</sub></sub> =4.6 nm, d.) t <sub>SiO<sub>x</sub></sub> =9.4 nm, e.) t <sub>SiO<sub>x</sub></sub> =19.8 nm SiO <sub>x</sub> films. f.) Percent areal coverage of holes, hole density, and average hole depth normalized by the ellipsometry measured SiO <sub>x</sub> thickness for each SiO <sub>x</sub> film thickness. Characteristics in (f) were calculated from 15 1 μm <sup>2</sup> images from each sample. ....	134
Figure 4.4. XPS characterization of SiO <sub>x</sub> overlayer. X-ray photoelectron spectra of SiO <sub>x</sub>  Pt electrodes a.) Si 2p, b.) Pt 4f, c.) O 1s, and d.) C 1s for various SiO <sub>x</sub> thicknesses: t <sub>SiO<sub>x</sub></sub> =0	

nm (red),  $t_{\text{SiO}_x}=1.9$  nm (blue),  $t_{\text{SiO}_x}=4.6$  nm (green),  $t_{\text{SiO}_x}=9.4$  nm (black), and  $t_{\text{SiO}_x}=19.8$  nm (purple). The C 1s peaks were shifted and centered to 284.8 eV and the O 1s peaks associated with the  $\text{SiO}_x$  overlayers were shifted by the same amount. .... 137

Figure 4.5. Measuring ECSA with  $H_{\text{upd}}$ . a.) CV  $H_{\text{upd}}$  in deaerated 0.1 M  $\text{H}_2\text{SO}_4$  for  $\text{SiO}_x|\text{Pt}$  electrodes containing:  $t_{\text{SiO}_x}=0$  nm (red),  $t_{\text{SiO}_x}=1.9$  nm (blue),  $t_{\text{SiO}_x}=4.6$  nm (green),  $t_{\text{SiO}_x}=9.4$  nm (black), and  $t_{\text{SiO}_x}=19.8$  nm (purple)  $\text{SiO}_x$  films at 100  $\text{mV s}^{-1}$  and b.) 25  $\text{mV s}^{-1}$  in. c.)  $H_{\text{upd}}$  determined ECSAs at different scan rates for  $\text{SiO}_x|\text{Pt}$  electrodes in (a). Error bars represent 2-sided 95% confidence intervals based on repeated CV measurements..... 139

Figure 4.6. Measuring ECSA with  $\text{Cu}_{\text{upd}}$ . Cu stripping in 2 mM  $\text{CuSO}_4$  and 0.1 M  $\text{H}_2\text{SO}_4$  (solid curves) and background current in the 0.1 M  $\text{H}_2\text{SO}_4$  supporting electrolyte (dashed curves) at 100  $\text{mV s}^{-1}$  for a.)  $t_{\text{SiO}_x}=0$  nm (red) and  $t_{\text{SiO}_x}=1.9$  nm (blue), and b.)  $t_{\text{SiO}_x}=4.6$  nm (green),  $t_{\text{SiO}_x}=9.4$  nm (black), and  $t_{\text{SiO}_x}=19.8$  nm (purple)  $\text{SiO}_x|\text{Pt}$  electrodes. c.)  $H_{\text{upd}}$  (red) and  $\text{Cu}_{\text{upd}}$  (blue) determined ECSAs normalized by the respective  $H_{\text{upd}}$  (at 25  $\text{mV s}^{-1}$ ) and  $\text{Cu}_{\text{upd}}$  determined ECSAs for the bare Pt electrode and the fraction hole coverage from AFM (green) for each  $\text{SiO}_x|\text{Pt}$  electrode. All measurements were performed in deaerated solutions. .... 141

Figure 4.7.  $\text{H}_2$  evolution activity of  $\text{SiO}_x|\text{Pt}$  thin film electrocatalysts. LSV measurements in 0.1 M  $\text{H}_2\text{SO}_4$  for “x” nm  $\text{SiO}_x|\text{Pt}$  for various  $\text{SiO}_x$  thicknesses from 0 nm < x < 20 nm. All measurements were performed at 20  $\text{mV s}^{-1}$  in deaerated solutions. .... 144

Figure 4.8.  $\text{H}_2$  evolution activity of a bilayer  $\text{SiO}_x|\text{Pt}$  electrode. Schematic side view illustrating the sequential deposition of the a.) first and b.) second  $\text{SiO}_x$  layer to create the bilayer  $\text{SiO}_x|\text{Pt}$  electrode. AFM images of a c.)  $t_{\text{SiO}_x}=1.9$  nm  $\text{SiO}_x|\text{Pt}$  electrode and d.) the same

electrode after and additional $t_{\text{SiO}_x}=1.9$ nm $\text{SiO}_x$ layer. e.) LSV measurement in 0.1 M $\text{H}_2\text{SO}_4$ for the bilayer $\text{SiO}_x \text{Pt}$ MCEC described in (d). All measurements were performed at $20 \text{ mV s}^{-1}$ in deaerated solutions.....	146
Figure 4.9 Measuring selective proton transport through $\text{SiO}_x$ . Constant current ( $-5 \text{ mA cm}^{-2}$ ) stability tests conducted on a.) $t_{\text{SiO}_x}=0$ nm (red) and b.) $t_{\text{SiO}_x}=4.6$ nm (green) $\text{SiO}_x \text{Pt}$ electrodes in 0.5 M $\text{H}_2\text{SO}_4$ with and without (black) 0.2 mM $\text{CuSO}_4$ . SEM images of Cu deposits on c.) $t_{\text{SiO}_x}=0$ nm and d.) $t_{\text{SiO}_x}=4.6$ nm $\text{SiO}_x \text{Pt}$ electrodes after the 1 hour CP experiment in 0.2 mM $\text{CuSO}_4$ from a) and b).....	148
Figure 4.10. a.) Defining kinetic ( $\eta_{\text{HER}}$ ) and mass transfer ( $\eta_{\text{MT,bulk}}$ ) overpotential versus concentration overpotential ( $\eta_{\text{conc}}$ ) losses in LSVs for $t_{\text{SiO}_x}=0$ and $t_{\text{SiO}_x}=1.9$ nm MCEC electrodes. LSVs are $iR$ corrected. Comparison of experimental and modeled current density versus potential vs. RHE curves for b.) $t_{\text{SiO}_x}=1.9$ nm, c.) $t_{\text{SiO}_x}=4.6$ nm, and d.) $t_{\text{SiO}_x}=9.4$ nm MCEC electrodes. ....	152
Figure 4.11. $iR$ corrected LSVs normalized by ECSA. LSV measurements from Figure 4.7 for various $\text{SiO}_x$ thicknesses from $0 \text{ nm} < x < 10 \text{ nm}$ , zoomed in at relevant ECSA normalized current densities for electrolyzer operation. All LSVs are $iR$ corrected ( $R_s = 16 \Omega$ ) and normalized by the $H_{\text{upd}}$ determined ECSA from CVs performed at $25 \text{ mV s}^{-1}$ . The LSV for the 19.8 nm $\text{SiO}_x$ film is not included due to the uncertainty in quantification of the $H_{\text{upd}}$ determined ECSA. The low $H_{\text{upd}}$ signals complicated the deconvolution from the double layer capacitance. All measurements were performed at $20 \text{ mV s}^{-1}$ in deaerated solutions. ....	155
Figure 4.12. Ellipsometric porosimetry results. Adsorbed volume of toluene as a function of relative pressure for a.) $\approx 164$ nm thick mesoporous silica film with a mean pore radius	



of $\approx 9.4$ nm [Adapted from <i>Langmuir</i> <b>2012</b> , 28 (8), 3852–3859] and b.) 9.5 nm (black) and 107 nm (red) SiO <sub>x</sub> films made by UV ozone (this work).....	158
Figure 4.13. a.) Bare Pt LSV from Figure 4.11 and b.) corresponding Tafel plot. LSVs from Figure 4.7 were normalized by ECSA and $iR$ corrected prior to analysis (Figure 4.11). ....	159
Figure 4.14. XPS results after Cu poisoning test. XPS of 4.6 nm SiO <sub>x</sub>  Pt electrodes before (green) and after operating at $-5 \text{ mA cm}^{-2}$ for 1 hour in 0.5 M H <sub>2</sub> SO <sub>4</sub> with 0.2 mM CuSO <sub>4</sub> (orange) a.) Survey, b.) Si 2p, c.) O 1s, d.) Pt 4f, and e.) Cu 2p. The C 1s peaks were shifted and centered to 284.8 eV and the O 1s peaks associated with the SiO <sub>x</sub> overlayers were shifted by the same amount.....	160
Figure 4.15. H <sub>2</sub> evolution activity of SiO <sub>x</sub> films electrocatalysts. LSV measurements in 0.1 M H <sub>2</sub> SO <sub>4</sub> for a 9.4 nm SiO <sub>x</sub>  p <sup>+</sup> Si electrode to demonstrate lack of HER activity on SiO <sub>x</sub> alone. All LSV measurements were performed at $20 \text{ mV s}^{-1}$ in deaerated solutions	161
Figure 5.1. Schematic side view illustrating methanol oxidation at a planar Pt electrocatalyst covered by an ultrathin, permeable SiO <sub>x</sub> overlayer with thickness $t_{\text{SiO}_x}$ . The overlayer enables (i) transport of reactants and products to and from the electrocatalytic Pt SiO <sub>x</sub> buried interface. Also shown are adsorbed CO intermediates located at (ii) the buried interface and (iii) an opening in the SiO <sub>x</sub> film which can create a triple phase boundary site.....	180
Figure 5.2. AFM images of as-made a) 0 nm, b) 2 nm, and c) 5 nm SiO <sub>x</sub>  Pt electrodes.....	185
Figure 5.3. a.) Si 2p, b.) O 1s, c.) C 1s and d) Pt 4f XPS spectras for 0 nm (black), 2 nm (blue), and 5 nm SiO <sub>x</sub>  Pt electrodes. The C 1s peaks were shifted and centered to 284.8 eV and the O 1s peaks associated with the SiO <sub>x</sub> overlayers were shifted by the same amount. ....	186

Figure 5.4. CV curves (30 <sup>th</sup> cycle) recorded at 100 mV s <sup>-1</sup> in deaerated 0.5 M H <sub>2</sub> SO <sub>4</sub> for SiO <sub>x</sub>  Pt electrodes containing: t <sub>SiO<sub>x</sub></sub> =0 nm (black), t <sub>SiO<sub>x</sub></sub> =2 nm (blue), t <sub>SiO<sub>x</sub></sub> =5 nm (green) SiO <sub>x</sub> films .....	187
Figure 5.5. CO stripping voltammetry curves measured in 0.5 M H <sub>2</sub> SO <sub>4</sub> at a scan rate of 20 mV s <sup>-1</sup> for Pt (black), 2 nm SiO <sub>x</sub>  Pt (blue), and 5 nm SiO <sub>x</sub>  Pt (green). Solid curves represent the first CV cycle that was carried out with CO adsorbed on the electrode surface, while dashed curves represent the second CV cycle that was performed after CO was stripped from the electrode surface during the first cycle. ....	188
Figure 5.6. Methanol oxidation CV curves (cycle 30) measured at a scan rate of 100 mV s <sup>-1</sup> for bare Pt (black), 2 nm SiO <sub>x</sub>  Pt (blue), and 5 nm SiO <sub>x</sub>  Pt (green) in deaerated 0.5 M H <sub>2</sub> SO <sub>4</sub> solution containing 0.5 M CH <sub>3</sub> OH.....	191
Figure 5.7. Ethanol oxidation CV curves (cycle 30) measured at a scan rate of 100 mV s <sup>-1</sup> for bare Pt (black) and 5 nm SiO <sub>x</sub>  Pt (green) in deaerated 0.5 M H <sub>2</sub> SO <sub>4</sub> solution containing 0.5 M C <sub>2</sub> H <sub>5</sub> OH.....	193
Figure 5.8. Formic acid oxidation CV curves (cycle 30) measured at a scan rate of 100 mV s <sup>-1</sup> for bare Pt (black) and 5 nm SiO <sub>x</sub>  Pt (green) in deaerated 0.5 M H <sub>2</sub> SO <sub>4</sub> solution containing 0.5 M HCOOH.....	194
Figure 5.9. Methanol oxidation CVs (steady state cycle 15) with different upper scan vertices for a) t <sub>SiO<sub>x</sub></sub> = 0 nm and b) t <sub>SiO<sub>x</sub></sub> = 5 nm SiO <sub>x</sub>  Pt MCEC. c) Peak MOR current densities recorded during the forward (I <sub>f</sub> ) and backward (I <sub>b</sub> ) scan segments as a function of upper vertex potential. CVs were performed in 0.5 M H <sub>2</sub> SO <sub>4</sub> containing 0.5 M CH <sub>3</sub> OH and measured at 100 mV s <sup>-1</sup> .....	196

Figure 5.10. 1 <sup>st</sup> (red), 10 <sup>th</sup> (green), 50 <sup>th</sup> (blue), and 100 <sup>th</sup> (black) CV cycles for a) bare Pt and b) 5 nm SiO <sub>x</sub>  Pt in 0.5 M H <sub>2</sub> SO <sub>4</sub> containing 0.5 M CH <sub>3</sub> OH and measured at 100 mV s <sup>-1</sup> . .....	197
Figure 5.11 Methanol oxidation CVs after a KOH etch on bare Pt (black) and 5 nm SiO <sub>x</sub>  Pt (no SiO <sub>x</sub> remaining after KOH etch) CVs were performed in deaerated 0.5 M H <sub>2</sub> SO <sub>4</sub> with 0.5 M CH <sub>3</sub> OH and at 100 mV s <sup>-1</sup> . ....	198
Figure 5.12. a) CO stripping and b) methanol oxidation CVs (cycle 30) in pH neutral electrolyte, 0.1 M sodium phosphate (buffered), with 0.5 M methanol for (b), for bare Pt (black) and 5 nm SiO <sub>x</sub>  Pt (green) electrodes at a scan rate of 100 mV s <sup>-1</sup> . ....	205
Figure 5.13. CO stripping voltammetry curves measured in 0.5 M H <sub>2</sub> SO <sub>4</sub> at 20 mV s <sup>-1</sup> scan rate for bare Pt electrode that underwent two hours of UV ozone exposure. Solid curves represent the first CV cycle that was carried out with CO adsorbed on the electrode surface, while and dashed curves represent the second CV cycle that was performed after CO was stripped from the electrode surface during the first cycle. ....	206
Figure 5.14. Methanol oxidation CVs with different anodic voltage limits for a) t <sub>SiO<sub>x</sub></sub> = 0 nm and b) t <sub>SiO<sub>x</sub></sub> = 5 nm SiO <sub>x</sub>  Pt MCEC. Upper limit voltages of 0.8 V (red), 0.9 V (blue), 1.0V (green), 1.1 V (black), and 1.2 V (orange) vs. RHE are shown. The CV was returned to an upper limit of 0.8 V vs. RHE (purple). Peak forward and backward current densities as a function of upper potential limit. CVs were performed in deaerated 0.5 M H <sub>2</sub> SO <sub>4</sub> with 0.5 M CH <sub>3</sub> OH and measured within a potential range of 0.0 V to 1.2 V vs. RHE at 100 mV s <sup>-1</sup> . ....	207
Figure 5.15. AFM images of as made a) 0 nm, b) 2 nm, and c) 5 nm SiO <sub>x</sub>  Pt electrodes following 100 methanol oxidation CV cycles. ....	207

Figure 5.16. a) Si 2p, b) O 1s, c) C 1s and d) Pt 4f XPS spectra of the 5 nm SiO <sub>x</sub>  Pt electrodes before (solid) and after (dashed) 100 CV cycles at 100 mV s <sup>-1</sup> between potentials of 0.02 and 1.2 V RHE in 0.5 M CH <sub>3</sub> OH containing 0.5 M H <sub>2</sub> SO <sub>4</sub> . Upon completion of CV measurements, electrodes were rinsed with DI water, dried with compressed N <sub>2</sub> , and loaded into the XPS loading chamber.....	208
Figure 6.1. a) CP stability measurements for 0 nm SiO <sub>x</sub>  Pt NP and 10 nm SiO <sub>x</sub>  Pt NP photoelectrode operating at -10 mA cm <sup>-2</sup> for 7 hrs under AM 1.5G illumination. b) LSV measurements (20 mV s <sup>-1</sup> ) before and after the CP in (a). Experiments were performed under AM 1.5G illumination in 0.5 M H <sub>2</sub> SO <sub>4</sub> that was stirred at 1000 rpm to facilitate bubble removal.....	224
Figure 6.2. SEM images taken at x200.00k magnification of a) 0 nm SiO <sub>x</sub>  Pt NP and b) 10 nm SiO <sub>x</sub>  Pt NP before and c)/d) after stability measurements in Figure 6.1, respectively. Histograms of particle diameters before and after the 7 hr CP for e) 0 nm SiO <sub>x</sub>  Pt NP and f) 10 nm SiO <sub>x</sub>  Pt NP. ....	225
Figure 6.3. Electrocatalysis poisoning test performed in Hudson River water. Constant current density (-5 mA cm <sup>-2</sup> ) stability tests conducted on a) t <sub>SiO<sub>x</sub></sub> =0 nm (red) and b) t <sub>SiO<sub>x</sub></sub> =4.6 nm (green) SiO <sub>x</sub>  Pt electrodes in 0.5 M H <sub>2</sub> SO <sub>4</sub> with and without (black) unfiltered water obtained directly from the Hudson River.....	227
Figure 6.4. XPS results after Hudson River water poisoning test. XPS spectra of a bare Pt electrode: a) Survey, b) Cu 2p, c) Ag 3d, d) S 2p, and e) C 1 s, after operating at -5 mA cm <sup>-2</sup> for 3 hours in Hudson River water modified with 0.5 M H <sub>2</sub> SO <sub>4</sub> to concentrate deposited contaminants onto Pt surface to a detectable level. Atomic percent of each were 6 %, .....	

3%, 1%, and 23% respectively, while the Pt and O were 15 % and 50 % respectively.

..... 229

## LIST OF TABLES

Table 3.1. Summary of Pt particle characterization (based on SEM images), electrode performance (based on Figure 3.10), and degradation behavior (based on Figure 3.12, 3.13, and 3.25). See section 3.2.2.1 for more details on SEM analysis of Pt loading, Pt particle density, Pt surface area, Pt coverage, average Pt particle sizes and distances.....	89
Table 3.2. Summary of Pt structure characterization from SEM image analysis based on SEM images taken at a magnification of x50.0k times.....	109
Table 3.3. Surface composition of samples with and without the SiO <sub>x</sub> overlayer determined by XPS measurements. The SiO <sub>x</sub> thickness of IIS and IMIS samples is 10 nm. The Pt loading for MIS and IMIS samples is 5 μg cm <sup>-2</sup> . All compositions are expressed as atomic percentages as described in the text .....	111
Table 3.4. Summary of Pt structure characterization from SEM image analysis for samples in Figure 3.14. ....	111
Table 3.5. Summary of Pt structure characterization from SEM image analysis for samples in Figure 3.23. ....	112
Table 4.1 Characterization of SiO <sub>x</sub> overlayers deposited on Pt thin films, including characterization of SiO <sub>x</sub> thickness (based on ellipsometry), hole coverage (based on AFM images), and ECSA (based on H <sub>upd</sub> and Cu <sub>upd</sub> measurements in Figure 4.5 and 4.6).....	141
Table 4.2 H <sup>+</sup> and H <sub>2</sub> permeability through SiO <sub>x</sub> overlayers deposited on Pt thin films. Analysis is based on modeled LSVs in Figure 4.10. ....	153

## ACKNOWLEDGEMENTS

I would like to thank my advisor, Dr. Daniel V. Esposito, for the endless guidance, patience, support, enthusiasm, opportunities, coffee chats, and Snickers® breaks he's given me over these past five years. This dissertation is truly a testament of both of our accomplishments. As Dr. Esposito's first graduate student, I have been afforded a unique opportunity to learn directly under his mentorship and expertise. Thanks to his encouragement, I have been fortunate to present this work at many national conferences and networking events. Next I would like to thank my collaborators at Columbia University (CU), National Institute of Standards and Technology (NIST), and Ghent University (UGent) who have made my research possible, at CU: Dr. Jeffrey Koberstein, Chaturanga de Silva, and Sebastian Russel, at NIST: Dr. Thomas Moffat, Dr. Haiyan Tan, Dr. and Rongyue Wang, at UGent: Ranjith Ramachandran and Dr. Christophe Detavernier. I have learned so much from each of you and I appreciate the time and care that went into obtaining experimental information included in this work. Thank you to committee members: Dr. Alan West, Dr. Jingguang Chen, and Dr Ngai Yip, for their advice and guidance. I acknowledge financial support from Columbia University and the National Science Foundation.

Next, I would like to thank those whom I've had the pleasure of mentoring: Xinxin Li, Yukun Liu, Eva Songcuan, Han Chen, Sophia Kurdziel, Saumya Gulati, Cody Hirashima, Amit Dhanda, Bicheng Xu, Matt Mulvehill, Benjamin Sartor, Brice Lee, David Brown, Lucas Taub, Jeffrey Murphy, and Saring Agata. Your help with control experiments and data analysis has been extremely helpful. I'd like to give a special thank you and acknowledgment to Jacob Robinson for his major contributions to the content in Chapter 5. I'd also like to thank all the (sassy) group members and visiting scholars: Jonathan Davis, Dr. Glen O'Neil, Anna Dorfi, Dr. Xiangye Liu, Dr. Tom Bosserez, Marissa Beatty, and Dr. Ali Dagar, for our discussions relating to these projects

and for their constant support and laughs. It has been a pleasure working with and learning from all of you. I'll miss our daily interactions in the Dungeon Office, minus the coffee grinder.

Thank you to all the chemical engineering support and staff at Columbia for your tireless work that is vital for running operations in the department: Kathy Marte, Aurna Malakar, Krystal Paulino, Michelle McCormack, Rezarta Binaj, Teresa Colaizzo, Irina Katz, Andrew Strycharz, and Ariel Sanchez. To the rest of the chemical engineering community thank you for your friendship and support, also: Ellie Buenning, Alison Fankhauser, Chris Hawxhurst, and Nicholas Brady, thank you keeping me sane and aiding me during the several instances I was handicapped; Weiming Wan, Porakrit Leophairatana, Billy Guan, and Kolade Ololade, thank you for all our fun study sessions during our 1<sup>st</sup> year, Dr. Shyno Matthew, Dr. Yannick Kimmel, Dr. Thu Vi, and Dr. Joe Woo, thank you for your advice and mentorship, Brian Tackett, Christianna Lininger, Jonathan Vardner, Dr. Kirsten Garcia, Dr. Beyza Bulutoglu, Dr. Harun Ferit Ozbakir, and Emily Hsu thank you for providing a strong and fun chemical engineering community with ChEGO and the Lenfest Center for Sustainable Engineering.

Lastly, I'd like to thank all of my friends and family who have kept me well-balanced during my time at Columbia. Thank you to my friends and roommates for keeping me grounded over the years: Jennifer Lande, Jessica Lee, Angel Chan, Kirsten Kim, Rachael Barron, Sara Williams, Diana Beck, Kiran Kanekal, and Jonathan Cook. I'd like to give a huge thank you to my family. To my supportive parents, Debbie and Bob, thank you making me into the independent person I have become and for your patience with my sister, Paige, and I. Last, but not least, thank you to my loving husband, Dr. Kevin Knehr, for your optimism, love, support, laughs, and silly faces that always make me smile. Thank you for being the catalyst for everything I do.



# CHAPTER 1

## INTRODUCTION

### 1.1 Solar Energy Storage and Solar Fuels

The amount of solar energy that reaches the Earth is nearly 10,000 times more than the total global energy use. Thus, harvesting energy directly from sunlight offers a desirable solution towards meeting global energy needs without any carbon emissions.<sup>1</sup> However, the ability to store this huge energy reservoir in an efficient and cost-effective manner remains a challenge due to sunlight's inherently diffuse and intermittent nature. Large-scale energy storage can be accomplished by converting excess solar energy into storable chemical energy; commonly referred to as “solar fuels”.<sup>2</sup> While the storability of solar fuels makes them attractive for overcoming solar intermittency, they can also serve as carbon-neutral fuels across all energy sectors.<sup>1</sup>

There are many different types of solar fuels. One of the simplest and most commonly-explored solar fuels is hydrogen ( $H_2$ ), a versatile energy carrier that can be produced from water and be used for a variety of applications such as ammonia production, solid state electronics processing, transportation, heating, stationary applications, and much more.<sup>3,4</sup> Liquid-phase alcohol fuels, such as methanol ( $CH_3OH$ ) and ethanol ( $C_2H_5OH$ ), are also of great interest in a sustainable energy future due to their high energy density, ease of storage, and existing distribution infrastructure.<sup>5,6</sup> Importantly, these solar fuels can be produced without any associated carbon dioxide ( $CO_2$ ) emissions if they are produced from light-driven electrochemistry, known as photoelectrochemistry,<sup>7</sup> or conventional electrolysis technologies that are powered by electricity produced by solar photovoltaics or wind energy.<sup>3</sup> Furthermore, storing solar energy in the form of solar fuels has potential to provide an economical means of scaling up energy storage to match solar electricity production and energy demands over a range of time scales.<sup>8</sup> Therefore, as the cost

of electricity from solar photovoltaics continues to drop, large-scale solar fuel energy storage and conversion technologies will play a major role in the future energy generation economy.<sup>9</sup>

## **1.2 Electrochemical Technologies for Solar Fuel Production and Conversion**

Electrochemical technologies such as fuel cells, electrolyzers, and photoelectrochemical cells are expected to be core technologies in a sustainable energy future because they can facilitate large-scale conversion between electrical energy and storable solar fuels.<sup>3,8</sup> A flow diagram illustrating key technologies for the production, storage, and conversion of solar-derived H<sub>2</sub> is shown in Figure 1.1. A solar photovoltaic (PV) panel converts solar power into electric power or electricity. The proton exchange membrane electrolysis cell (PEMEC or PEM electrolyzer) uses this electricity to convert low energy reactants into storable solar fuels such as hydrogen that can be converted back to electricity by a PEM fuel cell (PEMFC) at a later point when the sun is not shining. Also shown is an alternative method for producing solar fuels via a photoelectrochemical cell (PEC), which combines the functions of the solar panel and electrolyzer into one device.

Energy transformation by these electrochemical technologies is particularly attractive for large-scale energy storage that could compensate for seasonal variation in solar energy, because the rate of energy production may be decoupled from the net storage capacity. By this means, electrolyzers and fuel cells only need to be scaled to meet power demands (rate of energy consumption) instead of energy demands (total energy consumption, i.e. the integral of the power demand versus time curve). The burden of matching energy demand is placed on the least expensive and most easily scalable component, the solar fuel storage tank, in which the H<sub>2</sub> or alcohol solar fuel can be stored until it is needed for chemical processes, transportation fuel, or generating electricity.<sup>8</sup> However, improvement in the efficiency and lifetime of these technologies is critically important for the realization of a sustainable energy based on these technologies.<sup>10,11</sup>

A more detailed description of each of these electrochemical technologies is provided in the following subsections.

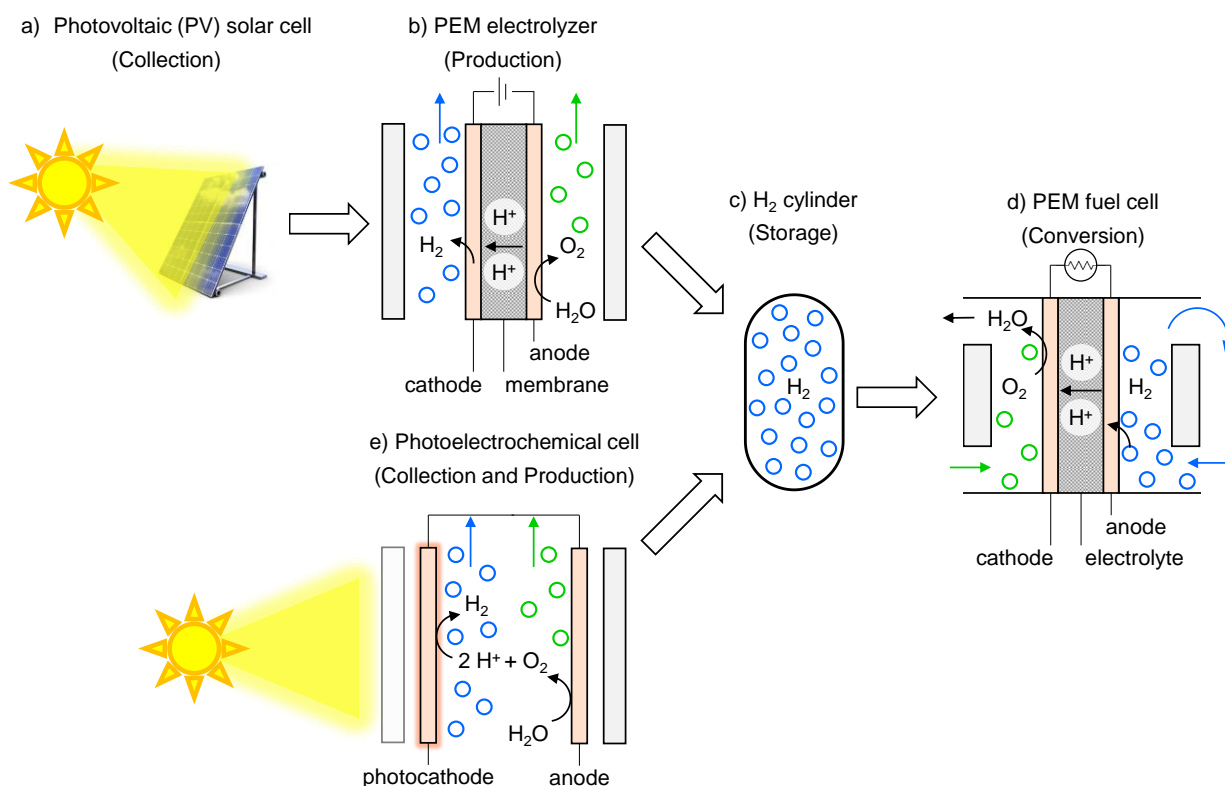


Figure 1.1. Schematic of key technologies for a solar fuels-based energy system. a) PV solar cell, b) PEM electrolyzer, c)  $\text{H}_2$  storage, d) PEM fuel cell, and e) photoelectrochemical (PEC) cell.

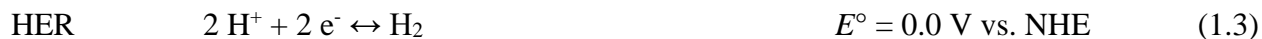
### 1.2.1 Electrolyzers

An electrolyzer uses electrical power, to overcome the thermodynamic and kinetic energy barriers of the non-spontaneous reversible reduction-oxidation (redox) reactions of interest. A schematic of a PEMEC is shown in Figure 1.1b. An electrolyzer is composed of two electrodes, an anode and a cathode, which are exposed to an ion-conducting electrolyte and typically separated by a membrane or porous divider. Electrical power is supplied to the electrolyzer with a voltage (V) applied across the two electrodes and electrical current ( $I$ ) flowing between them. Electrodes typically contain metallic nanoparticle electrocatalysts that catalyze electrochemical reactions of

interest, for which electrons are transferred between the electrocatalyst and reduction-oxidation (redox) species at the electrode|electrolyte interface. The ion-conducting membrane or divider prevents electrical contact between the electrodes while serving as a physical barrier to prevent crossover of product species between the electrodes.

In PEMECs, hydrogen fuel is produced via water (H<sub>2</sub>O) electrolysis, which is illustrated schematically in Figure 1.1b. The overall reaction (Equation 1.1) and half reactions in an acidic electrolyte (Equations 1.2 and 1.3) for water electrolysis are shown here:

Water PEM electrolyzer



where  $E^\circ$  is the standard reduction potential and  $\Delta E^\circ$  is the reversible cell potential. See reference electrode section 2.4.1.1 for a description of the normal hydrogen electrode (NHE).  $\Delta E^\circ$  represents the thermodynamic minimum voltage that is required to drive water electrolysis, and is equal to the difference in  $E^\circ$  of the reduction,  $E^\circ_{red}$ , and oxidation reactions,  $E^\circ_{ox}$ :

$$\Delta E^\circ = E^\circ_{red} - E^\circ_{ox} = 0.0 \text{ V vs. NHE} - 1.23 \text{ V vs. NHE} = -1.23 \text{ V} \quad (1.4)$$

Importantly, the negative sign on  $\Delta E^\circ$  signifies the overall reaction is non-spontaneous. This is more clearly understood based on the relationship between  $\Delta E^\circ$  and the change in Gibbs free energy,  $\Delta G^\circ$ :

$$\Delta G^\circ = -n \cdot F \cdot \Delta E^\circ \quad (1.5)$$

where  $n$  is the electron transfer number (moles of electrons per mole of product) and  $F$  is Faraday's constant (96,485 C mol<sup>-1</sup>). From Equation 1.5,  $\Delta G^\circ$  for water electrolysis is +237.1 kJ mol<sup>-1</sup>,

reaffirming the fact that water electrolysis is a non-spontaneous reaction that requires energy input to proceed.

When the voltage applied across two electrodes exceeds the thermodynamically required voltage to split water and overpotential penalties (the additional voltage required beyond  $\Delta E^\circ$ ), water electrolysis takes place. Water is oxidized to produce oxygen and protons ( $H^+$ ) at the positive electrode (anode), releasing electrons (Equation 1.2). Electrons from the anode conduct through the external circuit to the negative electrode (cathode) where they are used to reduce protons to form molecular hydrogen ( $H_2$ ) (Equation 1.3). Equations 1.2 and 1.3 are commonly referred to as the hydrogen evolution reaction (HER) and oxygen evolution reaction (OER), respectively. To complete the circuit within the electrolyzer cell and maintain electro-neutrality, ions are continually transported between the anode and cathode through the polymer electrolyte membrane.

### ***1.2.2 Photoelectrochemical Cells***

A PEC is an all-in-one unit that converts solar energy into energy stored in chemical bonds, which is similar to what nature accomplishes through photosynthesis.<sup>12,13</sup> The major difference in operation between a PEMEC and PEC is that an external power supply is not necessary in a PEC. In a PEC, at least one of the electrodes is comprised of a photo-active semiconducting material which absorbs sunlight to directly drive non-spontaneous electrochemical reactions. Such semiconducting electrodes are known as photoelectrodes. This essential component of PECs uses the photovoltaic effect to generate a voltage (photovoltage) to drive non-spontaneous electrochemical reactions such as water electrolysis.<sup>14</sup> Figure 1.1e shows a schematic of a PEC for water electrolysis. The schematic depicts a PEC that employs a photocathode where the HER takes place, although PECs based on a photoanode or dual photocathode/photoanode arrangements have also been demonstrated.<sup>12</sup> During operation of a photoelectrode, electron-hole pair charge carriers

are generated when photons having energy greater than the semiconductor band gap are absorbed. In a photocathode, the photo-generated electrons are collected at the photoelectrode|electrolyte interface, where they reduce the oxidant species of interest, as described in section 1.3.<sup>15,16</sup> Commercialization of PEC technology is inhibited by challenges to identify and develop photoelectrodes that are stable, efficient, and made from low-cost materials.<sup>17</sup> A more detailed description of the photoelectrode design and operation is provided in section 1.5.1.

### 1.2.3 Fuel Cells

A fuel cell is essentially an electrolyzer that is operated in the reverse (spontaneous) direction. Fuel cells are useful for converting fuels into electricity in a variety of transportation, stationary, and portable applications. During operation of a hydrogen PEM fuel cell (PEMFC), H<sub>2</sub> fuel and O<sub>2</sub> are fed into the fuel cell where they are oxidized and reduced, respectively, to produce water, heat, and usable energy (Figure 1.1d). In a hydrogen PEMFC the hydrogen oxidation reaction (HOR) occurs at the anode with the oxygen reduction reaction (ORR) at the cathode. The overall and half reactions of the cell are shown below with the reversible cell potential, along with the standard reduction potentials.

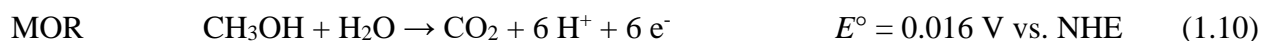
#### Hydrogen PEM fuel cell



Useful work is obtained from the electrons conducting between the two electrodes across the external circuit. Although the hydrogen PEMFC is not investigated in this dissertation, the electrocatalysts studied herein can be applied to this system.

Chapter 5 of this dissertation investigates alcohol fuels for direct alcohol fuel cells (DAFC). Alcohol fuels have gained wide attention for their high theoretical power densities. A schematic of a DAFC is shown in Figure 1.2. In DAFCs, the alcohol fuel is oxidized at the anode while ORR takes place at the cathode. The overall and half reactions of a direct methanol (DMFC) and ethanol fuel cells (DEFC) are shown below, along with the reversible cell potential for the overall reaction and standard reduction potentials for the half reactions.

#### Direct methanol fuel cell



#### Direct ethanol fuel cell

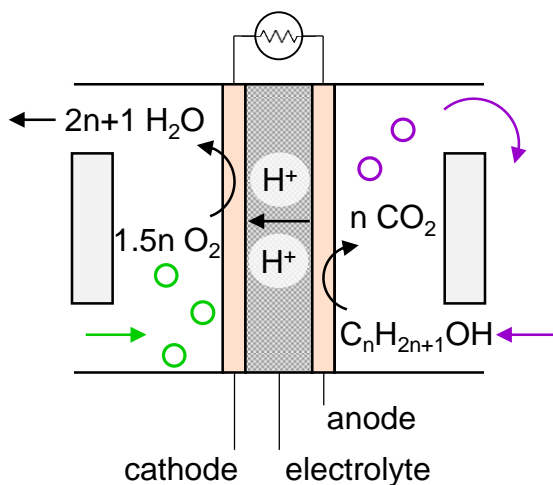
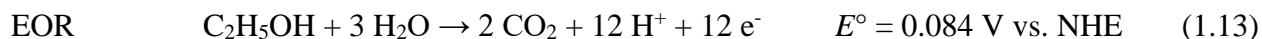
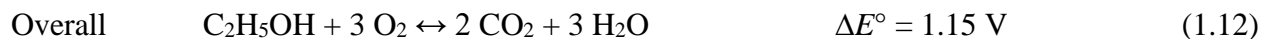


Figure 1.2. Schematic of a direct alcohol fuel cell for converting alcohol fuels to electricity.

In a DAFC, methanol ( $\text{CH}_3\text{OH}$ ) or ethanol ( $\text{C}_2\text{H}_5\text{OH}$ ) is oxidized at the anode to produce carbon dioxide ( $\text{CO}_2$ ) and protons (Equation 1.8 and 1.11 respectively). These reactions release electrons which flow through the external circuit to the cathode where they are used to reduce oxygen and protons to form water (Equation 1.9 and 1.12) through the ORR. Similar to the electrolyzer, ionic current flows between the anode and cathode through the polymer electrolyte membrane. Although  $\text{CO}_2$  is produced from a DAFC, it can be captured and converted back to alcohols through electrolysis to achieve a carbon neutral process. A major challenge in DAFCs is alcohol crossover from the anode to the cathode side which lowers cathode performance and wastes fuel. Additionally, the electrocatalyst performance is plagued by sluggish kinetics and poisoning from carbonaceous intermediate species.<sup>18,19</sup> If DAFCs are to achieve large-scale commercialization and penetration into the transportation market, it is imperative that the performance of alcohol oxidation electrocatalysts are significantly improved.

### 1.3 Electrolyzer, Photoelectrochemical Cell, and Fuel Cell Performance Metrics

The efficiency of PEMECs, PECs, PEMFCs, and DAFCs is defined by the ratio of the power ( $P$ ) output to power input. Power, which is the rate of energy use or generation, can be in the form of electrical, chemical, or optical power, depending on the device. Electrical power is determined by the product of the voltage ( $V$ ) across the electrodes and the current ( $I$ ) flowing between them:

$$P = I \cdot V \quad (1.15)$$

Chemical power is determined by the energy content of the fuel and the rate of fuel production or consumption. The energy content of a fuel is often taken to be the Gibbs free energy of reaction,  $\Delta G^\circ$ , associated with its formation. This free energy change corresponds to a thermodynamic cell potential,  $\Delta E^\circ$ , according to Equation 1.5, which represents the minimum required voltage for an



electrolysis reaction or maximum achievable voltage for a fuel cell. The rate of fuel production or consumption is controlled by the rates of the electrochemical reactions at the electrodes. For electrolyzers and PECs, the rate of fuel production is dependent on the current and the faradaic efficiency,  $\eta_f$ , which is the ratio of the current associated with the desired chemical electrochemical reaction to the total current passed. The power associated with the generation of the desired fuel is calculated as follows:

$$P = I \cdot \Delta E^\circ \cdot \eta_f \quad (1.16)$$

An electrolyzer requires electrical power input to produce chemical fuels. The actual voltage needed to drive the reaction,  $V_{electrolyzer}$ , deviates from the thermodynamic required voltage,  $\Delta E^\circ$ , due to additional voltage losses (overpotential) associated with the electrochemical processes:

$$V_{electrolyzer} = \Delta E^\circ + \eta_\Omega + \eta_{conc} + \eta_s \quad (1.17)$$

where  $\eta_\Omega$  is the voltage loss due to ohmic resistances associated with the flow of electrons and ions,  $\eta_{conc}$  is the concentration overpotential, which accounts for deviations from ideal behavior due to unfavorable mass transport of reactants and products to and from the electrode surface,  $\eta_s$  is the sum of the surface overpotentials associated with the reaction kinetics at both the electrode surfaces. When the chemical fuels are converted to electrical power in a fuel cell, the voltage output,  $V_{fuel\ cell}$ , is lower than  $\Delta E^\circ$  due to similar overpotential losses:

$$V_{fuel\ cell} = \Delta E^\circ - \eta_\Omega - \eta_{conc} - \eta_s \quad (1.18)$$

As a result of these overpotential losses, the voltage generated between the fuel cell anode and cathode is less than the thermodynamically achievable voltage. Minimizing the overpotential losses maximizes device efficiency. The magnitude of the overpotential losses within electrochemical devices are highly dependent on the operating current densities. Higher current densities require higher overpotentials due to increases in the energetic penalties associated with

maintaining high species fluxes and turn over frequencies. On the other hand, power is proportional to current (Equation 1.15 and 1.16). As a result, there is an optimal operating current density for a fuel cell that maximizes the electrical power produced by the fuel cell.

A photoelectrochemical cell requires solar power to produce chemical fuels. Unlike an electrolyzer, the power input to a PEC cannot be easily tuned because the input solar power is fixed by the solar spectrum (section 2.4.2.1) Therefore, PEC efficiency is maximized when the rate of fuel production (photocurrent) is also maximized. However, PECs also experience overpotential losses similar to electrolyzers and fuel cells, which create challenges with the electrode materials and design.

#### **1.4 Electrode Materials and Design**

Electrodes serve the important role of facilitating the electrochemical reactions in these electrochemical devices. Improved electrode materials and design are needed to improve the lifetime, efficiency, and cost of electrochemical devices. To satisfy all of these objectives optimally, one must understand the end-use requirements, challenges, and tradeoffs associated with electrode development and design.

First, all of the electrode materials must be stable in the chosen electrolyte. Second, an electrode architecture must be designed to ensure the electrocatalyst has access to both ions and electrons; if not the voltage losses due to ohmic resistances,  $\eta_{\Omega}$ , become significant. Electrodes used in commercial electrolyzers and fuel cells are typically made of porous structures that are designed to allow reactants and products to easily diffuse to and from the reaction sites to minimize concentration overpotential losses,  $\eta_{conc}$ . The porous structure also increases the electrode surface area to increase the density of reaction sites per mass and volume of electrode material. To facilitate electron transport, the electrode materials must be electronically conductive.

Finally, the reaction sites must be catalytically active towards the electrochemical reactions of interest to reduce the associated surface overpotential,  $\eta_s$ . Unfortunately, the best known electrochemically active materials for HER, OER, HOR, ORR, MOR and EOR tend to be the expensive and scarce precious metals,<sup>20</sup> resulting in a tradeoff between efficiency and materials cost. To overcome this tradeoff, electrodes commonly consist of a less expensive, conductive, high surface area, three-dimensional (3D) porous support materials that are decorated with small particles (on the order of nm) of a more expensive electrocatalyst material with inherently facile kinetics.<sup>21</sup> More details on the electrocatalysts requirements are discussed in section 1.6.

## **1.5 Photoelectrode Materials and Design**

Unlike the electrodes used in conventional electrolyzers and fuel cells, the key component of photoelectrode(s) within a PEC is the semiconducting photoabsorber.<sup>12,13</sup> Photoelectrodes typically assume planar geometries, although there is also extensive research focused on developing particle suspension and porous semiconductor electrodes.<sup>11</sup> However, these alternative designs also have their drawbacks in performance. This dissertation focuses on planar semiconductor photoelectrodes. Typically, the semiconductors require surface modification by protective coatings to prevent corrosion (section 1.5.3) and metallic electrocatalysts to overcome kinetic barriers (section 1.6).<sup>22</sup> Photoelectrode semiconductor and electrocatalyst materials are constrained by the operational requirements needed to achieve stable and efficient performance. Three fundamental processes must occur to convert solar energy to chemical energy: i) light absorption in the semiconductor to generate charge carriers and a photovoltage greater than the voltage required to drive the electrochemical reaction, ii) charge carrier diffusion, drift, and collection at the semiconductor|electrocatalyst interface to generate photocurrent, and iii) electrochemical charge transfer at the electrocatalyst|electrolyte interface to oxidize and reduce

species.<sup>23</sup> The following sections will provide a brief descriptions of the photoelectrode processes, challenges and requirements associated with photoelectrode materials and design, and the metal-insulator-semiconductor (MIS) photoelectrode architecture investigated in Chapter 3. The description of the electrochemical charge transfer process is provided in section 1.6 as this step also pertains to PEMEC, PEMFC, and DAFC electrodes.

### ***1.5.1 Light Absorption and Charge Carrier Generation***

A key parameter in determining whether the photoelectrode can absorb a photon, of given wavelength ( $\lambda$ ), is the band gap ( $E_g$ ) of the semiconductor. The band gap of a semiconductor is the difference between valence band maximum ( $E_v$ ) and conduction band minimum ( $E_c$ ). Importantly, the band gap energy corresponds to the minimum energy (e.g. from thermal or photon energy) required to excite an electron ( $e^-$ ) from its bound state in the valence band to a mobile state within the conduction band.<sup>24</sup> Figure 1.3 shows an energy band diagram of a semiconductor and illustrates light absorption by the semiconductor. Light absorption occurs when a photon having energy ( $h\nu$ ) greater than the band gap of a semiconductor excites an electron from  $E_v$  to  $E_c$  through a process known as fundamental absorption.<sup>25</sup> The excitation of the electron to  $E_c$  simultaneously leaves an electron vacancy, or hole ( $h^+$ ) in  $E_v$ . Together, the electron and hole are commonly referred to as an electron-hole pair, or exciton. As a result, the energy of the incident photon has been transferred to the exciton to generate a potential difference, or photovoltage.<sup>24</sup> This photovoltage, if larger than  $\Delta E^\circ$  for the reaction of interest, can be used to drive that non-spontaneous reaction without any additional bias voltage from an external power supply.<sup>26</sup> However, a high photovoltage does not by itself yield a reaction if the charge carriers are recombined and lost as heat.<sup>27</sup> Therefore, it is also necessary to separate and collect charge carriers to generate photocurrent (Equation 1.16).

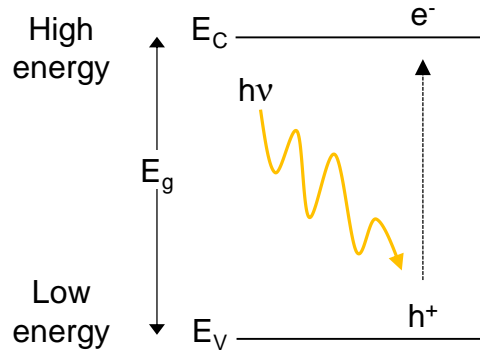


Figure 1.3. Energy band diagram of a semiconductor illustrating fundamental absorption. The photon energy is defined by  $h\nu$ , where  $h$  is Planck's constant and  $\nu$  is the frequency of the photon.  $E_g$  is the gap in energy between  $E_V$  (highest occupied energy level) and  $E_C$  (lowest unoccupied energy level).

### 1.5.2 Charge Carrier Separation, Diffusion, Drift, and Collection

Charge carrier separation, diffusion, and drift are achieved by a built-in electric field,  $E$ , across the junction between two different materials that causes electrons to move in the net direction opposite of the electric field.<sup>28</sup> For example, in a solar PV cell, a p-n junction<sup>25</sup> is formed between a positively-doped semiconductor (p-type) that possesses an excess amount of holes (i.e. the majority carrier) compared to free electrons (i.e. the minority carrier). In a negatively-doped semiconductor (n-type) semiconductor, free electrons are the majority carriers and holes are the minority carriers. When these two materials come into contact in the dark (see Figure 1.4a), the average energy of the charge carriers, Fermi level ( $E_f$ ), equilibrate, during which time excess electrons in the n-type (electron rich) material diffuse to the p-type (electron deficient) side. This equilibration process reduces the concentration of charge carriers in the region close to the junction, which is called the depletion region. Due to the charge imbalance that accompanies this process, an electric field forms within the depletion region that opposes additional electron transport from the n-type side to the p-type side. Under illumination, there is a gradient in the chemical potential of electrons across the depletion region, which is illustrated as “bent” bands

across the junction. This gradient causes minority carrier electrons generated within the p-type semiconductor to migrate, or “drift”, from the p-type to n-type side of the junction, while holes drift in the opposite direction.<sup>25</sup>

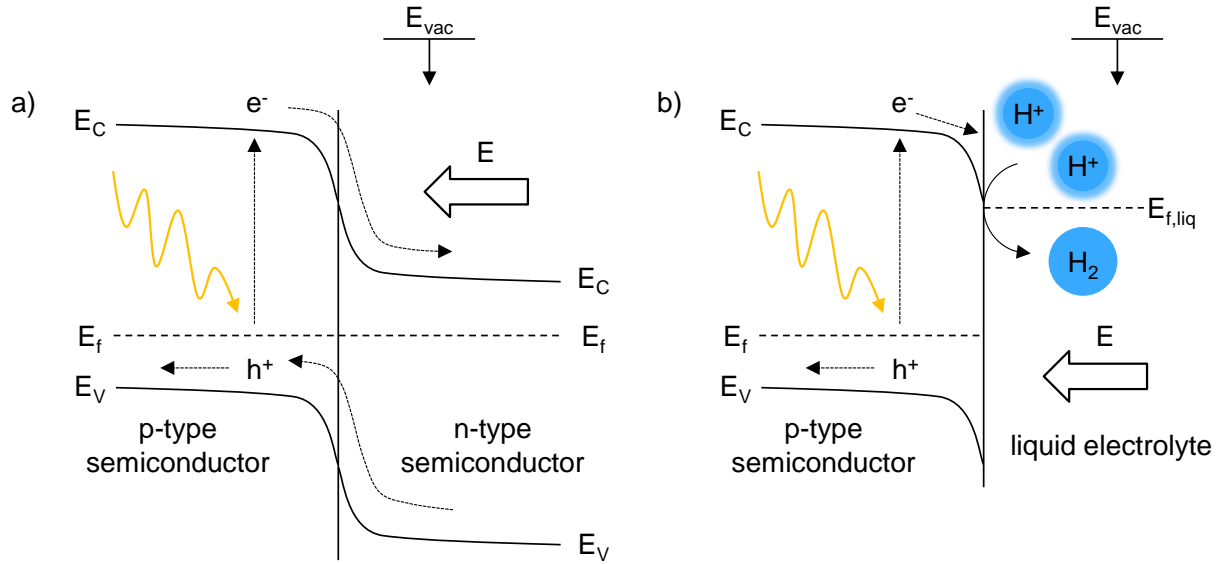


Figure 1.4. Energy band diagrams for a) p-n junction in a solar PV cell and b) liquid junction in a photocathode used in a PEC.

In equilibrium, the current due to electron diffusion and drift is balanced such that the net current from the PV is zero. However, illumination of the semiconductor with photons greater than the band gap energy increases the concentration of minority carrier electrons and holes within the p-type and n-type materials, respectively. This imbalance of charge carriers, combined with the electric field, increases the drift current of minority carriers (e.g. photoelectron drift from p-type to n-type), relative to the diffusion current in the reverse direction. The minority charge carriers that drift across the junction become majority carriers and continue to diffuse away from the junction into the bulk of the semiconductor which are collected by metal contacts on the back side (back contact) of the semiconductor to generate net electrical current.

For a photoelectrode, a liquid junction is formed between a semiconducting photoelectrode and the electrolyte in which it is immersed.<sup>29</sup> The energy band diagram in Figure 1.4b illustrates the charge separation process across the liquid-semiconductor junction, which behaves similar to a metal-semiconductor junction that is known as a Schottky junction. The electrolyte has an effective liquid fermi level ( $E_{f,liq}$ ) defined by the standard reduction potential of the species in solution with respect to vacuum ( $E_{vac}$ ).<sup>24</sup> Equilibrium between the semiconductor and the electrolyte is achieved in similar manner as the p-n junction. However, under illumination, minority carrier drift results in carrier collection at the liquid junction and subsequent charge transfer across the electrode|electrolyte interface through an electrochemical reaction. Figure 1.4b shows a p-type photocathode in which photo-generated electrons are used to reduce oxidant species at the electrode|electrolyte interface. For photoanodes, minority carrier holes are collected at the junction where they participate in an oxidation reaction. Chapter 3 of this dissertation will discuss p-type silicon (p-Si) photocathodes for the hydrogen evolution reaction.

### ***1.5.3 Challenges and Requirements***

The primary challenge for practical implementation of PECs is identifying photoelectrode materials that are efficient, stable, and made from low-cost materials that can be manufactured at large scale.<sup>17</sup> Ultimately, PEC devices must become cost competitive with conventional methods for producing electricity or chemical energy in order to penetrate the energy market.<sup>7</sup> Specific requirements for photoelectrodes include:

- i. Long term stability and resistance to corrosion.
- ii. Efficient light absorption, charge carrier generation and collection.
- iii. Sufficient photovoltage to drive the desired electrochemical reaction.
- iv. Proper band alignment of the semiconductor band edge energies with redox reactions.

- v. Facile kinetics of redox reactions to reduce overpotentials (see section 1.6).
- vi. Scalable materials and production (see section 2.1 and 2.2.1).

However, there are many trade-offs between all these requirements. One challenge in particular is developing a stable photoelectrode material that is capable of absorbing a large portion of the solar spectrum for high photocurrent and generating sufficient photovoltage to drive the desired electrochemical reaction.<sup>30</sup> Figure 1.5 shows the solar spectrum power density as a function of photon wavelength and the corresponding semiconductor band gap energy that can absorb the photon. Also shown is a visualization of theoretical power density output (integrated area under power density curve minus energy lost to heat) of a silicon (Si) and titanium dioxide (TiO<sub>2</sub>) semiconductor.  $E_g$  is strongly correlated with chemical bond strength and determines magnitude of photocurrent and photovoltage generated. Narrow band gap semiconductors,  $E_g < 2$  eV (e.g. Si), are able to absorb a large percentage of the ultraviolet-visible solar spectrum to achieve high photocurrents and efficiencies,<sup>31,32</sup> but are unstable against corrosion and do not generate sufficient photovoltage to drive relevant redox reactions such as water electrolysis.<sup>32</sup> On the other hand, more robust materials (e.g. TiO<sub>2</sub>) in aqueous solution, wide band gap semiconductors, achieve high photovoltages, but are insensitive to the visible spectrum and thus cannot achieve high water splitting efficiency.<sup>33</sup> In general, the potential impact of PECs is limited by the trade-off between photoelectrode stability and efficiency.<sup>12,13,34</sup> For example, Khaselev was able to achieve high efficiencies with a tandem GaAs photovoltaic and GaInP<sub>2</sub> photocathode in a standalone PEC device, but has proven to be unstable.<sup>35,36</sup> On the other end of the spectrum, wide  $E_g$  semiconductors like TiO<sub>2</sub> and WO<sub>3</sub> are very stable in certain aqueous electrolytes but have  $E_g$  too large for achieving high current densities.<sup>37–39</sup>



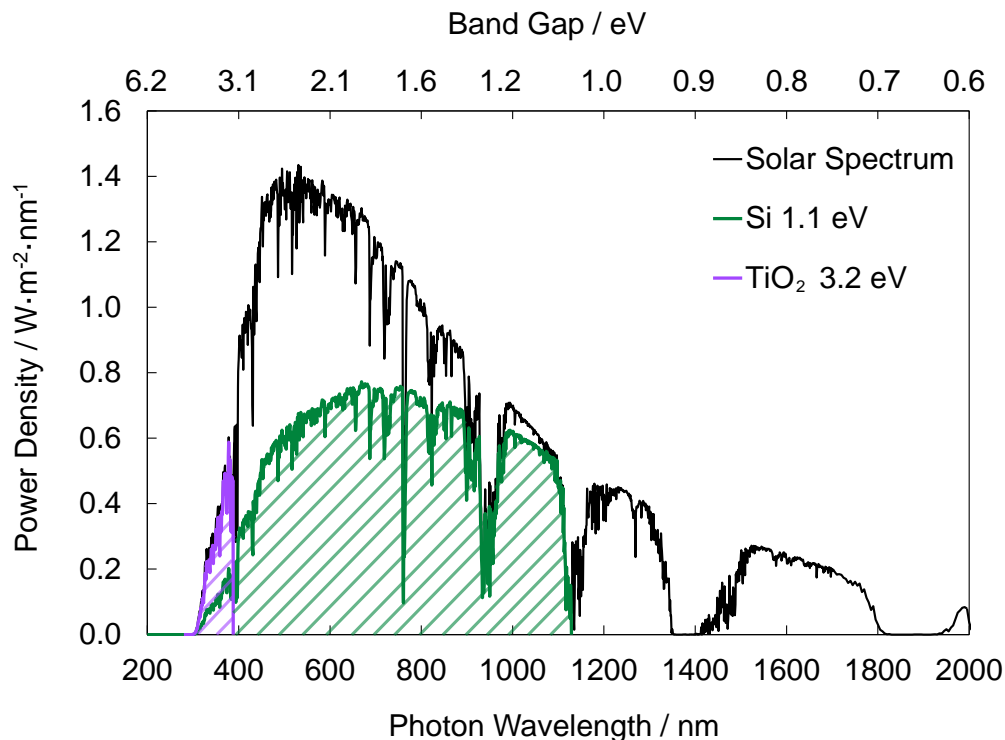


Figure 1.5. Solar spectrum power density as a function of photon wavelength and energy/band gap energy to illustrate the tradeoffs between photovoltage, photocurrent, power density, and stability

In addition to the requirement of generating photovoltage greater than  $\Delta E^\circ$ , the semiconductor must also possess proper band edge positions that straddle  $E^\circ$  of the two half reactions of interest.<sup>12</sup> For example, a photocathode conduction band edge must be positioned at more negative electrochemical potential than  $E^\circ$  in order for electron transfer from the semiconductor to the oxidant species to be favorable. In an effort to minimize overpotential losses and thereby reduce the photovoltage needed to drive the reactions, the semiconductor surface is typically modified with metallic catalyst collectors to improve the kinetics of the reaction.<sup>22,40–42</sup> However, it is imperative that these metallic collectors do not introduce parasitic losses such as increasing light reflection or increasing carrier recombination.<sup>43</sup> Therefore, the metal should be deposited such that it is nearly optically transparent and will not significantly affect the light absorption properties of the underlying semiconductor.

The charge carrier collection efficiency is dependent on the rate of recombination of photoelectron/hole pairs, which typically results in energy lost as heat.<sup>27</sup> The rate of minority carrier recombination is closely related to the minority carrier lifetime and the minority carrier diffusion length, all of which are strongly affected by defect density, dopant density, and conductivity.<sup>27</sup> Defects and impurities can introduce extra energy states within the band gap of the semiconductor that facilitate recombination processes. Defects are typically more concentrated at the semiconductor surface where the crystal lattice terminates and dangling bonds exist. Therefore, the sites where the semiconductor interfaces with another material (e.g. junction and back contact) tend to have higher recombination rates than in the bulk. In particular, contact of a metal, which has a high density of states, with a semiconductor often result in evanescent metal induced gap states (MIGS) within the semiconductor that allow photo-generated charge carriers to relax to a lower energy state and effectively reduce the photovoltage.<sup>44–46</sup>

#### ***1.5.4 Metal-Insulator-Semiconductor Photoelectrode***

To overcome the trade-offs between efficiency and stability that typically plague conventional photoelectrodes, an alternative photoelectrode design based on the metal-insulator-semiconductor (MIS) architecture (Figure 1.6) has been developed in recent years.<sup>47–49</sup> This MIS design shows great promise for achieving high performance, demonstrating both good efficiency and appreciable stability.<sup>47–53</sup> As illustrated in Figure 1.6a, the MIS architecture consists of a very thin insulating oxide layer (I) separating metallic electrocatalysts (M), from the semiconducting absorber layer (S). While all three components are important for efficient device operation, the insulating layer is the most crucial for its role in protecting the underlying semiconductor from corrosion while facilitating transport of photo-generated carriers between the semiconductor and

metal catalysts by quantum mechanical tunneling. As illustrated in Figure 1.6b, the MIS photocathode operation for HER proceeds through the following steps:

- i. Light absorption and charge carrier generation: A photon having energy ( $h\nu$ ) greater than the band gap of the semiconductor is absorbed to create an electron-hole pair and photovoltage ( $\approx E_{f,m} - E_{f,s}$ ) across the MIS junction.
- ii. Charge carrier collection: The photogenerated minority carrier electrons migrate towards the semiconductor|insulator interface, where they tunnel across the insulating layer to the metal. Quantum mechanical tunneling through an insulator such as silicon dioxide ( $\text{SiO}_2$ ) typically requires that the thickness of the insulating layer be less than 2 nm.<sup>54</sup>
- iii. Electrochemical charge transfer: Charge transfer between the metal electrocatalyst and electrolyte where electrons reduce  $\text{H}^+$  to  $\text{H}_2$  at a photocathode. For photoanodes, holes oxidize  $\text{H}_2\text{O}$  to  $\text{O}_2$ .

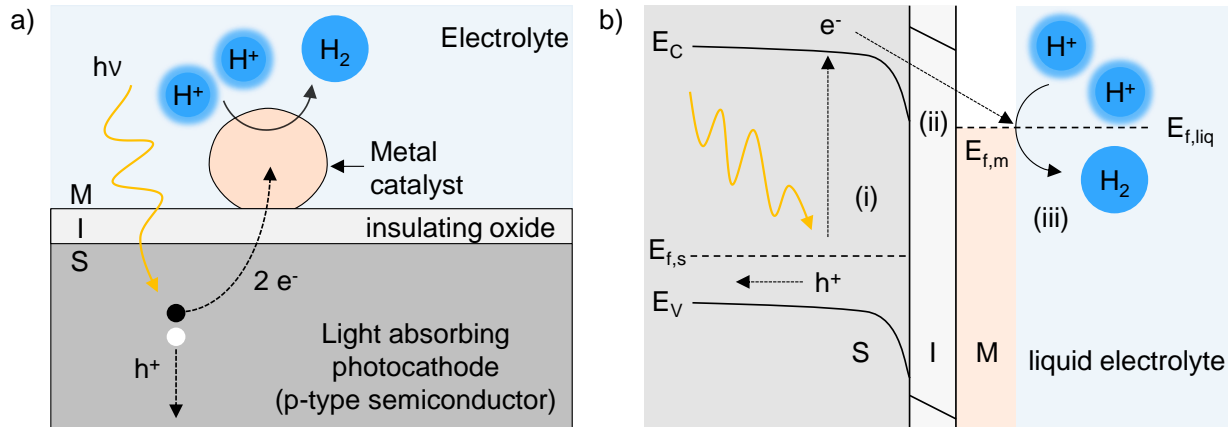


Figure 1.6. a) Side view schematic of a metal-insulator-semiconductor (MIS) photoelectrode for stable and efficient solar water splitting. b) Energy band diagram illustrating operation of a MIS photocathode with the HER occurring at liquid interface.

Aggour and Lewerenz demonstrated a MIS photoelectrode design known as a nanoemitter cell where platinum deposits were embedded into the semiconductor and protrude out of the

surface.<sup>44–47,55,56</sup> This device provided interesting insight into the operation of silicon based MIS-type photocathodes, elucidating the detrimental effect of Schottky junctions (M-S) on the photovoltage and further motivating the incorporation of an insulating barrier. The modified MIS photoelectrode design is able to mitigate this loss and overcome previously stated challenges in section 1.5.3 because: i) the stable insulating layer protects the semiconductor from the corrosive electrolyte and creates a barrier between the metal and semiconductor which reduces recombination and improves photovoltages by suppressing MIGS,<sup>16,57</sup> ii) the narrow band gap semiconducting material efficiently absorbs sunlight, and iii) the metallic electrocatalytic nanoparticles reduces kinetic overpotentials.<sup>22</sup>

## 1.6 Electrocatalyst Requirements

Enhancements in the lifetime and efficiency of PEMEC, PEC, PEMFC, and DAFC is of crucial importance for their commercial success. The commonality amongst these technologies are the electrocatalysts that serve the essential role of catalyzing the oxidation and reduction reactions of interest. The electrocatalysts are typically metallic nanoparticles that are supported on conductive, high surface area supports. In PEMECs, PEMFCs, and DAFCs the state-of-the-art electrocatalysts are nanoparticles of platinum (Pt) for HER,<sup>58</sup> HOR,<sup>59</sup> and ORR,<sup>60</sup> Pt alloys such as Pt-ruthenium (PtRu) for MOR<sup>61,62</sup> and Pt-tin (PtSn) for EOR,<sup>63–66</sup> and iridium (Ir) for OER.<sup>67</sup> Supported nanoparticles (< 5 nm diameter) are desirable for real-world applications because their high electrochemically active surface area (ECSA) per catalyst loading reduce surface overpotentials,  $\eta_s$ , and reduce the required loading of these expensive and scarce metals. Low catalyst loadings and coverage are of particular importance with photoelectrodes because it is desirable to minimize light reflectance off the catalyst and allow light absorption to the underlying semiconductor.<sup>68</sup>

The primary purpose of the electrocatalyst is to reduce kinetic surface overpotential losses,  $\eta_s$ , but electrocatalysts can also influence voltage losses due to ohmic resistance,  $\eta_\Omega$ , and concentration overpotentials,  $\eta_{conc}$  (Equation 1.17 and 1.18). Minimizing these overpotential losses maximizes device efficiency. Over the device lifetime, these overpotential losses can increase due to electrocatalyst degradation and/or impurities in the electrolyte that adsorb onto the catalyst, which would reduce the number of active reaction sites and/or alter the electronic and kinetic properties of the electrocatalyst. In addition, the electrocatalyst selectivity for the desired reaction can affect the electrocatalyst interactions with impurities (stability) and the device efficiency, as indicated by the faradaic efficiency parameter,  $\eta_f$ , in Equation 1.16. Thus, the device lifetime and performance is typically closely tied to the *stability*, *selectivity*, and *activity* of the electrocatalyst for the electrochemical reaction of interest.

### 1.6.1 Stability

Major research efforts have been made to explore the degradation mechanisms and to improve the stability of electrocatalysts. Pt nanoparticles (NP) supported on carbon (Pt|C) have been a frequent subject of electrocatalyst stability studies due to the common use of this catalyst|support combination in commercial fuel cells and electrolyzers.<sup>69–73</sup> Degradation of Pt|C electrocatalysts can depend strongly on the operating conditions (temperature, potential cycling, current density, electrolyte pH) and the nature of the catalysts.<sup>69,71,74</sup> Several degradation mechanisms of supported Pt NPs have been proposed and are illustrated in Figure 1.7:<sup>75–77</sup>

- i. Dissolution of Pt to form dissolved species in the electrolyte
- ii. Growth of Pt NPs via modified Ostwald ripening (re-deposition of dissolved Pt onto other particles) and aggregation (particle migration and coalescence)
- iii. Detachment of Pt particles from the support

- iv. Poisoning of Pt by impurity species in the electrolyte that deposits onto the surface of the catalyst and decreases its catalytic activity or enhances dissolution (section 1.6.2)

All of these degradation mechanisms decrease ECSA and increase  $\eta_s$ .

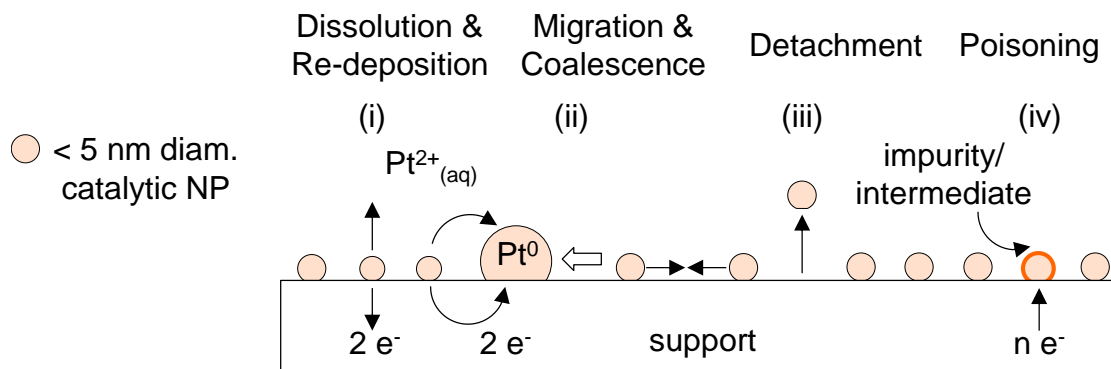


Figure 1.7. Schematic of four common electrocatalyst degradation mechanisms: i) dissolution, ii) re-deposition and/or aggregation (particle migration and coalescence), iii) detachment, and iv) poisoning by an impurity species.

Electrocatalyst dissolution is a common concern in electrocatalytic applications. Although Pt is thermodynamically stable in a large pH and potential window,<sup>78</sup> Pt is susceptible to oxidation and dissolution within the operating window of PEMFC and DAFC cathodes ( $> 0.7 \text{ V}$  vs. RHE and  $\text{pH} < 2$  at  $25^\circ\text{C}$ ).<sup>79–81</sup> Additionally, due to the harsh oxidation environment at the anode of an electrolyzer, OER catalysts are especially susceptible to dissolution.<sup>72,82</sup> For example, Ru-based catalysts are one of the most active OER catalysts,<sup>83</sup> but they are not stable in acidic environments.<sup>82</sup> Furthermore, it has been demonstrated that Pt dissolution is dependent on the particle size and oxide coverage in which the dissolution rate increases with decreasing particle size.<sup>84,85</sup> Particles smaller than  $2 \text{ nm}$  in diameter are expected to dissolve at accelerated rates, often orders of magnitude faster than larger ( $>10 \text{ nm}$ ) particles.<sup>86</sup> Besides decreasing ECSA, particle dissolution negatively impacts membrane performance in a membrane electrode assembly (MEA) by increasing ionic resistance as ions deposit in the membrane.<sup>87</sup>

Particle growth via Ostwald ripening and aggregation also reduces the ECSA.<sup>79,80,88,89</sup> Modified Ostwald ripening is a subsequent process of Pt dissolution,<sup>88,89</sup> in which dissolved Pt is redeposited on larger platinum particles driven by difference in surface free energy and local adsorbed atom concentration on the support surface, causing larger particles to grow at the expense of smaller particles. Aggregation involves the Brownian motion of NPs. This migration eventually leads to coalescence when particles come in close proximity to each other causing particle growth.<sup>88</sup> Physical detachment of electrocatalyst particles from the support generally results from a weak or weakening interaction between the Pt particles and support. This is especially challenging for Pt nanoparticle electrocatalysts on oxide-covered MIS photoelectrodes, which is the focus of Chapter 3. Particle detachment and aggregation are typically observed in parallel because the rates of both processes increase as the interaction between the electrocatalyst and support becomes weaker.

Under oxidizing conditions, these degradation mechanisms are exacerbated due to the electrochemical corrosion of the carbon supports, which directly initiates particle detachment and aggregation.<sup>90–94</sup> The corrosion of the support and the concomitant structural and chemical changes to the catalyst|support interface inevitably initiates a series of secondary degradation processes. For example, electrochemical corrosion of the support separates and electrically isolates catalysts particles from the support (increasing  $\eta_o$ ) and facilitates particle aggregation.

The strong influence of support oxidation and Pt dissolution on the overall degradation behavior emphasizes the importance of enhancing the oxidation resistance of both the support/substrate and Pt particles.<sup>95</sup> As a result, a vast majority of strategies to mitigate these degradation mechanisms have focused on modifying either the support material<sup>96–106</sup> or the active electrocatalyst.<sup>72,107–110</sup> A more detailed description of these approaches are discussed in Chapter

4 section 4.1. Researchers who have focused on increasing the stability of the support investigate interactions between the support and Pt NPs and methods to improve the adhesion of electrocatalysts to the support.<sup>111–114</sup> However, none of these solutions can completely eliminate catalyst poisoning because the active sites are still directly exposed to the electrolyte and any impurities.

Despite the promising solutions to minimize dissolution and aggregation, electrocatalyst performance can still degrade from a poison or impurity species. Precious metal HER catalysts, such as Pt, are particularly prone to adverse effects by poisons.<sup>115–118</sup> Contaminants from feed water or corrosion of stack components such as  $S^{2-}$ ,  $Cu^{2+}$ ,  $Ni^{2+}$ , or  $Fe^{3+}$  or impurities from air including  $SO_x$ ,  $NO_x$ , and  $H_2S$ , can strongly bind or deposit to the Pt surface and drastically decrease the electrocatalyst activity.<sup>115–118</sup> In PEM electrolyzers, impurities can also impact the stability of  $IrO_2$  OER electrocatalysts.<sup>72</sup> To avoid impurities and concomitant shortened MEA lifetime, a water purification unit is implemented upstream of the electrolyzer and system components are constructed with more expensive noncorrosive materials, which can add to the balance of system costs.

### **1.6.2 Selectivity**

Selectivity for the desired reaction pathway and product is less of a concern for relatively simple reactions such as HER/HOR and OER/ORR, but can be more important for more complex reaction mechanisms. Tuning electrocatalyst selectivity can impact: i) the electrocatalyst stability against undesired deposition or adsorption of poison species, ii) the faradaic efficiency ( $\eta_f$ ) for producing the desired end product, and iii) the surface overpotentials through modified reaction pathways with lowered energy barriers (section 1.6.3). All of these metrics strongly impact overall device performance. Furthermore, achieving high selectivity in complex electrochemical reactions



is critical for obtaining high product purity and decreasing requirements for downstream separation processes. Reaction selectivity for desired reactants and products is commonly achieved in the thermal catalysis field by controlling transport phenomena. For example, mesoporous or 3D catalysts such as zeolites,<sup>119–121</sup> metal organic frameworks (MOFs),<sup>122</sup> and enzymes<sup>123,124</sup> leverage differences in transport rates of species to selectively react and produce desired species. The relative rates of transport of electroactive species can depend on the size, shape, and/or charge of the species relative to the pores on these structures, which are concepts that underlie selectivity across membranes.<sup>125,126</sup> In electrocatalysis, the charge of electroactive species can also affect transport due to electrostatic interactions with their surroundings and electromigration in the presence of electric fields.<sup>127</sup> Controlling transport phenomena to modify reaction pathways is a promising approach to obtain high selectivity.

### 1.6.3 Activity

As previously mentioned, the primary role of the electrocatalyst is to reduce kinetic surface overpotential losses,  $\eta_s$ , and thereby improve device efficiency.  $\eta_s$  is the sum of the surface overpotentials at the anode,  $\eta_a$ , and cathode,  $\eta_c$ , where the magnitude of overpotential losses are highly dependent on the reaction of interest and choice of the electrocatalyst material. The activity of an electrocatalytic material is largely determined by how the reactant(s), intermediate(s), and product(s) bond to and interact with the electrocatalyst surface. For many reactions, electrocatalysts that effectively balance competition between adsorption and desorption of reactive intermediates, through intermediate binding energy strengths, tend to be the most active catalysts. This concept is known as Sabatier's principle.<sup>128</sup> Species that adsorb too strongly to the surface effectively poison the catalyst (e.g. carbon monoxide on Pt), whereas species that adsorb too weakly limit the reaction rate due to their inability to sustain a high enough coverage of the reactive

intermediate on the electrocatalyst surface. This principle manifests itself in the form of a volcano relationship between catalytic activity and reactant/surface bond strength or binding energy. As a result, this type of correlation enables the catalytic activity of different types of electrocatalysts/adsorption sites to be predicted based on the binding energy of the adsorbed intermediate, which can be calculated using density functional theory (DFT).<sup>129–131</sup> Correlations between catalytic activities and DFT-predicted binding energies of reactive intermediates are a highly useful conceptual platform for guiding the design of highly active electrocatalyst materials with minimal surface overpotential losses.<sup>132</sup>

## 1.7 Oxide Encapsulated Electrocatalysts

This dissertation focuses on developing an oxide encapsulated electrocatalyst architecture (Figure 1.8) that has the potential to achieve advanced catalytic functionalities: i) preventing four common degradation mechanisms (Figure 1.8), ii) leveraging selective transport to control reaction pathways, and iii) altering catalytic pathways for the desired redox chemistry through unique energetics at buried interfaces and/or direct participation in the catalysis.

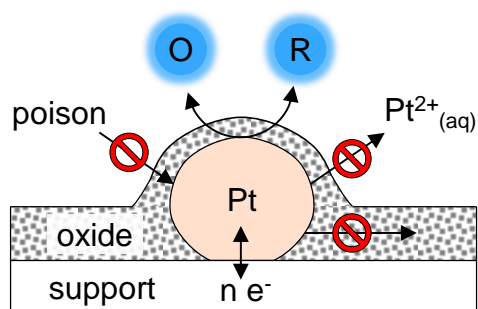


Figure 1.8. Side view schematic of an oxide coated electrocatalysts architecture in which an ultrathin oxide overlayer anchors catalyst (e.g. Pt) nanoparticles to the support surface to prevent migration and detachment

and selectively allows the desired redox chemistry ( $O + n e^- \leftrightarrow R$ ) while suppressing undesirable poisoning and dissolution.

### ***1.7.1 Overview of Similar Electrocatalyst Architectures***

Oxide coated catalyst structures have long been reported in the thermal catalysis field<sup>133–136</sup> and have often shown excellent resistance to particle coalescence (sintering).<sup>137,138</sup> These catalytic nanoparticles become fully or partially covered by ultrathin oxide layers from a spontaneous encapsulation of metal catalysts by oxide support materials at high temperatures, known as a strong metal support interaction (SMSI). Similar structures, such as silica coated Pt<sup>137,139</sup> and Ru<sup>140</sup> nanoparticles, that were intentionally made by the hydrolysis of silanes<sup>141</sup> or sol gel synthesis,<sup>142</sup> also showed high resistance to sintering and detachment during thermal catalytic reactions.

Takenaka et al. also studied silica coated Pt nanoparticle electrocatalysts (SiO<sub>2</sub>|Pt) for the ORR cathode in low temperature fuel cells to prevent Pt particle aggregation while significantly enhancing the stability of electrode performance during long term stability tests.<sup>100,143</sup> After the durability tests, the uncoated Pt particles aggregated to diameters exceeding 10 nm, significantly decreasing the ECSA, whereas the ECSA and particle size of the SiO<sub>2</sub>|Pt electrocatalysts remained constant (1–3 nm). Importantly, these studies demonstrated that the silica coating could improve electrocatalyst durability without compromising the ECSA or ORR activity compared to uncoated Pt electrocatalysts.<sup>144–146</sup> Furthermore, it was also shown that ultrathin silica coatings could suppress the dissolution of Pd, which would normally dissolve under ORR conditions.<sup>143,147</sup> These results suggest that silica overlayers might protect encapsulated electrocatalyst materials that are not normally stable for certain operating conditions and allow for selective transport of species

such as reactants and products while blocking others (e.g. dissolved electrocatalyst ions, undesired intermediate products, and impurities).

Selective transport through oxide overlayers has been leveraged to control reaction pathways and improve efficiency. For example, SiO<sub>2</sub>|Pd electrocatalysts decreased formation of undesirable hydroperoxide species during ORR compared to uncoated Pd.<sup>147</sup> In the PEC field, for which both HER and OER half reactions occur on the same photocatalytic particle, it is critically important to control reaction pathways and prevent undesired back reactions (e.g. HOR and ORR). Domen et al. have demonstrated that thin Cr<sub>2</sub>O<sub>3</sub> or MoO<sub>x</sub> overlayers can prevent ORR on encapsulated Rh<sup>148</sup> and Pt<sup>149</sup> HER electrocatalysts, respectively. Frei et al. fabricated a dense, 2–3 nm thick silica shell by plasma enhanced atomic layer deposition that served as a H<sup>+</sup> conducting, O<sub>2</sub> impermeable membrane. This shell separated the OER catalysts and O<sub>2</sub> products from the light absorber to prevent the ORR back reaction.<sup>150–155</sup> The dense silica synthesized by Frei et al. starkly contrasts the more porous silica used by Takenaka et al., which emphasizes the impact of different processing procedures on the structure and performance of oxide encapsulated electrocatalysts.

Oxide coated electrocatalysts have an inherently unique environment at buried interfaces between the oxide and electrocatalysts that has the potential to alter catalytic activity and selectivity by modifying energy barriers for reactions. This buried interface structure is similar in nature to so-called confined catalysts in which reactions take place within nanoscopic voids within electrocatalyst and/or support materials.<sup>156,157</sup> Catalyst and/or support atoms may interact with reactive intermediates differently (physically, chemically, and/or electronically) within these confined environments than if the electrocatalyst surface was directly exposed to the bulk electrolyte. This indicates the buried interface can modify reaction pathways through: i) confined (steric) molecular orientations, ii) multi-coordinated reactant/intermediate molecules with the

oxide and electrocatalyst, iii) varied concentrations of reactants and spectator ions, and iv) altered electric fields caused by disruption of the electrochemical double layer (ECDL).<sup>158–160</sup> These modifications can alter the binding energy of a reactant/intermediate molecule, and therefore influence the energy barriers of competing reaction pathways.

Oxides have also been suggested to participate in electrochemical reactions and thereby affect reaction pathways. Researchers have found that hydroxyl groups, provided by an oxide support (e.g.  $\text{TiO}_2$  or  $\text{SiO}_2$ ),<sup>161–164</sup> help to facilitate the removal of strongly adsorbed CO intermediates from Pt during the MOR and EOR. For example, Melvin et al. reported enhanced MOR activity on Pt| $\text{SiO}_2$  compared to Pt|C and attributed the improvement to the facile reaction between CO and surface hydroxyl groups on the silica support.<sup>165</sup> The hydroxyl groups provide an alternative reaction pathway to oxidize CO through the so-called bifunctional mechanism and improve Pt catalyst selectivity and efficiency.<sup>166</sup> Although most of these studies have been on oxide-supported electrocatalysts, the generality of these results suggest that oxide-encapsulated electrocatalysts also have the potential to modify reaction pathways through direct participation in the electrocatalysis.

### ***1.7.2 Challenges with the Rational Design of Oxide-Encapsulated Electrocatalysts***

Previous studies on oxide coated electrocatalysts have mostly focused on supported nanoparticles because of their high ECSA per catalyst loading. However, these nanoparticle-based architectures tend to have poorly defined and/or non-uniform structures which make it difficult to understand and elucidate fundamental kinetics and transport phenomena that occur at these structures. For example, in the Takenaka studies, the metal catalysts were considered to be uniformly covered with silica layers, based on TEM images, yet the catalysts were still active. Based on this observation, it was hypothesized the silica layers have a porous structure similar to

that of zeolites, and that reactants such as  $O_2$  and  $H_2O$  could diffuse to the metal surface through the pores.<sup>167,168</sup> However, detailed understanding of transport through the  $SiO_2$  was lacking because these powder catalysts are poorly defined and highly heterogeneous. In these types of nanoparticle-based oxide coated electrocatalysts, it is difficult to deconvolute electrochemical current due to reactions occurring i) at the buried interface associated with species transport through the overlayer or ii) at exposed electrocatalyst surfaces through pinholes and/or on uncoated portions of the nanoparticles. For this reason, this dissertation (Chapters 4 and 5) investigates well-defined oxide coated electrocatalysts, which can provide a model platform for gaining a fundamental understanding of kinetic and transport phenomena that underlie its operation.

One of the few examples of a model thin film electrode was reported by Garcia-Esparza et al., who investigated molybdenum oxide ( $MoO_x$ )-encapsulated Pt planar rotating disk electrodes for the prevention of HOR and ORR back reactions.<sup>149</sup> The  $MoO_x$  overlayer was able to block transport for both  $H_2$  and  $O_2$ , as desired. It was also suggested that the hydrated  $MoO_x$  overlayers could promote selective  $H_2O$  and  $H^+$  transport due to favorable chemical interactions between the  $MoO_x$  and  $H^+$ . Chapter 4 takes a similar approach for understanding transport through  $SiO_2$ . There have been several studies investigating species diffusion into  $SiO_2$ , suggesting  $SiO_2$  hydrates in water to improve  $H^+$  mobility via percolative diffusion and cross-ring proton hopping through  $SiO_2$ .<sup>169–175</sup> However, since these studies were not motivated by electrocatalysis and they did not investigate the optimization problem of maximizing the desired stability benefits (increasing thickness) without significantly affecting  $\eta_{conc}$  and  $\eta_s$ .

## 1.8 Dissertation Overview

This dissertation highlights the advanced catalytic functionalities of silicon oxide ( $SiO_x$ ) encapsulated Pt electrocatalysts ( $SiO_x|Pt$ ) and reports on the fundamental understanding of the

electrical, transport, and catalytic properties that govern their performance. Chapter 2 discusses the benefits and rationale for these materials and design, followed by detailed descriptions of electrode fabrication and synthesis techniques, and materials and electrochemical characterization methods to evaluate process-structure-performance relationships.

In Chapters 3–5, three separate studies are presented that demonstrate the ability of room temperature synthesized silicon oxide encapsulated Pt electrocatalysts (Figure 1.9) to: i) stabilize nanoparticles and improve electron transfer, ii) control reaction pathways through selective transport, and iii) affect catalytic pathways through unique catalytic properties at buried interfaces. Each study focuses on a different electrocatalyst requirement outlined in section 1.6 (stability, selectivity, and activity) and analyzes these advanced functionalities in different electrochemical systems (PEC, PEMEC, and DAFC). Chapter 3 first demonstrates that room temperature synthesized  $\text{SiO}_x$  overlayers can indeed improve nanoparticle electrocatalyst stability, specifically on a MIS photoelectrode (described in section 1.5.4) for PEC water splitting (described in section 1.2.2). The high surface area, Pt nanoparticle based MIS photoelectrode design is an inherently complex and composite structure (Figure 1.9a). In order to rationally design oxide encapsulated electrocatalysts it is critically important to study a simpler materials platform.

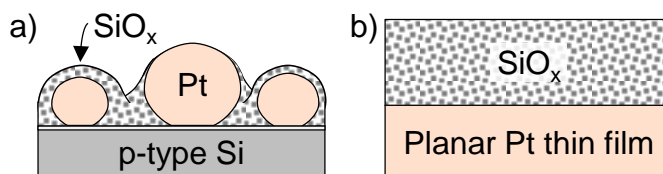


Figure 1.9. Side view schematics of silicon oxide ( $\text{SiO}_x$ )-encapsulated Pt electrocatalyst a) nanoparticles (Chapter 3) and b) thin films (Chapters 4 and 5) investigated in this dissertation. The substrate in (a) is a p-type Si (p-Si) semiconductor with an ultrathin native oxide layer (not labeled for clarity), whereas the substrate in (b) is the Pt film itself, which creates a well-defined, planar structure that removes complexities associated with semiconductors and non-uniformly coated nanoparticles.

The following studies investigate well-defined, low surface area electrodes, consisting of continuous SiO<sub>x</sub> overlayers of uniform thickness deposited onto smooth Pt thin films (Figure 1.9b). This simple design excludes effects of the support material (e.g. silicon or carbon) and allows for unambiguous characterization of key properties and performance metrics. Chapters 4 and 5 gain a more fundamental understanding of the ability to use SiO<sub>x</sub> as tunable overlayers that can mitigate electrocatalyst dissolution, migration, and detachment, and also prevent catalyst degradation due to poisoning and improve catalyst activity. Chapter 4 will focus on determining the structure and properties of the SiO<sub>x</sub> overlayer with the objective of demonstrating selective transport of desired reactants and products while preventing undesired transport of impurities. The planar SiO<sub>x</sub>|Pt electrode is operated as a PEMEC cathode for the HER to study selective H<sup>+</sup> and H<sub>2</sub> transport through SiO<sub>x</sub> that simultaneously blocks poison species (e.g. Cu<sup>2+</sup>).

Chapter 5 investigates the ability of SiO<sub>x</sub> to affect catalytic pathways through unique energetics at the buried interface and/or direct participation of the SiO<sub>x</sub> in the electrochemical reaction (section 1.7.1). This study seeks to improve the MOR and EOR catalytic activity for DAFCs with the hypothesis that the SiO<sub>x</sub> can i) alter interactions of reactant/intermediate species at the buried interface or ii) facilitate the removal of strongly adsorbed CO intermediates on Pt with proximal hydroxyl groups on SiO<sub>x</sub> through the so-called bifunctional mechanism (described in section 1.7.1). Through mechanistic understanding of transport and overlayer|catalysts interactions, this dissertation seeks to develop a broad knowledge base that will allow the oxide encapsulated electrocatalyst architecture to be applied to a wide range of materials and electrocatalytic applications.

Chapter 6 provides concluding remarks and suggestions for future directions of oxide encapsulated electrocatalysts and implications of their integration into commercial



electrochemical systems. Ultimately, this dissertation showcases oxide encapsulated electrocatalysts as highly versatile and potentially tunable electrocatalyst structures that may be applied to a wide range of electrode materials and electrochemical technologies for solar fuels production and conversion.

## 1.9 References

- (1) Lewis, N. S.; Nocera, D. G. Powering the Planet: Chemical Challenges in Solar Energy Utilization. *Proc. Natl. Acad. Sci.* **2006**, *103* (43), 15729–15735.
- (2) Gray, H. B. Powering the Planet with Solar Fuel. *Nat. Chem.* **2009**, *1*, 112.
- (3) Shaner, M. R.; Atwater, H. A.; Lewis, N. S.; McFarland, E. W. A Comparative Technoeconomic Analysis of Renewable Hydrogen Production Using Solar Energy. *Energy Environ. Sci.* **2016**, *9* (7), 2354–2371.
- (4) Turner, J.; Sverdrup, G.; Mann, M. K.; Maness, P.-C.; Kroposki, B.; Ghirardi, M.; Evans, R. J.; Blake, D. Renewable Hydrogen Production. *Int. J. Energy Res.* **2007**, *32*, 379–407.
- (5) Roy, S. C.; Varghese, O. K.; Paulose, M.; Grimes, C. a. Toward Solar Fuels: Photocatalytic Conversion of Carbon Dioxide to Hydrocarbons. *ACS Nano* **2010**, *4* (3), 1259–1278.
- (6) Mikkelsen, M.; Jørgensen, M.; Krebs, F. C. The Teraton Challenge. A Review of Fixation and Transformation of Carbon Dioxide. *Energy Environ. Sci.* **2010**, *3*, 43–81.
- (7) McKone, J. R.; Lewis, N. S.; Gray, H. B. Will Solar-Driven Water-Splitting Devices See the Light of Day? *Chem. Mater.* **2014**, *26*, 407–414.
- (8) Newman, J.; Hoertz, P. G.; Bonino, C. a.; Trainham, J. A. Review: An Economic Perspective on Liquid Solar Fuels. *J. Electrochem. Soc.* **2012**, *159* (10), A1722–A1729.
- (9) Chu, S.; Cui, Y.; Liu, N. The Path towards Sustainable Energy. *Nat. Mater.* **2017**, *16* (1), 16–22.
- (10) Lewis, N. S. Research Opportunities to Advance Solar Energy Utilization. *Science* **2016**, *351* (6271), aad1920-aad1920.
- (11) Pinaud, B. A.; Benck, J. D.; Seitz, L. C.; Forman, A. J.; Chen, Z.; Deutsch, T. G.; James, B. D.; Baum, K. N.; Baum, G. N.; Ardo, S.; et al. Technical and Economic Feasibility of Centralized Facilities for Solar Hydrogen Production via Photocatalysis and Photoelectrochemistry. *Energy Environ. Sci.* **2013**, *6* (7), 1983.
- (12) Walter, M. G.; Warren, E. L.; McKone, J. R.; Boettcher, S. W.; Mi, Q.; Santori, E. A.; Lewis, N. S. Solar Water Splitting Cells. *Chem. Rev.* **2010**, *110* (11), 6446–6473.

- (13) Gratzel, M. Photoelectrochemical Cells. *Nature* **2001**, *414*, 338–344.
- (14) Zhou, H.; Fan, T.; Zhang, D. An Insight into Artificial Leaves for Sustainable Energy Inspired by Natural Photosynthesis. *ChemCatChem*. 2011, pp 513–528.
- (15) Szklarczyk, M.; Bockris, J. O. Photoelectrocatalysis and Electrocatalysis on P-Silicon. *J. Phys. Chem.* **1984**, *88*, 1808–1815.
- (16) Nozik, A. J.; Memming, R. Physical Chemistry of Semiconductor - Liquid Interfaces. *J. Phys. Chem.* **1996**, *100*, 13061–13078.
- (17) Lewis, N. S. Frontiers of Research in Photoelectrochemical Solar Energy Conversion. *J. Electroanal. Chem.* **2001**, *508*, 1–10.
- (18) Li, Q.; He, R.; Gao, J.-A.; Jensen, J. O.; Bjerrum, N. J. The CO Poisoning Effect in PEMFCs Operational at Temperatures up to 200°C. *J. Electrochem. Soc.* **2003**, *150* (12), A1599.
- (19) Camara, G. A.; Ticianelli, E. A.; Mukerjee, S.; Lee, S. J.; McBreen, J. The CO Poisoning Mechanism of the Hydrogen Oxidation Reaction in Proton Exchange Membrane Fuel Cells. *J. Electrochem. Soc.* **2002**, *149* (6), A748.
- (20) Vesborg, P. C. K.; Jaramillo, T. F. Addressing the Terawatt Challenge: Scalability in the Supply of Chemical Elements for Renewable Energy. *RSC Adv.* **2012**, *2* (21), 7933.
- (21) Sharma, S.; Pollet, B. G. Support Materials for PEMFC and DMFC Electrocatalysts—A Review. *J. Power Sources* **2012**, *208*, 96–119.
- (22) Dominey, R. N.; Lewis, N. S.; Bruce, J. A.; Bookbinder, D. C.; Wrighton, M. S. Improvement of Photoelectrochemical Hydrogen Generation by Surface Modification of P-Type Silicon Semiconductor Photocathodes. *J. Am. Chem. Soc.* **1982**, *104*, 467–482.
- (23) Esposito, D. V.; Lee, Y.; Yoon, H.; Haney, P. M.; Labrador, N. Y.; Moffat, T. P.; Talin, A. A.; Szalai, V. A. Deconvoluting the Influences of 3D Structure on the Performance of Photoelectrodes for Solar-Driven Water Splitting. *Sustain. Energy Fuels* **2017**.
- (24) Bard, A. J.; Memming, R.; Miller, B. Terminology in Semiconductor Electrochemistry and Photoelectrochemical Energy Conversion. *Pure Appl. Chem.* **1991**, *63* (4), 569–596.
- (25) Green, M. A. *Solar Cells- Operating Principles, Technology and System Applications*; 1982.
- (26) Scheuermann, A. G.; Lawrence, J. P.; Kemp, K. W.; Ito, T.; Walsh, A.; Chidsey, C. E. D.; Hurley, P. K.; McIntyre, P. C. Design Principles for Maximizing Photovoltage in Metal-Oxide-Protected Water-Splitting Photoanodes. *Nat. Mater.* **2015**, *15* (October), 1–8.
- (27) Shockley, W.; Read, W. T. Statistics of the Recombinations of Holes and Electrons. *Phys. Rev.* **1952**, *87* (5), 835–842.

- (28) Yang, Y.; Gu, J.; Young, J. L.; Miller, E. M.; Turner, J. A.; Neale, N. R.; Beard, M. C. Semiconductor Interfacial Carrier Dynamics via Photoinduced Electric Fields. *Science* **2015**, *350* (6264), 1061–1065.
- (29) Bott, A. W. Electrochemistry of Semiconductors. *Curr. Sep.* **1998**, *17* (3), 87–91.
- (30) Weber, M. .; Dignam, M. . Splitting Water with Semiconducting Photoelectrodes—efficiency Considerations. *Int. J. Hydrogen Energy* **1986**, *11* (4), 225–232.
- (31) Warren, E. L.; Boettcher, S. W.; McKone, J. R.; Lewis, N. S. Photoelectrochemical Water Splitting: Silicon Photocathodes for Hydrogen Evolution. *Nanotechnology* **2010**, *7770*, 77701F–77701F–7.
- (32) Sun, K.; Shen, S.; Liang, Y.; Burrows, P. E.; Mao, S. S.; Wang, D. Enabling Silicon for Solar-Fuel Production. *Chem. Rev.* **2014**, *114*, 8662–8719.
- (33) Fujishima, A.; Honda, K. Electrochemical Photolysis of Water at a Semiconductor Electrode. *Nature* **1972**, *238* (5358), 37–38.
- (34) Castelli, I. E.; Olsen, T.; Datta, S.; Landis, D. D.; Dahl, S.; Thygesen, K. S.; Jacobsen, K. W. Computational Screening of Perovskite Metal Oxides for Optimal Solar Light Capture. *Energy Environ. Sci.* **2012**, *5*, 5814.
- (35) Khaselev, O.; Turner, J. A. Electrochemical Stability of P-GaInP<sub>2</sub> in Aqueous Electrolytes Toward Photoelectrochemical Water Splitting. *J. Electrochem. Soc.* **1998**, *145* (10), 3335–3339.
- (36) Khaselev, O.; Turner, J. A. A Monolithic Photovoltaic-Photoelectrochemical Device for Hydrogen Production via Water Splitting. *Science* **1998**, *280* (5362), 425–427.
- (37) Jayaraman, S.; Jaramillo, T. F.; Baeck, S.-H.; McFarland, E. W. Synthesis and Characterization of Pt-WO<sub>3</sub> as Methanol Oxidation Catalysts for Fuel Cells. *J. Phys. Chem. B* **2005**, *109*, 22958–22966.
- (38) Gaillard, N.; Chang, Y.; Kaneshiro, J.; Deangelis, A.; Miller, E. L. Status of Research on Tungsten Oxide-Based Photoelectrochemical Devices at the University of Hawai'i N. **2010**, *7770*.
- (39) Miller, E. L.; Gaillard, N.; Kaneshiro, J.; Deangelis, A.; Garland, R. Progress in New Semiconductor Materials Classes for Solar Photoelectrolysis. *Int. J. Energy Res.* **2010**, *34*, 1215–1222.
- (40) Nellist, M. R.; Laskowski, F. A. L.; Lin, F.; Mills, T. J.; Boettcher, S. W. Semiconductor-Electrocatalyst Interfaces: Theory, Experiment, and Applications in Photoelectrochemical Water Splitting. *Acc. Chem. Res.* **2016**, *49* (4).
- (41) Heller, A. Hydrogen-Evolving Solar Cells. *Science* **1984**, 1141–1148.

- (42) Heller, A.; Vadimsky, R. G. Efficient Solar to Chemical Conversion: 12% Efficient Photoassisted Electrolysis in the [p-Type InP(Ru)]/HCl-KCl/Pt(Rh) Cell. *Phys. Rev. Lett.* **1981**, *46* (17), 1153–1156.
- (43) Heller, A.; Aspnes, D. E.; Porter, J. D.; Sheng, T. T.; Vadimsky, R. G. Transparent Metals Preparation and Characterization of Light-Transmitting Platinum Films. *J. Phys. Chem.* **1985**, *89* (1982), 4444–4452.
- (44) Lewerenz, H. J. Micro- and Nanotopographies for Photoelectrochemical Energy Conversion. I: The Photovoltaic Mode. *Electrochim. Acta* **2011**, *56*, 10713–10725.
- (45) Muñoz, A.; Skorupska, K.; Lewerenz, H. Nanostructure Approaches for Photoelectrocatalysis. *ECS Trans.* **2009**, *21* (1), 35–56.
- (46) Lewerenz, H. J.; Heine, C.; Skorupska, K.; Szabo, N.; Hannappel, T.; Vo-Dinh, T.; Campbell, S. A.; Klemm, H. W.; Muñoz, A. G. Photoelectrocatalysis: Principles, Nanoemitter Applications and Routes to Bio-Inspired Systems. *Energy Environ. Sci.* **2010**, *3*, 748–760.
- (47) Aggour, M.; Skorupska, K.; Stempel Pereira, T.; Jungblut, H.; Grzanna, J.; Lewerenz, H. J. Photoactive Silicon-Based Nanostructure by Self-Organized Electrochemical Processing. *J. Electrochem. Soc.* **2007**, *154* (9), H794–H797.
- (48) Chen, Y. W.; Prange, J. D.; Dühnen, S.; Park, Y.; Gunji, M.; Chidsey, C. E. D.; McIntyre, P. C. Atomic Layer-Deposited Tunnel Oxide Stabilizes Silicon Photoanodes for Water Oxidation. *Nat. Mater.* **2011**, *10* (7), 539–544.
- (49) Esposito, D. V.; Levin, I.; Moffat, T. P.; Talin, A. A. H<sub>2</sub> Evolution at Si-Based Metal-Insulator-Semiconductor Photoelectrodes Enhanced by Inversion Channel Charge Collection and H Spillover. *Nat. Mater.* **2013**, *12* (6), 562–568.
- (50) Hill, J. C.; Landers, A. T.; Switzer, J. A. An Electrodeposited N-Si/SiO<sub>x</sub>/Co/CoOOH Inhomogeneous Metal-Insulator-Semiconductor Junction for Efficient Photoelectrochemical Water Oxidation. *Nat. Mater.* **2015**, *14*, 6751–6755.
- (51) Zhu, T.; Chong, M. N. Prospects of Metal–insulator–semiconductor (MIS) Nanojunction Structures for Enhanced Hydrogen Evolution in Photoelectrochemical Cells: A Review. *Nano Energy* **2015**, *12*, 347–373.
- (52) Digdaya, I. A.; Adhyaksa, G. W. P.; Trześniewski, B. J.; Garnett, E. C.; Smith, W. A. Interfacial Engineering of Metal-Insulator-Semiconductor Junctions for Efficient and Stable Photoelectrochemical Water Oxidation. *Nat. Commun.* **2017**, *8* (May), 15968.
- (53) Har-Lavan, R.; Ron, I.; Thieblemont, F.; Cahen, D. Toward Metal-Organic Insulator-Semiconductor Solar Cells, Based on Molecular Monolayer Self-Assembly on n-Si. *Appl. Phys. Lett.* **2009**, *94* (4), 043308.
- (54) Singh, R.; Green, M. A.; Rajkanan, K. Review of Conductor-Insulator-Semiconductor

- (CIS) Solar Cells. *Sol. Cells* **1981**, 3 (2), 95–148.
- (55) Lewerenz, H. J.; Skorupska, K.; Muñoz, A. G.; Stempel, T.; Nüsse, N.; Lublow, M.; Vo-Dinh, T.; Kulesza, P. Micro- and Nanotopographies for Photoelectrochemical Energy Conversion. II: Photoelectrocatalysis – Classical and Advanced Systems. *Electrochim. Acta* **2011**, 56, 10726–10736.
  - (56) Muñoz, A. G.; Lewerenz, H. J. Advances in Photoelectrocatalysis with Nanotopographical Photoelectrodes. *ChemPhysChem* **2010**, 11 (8), 1603–1615.
  - (57) Kaplan, R.; Kaplan, B.; Hegedus, S. S. A Comparative Study of Photoconductivity and Carrier Transport in A-Si:H P–i–n Solar Cells with Different Back Contacts. *Solid. State. Electron.* **2010**, 54, 22–27.
  - (58) Kitchin, J. R.; Nørskov, J. K.; Barteau, M. A.; Chen, J. G. Trends in the Chemical Properties of Early Transition Metal Carbide Surfaces: A Density Functional Study. *Catal. Today* **2005**, 105 (1 SPEC. ISS.), 66–73.
  - (59) Sheng, W.; Gasteiger, H. A.; Shao-Horn, Y. Hydrogen Oxidation and Evolution Reaction Kinetics on Platinum: Acid vs Alkaline Electrolytes. *J. Electrochem. Soc.* **2010**, 157 (11), B1529.
  - (60) Stephens, I. E. L.; Bondarenko, A. S.; Grønbjerg, U.; Rossmeisl, J.; Chorkendorff, I. Understanding the Electrocatalysis of Oxygen Reduction on Platinum and Its Alloys. *Energy Environ. Sci.* **2012**, 5 (5), 6744.
  - (61) Liu, Z.; Ling, X. Y.; Su, X.; Lee, J. Y. Carbon-Supported Pt and PtRu Nanoparticles as Catalysts for a Direct Methanol Fuel Cell. *J. Phys. Chem. B* **2004**, 108 (24), 8234–8240.
  - (62) Selvaraj, V.; Alagar, M. Pt and Pt-Ru Nanoparticles Decorated Polypyrrole/Multiwalled Carbon Nanotubes and Their Catalytic Activity towards Methanol Oxidation. *Electrochem. commun.* **2007**, 9 (5), 1145–1153.
  - (63) Antolini, E.; Gonzalez, E. R. Effect of Synthesis Method and Structural Characteristics of Pt–Sn Fuel Cell Catalysts on the Electro-Oxidation of CH<sub>3</sub>OH and CH<sub>3</sub>CH<sub>2</sub>OH in Acid Medium☆. *Catal. Today* **2011**, 160 (1), 28–38.
  - (64) Akhairi, M. A. F.; Kamarudin, S. K. Catalysts in Direct Ethanol Fuel Cell (DEFC): An Overview. *Int. J. Hydrogen Energy* **2016**, 41 (7), 4214–4228.
  - (65) Léger, J.-M.; Rousseau, S.; Coutanceau, C.; Hahn, F.; Lamy, C.; Kamarudin, M. Z. F.; Kamarudin, S. K.; Masdar, M. S.; Daud, W. R. W.; Akhairi, M. A. F.; et al. Review: Direct Ethanol Fuel Cells. *Int. J. Hydrogen Energy* **2015**, 50 (7), 4214–4228.
  - (66) Chen, Y.; Bellini, M.; Bevilacqua, M.; Fornasiero, P.; Lavacchi, A.; Miller, H. A.; Wang, L.; Vizza, F. Direct Alcohol Fuel Cells: Toward the Power Densities of Hydrogen-Fed Proton Exchange Membrane Fuel Cells. *ChemSusChem* **2015**, 8 (3), 524–533.

- (67) McCrory, C. C. L.; Jung, S.; Peters, J. C.; Jaramillo, T. F. Benchmarking Heterogeneous Electrocatalysts for the Oxygen Evolution Reaction. *J. Am. Chem. Soc.* **2013**, *135* (45), 16977–16987.
- (68) Kemppainen, E.; Bodin, A.; Sebok, B.; Pedersen, T.; Seger, B.; Mei, B.; Bae, D.; Vesborg, P. C. K.; Halme, J.; Hansen, O.; et al. Scalability and Feasibility of Photoelectrochemical H<sub>2</sub> Evolution: The Ultimate Limit of Pt Nanoparticle as an HER Catalyst. *Energy Environ. Sci.* **2015**.
- (69) Ferreira, P. J.; la O', G. J.; Shao-Horn, Y.; Morgan, D.; Makharia, R.; Kocha, S.; Gasteiger, H. A. Instability of Pt/C Electrocatalysts in Proton Exchange Membrane Fuel Cells. *J. Electrochem. Soc.* **2005**, *152* (11), A2256–A2271.
- (70) Pavlišić, A.; Jovanović, P.; Šelih, V. S.; Šala, M.; Hodnik, N.; Hočevár, S.; Gabersček, M. The Influence of Chloride Impurities on Pt/C Fuel Cell Catalyst Corrosion. *Chem. Commun.* **2014**, *50* (28), 3732–3734.
- (71) Shao-Horn, Y.; Sheng, W. C.; Chen, S.; Ferreira, P. J.; Holby, E. F.; Morgan, D. Instability of Supported Platinum Nanoparticles in Low-Temperature Fuel Cells. *Top. Catal.* **2007**, *46* (3–4), 285–305.
- (72) Spöri, C.; Kwan, J. T. H.; Bonakdarpour, A.; Wilkinson, D. P.; Strasser, P. The Stability Challenges of Oxygen Evolving Catalysts: Towards a Common Fundamental Understanding and Mitigation of Catalyst Degradation. *Angew. Chemie Int. Ed.* **2017**, *56* (22), 5994–6021.
- (73) Li, L.; Hu, L.; Li, J.; Wei, Z. Enhanced Stability of Pt Nanoparticle Electrocatalysts for Fuel Cells. *Nano Res.* **2015**, *8* (2), 418–440.
- (74) Topalov, A. A.; Cherevko, S.; Zeradjanin, A. R.; Meier, J. C.; Katsounaros, I.; Mayrhofer, K. J. J. Towards a Comprehensive Understanding of Platinum Dissolution in Acidic Media. *Chem. Sci.* **2014**, *5* (2), 631.
- (75) Shrestha, S.; Liu, Y.; Mustain, W. E. Electrocatalytic Activity and Stability of Pt Clusters on State-of-the-Art Supports: A Review. *Catalysis Reviews - Science and Engineering*. 2011, pp 256–336.
- (76) Dubau, L.; Castanheira, L.; Maillard, F.; Chatenet, M.; Lottin, O.; Maranzana, G.; Dillet, J.; Lamibrac, A.; Perrin, J. C.; Moukheiber, E.; et al. A Review of PEM Fuel Cell Durability: Materials Degradation, Local Heterogeneities of Aging and Possible Mitigation Strategies. *Wiley Interdisciplinary Reviews: Energy and Environment*. 2014, pp 540–560.
- (77) Su, L.; Jia, W.; Li, C.-M.; Lei, Y. Mechanisms for Enhanced Performance of Platinum-Based Electrocatalysts in Proton Exchange Membrane Fuel Cells. *ChemSusChem* **2014**, *7* (2).
- (78) Pourbaix, M. *Atlas of Electrochemical Equilibria in Aqueous Solutions*; Oxford: Pergamon Press: New York, 1974.

- (79) Merte, L. R.; Behafarid, F.; Miller, D. J.; Friebe, D.; Cho, S.; Mbuga, F.; Sokaras, D.; Alonso-Mori, R.; Weng, T. C.; Nordlund, D.; et al. Electrochemical Oxidation of Size-Selected Pt Nanoparticles Studied Using in Situ High-Energy-Resolution X-Ray Absorption Spectroscopy. *ACS Catal.* **2012**, 2 (11), 2371–2376.
- (80) Ishimoto, T.; Ogura, T.; Umeda, M.; Koyama, M. Theoretical Study on Dissolution and Reprecipitation Mechanism of Pt Complex in Pt Electrocatalyst. *J. Phys. Chem. C* **2011**, 115 (7), 3136–3142.
- (81) Noël, J. M.; Yu, Y.; Mirkin, M. V. Dissolution of Pt at Moderately Negative Potentials during Oxygen Reduction in Water and Organic Media. *Langmuir* **2013**, 29 (5), 1346–1350.
- (82) Kasian, O.; Geiger, S.; Stock, P.; Polymeros, G.; Breitbach, B.; Savan, A.; Ludwig, A.; Cherevko, S.; Mayrhofer, K. J. J. On the Origin of the Improved Ruthenium Stability in RuO<sub>2</sub>–IrO<sub>2</sub> Mixed Oxides. *J. Electrochem. Soc.* **2016**, 163 (11), F3099–F3104.
- (83) Lee, Y.; Suntivich, J.; May, K. J.; Perry, E. E.; Shao-Horn, Y. Synthesis and Activities of Rutile IrO<sub>2</sub> and RuO<sub>2</sub> Nanoparticles for Oxygen Evolution in Acid and Alkaline Solutions. *J. Phys. Chem. Lett.* **2012**, No. pH 1, 399–404.
- (84) Rinaldo, S. G.; Stumper, J.; Eikerling, M. Physical Theory of Platinum Nanoparticle Dissolution in Polymer Electrolyte Fuel Cells. *J. Phys. Chem. C* **2010**, 114 (13), 5773–5785.
- (85) Tang, L.; Han, B.; Persson, K.; Friesen, C.; He, T.; Sieradzki, K.; Ceder, G. Electrochemical Stability of Nanometer-Scale Pt Particles in Acidic Environments. *J. Am. Chem. Soc.* **2010**, 132 (2), 596–600.
- (86) Topalov, A. A.; Katsounaros, I.; Auinger, M.; Cherevko, S.; Meier, J. C.; Klemm, S. O.; Mayrhofer, K. J. J. Dissolution of Platinum: Limits for the Deployment of Electrochemical Energy Conversion? *Angew. Chemie - Int. Ed.* **2012**, 51 (50), 12613–12615.
- (87) Wang, X.; Zhang, L.; Li, G.; Zhang, G.; Shao, Z. G.; Yi, B. The Influence of Ferric Ion Contamination on the Solid Polymer Electrolyte Water Electrolysis Performance. *Electrochim. Acta* **2015**, 158, 253–257.
- (88) Hansen, T. W.; Delariva, A. T.; Challa, S. R.; Datye, A. K. Sintering of Catalytic Nanoparticles: Particle Migration or Ostwald Ripening? *Acc. Chem. Res.* **2013**, 46 (8), 1720–1730.
- (89) Yoshida, K.; Bright, A.; Tanaka, N. Direct Observation of the Initial Process of Ostwald Ripening Using Spherical Aberration-Corrected Transmission Electron Microscopy. *J. Electron Microsc.* (Tokyo). **2012**, 61 (2), 99–103.
- (90) Iojoiu, C.; Guilminot, E.; Maillard, F.; Chatenet, M.; Sanchez, J.-Y.; Claude, E.; Rossinot, E. Membrane and Active Layer Degradation Following PEMFC Steady-State Operation. *J. Electrochem. Soc.* **2007**, 154 (11), B1115.
- (91) Kangasniemi, K. H.; Condit, D. A.; Jarvi, T. D. Characterization of Vulcan

- Electrochemically Oxidized under Simulated PEM Fuel Cell Conditions. *J. Electrochem. Soc.* **2004**, *151* (4), E125.
- (92) Wang, J.; Yin, G.; Shao, Y.; Zhang, S.; Wang, Z.; Gao, Y. Effect of Carbon Black Support Corrosion on the Durability of Pt/C Catalyst. *J. Power Sources* **2007**, *171* (2), 331–339.
  - (93) He, Q.; Joy, D. C.; Keffer, D. J. Impact of Oxidation on Nanoparticle Adhesion to Carbon Substrates. *RSC Adv.* **2013**, *3* (36), 15792.
  - (94) Dam, V. A. T.; de Bruijn, F. A. The Stability of PEMFC Electrodes. *J. Electrochem. Soc.* **2007**, *154* (5), B494.
  - (95) Marcu, A.; Toth, G.; Pietrasz, P.; Waldecker, J. Cathode Catalysts Degradation Mechanism from Liquid Electrolyte to Membrane Electrode Assembly. *Comptes Rendus Chim.* **2014**, *17* (7), 752–759.
  - (96) Wang, S.; Zhang, L.; Xia, Z.; Roy, A.; Chang, D. W.; Baek, J. B.; Dai, L. BCN Graphene as Efficient Metal-Free Electrocatalyst for the Oxygen Reduction Reaction. *Angew. Chemie - Int. Ed.* **2012**, *51* (17), 4209–4212.
  - (97) Park, J.; Jang, Y. J.; Kim, Y. J.; Song, M.; Yoon, S.; Kim, D. H.; Kim, S.-J. Sulfur-Doped Graphene as a Potential Alternative Metal-Free Electrocatalyst and Pt-Catalyst Supporting Material for Oxygen Reduction Reaction. *Phys. Chem. Chem. Phys.* **2014**, *16* (1), 103–109.
  - (98) Pylypenko, S.; Borisevich, A.; More, K. L.; Corpuz, A. R.; Holme, T.; Dameron, A. A.; Olson, T. S.; Dinh, H. N.; Gennett, T.; O’Hayre, R. Nitrogen: Unraveling the Secret to Stable Carbon-Supported Pt-Alloy Electrocatalysts. *Energy Environ. Sci.* **2013**, *6* (10), 2957–2964.
  - (99) Zhou, X.; Qiao, J.; Yang, L.; Zhang, J. A Review of Graphene-Based Nanostructural Materials for Both Catalyst Supports and Metal-Free Catalysts in PEM Fuel Cell Oxygen Reduction Reactions. *Advanced Energy Materials*. 2014.
  - (100) Takenaka, S.; Miyamoto, H.; Utsunomiya, Y.; Matsune, H.; Kishida, M. Catalytic Activity of Highly Durable Pt/CNT Catalysts Covered with Hydrophobic Silica Layers for the Oxygen Reduction Reaction in PEFCs. *J. Phys. Chem. C* **2014**, *118* (2), 774–783.
  - (101) Kuo, P. L.; Hsu, C. H.; Wu, H. M.; Hsu, W. S.; Kuo, D. Controllable-Nitrogen Doped Carbon Layer Surrounding Carbon Nanotubes as Novel Carbon Support for Oxygen Reduction Reaction. *Fuel Cells*. **2012**, *12* (4), 649–655.
  - (102) Esposito, D. V.; Hunt, S. T.; Stottlemeyer, A. L.; Dobson, K. D.; McCandless, B. E.; Birkmire, R. W.; Chen, J. G. Low-Cost Hydrogen-Evolution Catalysts Based on Monolayer Platinum on Tungsten Monocarbide Substrates. *Angew. Chemie Int. Ed.* **2010**, *49* (51), 9859–9862.
  - (103) Tripković, V.; Abild-Pedersen, F.; Studt, F.; Cerri, I.; Nagami, T.; Bligaard, T.; Rossmeisl, J. Metal Oxide-Supported Platinum Overlayers as Proton-Exchange Membrane Fuel Cell



- Cathodes. *ChemCatChem* **2012**, 4 (2), 228–235.
- (104) Danilovic, N.; Subbaraman, R.; Chang, K. C.; Chang, S. H.; Kang, Y. J.; Snyder, J.; Paulikas, A. P.; Strmcnik, D.; Kim, Y. T.; Myers, D.; et al. Activity-Stability Trends for the Oxygen Evolution Reaction on Monometallic Oxides in Acidic Environments. *J. Phys. Chem. Lett.* **2014**, 5 (14), 2474–2478.
  - (105) Pan, Z.; Xiao, Y.; Fu, Z.; Zhan, G.; Wu, S.; Xiao, C.; Hu, G.; Wei, Z. Hollow and Porous Titanium Nitride Nanotubes as High-Performance Catalyst Supports for Oxygen Reduction Reaction. *J. Mater. Chem. A* **2014**, 2 (34), 13966–13975.
  - (106) Shao, Y.; Liu, J.; Wang, Y.; Lin, Y. Novel Catalyst Support Materials for PEMfuelcells: Current Status and Future Prospects. *J. Mater. Chem.* **2009**, 19 (1), 46–59.
  - (107) Sun, X.; Li, D.; Ding, Y.; Zhu, W.; Guo, S.; Wang, Z. L.; Sun, S. Core/Shell Au/CuPt Nanoparticles and Their Dual Electrocatalysis for Both Reduction and Oxidation Reactions. *J. Am. Chem. Soc.* **2014**, 136 (15), 5745–5749.
  - (108) Liu, X.; Fu, G.; Chen, Y.; Tang, Y.; She, P.; Lu, T. Pt-Pd-Co Trimetallic Alloy Network Nanostructures with Superior Electrocatalytic Activity towards the Oxygen Reduction Reaction. *Chem. - A Eur. J.* **2014**, 20 (2), 585–590.
  - (109) Zhang, J.; Lima, F. H. B.; Shao, M. H.; Sasaki, K.; Wang, J. X.; Hanson, J.; Adzic, R. R. Platinum Monolayer on Nonnoble Metal–Noble Metal Core–Shell Nanoparticle Electrocatalysts for O<sub>2</sub> Reduction. *J. Phys. Chem. B* **2005**, 109 (48), 22701–22704.
  - (110) Sasaki, K.; Naohara, H.; Choi, Y.; Cai, Y.; Chen, W.-F.; Liu, P.; Adzic, R. R. Highly Stable Pt Monolayer on PdAu Nanoparticle Electrocatalysts for the Oxygen Reduction Reaction. *Nat. Commun.* **2012**, 3, 1–9.
  - (111) Ashton, S. J.; Arenz, M. Comparative DEMS Study on the Electrochemical Oxidation of Carbon Blacks. *J. Power Sources* **2012**, 217, 392–399.
  - (112) Feng, C.; Wang, J.; Cheng, Y.; He, P.; Liew, K. M. Diffusion Mechanism of Platinum Nanoclusters on Well-Aligned Carbon Nanotubes. *RSC Adv.* **2014**, 4 (105), 60711–60719.
  - (113) Esposito, D. V.; Hunt, S. T.; Kimmel, Y. C.; Chen, J. G. A New Class of Electrocatalysts for Hydrogen Production from Water Electrolysis: Metal Monolayers Supported on Low-Cost Transition Metal Carbides. *J. Am. Chem. Soc.* **2012**, 134 (6), 3025–3033.
  - (114) Zhang, Z.; Liu, J.; Gu, J.; Su, L.; Cheng, L. An Overview of Metal Oxide Materials as Electrocatalysts and Supports for Polymer Electrolyte Fuel Cells. *Energy Environ. Sci.* **2014**, 7 (8), 2535.
  - (115) Tavares, M. .; Machado, S. A. .; Mazo, L. . Study of Hydrogen Evolution Reaction in Acid Medium on Pt Microelectrodes. *Electrochim. Acta* **2001**, 46 (28), 4359–4369.
  - (116) Tan, S. M.; Sofer, Z.; Pumera, M. Sulfur Poisoning of Emergent and Current

- Electrocatalysts: Vulnerability of MoS<sub>2</sub> and Direct Correlation to Pt Hydrogen Evolution Reaction Kinetics. *Nanoscale* **2015**, 7 (19).
- (117) Protopopoff, E.; Marcus, P. Poisoning of the Cathodic Hydrogen Evolution Reaction by Sulfur Chemisorbed on Platinum (110). *J. Electrochem. Soc.* **1988**, 135 (12), 3073–3075.
- (118) Nasri, N. S.; Jones, J. M.; Dupont, V. A.; Williams, A. A Comparative Study of Sulfur Poisoning and Regeneration of Precious-Metal Catalysts. *Energy & Fuels* **1998**, 12 (6), 1130–1134.
- (119) Csicsery, S. M. Shape-Selective Catalysis in Zeolites. *Zeolites* **1984**, 4 (3), 202–213.
- (120) Taguchi, A.; Schüth, F. *Ordered Mesoporous Materials in Catalysis*; 2005; Vol. 77.
- (121) Haw, J. F.; Song, W.; Marcus, D. M.; Nicholas, J. B. The Mechanism of Methanol to Hydrocarbon Catalysis. *Acc. Chem. Res.* **2003**, 36 (5), 317–326.
- (122) Corma, A.; García, H.; Llabrés i Xamena, F. X. Engineering Metal Organic Frameworks for Heterogeneous Catalysis. *Chem. Rev.* **2010**, 110 (8), 4606–4655.
- (123) Wheeldon, I.; Minter, S. D.; Banta, S.; Barton, S. C.; Atanassov, P.; Sigman, M. Substrate Channelling as an Approach to Cascade Reactions. *Nat. Chem.* **2016**, 8 (4), 299–309.
- (124) Bulutoglu, B.; Garcia, K. E.; Wu, F.; Minter, S. D.; Banta, S. Direct Evidence for Metabolon Formation and Substrate Channeling in Recombinant TCA Cycle Enzymes. *ACS Chem. Biol.* **2016**, 11 (10), 2847–2853.
- (125) Rangnekar, N.; Mittal, N.; Elyassi, B.; Caro, J.; Tsapatsis, M. Zeolite Membranes - a Review and Comparison with MOFs. *Chem. Soc. Rev.* **2015**, 44 (20), 7128–7154.
- (126) Gascon, J.; Kapteijn, F.; Zornoza, B.; Sebastián, V.; Casado, C.; Coronas, J. Practical Approach to Zeolitic Membranes and Coatings: State of the Art, Opportunities, Barriers, and Future Perspectives. *Chem. Mater.* **2012**, 24 (15), 2829–2844.
- (127) Newman, J.; Thomas-Alyea, K. E. *Electrochemical Systems*, 3rd ed.; Wiley, 2004.
- (128) Sabatier, P. Hydrogenation and Dehydrogenation Catalysis. *Berichte der Dtsch. Chem. Gesellschaft* **1911**, 44 (3), 3180–3180.
- (129) Medford, A. J.; Vojvodic, A.; Hummelshøj, J. S.; Voss, J.; Abild-Pedersen, F.; Studt, F.; Bligaard, T.; Nilsson, A.; Nørskov, J. K. From the Sabatier Principle to a Predictive Theory of Transition-Metal Heterogeneous Catalysis. *J. Catal.* **2015**, 328, 36–42.
- (130) Nørskov, J. K.; Bligaard, T.; Logadottir, A.; Kitchin, J. R.; Chen, J. G.; Pandelov, S.; Stimming, U. Trends in the Exchange Current for Hydrogen Evolution. *J. Electrochem. Soc.* **2005**, 152 (3), J23.
- (131) Greeley, J.; Jaramillo, T. F.; Bonde, J.; Chorkendorff, I. B.; Nørskov, J. K. Computational

- High-Throughput Screening of Electrocatalytic Materials for Hydrogen Evolution. *Nat. Mater.* **2006**, *5* (11), 909–913.
- (132) She, Z. W.; Kibsgaard, J.; Dickens, C. F.; Chorkendorff, I.; Nørskov, J. K.; Jaramillo, T. F. Combining Theory and Experiment in Electrocatalysis: Insights into Materials Design. *Science*. 2017.
- (133) Pesty, F.; Steinrück, H. P.; Madey, T. E. Thermal Stability of Pt Films on TiO<sub>2</sub>(110): Evidence for Encapsulation. *Surf. Sci.* **1995**, *339* (1–2), 83–95.
- (134) Strayer, M. E.; Binz, J. M.; Tanase, M.; Kamali Shahri, S. M.; Sharma, R.; Rioux, R. M.; Mallouk, T. E. Interfacial Bonding Stabilizes Rhodium and Rhodium Oxide Nanoparticles on Layered Nb Oxide and Ta Oxide Supports. *J. Am. Chem. Soc.* **2014**, *136*, 5687–5696.
- (135) Strayer, M. E.; Senftle, T. P.; Winterstein, J. P.; Vargas-Barbosa, N. M.; Sharma, R.; Rioux, R. M.; Janik, M. J.; Mallouk, T. E. Charge Transfer Stabilization of Late Transition Metal Oxide Nanoparticles on a Layered Niobate Support. *J. Am. Chem. Soc.* **2015**, *137* (51), 16216–16224.
- (136) Chandler, B. D. Strong Metal-Support Interactions: An Extra Layer of Complexity. *Nat. Chem.* **2017**, *9* (2), 108–109.
- (137) Joo, S. H.; Park, J. Y.; Tsung, C.-K.; Yamada, Y.; Yang, P.; Somorjai, G. A. Thermally Stable Pt/Mesoporous Silica Core-Shell Nanocatalysts for High-Temperature Reactions. *Nat. Mater.* **2009**, *8* (2), 126–131.
- (138) Gould, T. D.; Izar, A.; Weimer, A. W.; Falconer, J. L.; Medlin, J. W. Stabilizing Ni Catalysts by Molecular Layer Deposition for Harsh, Dry Reforming Conditions. *ACS Catal.* **2014**, *4* (8), 2714–2717.
- (139) TAKENAKA, S.; ARIKE, T.; MATSUNE, H.; TANABE, E.; KISHIDA, M. Preparation of Carbon Nanotube-Supported Metal Nanoparticles Coated with Silica Layers. *J. Catal.* **2008**, *257* (2), 345–355.
- (140) Arike, T.; Takenaka, S.; Matsune, H.; Kishida, M. Improvement in the Durability of Carbon Nanotube-Supported Ruthenium Catalysts by Coverage with Silica Layers. *Bull. Chem. Soc. Jpn.* **2010**, *83* (8), 953–959.
- (141) Takenaka, S.; Arike, T.; Nakagawa, K.; Matsune, H.; Kishida, M.; Tanabe, E. Synthesis of Carbon Nanotube-Supported Pt Nanoparticles Covered with Silica Layers. *Carbon N. Y.* **2008**, *46* (2), 365–368.
- (142) Joo, S. H.; Park, J. Y.; Tsung, C.-K.; Yamada, Y.; Yang, P.; Somorjai, G. A. Thermally Stable Pt/Mesoporous Silica Core-shell Nanocatalysts for High-Temperature Reactions. *Nat. Mater.* **2009**, *8* (2), 126–131.
- (143) Takenaka, S.; Kishida, M. Functionalization of Carbon Nanotube-Supported Precious Metal Catalysts by Coverage with Metal Oxide Layers. *Catal. Surv. from Asia* **2013**, *17* (2), 71–

- (144) Takenaka, S.; Matsumori, H.; Nakagawa, K.; Matsune, H.; Tanabe, E.; Kishida, M. Improvement in the Durability of Pt Electrocatalysts by Coverage with Silica Layers. *J. Phys. Chem. C* **2007**, *111* (42), 15133–15136.
- (145) Matsumori, H.; Takenaka, S.; Matsune, H.; Kishida, M. Preparation of Carbon Nanotube-Supported Pt Catalysts Covered with Silica Layers; Application to Cathode Catalysts for PEFC. *Appl. Catal. A Gen.* **2010**, *373* (1–2), 176–185.
- (146) Takenaka, S.; Matsumori, H.; Matsune, H.; Tanabe, E.; Kishida, M. High Durability of Carbon Nanotube-Supported Pt Electrocatalysts Covered with Silica Layers for the Cathode in a PEMFC. *J. Electrochem. Soc.* **2008**, *155* (9), B929.
- (147) Takenaka, S.; Susuki, N.; Miyamoto, H.; Tanabe, E.; Matsune, H.; Kishida, M. Highly Durable Carbon Nanotube-Supported Pd Catalysts Covered with Silica Layers for the Oxygen Reduction Reaction. *J. Catal.* **2011**, *279* (2), 381–388.
- (148) Maeda, K.; Teramura, K.; Lu, D.; Saito, N.; Inoue, Y.; Domen, K. Noble-Metal/Cr<sub>2</sub>O<sub>3</sub> Core/Shell Nanoparticles as a Cocatalyst for Photocatalytic Overall Water Splitting. *Angew. Chemie Int. Ed.* **2006**, *45* (46), 7806–7809.
- (149) Garcia-Esparza, A. T.; Shinagawa, T.; Ould-Chikh, S.; Qureshi, M.; Peng, X.; Wei, N.; Anjum, D. H.; Clo, A.; Weng, T.-C.; Nordlund, D.; et al. An Oxygen-Insensitive Hydrogen Evolution Catalyst Coated by a Molybdenum-Based Layer for Overall Water Splitting. *Angew. Chemie Int. Ed.* **2017**, *56* (21), 5780–5784.
- (150) Yuan, G.; Agiral, A.; Pellet, N.; Kim, W.; Frei, H. Inorganic Core–shell Assemblies for Closing the Artificial Photosynthetic Cycle. *Faraday Discuss.* **2014**, *176*, 233–249.
- (151) Kim, W.; Edri, E.; Frei, H. Hierarchical Inorganic Assemblies for Artificial Photosynthesis. *Acc. Chem. Res.* **2016**, *49* (9), 1634–1645.
- (152) Nakamura, R.; Frei, H. Visible Light-Driven Water Oxidation by Ir Oxide Clusters Coupled to Single Cr Centers in Mesoporous Silica. *J. Am. Chem. Soc.* **2006**, *128* (33), 10668–10669.
- (153) Edri, E.; Frei, H. Charge Transport through Organic Molecular Wires Embedded in Ultrathin Insulating Inorganic Layer. *J. Phys. Chem. C* **2015**, *119* (51), 28326–28334.
- (154) Agiral, A.; Soo, H. Sen; Frei, H. Visible Light Induced Hole Transport from Sensitizer to Co<sub>3</sub>O<sub>4</sub> Water Oxidation Catalyst across Nanoscale Silica Barrier with Embedded Molecular Wires. *Chem. Mater.* **2013**, *25* (11), 2264–2273.
- (155) Jiao, F.; Frei, H. Nanostructured Cobalt Oxide Clusters in Mesoporous Silica as Efficient Oxygen-Evolving Catalysts. *Angew. Chemie - Int. Ed.* **2009**, *48* (10), 1841–1844.
- (156) Doyle, A. D.; Montoya, J. H.; Vojvodic, A. Improving Oxygen Electrochemistry through Nanoscopic Confinement. *ChemCatChem* **2015**, *7* (5), 738–742.

- (157) Gao, D.-W.; Gu, Q.; Zheng, C.; You, S.-L. Synthesis of Planar Chiral Ferrocenes via Transition-Metal-Catalyzed Direct C–H Bond Functionalization. *Acc. Chem. Res.* **2017**, *acs.accounts.6b00573*.
- (158) Lopes, P. P.; Strmcnik, D.; Jirkovsky, J. S.; Connell, J. G.; Stamenkovic, V.; Markovic, N. Double Layer Effects in Electrocatalysis: The Oxygen Reduction Reaction and Ethanol Oxidation Reaction on Au(111), Pt(111) and Ir(111) in Alkaline Media Containing Na and Li Cations. *Catal. Today* **2015**, *262*, 41–47.
- (159) Favaro, M.; Jeong, B.; Ross, P. N.; Yano, J.; Hussain, Z.; Liu, Z.; Crumlin, E. J.; Zaera, F.; Devanathan, M. A. V.; Tilak, B. V. K.; et al. Unravelling the Electrochemical Double Layer by Direct Probing of the Solid/Liquid Interface. *Nat. Commun.* **2016**, *7* (May), 12695.
- (160) Zhao, S. F.; Horne, M.; Bond, A. M.; Zhang, J. Is the Imidazolium Cation a Unique Promoter for Electrocatalytic Reduction of Carbon Dioxide? *J. Phys. Chem. C* **2016**, *120* (42), 23989–24001.
- (161) Ting, C.-C.; Liu, C.-H.; Tai, C.-Y.; Hsu, S.-C.; Chao, C.-S.; Pan, F.-M. The Size Effect of Titania-Supported Pt Nanoparticles on the Electrocatalytic Activity towards Methanol Oxidation Reaction Primarily via the Bifunctional Mechanism. *J. Power Sources* **2015**, *280*, 166–172.
- (162) Ranga Rao, G.; Justin, P.; Meher, S. K. Metal Oxide Promoted Electrocatalysts for Methanol Oxidation. *Catal. Surv. from Asia* **2011**, *15* (4), 221–229.
- (163) Rigdon, W. A.; Huang, X. Carbon Monoxide Tolerant Platinum Electrocatalysts on Niobium Doped Titania and Carbon Nanotube Composite Supports. *J. Power Sources* **2014**, *272*, 845–859.
- (164) Zhuang, Y.; Ding, W.; Liu, Y.; Mou, Z.; Sun, J.; Guan, M. Reduced Nanostructured Titanium Oxide Coating as an Electrocatalyst Support for Methanol Oxidation. *J. Mater. Sci.* **2015**, *50* (11), 3875–3882.
- (165) Melvin, A. A.; Joshi, V. S.; Poudyal, D. C.; Khushalani, D.; Haram, S. K. Electrocatalyst on Insulating Support?: Hollow Silica Spheres Loaded with Pt Nanoparticles for Methanol Oxidation. *ACS Appl. Mater. Interfaces* **2015**, *7* (12), 6590–6595.
- (166) Tong; Kim, H. S.; Babu, P. K.; Waszczuk, P.; Wieckowski, A.; Oldfield, E. An NMR Investigation of CO Tolerance in a Pt/Ru Fuel Cell Catalyst. *J. Am. Chem. Soc.* **2002**, *124* (3), 468–473.
- (167) Takenaka, S.; Hori, K.; Matsune, H.; Kishida, M. Control of Selectivity Based on the Diffusion Rates of the Reactants in the Oxidation of Mixed Hydrocarbons with Molecular Oxygen over Silica-Coated Pt Catalysts. *Chem. Lett.* **2005**, *34* (12), 1594–1595.
- (168) Takenaka, S.; Orita, Y.; Arike, T.; Matsune, H.; Tanabe, E.; Kishida, M. Fabrication of Nanocomposites Composed of Carbon Nanotubes and Silica-Coated Pt-Based Alloy Nanoparticles. *Chem. Lett.* **2007**, *36* (10), 1250–1251.

- (169) Dignam, M. J. Transition Layer Model of the Oxide–electrolyte Interface. *Can. J. Chem.* **1978**, 56 (5), 595–605.
- (170) LANFORD, W. A. Glass Hydration: A Method of Dating Glass Objects. *Science* **1977**, 196 (4293), 975–976.
- (171) Smets, B. M. J.; Tholen, M. G. W.; Lommen, T. P. A. The Effect of Divalent Cations on the Leaching Kinetics of Glass. *J. Non. Cryst. Solids* **1984**, 65 (2–3), 319–332.
- (172) Bousse, L.; Bergveld, P. The Role of Buried OH Sites in the Response Mechanism of Inorganic-Gate PH-Sensitive ISFETs. *Sensors and Actuators* **1984**, 6 (1), 65–78.
- (173) Godet, J.; Pasquarello, A. Proton Diffusion Mechanism in Amorphous SiO<sub>2</sub>. *Phys. Rev. Lett.* **2006**, 97 (15), 155901.
- (174) Godet, J.; Pasquarello, A. Proton Diffusion in Amorphous SiO<sub>2</sub> and Hafnium Silicate by Ab Initio Molecular Dynamics. In *AIP Conference Proceedings*; AIP, 2007; Vol. 893, pp 195–196.
- (175) Fogarty, J. C.; Aktulga, H. M.; Grama, A. Y.; van Duin, A. C. T.; Pandit, S. A. A Reactive Molecular Dynamics Simulation of the Silica-Water Interface. *J. Chem. Phys.* **2010**, 132 (17), 174704.

## CHAPTER 2

### EXPERIMENTAL METHODS

This chapter describes experimental methods used for materials synthesis, materials characterization, and evaluation of electrocatalytic activity and stability. These techniques are highly complementary for proper characterization and measurement of the fundamental properties of electrocatalytic and photoelectrode materials. First, the rationale for the material/materials platform is discussed followed by materials synthesis and characterization techniques used throughout this dissertation. Lastly, electroanalytical techniques used to determine photo/electrocatalytic activity and stability are presented.

#### 2.1 Materials

##### 2.1.1 *Silicon*

The light absorbing semiconductor provides the driving force for PEC devices. Without the semiconductor, light absorbed by the insulating and metal components in a MIS photoelectrode would not result in the additional potential energy (photovoltage) that is required to split water. Indicators for selecting a suitable semiconductor material for PEC operation include the magnitude of the band gap ( $E_g < 2$  eV) and the appropriate band energy alignment straddling water redox reactions.

As mentioned in section 1.5.3, the width of the band gap is strongly correlated with chemical bond strength which can drastically affect PEC performance over long periods of time. Semiconductors with narrow band gaps absorb more of the visible light spectrum to increase conversion efficiency, but are typically thermodynamically unstable against corrosion. The most stable semiconductors in aqueous solution are oxides, but their band gaps are either too large for efficient light absorption or their semiconductor characteristics are poor.<sup>1</sup> In the MIS

photoelectrode, combining electrochemically stable, large band gap, and efficient light absorbing semiconductors, small band gap, overcomes this challenge by decoupling stability and efficiency.

Before this MIS device architecture was recognized in 2007 for PEC applications, many attempts at PEC devices consisted of materials with stability, efficiency, or economic shortcomings. Memming demonstrated high performance of GaP ( $E_g=2.26$  eV), but was unstable in aqueous solution.<sup>2</sup> Also, a major drawback of GaP is the small minority carrier diffusion lengths relative to the absorption depth of light constraining the charge carrier collection step of the process. GaInP<sub>2</sub> has a band gap ( $E_g=1.83$  eV) large enough to split water, but the band energetics do not properly align with water splitting reactions.<sup>3,4</sup> Thus, an additional bias is needed to effect the overall decomposition of water, reducing its performance. Heller et al. were able to achieve 12% photoelectrode conversion efficiency for the production of H<sub>2</sub> (not  $\eta_{STH}$ ) with InP ( $E_g=1.35$  eV), a good solar absorber.<sup>5</sup> However the scarcity and high demand of indium limit the commercial viability of the material.<sup>6</sup>

For this dissertation, crystalline silicon based devices ( $E_g=1.12$  eV) are studied. Si is desirable for its light absorption properties as well as its large carrier diffusion lengths.<sup>7-9</sup> Furthermore, Si already dominates 90% of the photovoltaic industry, making it a well-established and scalable material. Si is also attractive for MIS photoelectrodes for its narrow band gap and native oxide which serves as an insulating layer to protect Si.

Monocrystalline p-type Si(100) wafers (1-5  $\Omega$  cm, 500-550  $\mu$ m thick, WRS materials) with native oxide were used as the semiconductor substrates in Chapter 3. Monocrystalline degenerately doped Si(100) wafers ( $p^+$ Si, < 0.005  $\Omega$  cm, 500-550  $\mu$ m thick, WRS materials) were used as flat, conductive substrates in Chapters 4 and 5.



### 2.1.2 Silicon Oxide

After light is absorbed by the semiconductor, the newly freed electron must be transported to the metal electrocatalyst. Oxide layers located between semiconductor and metal components are often undesirable as they can prevent carrier transport between the two layers.<sup>10–12</sup> However, a robust oxide layer is typically required to protect the semiconductor from corrosion, as described in section 2.1.1.<sup>1</sup> Silicon oxide ( $\text{SiO}_2$ ) is thermodynamically stable over a wide range of pH and potentials.<sup>13,14</sup> Electron tunneling is facile for  $\text{SiO}_2$  thicknesses less than 2 nm, although it must be noted that tunneling probability decreases exponentially with increasing thickness.<sup>15</sup> Furthermore, the insulating layer has two major benefits: the ability to protect of the semiconductor from corrosion and to prevent the formation of undesirable energy states known as metal induced gap states (MIGS).

Unlike the MIS architecture, the performance of photoelectrodes consisting of metal-semiconductor junctions, known as a Schottky junction, are greatly affected by MIGS. As stated previously in section 1.5.4, the nanoemitter cell, a type of MIS structure, was unable to achieve high photovoltage and performance despite having a protective oxide layer.<sup>12,16,17</sup> The predicted built-in-voltage of the MIS junction, which corresponds to the maximum photovoltage, is defined by the difference in work functions of the semiconductor ( $E_{f,s}$ ) and metal ( $E_{f,m}$ ) components. However, a metal-semiconductor junction results in a phenomena known as “fermi level pinning” making the built-in-voltage relatively independent of work function differences, by creating extra allowable energy states MIGS that were previously forbidden. MIGS allow the excited electrons to relax to a lower energy state (below  $E_{f,m}$ ), and as a result, reduce the built-in-photovoltage and increase recombination of electron/hole pairs. In addition, interfacial defects or gap states due to lattice or energy mismatch can create recombination centers. MIGS are typically less of an issue

between semiconductor-insulator interfaces, thereby reducing this effect and increasing photovoltage. Si with its native SiO<sub>2</sub>, is especially desirable for minimizing these interfacial defects and gap states because no additional processing step is required to deposit the oxide, which would otherwise provide an opportunity to introduce defects.

SiO<sub>2</sub> overlayers for encapsulating electrocatalysts were used in this dissertation for their facile, room temperature fabrication method (section 2.1.2) and compatibility with other electrode materials and electrolytes investigated in this dissertation. SiO<sub>2</sub> has several other desirable properties for an overlayer material including, but not limited to its: i) permeability to water transport,<sup>18</sup> ii) ability to form hydroxyl groups<sup>19–21</sup> that are desirable for alcohol oxidation reactions (section 1.6.3), and iii) stability in acidic electrolytes relevant for PEM based technologies.<sup>22</sup>

SiO<sub>x</sub> overlayers were synthesized with a polydimethylsiloxane precursor (section 2.1.3) and UV ozone conversion process (section 2.2.3).

### 2.1.3 Polydimethylsiloxane

Polydimethylsiloxane (PDMS) is an inorganic polymer whose backbone consists of alternating silicon and oxygen atoms as shown in Figure 2.1.

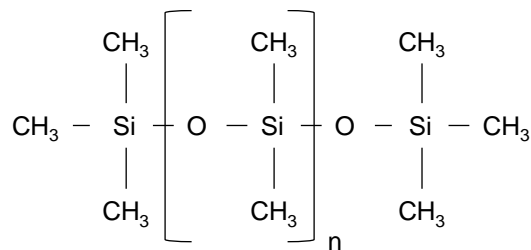


Figure 2.1. Polydimethylsiloxane (PDMS) polymer structure.

The organic-inorganic nature of the backbone ((CH<sub>3</sub>)<sub>2</sub>–SiO) allows higher local flexibility compared to traditional hydrocarbon polymers, in which methyl groups (CH<sub>3</sub>) rotate about the Si–O bond with ease.<sup>23</sup> The PDMS flexibility gives it interesting and useful properties for the SiO<sub>x</sub>

film fabrication process including: glass transition temperature ( $-123\text{ }^{\circ}\text{C}$ ), low solubility parameter, low surface tension, low surface energy, and high spreading coefficient. Additionally, PDMS is transparent to visible and UV radiation, highly permeable, and chemically inert. All of the properties make PDMS a good candidate for forming uniform films through the Langmuir-Blodgett molecular assembly and UV ozone process (section 2.2.3). When PDMS is coated onto a substrate, the overall surface energy of the system is lowered as the low surface energy PDMS spreads across the higher energy substrate, such that a complete and uniform PDMS coating is formed.

Trimethylsiloxy terminated 500,000 molecular weight polydimethylsiloxane with viscosity of 600,000 cST (Gelest Inc., DMS-T56-100GM, Lot #: 2C-17985) was used as precursor for the  $\text{SiO}_x$  films in this dissertation.

#### **2.1.4 Platinum**

As discussed in section 1.6, a major contribution to efficiency losses in electrochemical processes is the magnitude of the surface overpotential losses incurred at both electrode surfaces. For example, Si electrodes have band-edge positions that are appropriate for the photoelectrochemical reduction of protons, however the kinetics of HER on the bare  $\text{SiO}_2/\text{Si}$  surface generally limit the efficiency of this reaction.<sup>14</sup> To overcome kinetic limitations and reduce surface overpotential losses, the catalytic activity of the electrode surfaces can be enhanced by modifying the surface with more active materials.<sup>9,24</sup> Platinum (Pt) is commonly used to modify electrode surfaces because it is the state-of-the-art catalyst for many electrochemical reactions. Although Pt is an excellent HER catalyst, it is very scarce and expensive, thus many research efforts have been focused on alternative, earth abundant catalyst materials. This dissertation does

not focus on the development of novel non-precious catalytic materials. Rather, Pt is studied as a model active catalyst component for oxide encapsulated electrocatalysis.

Pt was deposited by electrodeposition (section 2.2.1) from a Pt salt precursor (potassium tetrachloroplatinate,  $\text{K}_2\text{PtCl}_4$ , Sigma Aldrich, ACS reagent) and evaporative deposition (section 2.2.2) from Pt pellets (Kurt J Lesker, 99.99%).

### ***2.1.5 Nanoparticles versus Thin Films***

Both nanoparticle and thin film structures are investigated in this dissertation. Three-dimensional (3D) nanoparticles are desirable for their high surface area to volume ratio, reducing the catalyst loading and associated cost without adversely affecting performance. High-current density applications ( $> 1 \text{ A cm}^{-2}$ ), such as PEMEC or PEMFC, require high surface area catalytic surfaces to minimize overpotential losses. Catalyst nanoparticles are especially advantageous for front-illuminated photoelectrodes, because the addition of metal catalysts tend to have a detrimental effect on the optical performance by absorbing and/or reflecting light before it can reach the semiconductor. Discontinuous nanoparticles, smaller than the wavelength of incident photons, are effectively optically transparent and do not significantly affect the light absorption properties of the semiconductor.<sup>25</sup> Therefore, nanoparticles are highly relevant for electrochemical and photoelectrochemical systems.

On the other hand, two-dimensional (2D) thin films are advantageous for studying well-defined and controlled surfaces, providing model platforms for determining fundamental properties of complex materials configurations (e.g. 3D nanoparticles). The simple 2D design makes synthesis and characterization relatively easy compared to analogous 3D structures, in which the surface roughness or area can vary between supposedly identical samples. For example, Pt and  $\text{SiO}_x$  film synthesis can be achieved with physical vapor deposition and spincoating

deposition methods, respectively, which allow for nanometer control over the film thickness. Studying thin film materials eliminates numerous variables associated with non-uniformities (e.g. thickness or composition), allowing for well-controlled experiments and quick evaluation of catalytic properties.

## **2.2 Materials Synthesis Methods**

There are many material synthesis methods for fabricating the metal and oxide components of oxide encapsulated electrocatalysts. Common techniques for metal deposition include: electrodeposition, physical vapor deposition (sputtering and evaporation), and chemical vapor deposition. Conventional methods for oxide synthesis include: ultraviolet ozone photochemistry, sol-gel synthesis, and chemical vapor deposition. Each synthesis technique has specific advantages (e.g. purity, scalability, or controllability over thickness and geometry) and disadvantages (e.g. high temperature, low pressure vacuum, low throughput). Therefore, different techniques may be appropriate for one application but not another depending on the design specifications. The following provides brief descriptions of the material synthesis methods used in this dissertation.

### **2.2.1 *Electrodeposition***

Electrodeposition is a room temperature and scalable method for depositing metals. From an economic standpoint, this technique also optimizes the use of raw materials, equating to major cost savings. In order to fabricate the metal components of MIS electrodes at lower cost and improved scalability, room temperature electrodeposition processes are preferred to high temperature and vacuum processes (e.g. physical vapor deposition). Electrodeposition involves an electrode substrate that is immersed in metal-ion containing electrolyte and subjected to reducing conditions, at potentials more negative than the standard reduction potential of the metal ion species of interest. Illumination is also required for electrodeposition onto a photocathode (p-type

semiconductor) to generate photoelectron minority carriers. Electrons having electric potential energy more negative than the thermodynamically required potential to reduce the metal ion are able to transfer to metal ions in the electrolyte and create a metallic deposit. Tuning the applied potential/current can allow for control over particle morphology, size, and coverage.

For reproducible results, the electrodeposition process must be finely tuned to control parameters such as particle density and size.<sup>25,26</sup> This can be accomplished by determining the nucleation and growth regimes for different metal deposits. The deposition reaction of interest, in this dissertation, is the reduction of platinum species from tetrachloroplatinate (II) ions:



Pt electrodeposition is unique in that hydrogen underpotential deposition (section 2.4.3) can also occur on Pt surfaces. This property was leveraged by Liu et al. to controllably deposit Pt monolayers through an atomic layer-type deposition mechanism.<sup>27</sup> After the potential is quickly pulsed to deposit Pt, the potential is adjusted to favor hydrogen termination on the Pt surface, effectively quenching further Pt deposition. This process can be repeated to obtain particles of relatively uniform size or films of controlled thickness. A similar procedure was implemented to deposit Pt onto Si photocathodes in Chapter 3.

Pt nanoparticles were electrodeposited onto p-type Si(100) with native silicon oxide, in 3 mM potassium tetrachloroplatinate ( $\text{K}_2\text{PtCl}_4$ ) solution containing 0.5 M sodium chloride (NaCl) supporting electrolyte under  $100 \text{ mW cm}^{-2}$  illumination intensity.

### **2.2.2 Electron Beam Physical Vapor Deposition**

Physical vapor deposition (PVD) is a vacuum deposition method used to deposit thin films from a material in vapor phase. Electron beam physical vapor deposition (EBPVD) is a type of PVD that is a line-of-sight evaporative deposition method with nanometer control over thickness.

The material source, commonly in the form of metal pellets, is heated by a power-adjustable electron beam source (charged tungsten filament) to evaporate the metal into the gaseous phase. The target substrate is located above the material source allowing for metal vapors to precipitate into a solid film on its surface. This technique coats everything within the vacuum chamber, such that a portion of the source material is wasted.

A titanium (99.99%) adhesion layer and Pt (99.99%) layers were sequentially deposited at  $0.2 \text{ A s}^{-1}$  by EBPVD onto the silicon substrates without breaking vacuum and without substrate heating in a Angstrom EvoVac evaporator system with a base pressure of  $1.0 \times 10^{-7}$  Torr. Film thicknesses were monitored with quartz crystal thickness monitors. The amount of metal deposited was then controlled by adjusting the amount of time that the substrate was exposed to the source.

### **2.2.3 Ultraviolet Ozone Photochemistry**

Ultraviolet (UV) ozone photochemistry converts PDMS to  $\text{SiO}_x$  films.<sup>28,29</sup> This process occurs at room temperature and atmospheric pressure, which allows for the formation of  $\text{SiO}_x$  films on various material surfaces that PDMS can wet. The UV ozone photochemical conversion of PDMS to  $\text{SiO}_x$  has been proposed to occur via the generation of radical species from the polymer backbone due to atomic oxygen attack. During the UV ozone conversion process, ozone first forms under ultraviolet ( $< 240 \text{ nm}$ ) photodissociation of molecular oxygen ( $\text{O}_2$ ). Next, gaseous ozone decomposes to oxygen atoms and molecules by absorbing photons in the UV and visible spectrum. Photons having  $254 \text{ nm}$  wavelength cause a chain decomposition to form highly energetic and reactive atomic oxygen species, which then initiates the decomposition of silicones. Previous literature proposed atomic oxygen cleaves C-H bonds, in the methyl groups, or Si-C bonds to create intermediate radical species that crosslink. The products of the crosslinked structures are the silicon oxide film, and carbon dioxide and water volatiles.

To synthesize  $\text{SiO}_x$  films, a spincoater (Laurell Technologies Corp.) was used to coat PDMS on the substrate from an organic toluene solution.<sup>29,30</sup> Due to the low surface energy, (section 2.1.3) the PDMS uniformly coats the substrate. The samples were then dried in a vacuum oven at 70 °C for 60 minutes to evaporate the solvent. Afterwards, the PDMS was converted to  $\text{SiO}_x$  in a UV ozone cleansing chamber in air for 2 hours (UVOCS, T10X10/OES). The mercury light source generates UV light in the 254 nm and 185 nm range relevant for generating ozone and exciting organic molecules.<sup>28,29</sup> The thickness of the resulting film was controlled by adjusting the concentration of PDMS in organic solution and the spin coating speed rate. This relation between thickness, concentration and spin rate produces reproducible films with known thickness. Specific details regarding the concentration of PDMS/toluene solution ( $\text{mg ml}^{-1}$ ) and the spincoating speed rate (rpm) are provided in the individual chapters, as these parameters varied with each study.

## **2.3 Materials Characterization Techniques**

Physical and chemical characterization techniques are often complimentary techniques which provide useful information: the thickness, structure, physical properties and chemical composition of a film.

### **2.3.1 Ellipsometry**

Ellipsometry is a non-destructive optical technique used for measuring the refractive index and thickness of films on reflective substrates. Ellipsometry uses polarized light that reflects off a solid surface and undergoes a change in polarization state upon reflection.<sup>31</sup> The ellipsometer analyzer and detector quantifies changes between the initial and final state of polarized light.<sup>32</sup> The complex optical parameters,  $\psi$  and  $\Delta$ , are modeled based on known optical constants for the substrate and film materials to determine the film thickness.



The thickness of the SiO<sub>x</sub> film was measured with a variable angle spectroscopic ellipsometer (Woollam alpha-SE). Ellipsometric data was fit using a Cauchy model, with final parameters corresponding to those that minimize the mean square error between the modeled curve to experimental data.

### **2.3.2 *Scanning Electron Microscopy***

Scanning electron microscopy (SEM) is a high resolution imaging technique that provides visualization of material structures (e.g. surface topography and morphology) and provides qualitative information on composition and crystallography.<sup>33</sup> SEM involves an electron gun to produce an electron beam that is focused through a series of lenses. The electron beam rasters across a sample surface to image the material of interest with nanometer resolution. Electrons interact with a material through elastic and inelastic scattering events. Back scattered electron (BSE) imaging uses elastic electron scattering of high energy electrons. BSE imaging is very sensitive to atomic number (Z), providing high contrast of compositional variations in the imaged surface.<sup>33</sup> High Z elements, such as Pt, create more BSE than low Z elements, such as Si or O, making Pt appear relatively “bright” on SiO<sub>2</sub>/Si substrates. Secondary electron (SE) imaging uses inelastic electron scattering of low energy electrons.

Secondary electron images were obtained with a Hitachi S4700 field emission SEM in Chapter 3 and a Zeiss Sigma VP Schottky Thermal Field emission SEM microscope in Chapter 4. The electron gun was operated with an accelerating voltage of 10 kV and 5 kV and a working distance of 12 mm and 3 mm for the Hitachi and Zeiss Sigma systems, respectively.

### **2.3.3 *Atomic Force Microscopy***

Atomic force microscopy (AFM) is a high resolution imaging technique that provides information on surface topologies and other mechanical properties (e.g. Young’s modulus). AFM

acquires surface features that are detected with a physical scanning probe that is in contact with a surface. The measurement uses a piezo electric cantilever with a low spring constant to raster across a surface by use of piezo electric ceramics. Meanwhile, deflections in the cantilever are detected optically by a laser incident on the cantilever that reflects off to a detector, which allows for imaging of the surface topography. Due to the low forces used, AFM is usually non-destructive and is surface sensitive. AFM acquires nearly atomic resolution of material surfaces resulting in 3D topographical image of the surface. This information is highly valuable in characterizing the uniformity and roughness of thin films.

AFM images were obtained using a Bruker Dimension Icon AFM under ambient conditions with NanoScope Analysis 1.8 software. A ScanAsyst silicon tip on a nitride lever silicon cantilever with a 25 nm tip radius, spring force constant of  $0.4 \text{ N m}^{-1}$  and a resonant frequency of 70 kHz was used. All AFM images were acquired with a 0.1 Hz scan rate in peak force quantitative nanomechanical mapping mode. The feedback gain was varied to minimize the peak force error.

#### ***2.3.4 Ultraviolet-Visible Spectroscopy***

Ultraviolet-visible (UV-vis) spectroscopy directly measures the optical transmittance (% $T$ ) of a material as a function of the incident light wavelength. A UV-vis spectrometer uses a light source that produces wide range of wavelengths, typically over the ultraviolet, visible, and infrared range which are relevant for solar spectrum and solar applications. During the measurement, a monochromator filters light to a narrow wavelength range that is incrementally adjusted to cover the range of wavelengths of interest. Monochromatic light is directed to the sample and the % $T$  is measured at the detector as a ratio of the light intensity transmitted ( $I_o$ ) to incident light intensity ( $I$ ):

$$\%T = I_o/I \quad (2.2)$$

In addition to %T, UV-vis spectroscopy can also provide reflectance (%R) and absorbance (%A). All of these optical parameters are important and relevant properties for PEC materials design. For example, catalyst loading can affect %T and %R and thus %A of the underlying semiconductor.

In Chapter 3, %T through electrodeposited Pt catalysts was measured with Agilent Cary 60 UV-Vis spectrophotometer over wavelengths ranging between 300–1000 nm.

### 2.3.5 *X-ray Photoelectron Spectroscopy*

X-ray photoelectron spectroscopy (XPS) is a surface-sensitive quantitative spectroscopic technique that measures elemental composition and chemical states. XPS leverages the photoelectric effect, a process that involves the absorption of x-rays and subsequent excitation and ejection of photoelectrons. The emitted photoelectrons escape the material with a kinetic energy ( $KE$ ) that is quantified by an analyzer equipped with an adjustable capacitor. High resolution information is obtained when the capacitor filters photoelectrons having a specified narrow  $KE$  range, called the pass energy, to pass through to the detector. The  $KE$  of the ejected electrons is related to the binding energy ( $BE$ ), the amount of energy required to remove an electron from the parent atom, with the following relation:

$$KE = h\nu - BE - \phi_s \quad (2.2)$$

where  $h\nu$  is the energy of the incident monochromatic photon, typically produced from the K edge of an aluminum (Al, 1486.7 eV) or magnesium (Mg, 1253.6 eV) anode, and  $\phi_s$  is the calibrated work function of the spectrophotometer.

Each element has a unique set of BE signatures, associated with different atomic energy levels, and is used to identify individual elements contained within a material. Shifts in  $BE$ , from

reported values, indicate differences in oxidation state, molecular environment, and/or crystal structure. Due to the sensitivity of information associated with *BE*, this technique requires an ultrahigh vacuum environment to prevent inelastic collisions between ejected photoelectrons and gaseous molecules that would otherwise provide inaccurate *KE* information between point of emission and detection. For example, a shift to higher *BE* is observed when atoms are bonded to more electronegative species (e.g. Si–O versus Si–Si) that pull on the valence electrons, resulting in a stronger attraction between the nucleus and core shell electrons. In a suitable vacuum environment, shifted core level spectra are assumed to correlate to differences in chemical states of the surface elements present, rather than decreases in *KE* from inelastic collisions.

The surface sensitivity arises from the small inelastic mean free path (IMFP) of core level photoelectrons in solid materials. IMFP is the average distance an electron travels in a material before being reabsorbed or colliding and losing *KE*. X-rays can penetrate deep into a sample surface, but photoelectrons generated deep into the sample are not able to escape from the material without losing considerable *KE*. XPS is surface-sensitive because the probability of a photoelectron emitting without loss to *KE* decreases exponentially with escape depth. The surface sensitivity of XPS is extremely useful for studying electrocatalytic surfaces since the atoms closest to the electrode surface have the largest influence on the electrochemical reactions occurring there.

XPS measurements in Chapter 3 were conducted with a Kratos AXIS Ultra DLD XPS system that was operated at a base pressure of  $3 \times 10^{-10}$  Torr using a monochromatic  $\text{Al}_{K\alpha}$  source (X-ray power 13 kV, 8 mA) without a neutralizer. The pass energy was 10 eV and the drain current through the sample stage was 0.4 nA. XPS measurements in Chapter 4 and 5 were conducted with a Phi XPS system that was operated at a base pressure of  $2 \times 10^{-10}$  Torr using a monochromatic

Al<sub>Kα</sub> source (X-ray power 15 kV, 20 mA) and a neutralizer. The pass energy was 23.5 eV. The angle,  $\phi$ , between the x-ray source and analyzer was fixed at 54.7° for both systems.

### 2.3.5.1 Quantitative Data Analysis

XPS spectra peaks can be fit to quantify the *BE* associated with each peak. These *BEs* are referenced to literature reported values in the Handbook of X-ray Photoelectron spectroscopy<sup>34</sup> to identify elemental signatures and chemical states. The atomic concentrations of elemental species are calculated based on the fitted peak areas,  $I_i$ , of each element,  $i$ . The atomic concentration of element  $i$ ,  $C_i$ , is calculated by Equation 2.3:

$$C_i = \frac{I_i/ASF_i}{\sum I_x/ASF_x} \quad (2.3)$$

where  $ASF_i$  is the atomic sensitivity factor of element  $i$  and the denominator is the summation of the ratio  $I_x/ASF_x$  for all elements detected. Sensitivity factors are dependent on multiple factors and will vary with different XPS systems.

XPSpeak 4.1 software was used to evaluate the peak areas of Si 2p, C 1s, O 1s, Pt 4f, and Cu 2p, spectra based on Shirley's algorithm for background subtraction. The C 1s peaks were shifted and centered to 284.8 eV, and the Si 2p and O 1s peaks associated with the SiO<sub>x</sub> overlayers were shifted by the same amount. The peak area ratios were calculated after accounting for the  $ASF_i$  for a system operated at  $\phi=54.7^\circ$  ( $ASF_{Si} = 0.180$ ,  $ASF_C = 0.296$ ,  $ASF_O = 0.711$ ,  $ASF_{Pt} = 5.575$ , and  $ASF_{Cu} = 5.321$ ).<sup>34</sup> The value of the Si atomic sensitivity factor was adjusted (from  $ASF_{Si} = 0.339$ ) to account for the difference in atomic density and attenuation lengths between Si in SiO<sub>2</sub> and Si.

## 2.4 Electrochemical Characterization

Electrochemical characterization techniques are conducted to evaluate the active surface area, electrode stability, and overpotential losses associated with the electrochemical reactions at the electrodes.

### 2.4.1 *Three-Electrode Electrochemical Cell*

A standard three-electrode electrochemical cell is used to isolate the performance of an individual electrode (e.g. cathode or anode). The electrochemical cell consists of a working electrode (WE), reference electrode (RE), and counter electrode (CE) that are immersed in an electrolyte and are externally connected to a potentiostat. The WE is the electrode of interest with one half reaction (e.g. HER) occurring at the electrode surface, whereas the CE provides a surface for the other half reaction (e.g. OER). The reference electrode is an electrode that has a stable and well-defined potential (section 2.4.1.1). The potentiostat controls/measures the applied/output voltage or current. In a typical measurement a voltage is applied between the WE and CE, where the WE potential is controlled/measured with respect to the known potential of the RE. The resulting current flows between the WE and CE and is measured.

All electrochemical measurements were performed using a SP-200 BioLogic potentiostat controlled by EC-Lab software. A silver/silver chloride reference electrode (Ag|AgCl/sat. 3 M KCl, section 2.4.1.1) and a Pt mesh counter electrode was used. All aqueous electrolytes were prepared with 18 M $\Omega$  deionized water (Millipore, Milli-Q Direct 8) and were purged with nitrogen gas (N<sub>2</sub>) for 20 min prior to measurements to deaerate the electrolyte. Purging removes dissolved oxygen and eliminates complexities associated with the ORR. During measurements, the head space of the electrochemical cell was continuously purged with N<sub>2</sub>.

#### 2.4.1.1 Reference Electrode

A reference electrode (RE) is conventionally in its own one-electrode cell containing electrolyte that is separated from the electrolyte in the main electrochemical cell by an ion conducting separator. The RE has a constant redox potential that is defined by the standard reaction potential,  $E^\circ$ , of the electrode material with complementary ionic electrolyte.  $E^\circ$  is the standard reduction potential with respect to the normal hydrogen electrode (NHE). Standard conditions are at 25°C with 1 M concentration of the ionic species and 1 atm partial pressure of the gas/gasses participating in the redox reaction, respectively. For example NHE is a Pt wire in 1 M  $H^+$  aqueous solution with a partial pressure of 1 atm  $H_2$  at 25°C. Most potentials reported in publications on water electrolysis are given with respect to the reversible hydrogen electrode (RHE) in order to account for variations in electrolyte pH:

$$E(\text{RHE}) = 0.0000 \text{ V} - 0.0591 \text{ V} \cdot \text{pH vs. NHE} \quad (2.4)$$

A Hach (E21M002) silver/silver chloride reference electrode ( $\text{Ag}|\text{AgCl}/\text{sat. 3 M KCl}$ , +0.210 V vs. NHE) was typically used in this dissertation. For extended time measurements (> 1 hr) a home-made RHE was used as a reference electrode instead of  $\text{Ag}|\text{AgCl}$  to minimize possible Ag contamination during the extended testing period. The RHE consisted of a Pt wire partially encased within a glass body with a small capillary opening at one end. The RHE glass body was filled with the same electrolyte as used in the main electrochemical cell and connected as the WE to a three-electrode set-up. A constant negative current was applied for 10 min to produce  $H_2$  bubbles on the Pt wire. The open circuit potential was then measured with respect to  $\text{Ag}|\text{AgCl}$  before and after measurements to detect any drift in potential.

### 2.4.2 Photoelectrochemical Test Cell

A photoelectrochemical (PEC) test cell is a modified electrochemical cell that typically uses a quartz lens to maximize the amount of light that passes through to the photoelectrode WE. A two compartment PEC test cell was used to evaluate the performance of the photoelectrodes, in which the WE and CE compartments are separated by a glass frit to prevent product crossover (Figure 2.2). A Pt mesh (Alfa Aesar, 99.9%) counter electrode was located in a secondary compartment separated by a glass frit. A commercial Ag|AgCl/sat. 3 M KCl reference electrode (Hach, E21M002) was located in the main WE compartment. All solutions were bubbled with N<sub>2</sub> gas for 20 minutes to purge dissolved oxygen. During all electrochemical measurements, the head space of the working electrode compartment was continuously purged with N<sub>2</sub>.

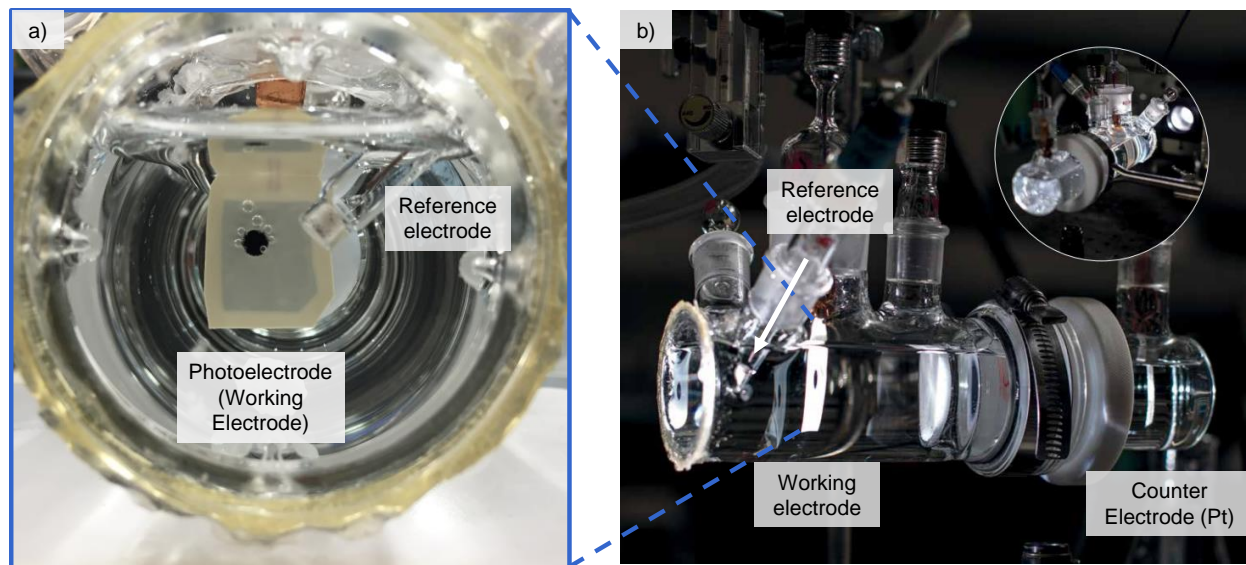


Figure 2.2. a) Front view image of the photoelectrochemical (PEC) test cell used in this dissertation. Shown is a photoelectrode working electrode (WE) and reference electrode (RE). b) Side view image of PEC cell under illumination (light source originating from the left side of the image). A Pt counter electrode is shown in a separate compartment from the WE and RE.



#### 2.4.2.1 *Light Source Calibration*

The spectral distribution and integrated intensity of a light source are critically important parameters to keep consistent across all studies in order to compare the performance of PV and PEC materials. The sun is the most natural choice for a light source, however, several factors (latitude, climate, moisture, and time of year) can cause variation in the solar spectrum and intensity. For this reason, laboratory light sources have been standardized using a simulated air mass 1.5 global (AM 1.5G) light source.<sup>35</sup> An AM 1.5G light source produces a light spectrum and intensity ( $100 \text{ mW cm}^{-2}$ ) that closely matches the solar spectrum of direct normal sunlight that is incident on the earth's surface at a zenith angle of  $48^\circ$ . Reference solar cells are used to calibrate the light intensity by adjusting either the power to, distance from, and/or collimation of the light source until the short-circuit current of the reference cells matches the measured value on a certified light AM 1.5G light source.

AM 1.5G illumination was achieved with a 300 W xenon arc lamp (Newport, 67005) and AM 1.5G filter (Newport, 81094) in a Newport housing powered by a power supply (Newport, 69911). The intensity was calibrated to  $100 \text{ mW cm}^{-2}$  with a solar reference cell (VLSI Standards, SRC-1000-RTD-QZ).

#### 2.4.3 *Standard Electroanalytical Techniques*

Three standard electroanalytical measurements were used throughout this dissertation:

- i. Linear sweep voltammetry (LSV): potential is scanned at a constant rate from a starting potential to an ending potential while the resulting current is recorded as a function of electrochemical potential. This technique is useful for characterizing the electrochemical activity in which it is desirable to achieve high currents at potentials close to  $E^\circ$ .

- ii. Cyclic voltammetry (CV): potential is cycled at a constant scan rate between two potential limits and the resulting current is recorded as a function of electrochemical potential. This technique is useful for characterizing hysteresis in scans and electrochemically active surface areas (ECSAs). For example, hydrogen underpotential deposition ( $H_{\text{upd}}$ ) is a standard CV technique used to measure the ECSA of Pt. This involves the absorption of a single layer of atomic hydrogen onto Pt during the negative scan of the CV and then subsequent desorption during the positive scan.  $H_{\text{upd}}$  occurs at potentials more positive than the  $E^\circ$  for HER (typically 0 V vs. RHE < V < 0.4 V vs. RHE). A more detailed description of this technique and the associated surface area analysis are provided in Chapter 4.
- iii. Chronopotentiometry (CP): a constant current is applied and the potential required to maintain that current is measured as a function of time. This technique is also useful for stability measurements.

## 2.5 References

- (1) Choi, M. J.; Jung, J.-Y.; Park, M.-J.; Song, J.-W.; Lee, J.-H.; Bang, J. H. Long-Term Durable Silicon Photocathode Protected by a Thin  $\text{Al}_2\text{O}_3/\text{SiO}_x$  Layer for Photoelectrochemical Hydrogen Evolution. *J. Mater. Chem. A* **2014**, 2, 2928.
- (2) Memming, R.; Schwandt, G. ELECTROCHEMICAL PROPERTIES OF GALLIUM PHOSPHIDE IN AQUEOUS SOLUTIONS. *Electrochim. Acta* **1968**, 13, 1299–1310.
- (3) Kocha, S. S.; Turner, J. a.; Nozik, A. J. Study of the Schottky Barrier and Determination of the Energetic Positions of Band Edges at the N- and p-Type Gallium Indium Phosphide Electrode | Electrolyte Interface. *J. Electroanal. Chem.* **1994**, 367, 27–30.
- (4) Khaselev, O.; Turner, J. A. A Monolithic Photovoltaic-Photoelectrochemical Device for Hydrogen Production via Water Splitting. *Science* **1998**, 280 (5362), 425–427.
- (5) Heller, A.; Vadimsky, R. G. Efficient Solar to Chemical Conversion: 12% Efficient Photoassisted Electrolysis in the [p-Type  $\text{InP}(\text{Ru})$ ]/ $\text{HCl-KCl/Pt}(\text{Rh})$  Cell. *Phys. Rev. Lett.* **1981**, 46 (17), 1153–1156.
- (6) MINERAL COMMODITY SUMMARIES 2010.

- (7) Hamann, T. W.; Lewis, N. S. Control of the Stability, Electron-Transfer Kinetics, and PH-Dependent Energetics of Si/H<sub>2</sub>O Interfaces through Methyl Termination of Si(111) Surfaces. *J. Phys. Chem. B* **2006**, *110* (45), 22291–22294.
- (8) Nakato, Y.; Yano, H.; Nishiura, S.; Ueda, T.; Tsubomura, H. Hydrogen Photoevolution at P-Type Silicon Electrodes Coated with Discontinuous Metal Layers. *J. Electroanal. Chem.* **1987**, *228*, 97–108.
- (9) Dominey, R. N.; Lewis, N. S.; Bruce, J. A.; Bookbinder, D. C.; Wrighton, M. S. Improvement of Photoelectrochemical Hydrogen Generation by Surface Modification of P-Type Silicon Semiconductor Photocathodes. *J. Am. Chem. Soc.* **1982**, *104*, 467–482.
- (10) Gaillard, N.; Chang, Y.; Kaneshiro, J.; Deangelis, A.; Miller, E. L. Status of Research on Tungsten Oxide-Based Photoelectrochemical Devices at the University of Hawai'i N. **2010**, 7770.
- (11) Kawamura, Y. L.; Sakka, T.; Ogata, Y. H. Photoassisted Control of Pt Electrodeposition on P-Type Si. *J. Electrochem. Soc.* **2005**, *152*, C701.
- (12) Lewerenz, H. J. Micro- and Nanotopographies for Photoelectrochemical Energy Conversion. I: The Photovoltaic Mode. *Electrochim. Acta* **2011**, *56*, 10713–10725.
- (13) Kenney, M. J.; Gong, M.; Li, Y.; Wu, J. Z.; Feng, J.; Lanza, M.; Dai, H. High-Performance Silicon Photoanodes Passivated with Ultrathin Nickel Films for Water Oxidation. *Science* **2013**, *342* (6160), 836–840.
- (14) Esposito, D. V.; Levin, I.; Moffat, T. P.; Talin, A. A. Supplementary Information: H<sub>2</sub> Evolution at Si-Based Metal–insulator–semiconductor Photoelectrodes Enhanced by Inversion Channel Charge Collection and H Spillover. *Nat. Mater.* **2013**.
- (15) Singh, R.; Green, M. A.; Rajkanan, K. Review of Conductor-Insulator-Semiconductor (CIS) Solar Cells. *Sol. Cells* **1981**, *3* (2), 95–148.
- (16) Muñoz, A.; Skorupska, K.; Lewerenz, H. Nanostructure Approaches for Photoelectrocatalysis. *ECS Trans.* **2009**, *21* (1), 35–56.
- (17) Aggour, M.; Skorupska, K.; Stempel Pereira, T.; Jungblut, H.; Grzanna, J.; Lewerenz, H. J. Photoactive Silicon-Based Nanostructure by Self-Organized Electrochemical Processing. *J. Electrochem. Soc.* **2007**, *154* (9), H794–H797.
- (18) Velmurugan, J.; Zhan, D.; Mirkin, M. V. Electrochemistry through Glass. *Nat. Chem.* **2010**, *2* (6), 498–502.
- (19) Azam, M. S.; Weeraman, C. N.; Gibbs-Davis, J. M. Specific Cation Effects on the Bimodal Acid–Base Behavior of the Silica/Water Interface. *J. Phys. Chem. Lett.* **2012**, *3* (10), 1269–1274.
- (20) Ong, S.; Zhao, X.; Eisenthal, K. B. Polarization of Water Molecules at a Charged Interface:

- Second Harmonic Studies of the Silica/Water Interface. *Chem. Phys. Lett.* **1992**, *191* (3–4), 327–335.
- (21) Leung, K.; Nielsen, I. M. B.; Criscenti, L. J. Elucidating the Bimodal Acid–Base Behavior of the Water–Silica Interface from First Principles. *J. Am. Chem. Soc.* **2009**, *131* (51), 18358–18365.
  - (22) Pourbaix, M. *Atlas of Electrochemical Equilibria in Aqueous Solutions*; Oxford: Pergamon Press: New York, 1974.
  - (23) Rochow, E. B. *Silicone and Silicones*; Springer-Verlag: Berlin, 1987.
  - (24) Bocarsly, A. B.; Bookbinder, D. C.; Dominey, R. N.; Lewis, N. S.; Wrighton, M. S. Photoreduction at Illuminated P-Type Semiconducting Silicon Photoelectrodes. Evidence for Fermi Level Pinning. *Am. Chem. Soc.* **1980**, *102* (11), 3683–3688.
  - (25) Heller, A.; Aspnes, D. E.; Porter, J. D.; Sheng, T. T.; Vadimsky, R. G. Transparent Metals Preparation and Characterization of Light-Transmitting Platinum Films. *J. Phys. Chem.* **1985**, *89* (1982), 4444–4452.
  - (26) Esposito, D. V.; Levin, I.; Moffat, T. P.; Talin, A. A. H<sub>2</sub> Evolution at Si-Based Metal-Insulator-Semiconductor Photoelectrodes Enhanced by Inversion Channel Charge Collection and H Spillover. *Nat. Mater.* **2013**, *12* (6), 562–568.
  - (27) Liu, Y. H.; Gokcen, D.; Bertocci, U.; Moffat, T. P. Self-Terminating Growth of Platinum Films by Electrochemical Deposition. *Science* (80-. ). **2012**, *338*, 1327–1330.
  - (28) Ouyang, M.; Yuan, C.; Muisener, R. J.; Boulares, A.; Koberstein, J. T. Conversion of Some Siloxane Polymers to Silicon Oxide by UV/Ozone Photochemical Processes. *Chem. Mater.* **2000**, *12* (29), 1591–1596.
  - (29) Mirley, C.; Koberstein, J. A Room Temperature Method for the Preparation of Ultrathin SiO<sub>x</sub> Films from Langmuir-Blodgett Layers. *Langmuir* **1995**, *11* (4), 0–3.
  - (30) Phely-Bobin, T. S.; Muisener, R. J.; Koberstein, J. T.; Papadimitrakopoulos, F. Site-Specific Self-Assembly of Si/SiO<sub>x</sub> Nanoparticles on Micropatterned Poly(Dimethylsiloxane) Thin Films. *Synth. Met.* **2001**, *116* (1–3), 439–443.
  - (31) Woollam, J. A.; Snyder, P. G. Fundamentals and Applications of Variable Angle Spectroscopic Ellipsometry. *Mater. Sci. Eng. B* **1990**, *5* (2), 279–283.
  - (32) Palik, E. D. *Handbook of Optical Constants of Solids*; Academic Press: Boston, 1998.
  - (33) Goldstein, J. I.; Romig, A. D. J.; Newbury, D. E.; Lyman, C. E.; Echlin, P.; Fiori, C.; Joy, D. C.; Lifshin, E. *Scanning Electron Microscopy and X-Ray Microanalysis. A Text for Biologists, Material Scientists and Geologists*, 2nd ed.; New York, 1992.
  - (34) Moulder, J. F.; Stickle, W. F.; Sobol, P. E.; Bomben, K. D. *Handbook of X-Ray*

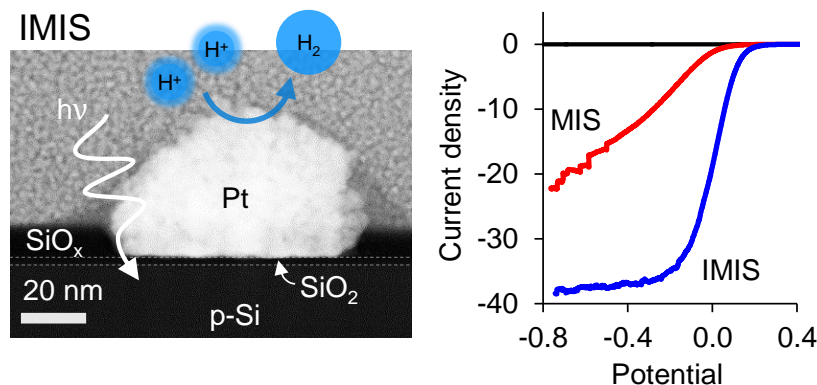
*Photoelectron Spectroscopy*; Chastain, J., King, R. C. J., Eds.; Physical Electronics, Inc.: Eden Prairie, MN, 1995.

- (35) Matson, R. J.; Emery, K. A.; Bird, R. E. Terrestrial Solar Spectra, Solar Simulation and Solar Cell Short-Circuit Current Calibration: A Review. *Sol. Cells* **1984**, *11* (2), 105–145.

## CHAPTER 3

### ENHANCED PERFORMANCE OF SILICON MIS PHOTOCATHODES CONTAINING OXIDE-COATED NANOPARTICLE ELECTROCATALYSTS

Chapter 3 establishes the ability of room temperature synthesized silicon oxide ( $\text{SiO}_x$ ) coatings to stabilize nanoparticle electrocatalysts by mitigating electrocatalyst migration, coalescence, and detachment. The oxide-encapsulated electrocatalyst architecture is applied to a metal-insulator-semiconductor (MIS) photoelectrode (section 1.5.4) for photoelectrochemical (PEC) water splitting (section 1.2.2). Unfortunately, securely anchoring nanoparticles to the photoelectrode surface can be challenging especially if the surface is covered by a thin insulating overlayer. This chapter reports on Si-based photocathodes for the hydrogen evolution reaction that overcome this problem through the use of a 2–10 nm thick layer of  $\text{SiO}_x$  that is deposited on top of Pt nanoparticle catalysts that were first electrodeposited on a 1.5 nm  $\text{SiO}_2$ /p-Si absorber layer (IMIS). The photoelectrodes containing oxide-encapsulated electrocatalysts exhibit superior durability and electron transfer (ohmic) properties compared to the photoelectrode that lacked the  $\text{SiO}_x$  encapsulation. Importantly, the oxide-encapsulated electrocatalysts architecture is proven to be a highly effective approach for stabilizing electrocatalytic nanoparticles deposited on insulating overlayers without adversely affecting mass transport of reactant and product species associated with the hydrogen evolution reaction.



### 3.1 Introduction

As the cost of solar photovoltaic technology continues to drop, a major hurdle limiting the widespread use of variable solar energy is the lack of efficient and cost-effective energy storage.<sup>1–3</sup> Photoelectrochemical cells (PECs) provide one promising approach for storing solar energy by converting it into chemical energy, much as nature accomplishes with photosynthesis.<sup>4–7</sup> Central to the operation of PEC technologies are semiconducting photoelectrodes that convert sunlight into an electronic driving force, or photovoltage, which is then used to drive non-spontaneous electrochemical reactions such as water electrolysis. By this means, PEC technology is capable of converting abundant and renewable sunlight into storable “solar fuels” such as hydrogen (H<sub>2</sub>).

Despite the great promise of PEC technology to contribute to a sustainable energy future, there remain several key barriers in the development of commercially viable PEC materials and devices that must be overcome.<sup>8–10</sup> One major challenge for PEC water-splitting technology has been the trade-off between photoelectrode stability and efficiency.<sup>5,6,11</sup> Consequently, many recent efforts in the field have focused on stabilizing efficient narrow band gap materials like silicon (Si) by coating them with thin, transparent overlayers of insulating materials such as SiO<sub>2</sub><sup>12–17</sup> or TiO<sub>2</sub>.<sup>18–20</sup> These efforts have included the protection of buried p-n junctions,<sup>21–24</sup> as well as photoelectrodes based on a metal-insulator-semiconductor (MIS) architecture in which photovoltage is generated across an MIS Schottky junction.<sup>11,14,18,25</sup> In MIS photoelectrodes the metallic component is of great importance for generating high photovoltage across the MIS junction as well as for enabling efficient electrocatalysis at the electrode|electrolyte interface.<sup>26–29</sup> Additionally, it is critically important that the metal itself also be stable.<sup>30,31</sup> This requirement

entails not only resistance to oxidation and dissolution, but also strong physical adhesion and robust electronic contact to the underlying photoelectrode. The latter two issues are especially important when the metal layer takes the form of metallic nanoparticles, which naturally have a small contact area with the underlying electrode surface. Despite this challenge, nanoparticle catalysts are attractive for minimizing the loading and cost of expensive catalysts,<sup>32</sup> minimizing optical losses,<sup>33</sup> and taking advantage of pinch off effects to achieve higher photovoltages.<sup>34–37</sup>

One potentially scalable and low-cost means of depositing metal nanoparticles or ultra-thin films on photoelectrodes is electrodeposition.<sup>38–41</sup> However, it has been observed that the adhesion of metal nanoparticles to the surface of thin insulating materials like SiO<sub>2</sub> is very poor,<sup>17,42</sup> creating a large challenge for the use of electrodeposition for PEC applications. In this paper, we present a means of stabilizing electrodeposited Pt nanoparticles on a SiO<sub>2</sub>|p-Si surface while simultaneously reducing charge transfer resistance across the nano-scale Pt|SiO<sub>2</sub>|Si MIS junction. These improvements were achieved by coating the nanoparticle-containing photoelectrode surface with a thin (2 nm – 10 nm) silicon oxide (SiO<sub>x</sub>) overlayer, which was applied by a simple, room-temperature UV ozone process.<sup>43</sup> Adding this secondary SiO<sub>x</sub> layer creates what is referred to herein as an insulator-metal-insulator-semiconductor (IMIS) photoelectrode, which is illustrated schematically in Figure 3.1. The SiO<sub>x</sub>-coated Pt nanoparticle structure is similar in nature to core-shell nanoparticles that have previously been used for high temperature heterogeneous catalysis to enhance thermal stability,<sup>44–46</sup> improving the stability of Pt for oxygen reduction catalysis,<sup>47</sup> and for suppressing undesired back-reactions in photoelectrochemical applications.<sup>48,49</sup> However, the IMIS photoelectrode takes this core-shell concept a step further, anchoring the catalytic core directly to the surface of the photoelectrode in an architecture that protects both the nanoparticle and the semiconductor.



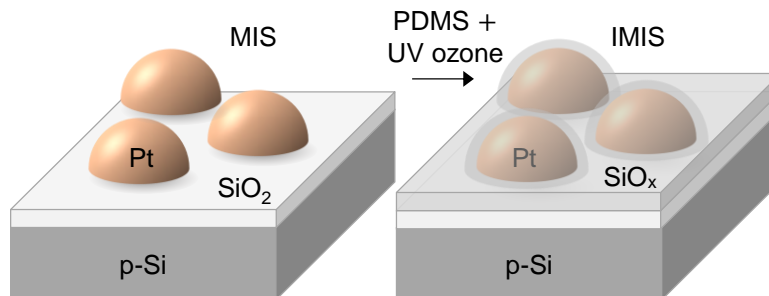


Figure 3.1. Nanoparticle-based MIS and IMIS photoelectrodes. Schematic side views of a metal-insulator-semiconductor (MIS) photoelectrode decorated with electrodeposited Pt nanoparticles and an insulator-metal-insulator-semiconductor (IMIS) photoelectrode containing an additional SiO<sub>x</sub> overlayer.

## 3.2 Experimental Methods

### 3.2.1 SiO<sub>x</sub>/Pt/native SiO<sub>2</sub>/Si Fabrication

#### 3.2.1.1 SiO<sub>2</sub>/Si Electrode Preparation

Monocrystalline p-type Si(100) wafers (1-5  $\Omega$  cm, 500-550  $\mu$ m thick, WRS materials) were cleaved into 1.5  $\times$  2 cm pieces. A diamond scribe was used to scratch and remove native oxide on the back side. An electrical back contact was made with indium solder and a copper wire. Back contact resistance was typically  $\approx$  12  $\Omega$ . Finally, the wafers were sealed in 3M Electroplater's tape to protect the back contact and create a well-defined 0.246 cm<sup>2</sup> circular opening on the front of the electrode for PEC measurements.

#### 3.2.1.2 Platinum Photoelectrodeposition

Photoelectrodeposition was carried out in a Pt plating solution, 3 mmol L<sup>-1</sup> potassium tetrachloroplatinate (K<sub>2</sub>PtCl<sub>4</sub>, Sigma Aldrich, ACS reagent) with 0.5 mol L<sup>-1</sup> sodium chloride (NaCl, Sigma Aldrich, ACS reagent) as supporting electrolyte and under approximately 1 sun intensity by a Xe arc lamp. The solution was modified with hydrochloric acid (HCl, Sigma Aldrich) to pH 3.5 and bubbled with nitrogen gas for 20 minutes to purge dissolved oxygen. A Pt mesh (Alfa Aesar, 99.9%) and glass frit-isolated Ag|AgCl/sat. 3 mol L<sup>-1</sup> KCl were used as a counter

and reference electrode respectively. Light was used to irradiate and assist electrodeposition on p-type Si.

Figure 3.2 shows cyclic voltammetry (CV) curves for  $\text{SiO}_2/\text{p-Si}$  (100) in  $3 \text{ mmol L}^{-1}$  potassium tetrachloroplatinate. Pt was electrodeposited by performing CV between  $-50 \text{ mV}$  to  $-450 \text{ mV}$  vs.  $\text{Ag}|\text{AgCl}$  with a  $50 \text{ mV s}^{-1}$  scan rate. The number of CV cycles was varied, 5, 10, and 20 cycles, to produce the different platinum loadings, 1, 5, and  $20 \mu\text{g cm}^{-2}$  (Figure 3.2a-c). This deposition potential range was determined by two CV curves conducted in the deposition solution over a wider potential window,  $+450 \text{ mV}$  to  $-800 \text{ mV}$ , for a fresh sample (Figure 3.2d). In the first scan, reduction current corresponding to the onset of Pt deposition is observed at  $\approx -0.4 \text{ V}$  vs.  $\text{Ag}|\text{AgCl}$ , and shifts to  $+0.4 \text{ V}$  vs.  $\text{Ag}|\text{AgCl}$  in the second scan. This shift can be attributed to the difference in nucleation kinetics for Pt on the  $\text{SiO}_2$  surface compared to deposition on Pt particles that were present during the second scan.

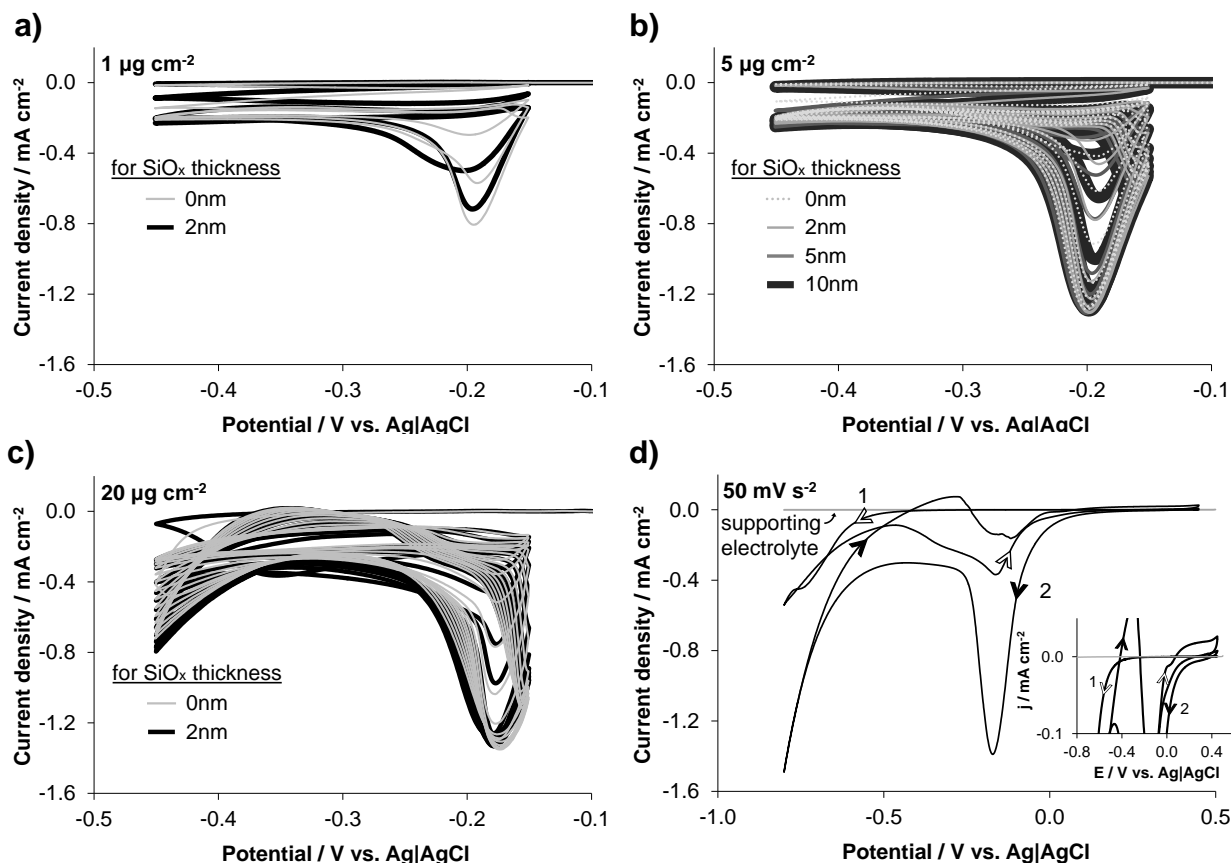


Figure 3.2. CV and LSV in electrodeposition solution. Current-potential curves for  $\text{SiO}_2/\text{p-Si}$  (100) in  $3 \text{ mmol L}^{-1}$  potassium tetrachloroplatinate. CV scan between  $-50 \text{ mV}$  to  $-450 \text{ mV}$  vs.  $\text{Ag}|\text{AgCl}$  at  $50 \text{ mV s}^{-1}$  scan rate for a) 5, b) 10, and c) 20 cycles. d) CV scan between  $+450 \text{ mV}$  to  $-800 \text{ mV}$   $\text{Ag}|\text{AgCl}$  at  $50 \text{ mV s}^{-1}$  scan rate to determine potential range for electrodeposition. Inset zooms in on the onset potentials for Pt deposition in scans 1 and 2.

### 3.2.1.3 $\text{SiO}_x$ Film Synthesis

Trimethylsiloxy terminated polydimethylsiloxane (PDMS) was spin coated onto electrodeposited  $\text{Pt}/\text{p-Si}$  substrates at a speed of  $2000 \text{ rpm}$  for  $1 \text{ min}$  from a toluene solution.<sup>50,51</sup> The concentration of PMDS/toluene solution,  $1.4 \text{ mg mL}^{-1}$ ,  $2.8 \text{ mg mL}^{-1}$ ,  $4.5 \text{ mg mL}^{-1}$ , was selected to produce  $\text{SiO}_x$  films with thickness of  $2 \text{ nm}$ ,  $5 \text{ nm}$ , and  $10 \text{ nm}$  respectively. The samples were then dried in a vacuum oven at  $70^\circ \text{C}$  for  $60 \text{ minutes}$  to evaporate the solvent. Afterwards, the

PDMS was converted to SiO<sub>x</sub> in a ultraviolet (UV) ozone cleansing chamber for 2 hours (UVOCS, T10X10/OES) which generates UV light in the 254 nm and 185 nm range.<sup>50,52</sup> The thickness of the SiO<sub>x</sub> film was measured with an alpha-SE<sup>®</sup> Ellipsometer and fit with Cauchy model.

#### *3.2.1.4 Electron Beam Evaporated Metal Layers*

Continuous metallic films (for ferri/ferrocyanide measurements) and ordered arrays of circular metallic dots (for effective diffusion length measurements) were deposited onto native SiO<sub>2</sub>/p-Si(100) wafers at 0.2 A s<sup>-1</sup> by e-beam evaporation in a Angstrom EvoVac evaporator system with a base pressure of 1.0×10<sup>-7</sup> torr. The patterned samples were made by evaporating the metal through single layer shadow masks possessing circular holes with 0.5 mm diameters. 3 nm thick Pt (99.99%) and 2 nm thick Ti (99.99%) layers were sequentially deposited without breaking vacuum and without substrate heating. Film thicknesses were monitored with quartz crystal thickness monitors.

### **3.2.2 Materials Characterization**

#### *3.2.2.1 Scanning Electron Microscopy*

SEM was carried out with a Hitachi S4700 field emission SEM microscope. SEM images of several locations for every sample were analyzed with a MatLab image analysis program to characterize Pt nanoparticle coverage, density (particles μm<sup>-2</sup>), diameter, spacing, surface area (cm<sup>2</sup> Pt per geometric cm<sup>2</sup>) and loading. The image analysis software approximates each particle as a circle, returning its effective diameter. Particle loading values were estimated based on the measured particle diameters, the density of Pt (21.45 g cm<sup>-3</sup> Pt), a void fraction of 0.54,<sup>53</sup> and assuming a hemispherical particle geometry. The hemispherical geometry is a reasonable approximation based on typical particle shape observed in cross-sectional SEM and TEM. The reported average particle separation distances between neighboring particles were estimated as the

distance between particles if all detected particles in an SEM image were positioned in a square lattice arrangement where all particles are equidistant. The particle coverage, density, distance, surface area, and loading are reported as averages over 8 different areas (SEM images) on each sample and the standard deviation between these different areas. The particle density, Pt particle surface area, and loading are normalized with respect to electrode geometric area of the exposed electrode. The reported particle diameters were calculated as an averages of all the effective particle diameters of >1000 particles from 8 different areas.

#### 3.2.2.2 *X-ray Photoelectron Spectroscopy*

X-ray photoelectron spectroscopy (XPS) measurements were conducted with a Kratos AXIS Ultra DLD XPS system that was operated at a base pressure of  $3 \times 10^{-10}$  Torr using a monochromated  $\text{Al}_{K\alpha}$  source (X-ray power 13 kV, 8 mA) and without a neutralizer. The pass energy was 10 eV and the drain current through the sample stage was 0.4 nA. The XPSpeak program was used in evaluating the peak areas of Si 2p, C 1s, O 1s, and Pt 4f spectra based on Shirley's algorithm for background subtraction. The peak shifts to higher binding energies corresponds to sample charging without the neutralizer, however this did not compromise the atomic ratio analysis. The peak area ratios were calculated after accounting for the atomic sensitivity factors ( $\text{ASF}_i$ ) ( $\text{ASF}_{\text{Si}} = 0.301$ ,  $\text{ASF}_{\text{C}} = 0.296$ ,  $\text{ASF}_{\text{O}} = 0.891$ ,  $\text{ASF}_{\text{Pt}} = 5.575$ ). The Si and O atomic sensitivity factors were obtained using a HF etched Si standard and a wet thermal oxide film ( $\approx 300$  nm  $\text{SiO}_2$  on Si and Ar sputtered at 500 eV for 3 min), whose stoichiometry was assumed to be exactly  $\text{SiO}_2$ . XPS was used to interrogate the composition of the additional  $\text{SiO}_x$  layer.

### *3.2.2.3 Scanning Transmission Electron Microscopy*

The cross section STEM sample (typically 50 nm in thickness) was prepared by focus ion beam (FIB) FEI Nova 600 NanoLab. An extra Pt-C protection layer was deposited by FIB to protect the sample surface; this overlayer directly contacted the Pt particles in some areas and was separated by a carbon film in other areas to clearly show the chemical compositions on the sample surface. High-angle annular dark-field (HAADF)-STEM images were acquired from the prepared lamellas using a probe corrected FEI Titan 80–300 microscope operated at 300 kV with spatial resolution of 0.1 nm. The probe convergence angle was 24 mrad and the HAADF detector collected signals between 70 mrad and 400 mrad. Energy Dispersive X-ray Spectroscopy (XEDS) spectral images were collected by Octane T Optima from EDAX, which provides a windowless detector with solid angles up to 0.5 sr. After background subtraction, The Pt and Si maps are generated by summing their M (2075 eV) and K (1740 eV) peaks respectively (window width 150 eV).

### *3.2.2.4 Ultraviolet-Visible Spectroscopy*

The light transmittance was measured through electrodeposited Pt on transparent indium tin oxide (ITO) with a UV-Vis Spectrophotometer (Agilent Cary 60). Pt was electrodeposited by methods described in section 1.2 and characterized by SEM to confirm similar Pt loadings with the MIS and IMIS samples used in this chapter.

## **3.2.3 Electrochemical Characterization**

### *3.2.3.1 Photoelectrochemical Characterization*

All electrochemical measurements were performed using a SP-200 BioLogic potentiostat controlled by EC-Lab v10.40 software. AM 1.5G illumination was achieved with a 300 W xenon arc lamp (Newport, 67005) and AM 1.5G filter (Newport, 81094) in a Newport housing powered

by a power supply (Newport, 69911). The intensity was calibrated to  $100 \text{ mW cm}^{-2}$  with solar reference cell (VLSI Standards, SRC-1000-RTD-QZ). Electrodes were tested in deaerated  $0.5 \text{ mol L}^{-1}$  sulfuric acid ( $\text{H}_2\text{SO}_4$ , Fisher Scientific, ACS grade), prepared from  $18 \text{ M}\Omega$  deionized water (Millipore, Milli-Q Direct 8). The solution was bubbled with nitrogen gas for 20 minutes to purge dissolved oxygen. During measurements the head space of the working electrode compartment was continuously purged with  $\text{N}_2$ . A Pt mesh counter electrode was located in a secondary compartment separated by a glass frit to prevent product crossover. An Ag|AgCl reference electrode was located in the main compartment. For the 12 hr chronopotentiometry (CP) stability test a reversible hydrogen electrode (RHE) was used as a reference electrode instead of Ag|AgCl to minimize possible Ag contamination during the extended testing period.

The electrolyte was stirred with a magnetic stir bar during PEC testing. The following measurements were performed on each sample: CV (5 cycles between  $+0.40 \text{ V}$  and  $-0.05 \text{ V}$  versus Ag|AgCl at  $50 \text{ mV s}^{-1}$ ), three LSVs under illumination and one in dark ( $+0.30$  to  $-1.23 \text{ V}$  versus Ag|AgCl at  $20 \text{ mV s}^{-1}$ ), and a CV (1 cycle,  $+0.40 \text{ V}$  to  $-1.23 \text{ V}$  vs. Ag/AgCl at  $20 \text{ mV s}^{-1}$ ). In addition, a stability test was conducted by operating the photoelectrodes at a constant current of  $-10 \text{ mA cm}^{-2}$  for 1 hour under illumination. During the test, the open circuit potential was sampled twice for one minute periods. An LSV was performed under illumination before and after the stability test. All LSVs presented in the manuscript and SI are iR corrected, unless otherwise noted.

#### 3.2.3.2 Scanning Photocurrent Microscopy

Effective minority carrier diffusion lengths ( $L_e$ ) were determined using scanning photocurrent microscopy (SPCM) measurements. In these experiments, an e-beam deposited Pt|Ti front contact was contacted by a tungsten probe, and laser beam-induced photocurrent ( $J_{\text{ph}}$ ), was measured under constant applied voltage ( $-1 \text{ mV}$ ) as a function of laser beam distance from the

edge of the circular contact ( $D_L$ ). A schematic of the measurement set-up is provided in Figure 3.3.  $L_e$  was calculated from the slope of a plot of the logarithm of normalized photocurrent,  $\ln(J_N)$ , versus  $D_L$ .<sup>54</sup> Effective diffusion lengths were calculated based on slopes between  $20\ \mu\text{m} < D_L < 50\ \mu\text{m}$  and for MIS and IMIS. Confidence intervals are provided at the 95 % confidence level and are derived from  $L_e$  values obtained from three measurements on each sample.

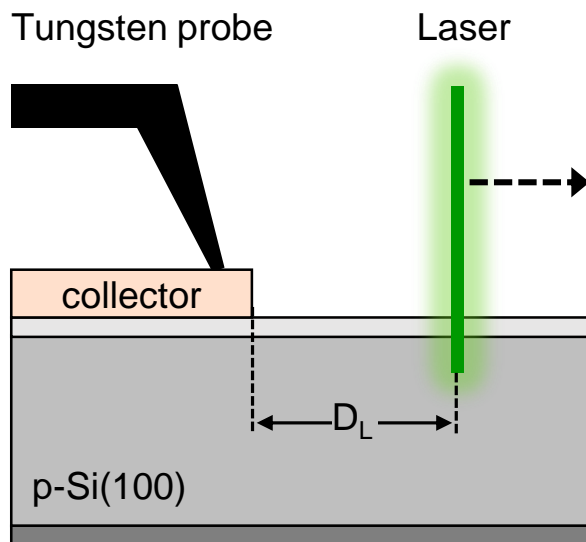


Figure 3.3. Side-view schematic of SPCM measurement set-up used for determining the effective diffusion length in MIS and IMIS control samples in which the metal component, or collector, consisted of e-beam deposited  $500\ \mu\text{m}$  bilayer islands with 3 nm Pt on top of 2 nm of Ti.

A similar set up was used for I-V measurements that were conducted in air on a  $45\ \mu\text{m}$  diameter 20 nm Pt|30 nm Ti circular contact that was e-beam deposited onto 2 nm rapid thermal oxide (RTO)  $\text{SiO}_2$ |p-Si for varying light intensities. The maximum current density was systematically increased by varying the 532 nm laser illumination intensity.

### 3.2.3.3 Ferri/Ferrocyanide Cyclic Voltammograms

The total device resistance of physical vapor deposited 3 nm Pt film|2 nm Ti|‘x’ nm  $\text{SiO}_x$ |native  $\text{SiO}_2$ |p-Si electrodes was evaluated by conducting cyclic voltammetry (CV) in a ferri/ferrocyanide solution under AM1.5G illumination. Potassium ferricyanide ( $\text{K}_3\text{Fe}(\text{CN})_6$ ) and



potassium ferrocyanide trihydrate ( $(\text{K}_3\text{Fe}(\text{CN})_6 \cdot 3\text{H}_2\text{O})$ ) were used to make a 1:1 solution containing  $10 \text{ mmol L}^{-1}$  of each species with  $1 \text{ mol L}^{-1}$  potassium chloride. Pt mesh was used as the counter electrode and an Ag|AgCl electrode was used as the reference electrode. All ferri/ferrocyanide CVs were measured at a scan rate of  $100 \text{ mV s}^{-1}$  in a static solution.

#### 3.2.3.4 Variable Illumination Intensity

MIS electrodes with low and high Pt coverages were PEC tested in  $0.5 \text{ mol L}^{-1} \text{ H}_2\text{SO}_4$  under 0.25 and 1 sun intensities. The light intensities were calibrated with the VLSI Si reference cell. MIS electrode stability was evaluated by performing five CV cycles between  $-0.8 \text{ V}$  to  $+0.6 \text{ V}$  vs. RHE and monitoring the decrease in operating current density (at a given potential) with each successive cycle.

### 3.3 Results

#### 3.3.1 Description of Insulator-Metal-Insulator-Semiconductor Photoelectrode

The basic operating principles of the IMIS photoelectrode are shown schematically in Figure 3.4. First, excitons must be generated within a distance less than the sum of the depletion width ( $W$ ) and effective minority carrier diffusion length ( $L_e$ ) in order for the minority carrier electrons to reach the MIS nano-junction at the base of the metal nanoparticle. Once the minority carrier electron reaches the  $\text{SiO}_2/\text{Si}$  interface, it tunnels through the thin  $\text{SiO}_2$  layer to reach the nanoparticle catalyst, a process that depends strongly on the  $\text{SiO}_2$  layer thickness.<sup>58</sup> Protons in solution are concurrently transported to the nanoparticle surface where they are reduced by the electrons, resulting in the hydrogen evolution reaction (HER).

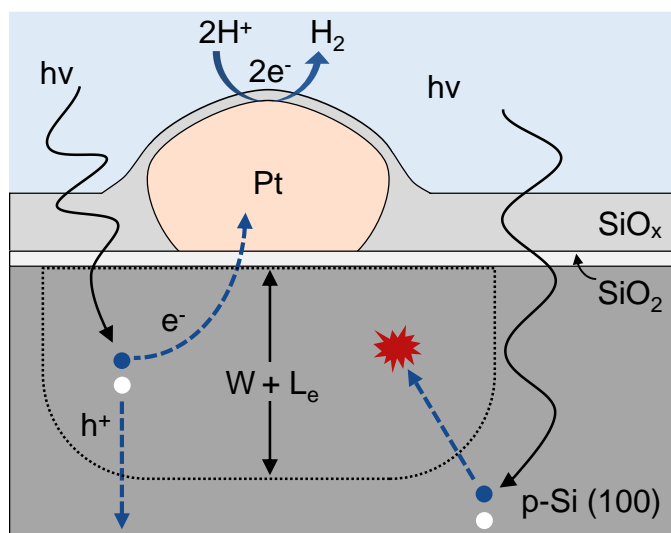


Figure 3.4. Schematic side-view illustrating the basic operating processes occurring in an IMIS photoelectrode.

### 3.3.2 Characterization

#### 3.3.2.1 Platinum Particle Analysis

This initial study of IMIS photoelectrodes was based upon photocathodes made from p-Si(100) wafers. First, the MIS structure (Figure 3.1) was fabricated by photoelectrodepositing platinum nanoparticles onto native SiO<sub>2</sub>/p-Si(100) from a 3 mmol L<sup>-1</sup> K<sub>2</sub>PtCl<sub>4</sub> solution. The platinum loading was controlled by varying the number of cyclic voltammetry (CV) cycles during electrodeposition (described in section 3.2.1.2). The resulting average particle size, coverage, spacing, and Pt loadings were determined from SEM analysis (Figure 3.5) and are provided in Appendix section 3.6.1, Table 3.2. Figure 3.5 contains SEM images performed on MIS structures with 1, 5, and 20 μg cm<sup>-2</sup> of electrodeposited Pt. The average particle size and spacing were observed to increase and decrease, respectively, with increased Pt loading.

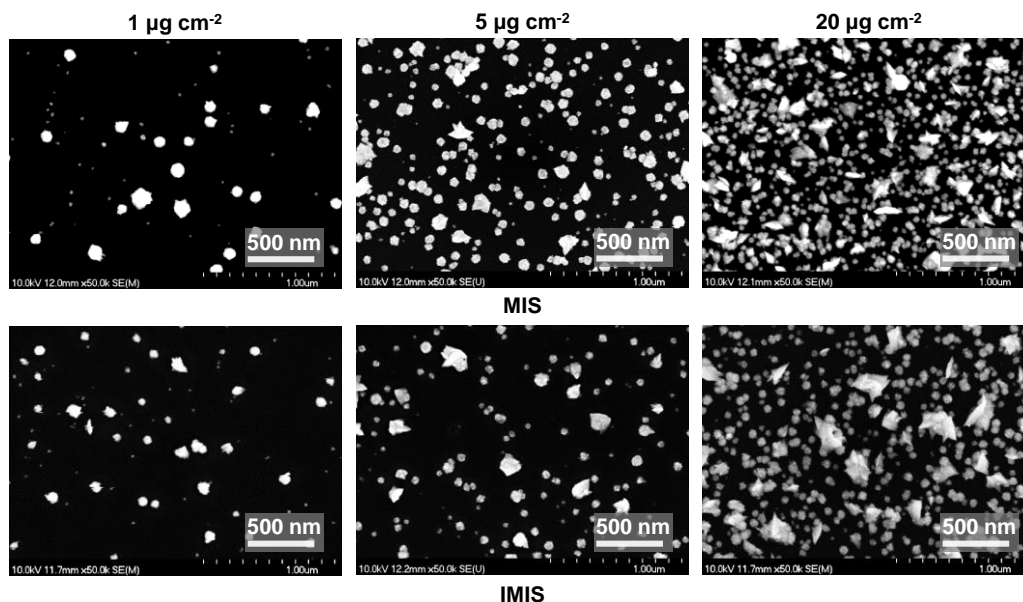


Figure 3.5. Top view SEM images. Representative SEM images of MIS photoelectrodes with Pt loadings of 1, 5, and 20  $\mu\text{g cm}^{-2}$ .

SEM images in Figure 3.6 reveal that the as-deposited Pt nanoparticles have a relatively rough and dendritic morphology. Following electrodeposition of the Pt nanoparticles, polydimethylsiloxane (PDMS) was spin coated onto the MIS and converted into  $\text{SiO}_x$  by a room-temperature ultraviolet (UV) ozone treatment to give the final IMIS structure (Figure 3.1).

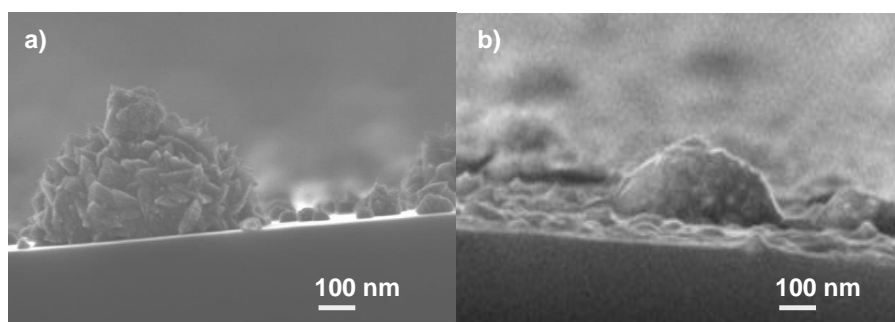


Figure 3.6. MIS and IMIS side-view. Representative cross sectional FE-SEM images of a) MIS and b) IMIS samples generally reveal smoother Pt nanoparticle features on the IMIS surface than compared to the MIS surface. The smooth features indicate the  $\text{SiO}_2$  overlayer coating over and around most of the spikey Pt nanoparticles as suggested by the schematics in Figure 3.1 and 3.4.

### 3.3.2.2 Chemical and Physical Structure

XPS characterization of the as-deposited  $\text{SiO}_x$  layer indicates that Si predominantly exists as silicon dioxide ( $\text{SiO}_2$ ) and residual carbon from PDMS remains in the  $\text{SiO}_2$ , consistent with previous studies of thin  $\text{SiO}_x$  films grown by this method (Figure 3.23).<sup>43,52</sup> These previous studies reported that, more than 55% of the C atoms are eliminated from PDMS films after 2 hours of UV ozone exposure for  $\text{SiO}_x$  films under 20 nm. Further details on the UV ozone treatment and characterization of  $\text{SiO}_x$  thin films can be found in literature.<sup>43,52,59,60</sup> Additionally, the Pt 4f signal was suppressed by 50% for the  $\text{SiO}_x|\text{Pt}|\text{SiO}_2|\text{Si}$  (IMIS) compared to the  $\text{Pt}|\text{SiO}_2|\text{Si}$  (MIS) sample indicating some  $\text{SiO}_x$  overlayer coverage on top of the Pt particles.

Cross sectional HAADF-STEM of an IMIS sample, 10 nm  $\text{SiO}_x|\text{Pt}|$ native  $\text{SiO}_2|\text{p-Si}$ , (Figure 3.7) shows elemental sensitive contrasts between Pt and Si that clearly reveal a well-defined  $\approx 1.5$  nm thick native  $\text{SiO}_2$  layer under the Pt particle and a  $\approx 10$  nm thick  $\text{SiO}_x$  layer covering the electrode surface in between the Pt nanoparticles.

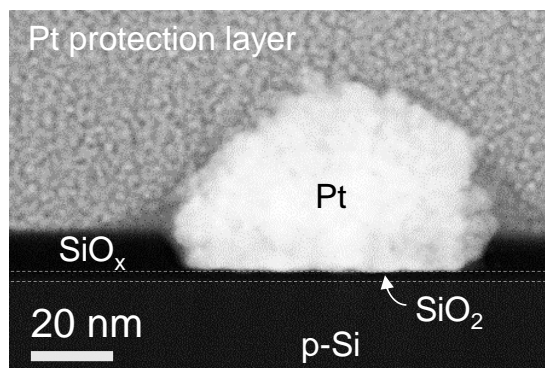


Figure 3.7. Cross sectional HAADF-STEM image of a  $\text{SiO}_x|\text{Pt}|$ native  $\text{SiO}_2|\text{p-Si}$  IMIS nanojunction based on a 10 nm thick  $\text{SiO}_x$  overlayer with Pt protection layer.

From other HAADF-STEM images, the observed  $\text{SiO}_2+\text{SiO}_x$  thickness varies across the sample (Figure 3.8a). In areas of high Pt particle density the  $\text{SiO}_x$  layer is thicker (up to 17 nm), and thinner ( $\approx 9$  nm) in areas where particles are relatively far apart. This average thickness

measured by STEM ( $11 \pm 2\text{ nm}$ ) is similar to the value measured using spectroscopic ellipsometry (thickness  $\approx 10\text{ nm}$ ) on a sample area with no Pt, a finding that can be attributed to the uniformity of the  $\text{SiO}_x$  layer in relatively smooth areas.

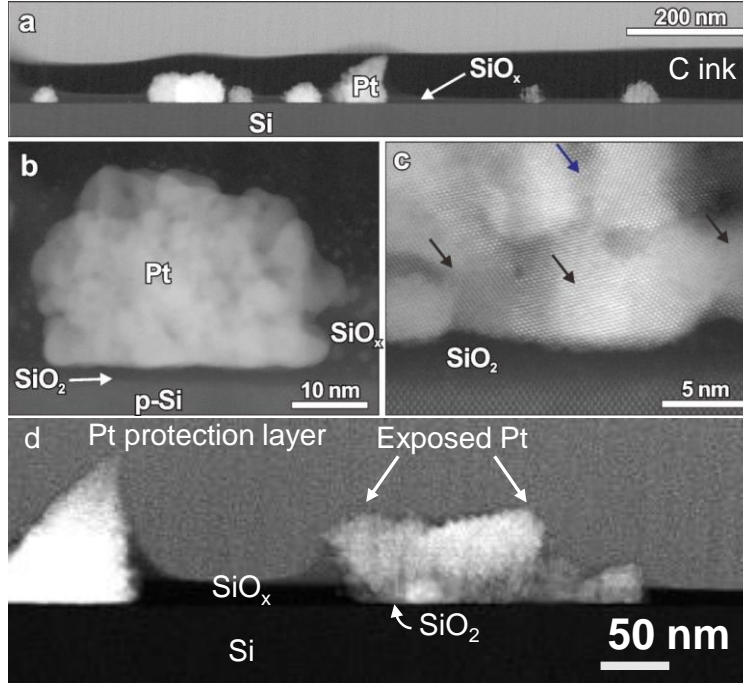


Figure 3.8. Cross section of the IMIS photoelectrodes revealed by HAADF-STEM. a) Low magnification STEM images of a  $10\text{ nm SiO}_x|\text{Pt}| \text{native SiO}_2|\text{p-Si}$  IMIS sample showing the  $\text{SiO}_x$  overlayer on native  $\text{SiO}_2|\text{Si}$  substrate. b) High resolution HAADF-STEM showing the structure details of an IMIS photoelectrode. c) Atomic resolved HAADF-STEM illustrates that the Pt cluster consists of small Pt particles oriented differently. The Pt area marked by the blue arrow is coincidentally laid in the zone axis to show clear 2D atomic column distribution, while in neighboring areas marked by black arrows the Pt particles are disoriented with different lattices. d) Additional STEM image revealing some larger particles protrude out of the  $\text{SiO}_x$  shell.

The high resolution HAADF-STEM images Figure 3.8b and 3.8c show variations in contrast inside the Pt cluster which implies that the Pt cluster is porous or consisting of small Pt nanoparticles. This porous structure with large surface area would enhance the catalysis properties

of Pt clusters. Additional STEM images (Figure 3.8d) suggest that some of the larger particles do not have a complete  $\text{SiO}_x$  shell, allowing some dendritic Pt nanoparticles to protrude out the  $\text{SiO}_x$  shell and directly contact the electrolyte. The observation of partial or full coverage of Pt nanoparticles by the thin  $\text{SiO}_x$  layer is further corroborated by a significant decrease in the Pt 4f XPS signal from the surface of an IMIS sample compared to an MIS sample of identical Pt loading, presumably due to screening by the  $\text{SiO}_x$  overlayer (Table 3.3).

The cross sectional HAADF-STEM and Energy Dispersive X-ray Spectroscopy (XEDS) mapping images in Figure 3.9 also clearly show a thin  $\text{SiO}_x$  overlayer covering the surface of the Pt nanoparticle. Figure 3.9a clearly shows the Pt cluster is hemispherical on top of the native  $\text{SiO}_2$  layer. The Si map illustrates a weak shell structure on top surface of the Pt, where the Si signal distributes on the surface of Pt cluster (Figure 3.9b). Si signal is strongly observed on the Pt contacting corners to the  $\text{SiO}_2$  layer (marked by white arrows in Figure 3.9c). The XEDS spectra shown in Figure 3.9d are from representative Site I (on Pt cluster), Site II (on the Si shell), and Site III (on the  $\text{SiO}_2$  layer) from Figure 3.9c. This XEDS spectra clearly shows that the Si-K peak signal is weak at the center of the Pt cluster and is relatively stronger on its outer shell. This evidence confirms that the Pt cluster is buried inside a thin  $\text{SiO}_x$  layer as illustrated in Figure 3.1 and 3.4.

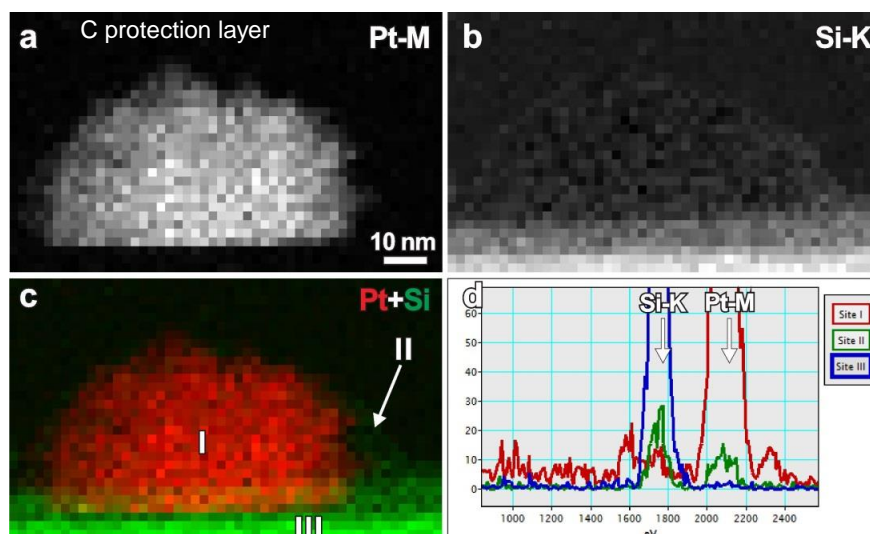


Figure 3.9. STEM-XEDS mapping of an IMIS photoelectrode. a) The Pt map showing a cluster of Pt on top of SiO<sub>2</sub> layer. b) The Si map shows a weak shell structure on the top surface of Pt cluster. c) The overlay of Pt (red) and Si (green) maps show the relative distribution of those two elements. d) The XEDS spectra from 3 representative sites showing the different presence of Si and Pt signal.

### 3.3.3 Photoelectrochemical Performance

PEC performance of the MIS and IMIS photoelectrodes was evaluated by performing consecutive linear sweep voltammograms (LSVs) in deaerated 0.5 mol L<sup>-1</sup> H<sub>2</sub>SO<sub>4</sub> under simulated AM 1.5 G illumination. Figure 3.10 contains the initial LSV curves for MIS and IMIS photoelectrodes with 1  $\mu\text{g cm}^{-2}$ , 5  $\mu\text{g cm}^{-2}$ , and 20  $\mu\text{g cm}^{-2}$  Pt loadings (Figure 3.10a-c). The SiO<sub>x</sub> overlayer on the IMIS samples was 2 nm thick, as measured by ellipsometry on control areas lacking any Pt nanoparticles. From Figure 3.10, it is immediately evident that there is a substantial improvement in the current-potential (I-E) characteristics of the IMIS samples compared to the MIS samples, with the former exhibiting larger limiting photocurrents and substantially steeper slopes in the LSV curve as it transitions from the photocurrent onset potential to the photo-limiting current plateau.

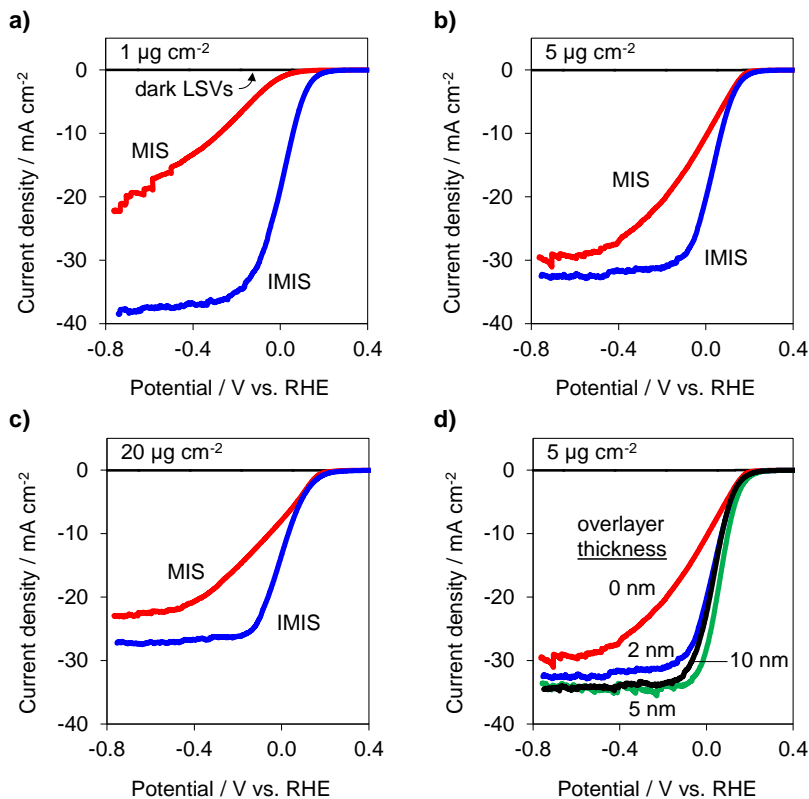


Figure 3.10. MIS and IMIS performance. LSV measurements for [Pt|native SiO<sub>2</sub>|p-Si(100) MIS (red) and [2 nm SiO<sub>x</sub>|Pt|native SiO<sub>2</sub>|p-Si(100) IMIS (blue) photoelectrodes for a.) 1  $\mu\text{g cm}^{-2}$  Pt, b.) 5  $\mu\text{g cm}^{-2}$  Pt, and c.) 20  $\mu\text{g cm}^{-2}$  Pt. d.) LSV measurements for [ $x$  nm SiO<sub>x</sub>|5  $\mu\text{g cm}^{-2}$  Pt|native SiO<sub>2</sub>|p-Si(100) for various SiO<sub>x</sub> thicknesses from 0 nm to 10 nm. All LSV measurements were performed at 20  $\text{mV s}^{-1}$  in 0.5 mole L<sup>-1</sup> H<sub>2</sub>SO<sub>4</sub> under AM 1.5 G illumination. Current densities are normalized with respect to the geometric area of the exposed photoelectrode.

Table 3.1 summarizes the performance of all photoelectrodes, as measured by the operating potential required to achieve -10  $\text{mA cm}^{-2}$  for the first LSV measured. The MIS photoelectrode with the lowest Pt loading exhibited the worst performance, requiring -280 mV vs. RHE to achieve -10  $\text{mA cm}^{-2}$ . By contrast, the IMIS photoelectrode with equivalent Pt loading was able to operate at +60 mV vs. RHE at the same current density. Significant improvements in the operating potential of IMIS samples with 5  $\mu\text{g cm}^{-2}$  and 20  $\mu\text{g cm}^{-2}$  Pt loading were observed



compared to their MIS counterparts, though not as dramatic as for the low Pt loading samples. The presence of the SiO<sub>x</sub> overlayer created the additional benefit of increasing the photo-limited current density. For IMIS samples, the limiting current density decreased monotonically with increasing Pt loading and can be explained by increased optical losses associated with the opaque Pt particles. The ability of the 1  $\mu\text{g cm}^{-2}$  IMIS sample to achieve a photo-limiting current density close to the theoretical maximum for crystalline Si ( $\approx 42 \text{ mA cm}^{-2}$  under AM 1.5 illumination) indicates that neither the Pt nanoparticles nor the SiO<sub>x</sub> overlayer contribute to any significant optical losses for that sample.

Table 3.1. Summary of Pt particle characterization (based on SEM images), electrode performance (based on Figure 3.10), and degradation behavior (based on Figure 3.12, 3.13, and 3.25). See section 3.2.2.1 for more details on SEM analysis of Pt loading, Pt particle density, Pt surface area, Pt coverage, average Pt particle sizes and distances.

	approximate Pt loading <sup>a</sup> ( $\mu\text{g cm}^{-2}$ )	SiO <sub>x</sub> thickness (nm)	average Pt nanoparticle diameter (nm)	Pt 2D coverage (%)	V vs. RHE (mV) at -10 mA $\text{cm}^{-2}$	$\Delta V$ (mV) between LSV 1 and 3 at - 10 mA $\text{cm}^{-2}$	$\Delta V/\text{hr}$ (mV/hr) during CP	$\Delta V$ (mV) between LSV before and after 1 hr CP at -10 mA $\text{cm}^{-2}$
MIS	1	0	$38 \pm 32$	$3.3 \pm 0.8$	-280	-200	-140	n/a <sup>b</sup>
MIS	5	0	$55 \pm 36$	$15 \pm 3.1$	+7	-70	-80	-260
MIS	20	0	$66 \pm 54$	$42 \pm 1.2$	-60	-30	-45	-110
IMIS	1	2	$37 \pm 30$	$3.9 \pm 0.6$	+60	-30	-11	-80
IMIS	5	2	$58 \pm 34$	$13 \pm 0.9$	+70	-40	-14	-30
IMIS	20	2	$70 \pm 53$	$32 \pm 1.6$	+30	-10	-6	-15
IMIS	5	5	$65 \pm 42$	$13 \pm 0.2$	+100	-20	-7	-12
IMIS	5	10	$53 \pm 38$	$14 \pm 1.1$	+70	-8	-5	-5

<sup>a</sup> Values determined by SEM image analysis provided in Appendix section 3.6.1.

<sup>b</sup> LSV performance of the MIS sample with lowest loading degraded so much that the photocurrent didn't reach 10 mA  $\text{cm}^{-2}$ .

IMIS photoelectrodes with varied SiO<sub>x</sub> thickness and a constant Pt particle loading of 5  $\mu\text{g cm}^{-2}$  were also fabricated to view the influence of SiO<sub>x</sub> thickness on PEC performance. Figure

3.10d shows LSV curves for IMIS samples with 2 nm, 5 nm, or 10 nm of SiO<sub>x</sub> layers. Although the onset potential of the LSV curves changed very little, there was a notable increase in the limiting photocurrent upon addition of just 2 nm of SiO<sub>x</sub>, which can be attributed to reduced reflection losses due to the presence of the thicker UV ozone SiO<sub>x</sub> layer compared to the native SiO<sub>2</sub>|Si interface. Increasing overlayer thickness beyond 2 nm resulted in a nominal increase in limiting photocurrent. More importantly, the thicker SiO<sub>x</sub> layers did not cause any decrease in PEC performance by limiting mass transport of protons to the Pt surface. This observation may have two explanations. First, some of the larger, dendritic Pt particles may not be entirely covered by the SiO<sub>x</sub> overlayer, meaning that proton transport from the bulk electrolyte will be unimpeded for those particles. In the case of encapsulated Pt nanoparticles, such as that shown in Figure 3.6, facile proton transport may also take place by diffusion through the thin SiO<sub>x</sub> overlayer. This explanation is consistent with evidence from previous studies that have reported the presence of proton and water transport through thin SiO<sub>2</sub> layers that were used to encapsulate Pt microelectrodes<sup>61</sup> and Pt oxygen reduction reaction catalysts.<sup>47</sup> It should also be noted that the SiO<sub>x</sub> thin films fabricated by the same UV ozone process used in this dissertation have been used as selective gas separation membranes for small molecules.<sup>59,60,62</sup>

### 3.3.3.1 Control Electrodes: UV Ozone Treated Platinum and SiO<sub>x</sub> without Platinum

A 5 μg cm<sup>-2</sup> Pt|native SiO<sub>2</sub>|p-Si(100) MIS sample was treated with identical processing steps as the IMIS samples with SiO<sub>x</sub>, except that no PDMS was spin coated onto the MIS sample. Toluene was spin coated onto the MIS sample, dried in a vacuum oven at 70 °C for 60 minutes, and treated with UV ozone for 2 hrs. The PEC LSV performance of the UV ozone treated MIS and SiO<sub>x</sub>|SiO<sub>2</sub>|p-Si control electrodes were evaluated. The results in Figure 3.11 confirm that the difference in PEC performance between the MIS and IMIS photoelectrodes was due to the

presence of the  $\text{SiO}_x$  overlayer and not a result of the UV ozone treatment nor HER catalysis associated with residual carbonaceous species in the  $\text{SiO}_x$ .

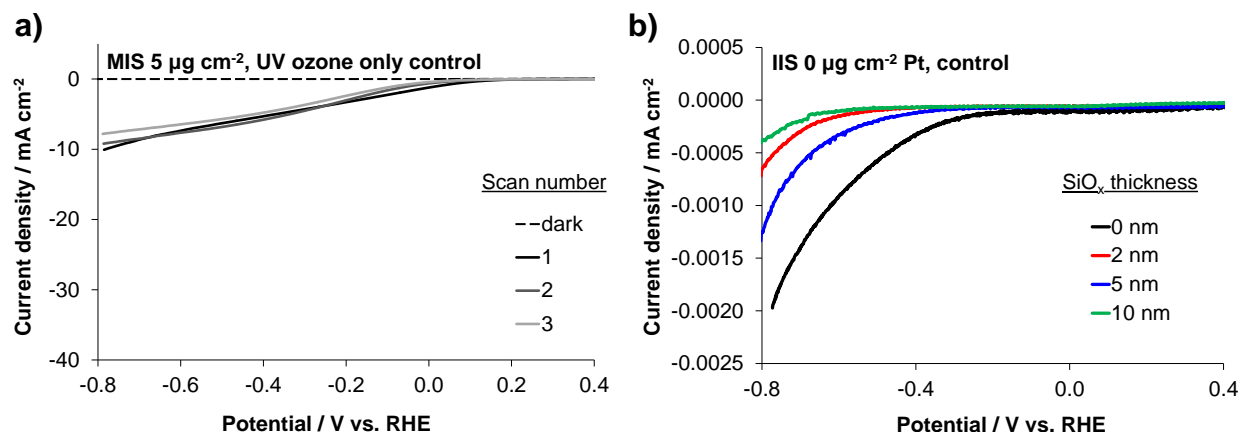


Figure 3.11. PEC performance of UV ozone treated MIS and bare  $\text{SiO}_2$  control samples. LSV measurements in  $0.5 \text{ mol L}^{-1} \text{ H}_2\text{SO}_4$  under 1 sun of AM 1.5G illumination for a) UV ozone treated MIS  $5 \text{ µg cm}^{-2} \text{ Pt/native SiO}_2/\text{p-Si}(100)$  and b) 'x' nm  $\text{SiO}_x/\text{native SiO}_2/\text{p-Si}(100)$  control samples.

### 3.3.4 Photoelectrochemical Stability

#### 3.3.4.1 Short-Term

The short-term stability of MIS and IMIS photocathodes was first evaluated by conducting two additional LSVs immediately following the LSVs of Figure 3.10 (Figure 3.12). The change in operating potentials at  $-10 \text{ mA cm}^{-2}$  between the first and third LSV are compared in Table 3.1. All of the MIS samples exhibited substantial instability, with the operating potential shifting more negative by 30 mV – 200 mV at an operating current of  $-10 \text{ mA cm}^{-2}$ . The  $20 \text{ µg cm}^{-2}$  MIS sample showed substantially less degradation in performance than the  $1 \text{ µg cm}^{-2}$  sample. In contrast to MIS photoelectrodes, all of the IMIS photoelectrodes demonstrated excellent stability, with very little change in operating potential (8 mV – 40 mV) between the first and third LSV curves.

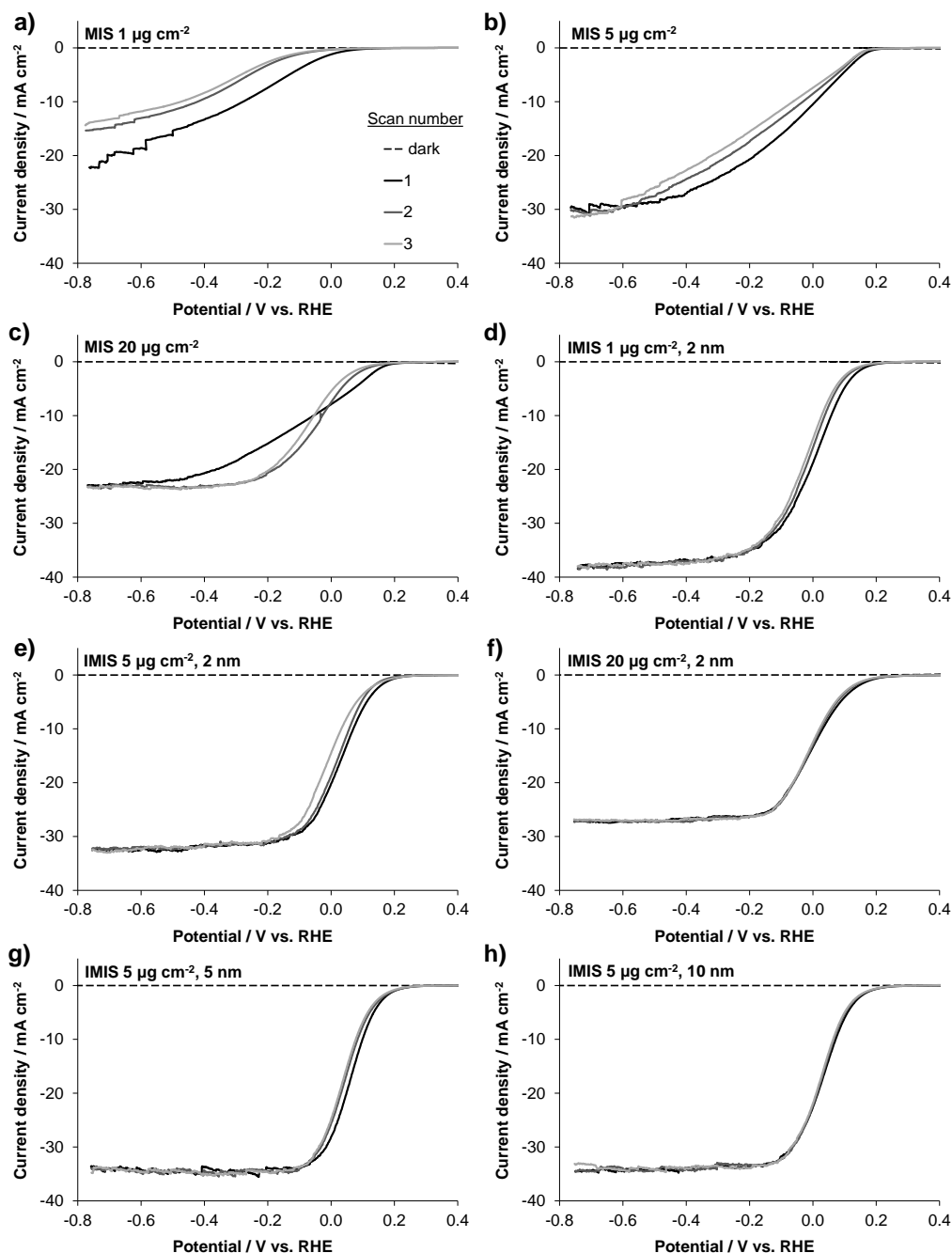


Figure 3.12. Short-term stability. LSV measurements in 0.5 mol L<sup>-1</sup> H<sub>2</sub>SO<sub>4</sub> under 1 sun of AM 1.5 G illumination for 'x' nm SiO<sub>x</sub>|'y' μg cm<sup>-2</sup> Pt|native SiO<sub>2</sub>|p-Si(100) for various SiO<sub>x</sub> thicknesses (x) from 0 nm to 10 nm and various amounts of Pt loading (y) from 1 to 20 μg cm<sup>-2</sup> and. Dark LSVs and LSV's 1, 2, and 3 are shown. a-c) 1, 5, and 20 μg cm<sup>-2</sup> Pt with 0 nm SiO<sub>x</sub>, d-f) with 2 nm SiO<sub>x</sub>, and g-h) 5 μg cm<sup>-2</sup> Pt with 5 and 10 nm SiO<sub>x</sub>. The LSV scan rate was 20 mV s<sup>-1</sup>.

### 3.3.4.2 Long-Term

The stability was also investigated under a constant applied current (chronopotentiometry (CP)) over the course of one hour, during which time the samples were intermittently subjected to open circuit potential (OCP) operation to simulate the periodic cycling conditions in a real device (Figure 3.13). The MIS samples without the SiO<sub>x</sub> overlayer failed to maintain a constant potential, whereas the IMIS samples with the SiO<sub>x</sub> overlayer were able to sustain a consistent potential for the duration of these stability tests. The operating potential required to produce -10 mA cm<sup>-2</sup> for the MIS samples decreased at 45 mV hr<sup>-1</sup> – 140 mV hr<sup>-1</sup>, whereas the IMIS samples exhibited excellent stability (5 mV hr<sup>-1</sup> – 14 mV hr<sup>-1</sup>). The changes in operating potentials for all samples are compared in Table 3.1. The 5 µg cm<sup>-2</sup> Pt loaded MIS sample exhibited sudden potential fluctuations likely due to the build-up and release of large hydrogen bubbles from the photoelectrode surface. All of the IMIS samples effectively removed hydrogen gas bubbles away from surface due to the hydrophilic nature of the SiO<sub>x</sub> over layer, as supported by the nominal potential fluctuations. The lowest Pt loaded MIS sample demonstrated an unexpected behavior where the operating potential decreased after the pulse to OCP.

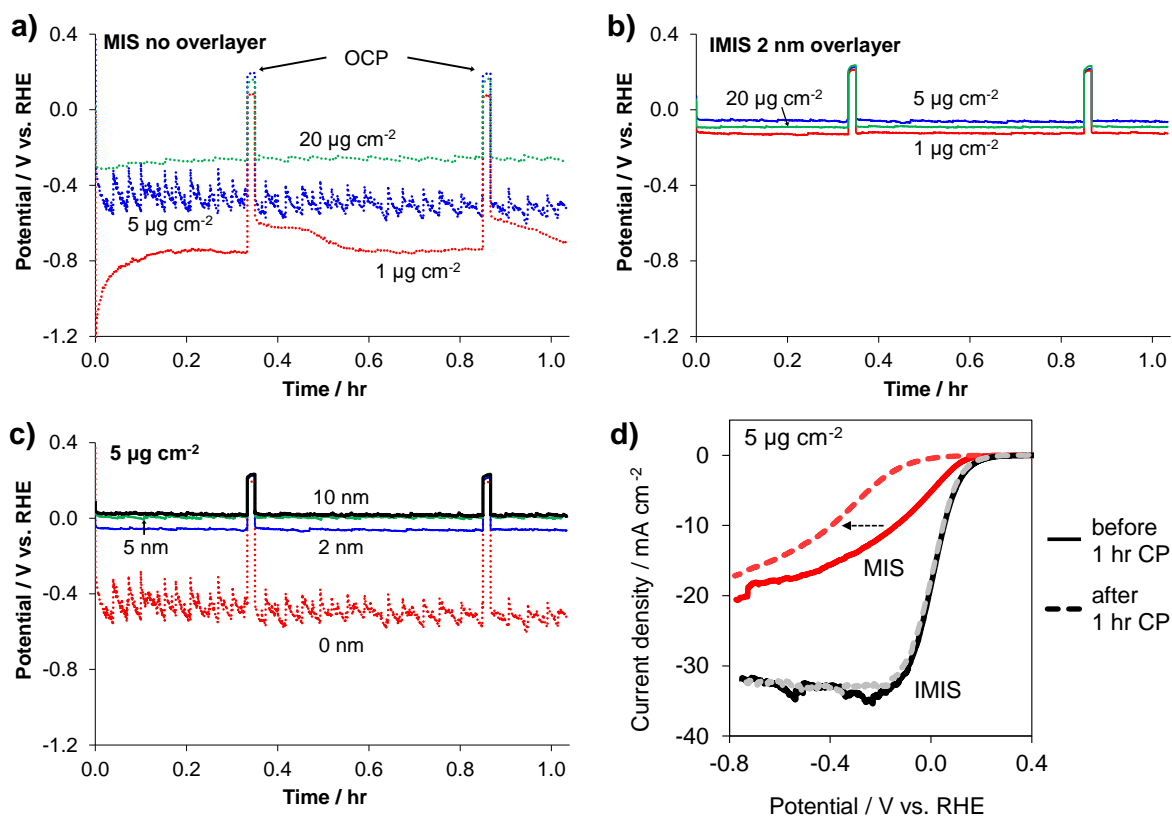


Figure 3.13. 1 hour stability tests. Chronopotentiometry stability measurements in 0.5 mol L<sup>-1</sup> H<sub>2</sub>SO<sub>4</sub> for a) MIS Pt|native SiO<sub>2</sub>|p-Si(100) and b) IMIS 2 nm SiO<sub>x</sub>|Pt|native SiO<sub>2</sub>|p-Si(100) for various amounts of Pt loading, and for c) 'x' nm SiO<sub>x</sub>|5  $\mu\text{g cm}^{-2}$  Pt|native SiO<sub>2</sub>|p-Si(100) for various SiO<sub>x</sub> thicknesses from 0 to 10 nm operating at -10 mA cm<sup>-2</sup> for 1 hr under 1 sun of AM 1.5G illumination. Open-circuit potentials were measured twice for 1 minute during the study. The larger fluctuations in potential for the MIS photoelectrode are caused by differences in bubble growth and detachment. d) LSV measurements for MIS (red) and IMIS (black) samples with 5  $\mu\text{g cm}^{-2}$  Pt loading before (solid lines) and after (dashed lines) the 1 hr CP stability test conducted at -10 mA cm<sup>-2</sup> for 1 hr. Measurements performed in 0.5 mole L<sup>-1</sup> H<sub>2</sub>SO<sub>4</sub> under simulated AM 1.5 G illumination.

Although neither the MIS nor IMIS samples dramatically failed during the CP stability tests, LSVs performed before and after the CP measurements revealed a substantial decrease in performance for the MIS samples but not for the IMIS samples (Figure 3.13d and 3.25). The

change in operating potential at  $-10 \text{ mA cm}^{-2}$  for the MIS samples during the 1 hr CP test was very small compared to the  $> 110 \text{ mV}$  shifts in potential observed in LSV curves before and after the 1 hr CP test (summarized in Table 3.1). In contrast, the IMIS sample with the 10 nm  $\text{SiO}_x$  overlayer demonstrated the lowest degradation with only a 5 mV shift at  $-10 \text{ mA cm}^{-2}$ . The observation of more severe performance degradation under potential cycling (i.e. LSV curves) compared to a long constant current measurement is consistent with those observed in Figure 3.12 and indicates that operating the MIS photoelectrodes under potential cycling is far more detrimental than continuous operation at a set current density or potential.

In a separate experiment, the long term stability of freshly-prepared  $12 \text{ } \mu\text{g Pt cm}^{-2}$  MIS and IMIS photoelectrodes (Table 3.4) were investigated by monitoring the change in operating potential required to sustain  $-10 \text{ mA cm}^{-2}$  during a 12 hr CP measurement (Figure 3.14). The operating potential of the MIS electrode decreased at  $40 \text{ mV hr}^{-1}$ , whereas the IMIS electrode remained very stable, only a  $2.5 \text{ mV hr}^{-1}$  decrease, for the duration of the 12 hour test.

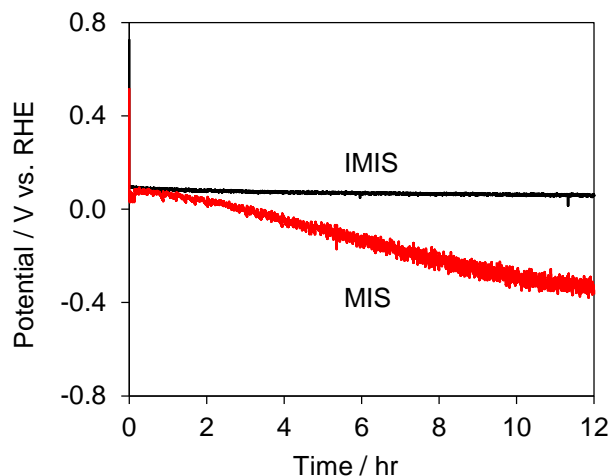


Figure 3.14. Long-term stability. CP stability measurements for MIS (red) and IMIS (black) samples with  $12 \text{ } \mu\text{g cm}^{-2}$  Pt loading operating at  $-10 \text{ mA cm}^{-2}$  for 12 hrs. Measurements performed in  $0.5 \text{ mole L}^{-1} \text{ H}_2\text{SO}_4$  under simulated AM 1.5 G illumination.

### 3.4 Discussion

The results of Figures 3.10–3.14 highlight the ability of the IMIS photoelectrode architecture to be employed for stable and efficient PEC energy conversion, but also raise three underlying questions: i.) why do the electrodeposited MIS photoelectrodes have such poor LSV performance in the first place? ii.) how does the addition of the secondary SiO<sub>x</sub> layer improve the LSV performance for IMIS photoelectrodes?, and iii.) why are IMIS photoelectrodes so much more stable than MIS photoelectrodes?

#### 3.4.1 Understanding Origins of Poor Performance

In addressing the first two questions, it is useful to recall the four fundamental processes illustrated in Figure 3.4 that are essential to MIS photoelectrode operation: i.) light absorption/electron-hole generation, ii.) minority carrier transport to the MIS junction, iii.) tunneling across the insulator, and iv.) electrocatalytic charge transfer at the electrode|electrolyte interface.

##### 3.4.1.1 Light Absorption and Catalysis

In order to understand the optical and catalytic properties of low-loading electrodeposited Pt nanoparticles, UV-Vis and LSV measurements were conducted on electrodeposited Pt on transparent indium tin oxide (ITO). UV-Vis measurements show that the 5  $\mu\text{g cm}^{-2}$  Pt loading possesses > 85 % light transmittance across the visible wavelengths (Figure 3.15a). These values are in accord with the limiting photocurrent densities observed for the 5  $\mu\text{g cm}^{-2}$  Pt loaded IMIS samples during photoelectrochemical testing, ranging between 34-37  $\text{mA cm}^{-2}$ . The HER LSV measurements show that 5  $\mu\text{g cm}^{-2}$  Pt|ITO|glass sample is capable of achieving -10  $\text{mA cm}^{-2}$  with less than 40 mV kinetic overpotential loss (Figure 3.15b). Only a 60-75 mV overpotential was required to achieve high current densities of interest (20-40  $\text{mA cm}^{-2}$ ), far less than the 440 mV to 200 mV shift (at -20  $\text{mA cm}^{-2}$ ) in the MIS photoelectrode LSV curves with respect to their IMIS



counterparts having the same Pt loading (based on SEM in Figure 3.15c). UV-Vis and LSV measurements performed on control samples consisting of electrodeposited Pt particles on transparent indium tin oxide reveal that neither light absorption nor kinetic overpotential losses can explain the poor performance of the MIS photoelectrodes.

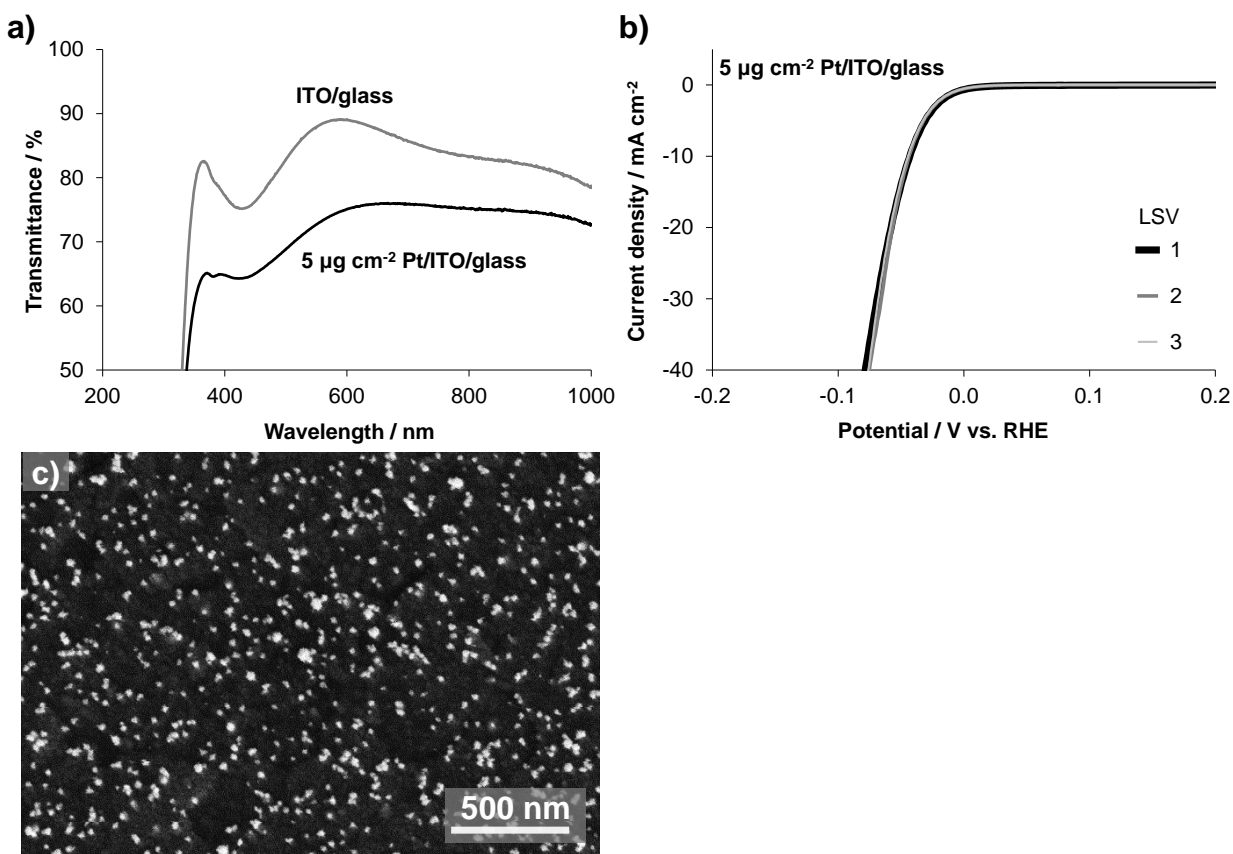


Figure 3.15. Light transmittance and catalytic activity of electrodeposited Pt particles. a) UV-Vis on Pt|transparent indium tin oxide (ITO) and b) LSV measurements in 0.5 mol L<sup>-1</sup> H<sub>2</sub>SO<sub>4</sub> for 5 μg cm<sup>-2</sup> Pt|ITO|glass sample. LSV scan rate was 20 mV s<sup>-1</sup>. c) SEM image of Pt|ITO|glass.

#### 3.4.1.2 Charge Carrier Transport

Differences in carrier collection efficiency between the MIS and IMIS samples can be ruled out because the effective minority carrier diffusion length of both samples was found to be nearly identical ( $L_e \approx 103 \mu\text{m}$ , see analysis in Appendix section 3.6.4, Figure 3.24). This distance is far

greater than the average distance between adjacent particles ( $<1 \mu\text{m}$ ), meaning that the carrier collection efficiency in both samples should be similar.

### 3.4.1.3 *Electron Tunneling*

At first glance, one would not expect that tunneling of carriers through the native  $\text{SiO}_2$  layer would be a major source of inefficiency in the MIS photoelectrodes because the tunneling probability through an  $\text{SiO}_2$  layer of thickness  $\approx 1.5 \text{ nm}$  is very high<sup>58,63</sup> and many MIS photovoltaic (PV) cells have been reported with excellent fill factors.<sup>64–68</sup> However, the key distinction between the aforementioned studies and the MIS photoelectrodes investigated in this work is the mismatch between the illuminated area and the MIS junction area. In most MIS PV cells and photoelectrodes demonstrated to date, the MIS junction area ( $A_j$ ) is similar or equal to the illuminated area ( $A_{\text{hv}}$ ), meaning that the photogenerated current density that is normalized by the junction area ( $I_j = I/A_j$ ) is very similar to the photogenerated current density that is normalized by the illumination area ( $I_L = I/A_{\text{hv}}$ ). Under AM 1.5 illumination, these current densities are typically  $25 \text{ mA cm}^{-2}$  to  $40 \text{ mA cm}^{-2}$  for c-Si. However, the photoelectrodes investigated in this work have a relatively small coverage of Pt particles, meaning that the net junction area is significantly smaller than the illuminated area ( $A_j \ll A_{\text{hv}}$ ). The consequence of this inequality is that  $I_j$  can substantially deviate from  $I_{\text{hv}}$ , as described by Equation 3.1:

$$I_j = \frac{I_L \cdot A_{\text{hv}}}{A_j} \quad (3.1)$$

In this work, the upper limit of  $A_j$  can be estimated as the net area covered by Pt particles, which was determined from the projected 2D area of Pt particles in SEM images.

#### 3.4.1.3.1 *High Tunneling Current Density*

To understand if these MIS photoelectrodes are limited by electron tunneling, the LSVs for MIS samples with different Pt loadings were normalized by the junction areas, as estimated from

the SEM-determined particle coverage (Figure 3.16). When the current is normalized by the junction area, we refer to this as the “tunneling current density”. The samples with 1 and 5  $\mu\text{g Pt cm}^{-2}$ , corresponding to Pt coverages of 3 % and 15 % respectively, demonstrate the highest tunneling current density because the junction area is much less than the illuminated area. Taking as an example the 1  $\mu\text{g cm}^{-2}$  Pt MIS sample with  $\theta_{\text{Pt}}=0.03$  and  $I_L \approx 21 \text{ mA cm}^{-2}$  illuminated area, the sample-averaged limiting current density through the MIS nanojunctions is -700 mA per  $\text{cm}^2$  of junction area (Figure 3.16). This current density is likely to be even larger when one considers that the physical contact area between the electrodeposited Pt particles and  $\text{SiO}_2$  substrate (Figure 3.8) is smaller than the projected 2D particle area indicated by SEM images (Figure 3.5). The small junction areas in the samples with low Pt loadings leads to very high local tunneling current densities and associated voltage penalties.

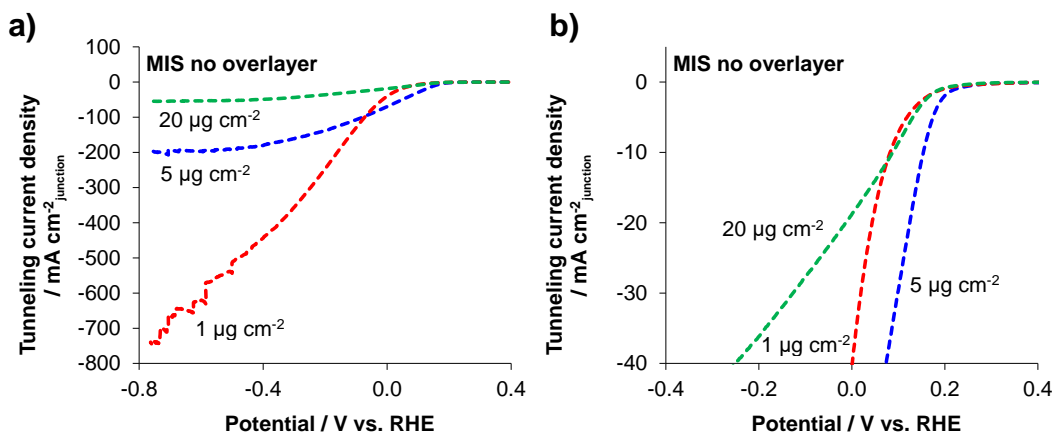


Figure 3.16. Current densities normalized to net particle area. a) LSV measurements from Figure 3.10a for MIS Pt|native  $\text{SiO}_2$ |p-Si(100) for various amounts of Pt loading normalized by illuminated and junction area and b) a zoomed in plot.

#### 3.4.1.3.2 Voltage Penalty

At such high local current densities, voltage losses due to tunneling will be significant, even for tunneling through a very thin 1.5 nm thick  $\text{SiO}_2$  insulator (Figure 3.17a).<sup>26</sup> In order to

experimentally determine the voltage penalty associated with high tunneling current densities, I-V measurements were conducted in air on a 45  $\mu\text{m}$  diameter circular metallic (20 nm Pt|30 nm Ti) contact on 2 nm RTO  $\text{SiO}_2$ |p-Si (Figure 3.17b) for varying light intensities. The IV plot is shown in Figure 3.17a, where the current density of all samples has been normalized to that of the photo-limited current density. For increasing light intensities, the fill factor decreases significantly, demonstrating that significant voltage penalties are incurred at high tunneling current densities. Although this e-beam deposited Pt|Ti|RTO  $\text{SiO}_2$ |p-Si sample is not truly representative of the electrodeposited Pt|native  $\text{SiO}_2$ |p-Si MIS electrodes investigated in this chapter, the similar MIS architecture and well-defined junction area associated with the circular metal contacts are valuable to directly view the adverse effect that high current densities have on IV curve characteristics.

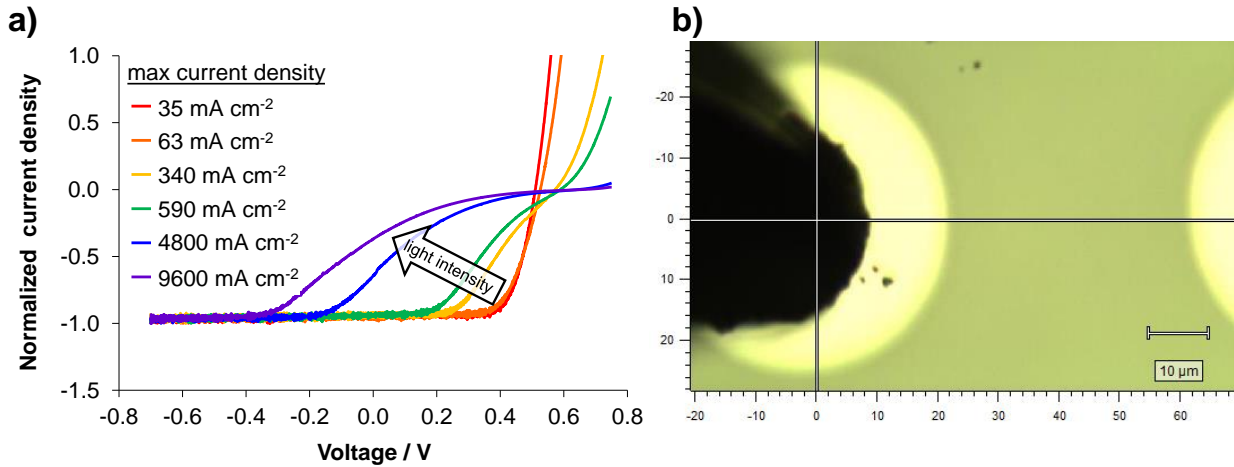


Figure 3.17. Voltage penalty at large tunneling current densities. a) Normalized I-V measurements in air for a 45  $\mu\text{m}$  diameter 20 nm Pt|30 nm Ti circular contact, that was e-beam deposited onto 2 nm RTO  $\text{SiO}_2$ |p-Si, under varying intensities of 532 nm laser illumination. The listed current densities are normalized to the junction area, taken to be the area of the e-beam deposited metal contact. b) Optical image of a tungsten probe in contact with a metal contact. I-V curves were measured at a scan rate of 100  $\text{mV s}^{-1}$ .

### 3.4.2 Hypothesis for Observed Improvement in Performance

For the reasons highlighted above, we conclude that the poor I-E performance of the MIS photoelectrodes is explained by large voltage drops needed to support high local current density across the MIS nanojunctions. It follows that the presence of the  $\text{SiO}_x$  overlayer substantially decreases or eliminates these tunneling-related voltage drops in the IMIS samples, but how? One possibility is that the  $\text{SiO}_x$  overlayer is moderately conductive, providing additional pathways through which minority carriers can reach the Pt nanoparticles (Figure 3.18). This has the effect of increasing the effective MIS junction area, thereby reducing the local tunneling current densities directly underneath the Pt particles. In addition to the conventional charge transfer pathway (Figure 3.18, path 1), we hypothesize that the  $\text{SiO}_x$  overlayer enables carriers to reach a given Pt particle by tunneling from the p-Si to the  $\text{SiO}_x$  (Figure 3.18, path 2), and possibly by lateral transport along  $\text{SiO}_x$  between neighboring Pt particles (Figure 3.18, path 3). In this latter case, the  $\text{SiO}_x$  overlayer can serve to distribute electrons between particles, especially those not in intimate electrical contact with the substrate.

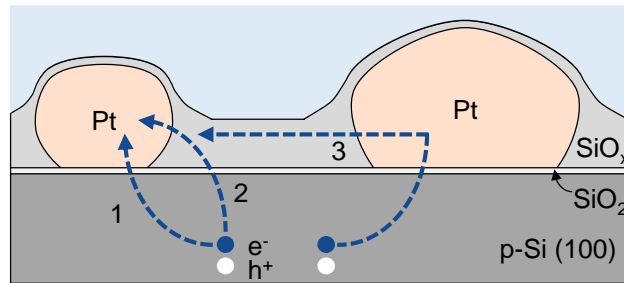


Figure 3.18. Alternative carrier transport pathways. Schematic side-view of IMIS photoelectrode illustrating possible charge transfer pathways between the Si substrate and Pt nanoparticles. Pathways include (1) conventional tunneling through MIS nano-junction and (2),(3) alternative charge transfer routes involving conduction through the  $\text{SiO}_x$ .

### 3.4.2.1 Additional Carrier Transport Pathways

The viability of the proposed alternative electron transport pathways is contingent upon the electronic conductivity of the  $\text{SiO}_x$  overlayer material. Pure  $\text{SiO}_2$  is an excellent insulator,<sup>69</sup> but defects, impurities, or slight variation in stoichiometry may change this. In this study, it is likely that traces of carbonaceous impurities remaining in the spin-coated  $\text{SiO}_x$  overlayers provide some degree of electrical conductivity. Indeed, XPS analysis of control samples with spin-coated  $\text{SiO}_x$  contain 30% higher C 1s signal compared to samples containing native  $\text{SiO}_2$  where the carbon only arises from adventitious carbon species. Furthermore, it is likely that the highest amount of unconverted carbon will remain in the  $\text{SiO}_x$  layer immediately surrounding the Pt particles due to shadowing during the UV ozone process, thus providing the highest conductivity at the MIS nanojunction where it is most needed. Another source of conductivity in the  $\text{SiO}_x$  layer could be protons or hydrogen atoms taken up from the acidic electrolyte. Previous studies have proposed that protons in silicon dioxide may be reduced to hydrogen atoms, which then serve as electron mediators for electrochemical reduction as demonstrated with 6 nm thick thermally-grown  $\text{SiO}_2$ .<sup>70</sup> Furthermore, the presence of Si-H bonds within  $\text{SiO}_2$  have been found to increase tunneling current through chemical  $\text{SiO}_2$ ,<sup>71</sup> which could also facilitate charge transfer in this study.

The conductivity of the  $\text{SiO}_x$  overlayer was investigated with cyclic voltammetry (CV) to measure charge transfer rates across continuous  $\text{SiO}_x$  films of varying thickness using a standard ferri/ferrocyanide redox couple, as previously used to evaluate the conductivity of ALD  $\text{TiO}_2$  layers in MIS photoanodes.<sup>18,57</sup> These measurements were conducted on a series of samples on which a bilayer film of 1 nm of Ti and 3 nm of Pt were sequentially deposited by physical vapor deposition onto 'x' nm  $\text{SiO}_x$ |native  $\text{SiO}_2$ |p-Si electrodes ( $0 \text{ nm} < x < 10 \text{ nm}$ ), as depicted in the inset of Figure 3.19a.

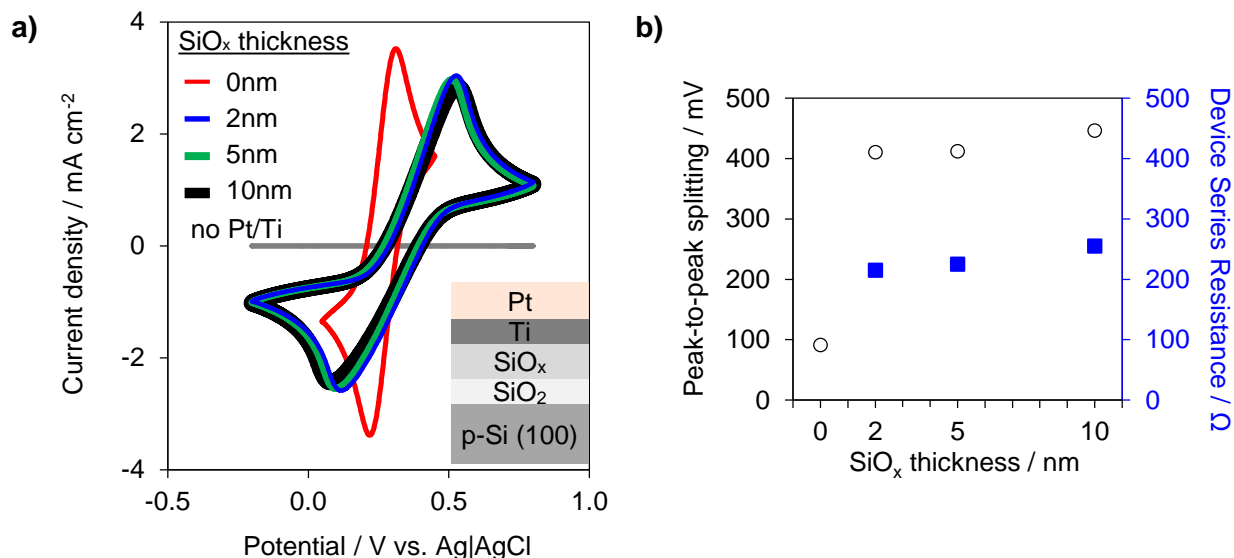


Figure 3.19. Analyzing carrier transport pathways. a.) CV measurements in 10 mmol  $\text{L}^{-1}$  ferri/ferrocyanide, 1 mole  $\text{L}^{-1}$  KCl solution for 3 nm Pt|2 nm Ti|‘x’ nm  $\text{SiO}_x$ |native  $\text{SiO}_2$ |p-Si(100) for various  $\text{SiO}_x$  thicknesses from 0 nm to 10 nm. The CV sweep rate was 100  $\text{mV s}^{-1}$ . b.) Peak-to-peak splitting voltage (circles) and corresponding charge transfer resistances (squares) associated with the CV curves in a.).

The electron transfer kinetics of ferri/ferrocyanide at the surface of the Pt top layer are very fast such that the largest source of resistance is associated with charge transfer across the  $\text{SiO}_2$ | $\text{SiO}_x$  stack. A control sample lacking the catalytic Pt layer exhibits orders of magnitude lower current density and no observable  $\text{Fe}^{2+}/\text{Fe}^{3+}$  redox features. As seen in Figure 3.19, the CV for the control sample with 0 nm of  $\text{SiO}_x$  demonstrated relatively small peak-to-peak splitting (< 100 mV). However, the addition of 2 nm of  $\text{SiO}_x$  resulted in an increase in the peak-to-peak splitting to 410 mV, indicating a significant increase in charge transfer resistance across the stack. Interestingly, increasing the  $\text{SiO}_x$  thickness beyond 2 nm did not lead to a significant increase in peak-to-peak splitting.

The lack of sensitivity of the charge transfer resistance on the  $\text{SiO}_x$  thickness (see description of CV modeling in Appendix section 3.6.6) suggests that the  $\text{SiO}_x$  does not behave like

a typical tunneling oxide, for which increasing oxide thickness should lead to an exponential decay in tunneling current and exponential increase in peak-to-peak splitting.<sup>18,19,57</sup> Instead, the nearly constant peak-to-peak splitting for all three SiO<sub>x</sub> layer thicknesses indicates the SiO<sub>x</sub> layer is moderately conductive, and that the effective charge transfer resistance associated with conduction across the SiO<sub>x</sub> is very small compared to that associated with tunneling between the p-Si substrate and SiO<sub>x</sub> overlayer (Figure 3.19b and Figure 3.26). Thus, the measurements in Figure 3.19 support the hypothesis that the spin-coated SiO<sub>x</sub> layer enables additional charge transfer pathways between the Si substrate and Pt nanoparticles, thereby reducing the voltage drops needed for tunneling across the MIS nanojunctions at high current densities. It should be noted that the initial increase in charge transfer resistance upon deposition of the first 2 nm of SiO<sub>x</sub> can be explained by a decrease in the tunneling probability across the native SiO<sub>2</sub> layer due to a decrease in density of states of SiO<sub>x</sub> compared to the metallic Pt|Ti layer.

### ***3.4.3 Understanding Origins of Instability during PEC Operation***

The source of poor stability for the uncoated MIS photoelectrodes is less clear, with possible explanations including catalyst poisoning, particle detachment, and reduced quality of the electrical contact. Control samples based on Pt particles electrodeposited on ITO|glass substrates reveal no loss in catalytic activity during HER experiments (Figure 3.15b). The stable performance observed in these LSV curves proves that the uncoated Pt particles can be stable under the conditions tested, and that the unstable behavior exhibited by the MIS samples cannot be attributed to poisoning by solution contaminants.

#### ***3.4.3.1 Pt Nanoparticle Adhesion***

The possible role of the SiO<sub>x</sub> layer to serve as a “glue” to physically adhere the nanoparticles to the substrate during operation was evaluated by taking SEM images of identical



locations on a MIS photoelectrode before and after three consecutive LSVs. Despite significant decrease in performance of the MIS photoelectrode during these measurements, these images reveal no substantial particle detachment or agglomeration over this short time period (Figure 3.20). However, due to the limited resolution of the SEM, the movement of sub-10 nm Pt particles, which are expected to be most mobile,<sup>72</sup> cannot be ruled out.

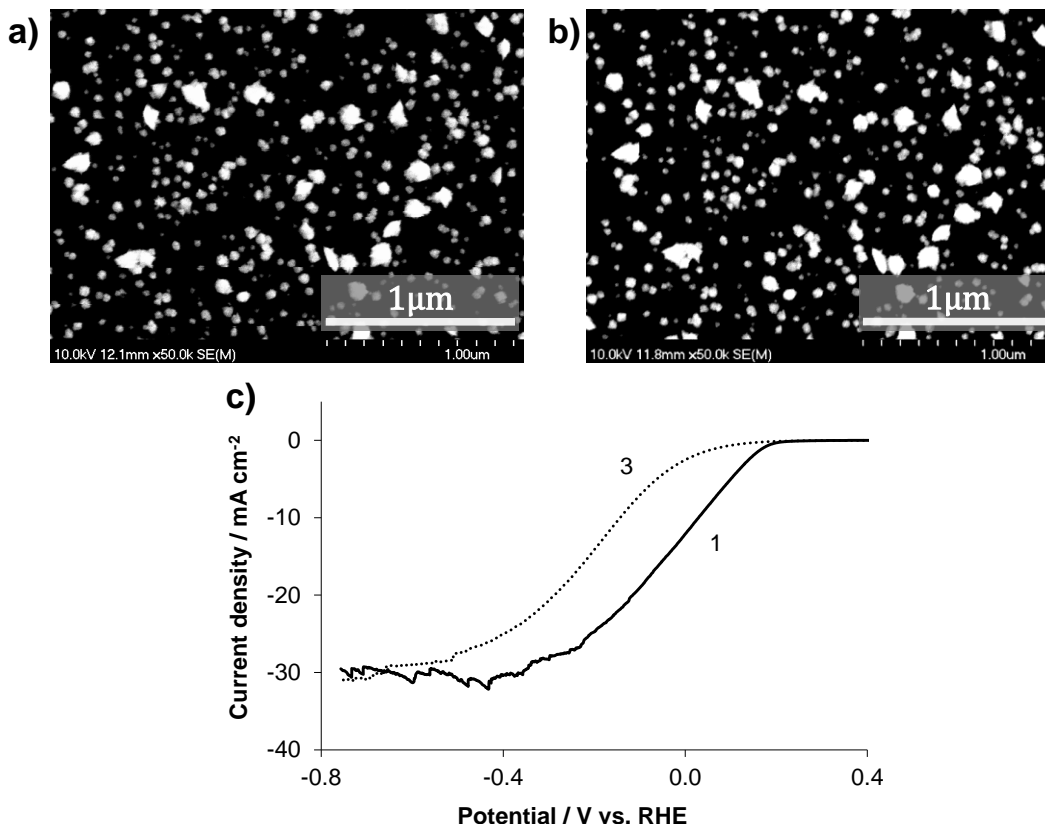


Figure 3.20. SEM images of MIS photoelectrode before and after PEC LSVs. SEM images of a  $5 \mu\text{g cm}^{-2}$  Pt|native  $\text{SiO}_2$ |p-Si(100) a) before and b) after 3 LSVs in  $0.5 \text{ mol L}^{-1} \text{ H}_2\text{SO}_4$ . c) First (solid) and third (dashed) LSV measurements in  $0.5 \text{ mol L}^{-1} \text{ H}_2\text{SO}_4$  under 1 sun of AM 1.5G illumination for  $5 \mu\text{g cm}^{-2}$  Pt|native  $\text{SiO}_2$ |p-Si(100).

In contrast, SEM images taken after the longer 12 hour CP stability test (Figure 3.21) suggest that particle adhesion does become an issue over longer time periods. These SEM images reveal a highly non-uniform Pt distribution on the surface of the MIS photoelectrode and a uniform

Pt distribution on the IMIS photoelectrode, suggesting Pt particle migration and/or detachment from the MIS surface. Large circular features ( $\approx 200\text{ }\mu\text{m}$  to  $2,000\text{ }\mu\text{m}$  diameter) are also evident on the MIS photoelectrode surface, which may correspond with the location of  $\text{H}_2$  bubbles that remained attached to the photoelectrode surface for prolonged times.

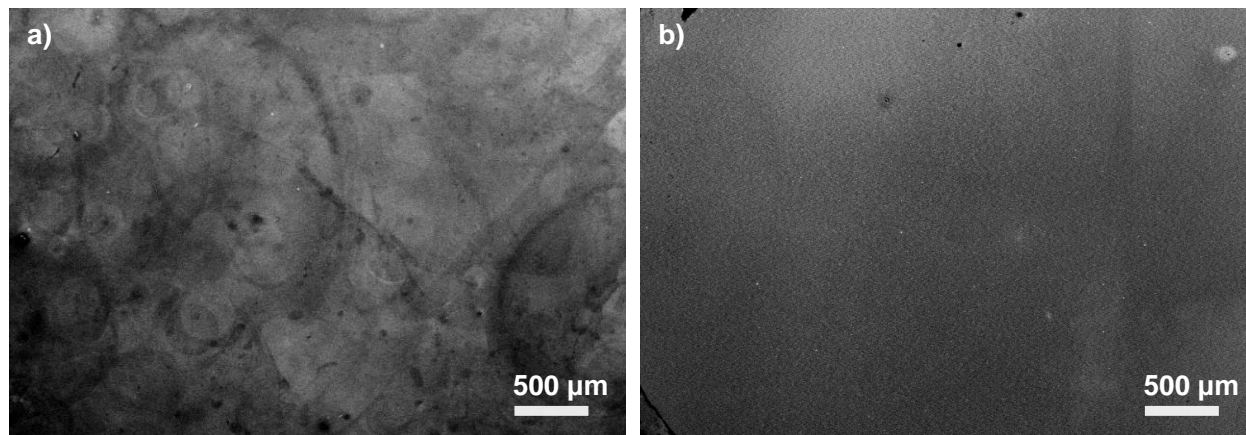


Figure 3.21. Low resolution SEM images of c.) MIS and d.) IMIS samples after the 12 hr CP stability test in Figure 3.14.

It is possible that  $\text{H}_2$  bubbles on MIS electrodes reduce the ECSA, forcing higher local current densities through accessible Pt nanoparticles near the bubble edges and thereby accelerating local degradation. In the case for IMIS electrodes, small  $\text{H}_2$  bubbles are also present on the surface, but the hydrophilic  $\text{SiO}_x$  overlayer facilitates bubble detachment at smaller diameters and reduces its average residence time on the photoelectrode surface. This facile bubble removal is evident in the IMIS chronopotentiometry stability tests, where the stochastic fluctuations associated with bubble dynamics are very small in comparison to those observed for the MIS electrode (Figure 3.13a and 3.14). This observation suggests a detrimental role of surface-bound  $\text{H}_2$  bubbles on the durability of the uncoated Pt nanoparticles.

### 3.4.3.2 Degradation Dependence on Operating Current Density

Another possible cause of instability is degradation of the  $\text{SiO}_2$  and/or the  $\text{SiO}_2/\text{Si}$  interface at MIS junctions resulting from heat dissipation under conditions of high local tunneling current densities that are present in samples with low and medium Pt loadings, and MIS electrodes masked with  $\text{H}_2$  bubbles. Typically, such thermal degradation of MIS junctions is observed in solid-state devices that undergo oxide breakdown and dielectric breakdown-induced epitaxy (DBIE) of the Si substrate<sup>73–75</sup> under application of a large reverse bias<sup>76</sup> or current surge.<sup>77</sup> It is possible that the large photo-driven current densities present in our samples could lead to similar phase change effects or particle detachment due to heat dissipation associated with the tunneling across the  $\text{SiO}_2$  insulating layer.

Regardless of the exact mechanism by which MIS sample performance degraded, it was consistently observed that the extent of performance degradation was proportional to the current density through the MIS nanojunctions. This was already noted in Table 3.1, which shows that performance degradation decreased with increasing Pt particle loading. In order to investigate this relationship further, MIS electrodes with 11 % and 30 % Pt coverages (Table 3.A.4) were tested in  $0.5 \text{ mol L}^{-1} \text{ H}_2\text{SO}_4$  under 0.25 and 1 sun intensities to systematically vary the current densities through the junctions (Figure 3.22). At 0.25 sun intensity, corresponding to low current density through the junction, both electrodes remained reasonably stable during the 5 CV cycles. However, upon operation under 1 sun illumination, corresponding to higher current density, the performance degraded after just 1 cycle. Importantly, the performance degradation was far greater for the MIS sample with low Pt loading and at high light intensity. The observations of poor stability for higher light intensity and/or lower loading thus indicate that degradation is greatest when the current density through the nanojunctions is highest. In IMIS electrodes, the  $\text{SiO}_x$  overlayer may alleviate

this issue by decreasing local current densities through the MIS nanojunctions. Our observations are consistent with both thermally-induced degradation, as well as H- or H<sub>2</sub> induced damage, which are expected to be more prominent at higher current densities.

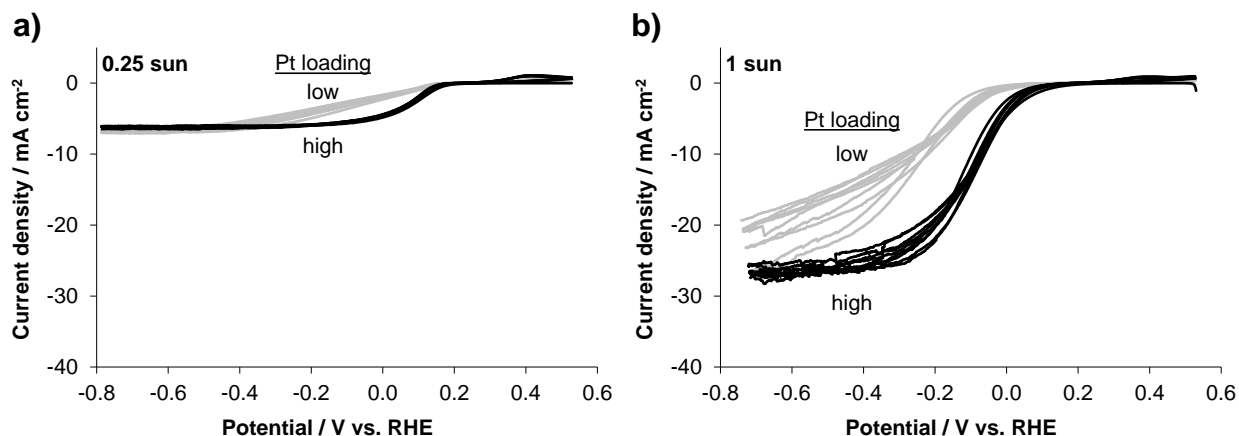


Figure 3.22. Effect of light intensity and tunneling current density on MIS stability. CV measurements in 0.5 mol L<sup>-1</sup> H<sub>2</sub>SO<sub>4</sub> for low and high Pt loaded MIS samples under a) 0.25 sun and b) 1 sun intensity. CV scan rate was 20 mV s<sup>-1</sup> for 5 cycles. Grey curves: low Pt loading. Black curves: high Pt loading.

### 3.5 Conclusions

In summary, this chapter has described a room-temperature and scalable means of stabilizing electrodeposited Pt nanoparticle catalysts on an insulating substrate for MIS photoelectrodes for solar water splitting. Systematic investigation of the influence of particle loading, SiO<sub>x</sub> layer thickness, and illumination intensity suggests that the SiO<sub>x</sub> layer possesses moderate conductivity, thereby reducing charge transfer resistance associated with high local tunneling current densities between the p-Si and Pt nanoparticles. The enhanced performance with the SiO<sub>x</sub> overlayer modification indicates improved carrier transport between the native SiO<sub>2</sub>/p-Si substrate and the electrodeposited Pt nanoparticles. Additionally, the IMIS photoelectrodes exhibit excellent stability, while the unmodified MIS photoelectrodes undergo gradual performance degradation related to the presence of H<sub>2</sub> bubbles on the photoelectrode surface. We hypothesize

that the improved current-potential performance of the IMIS samples results from a decrease in tunneling losses across the MIS nanojunctions, which is made possible by an increase in the effective junction area between the substrate and Pt particles. Based on this proposed mechanism, we expect that the IMIS approach will be broadly applicable to improving the efficiency and stability of MIS photoelectrodes based on low-loadings of nanoparticle catalysts.

### 3.6 Appendix

#### 3.6.1 Summary of Particle Characterization for Electrodes in Figures 3.10, 3.12, and 3.13

Table 3.2. Summary of Pt structure characterization from SEM image analysis based on SEM images taken at a magnification of x50.0k times.

	SiO <sub>x</sub> thickness (nm)	Particle coverage (%)	Particle density (particle $\mu\text{m}^{-2}$ )	Average Pt NP diameter (nm)	Average distance between particles (nm)	Surface area (cm <sup>2</sup> Pt/ geometric area cm <sup>2</sup> )	Pt loading ( $\mu\text{g cm}^{-2}$ )
MIS	0	$3.3 \pm 0.8$	$17 \pm 3$	$38 \pm 32$	$180 \pm 20$	$0.14 \pm 0.03$	$1.0 \pm 0.3$
MIS	0	$15 \pm 3.1$	$42 \pm 8$	$55 \pm 36$	$86 \pm 16$	$0.63 \pm 0.14$	$5.1 \pm 1.4$
MIS	0	$42 \pm 1.2$	$74 \pm 3$	$66 \pm 54$	$30 \pm 1$	$1.82 \pm 0.05$	$22 \pm 0.8$
IMIS	2	$3.9 \pm 0.6$	$22 \pm 2$	$37 \pm 30$	$155 \pm 13$	$0.17 \pm 0.02$	$1.1 \pm 0.2$
IMIS	2	$13 \pm 0.9$	$35 \pm 3$	$58 \pm 34$	$95 \pm 6$	$0.54 \pm 0.04$	$3.9 \pm 0.2$
IMIS	2	$32 \pm 1.6$	$52 \pm 7$	$70 \pm 53$	$49 \pm 4$	$1.36 \pm 0.07$	$18 \pm 3.6$
IMIS	5	$13 \pm 0.2$	$28 \pm 3$	$65 \pm 42$	$102 \pm 4$	$0.58 \pm 0.01$	$5.0 \pm 0.2$
IMIS	10	$14 \pm 1.1$	$41 \pm 5$	$53 \pm 38$	$86 \pm 7$	$0.59 \pm 0.05$	$4.4 \pm 0.5$

### 3.6.2 XPS Characterization of Pristine MIS, IMIS, and IIS Samples

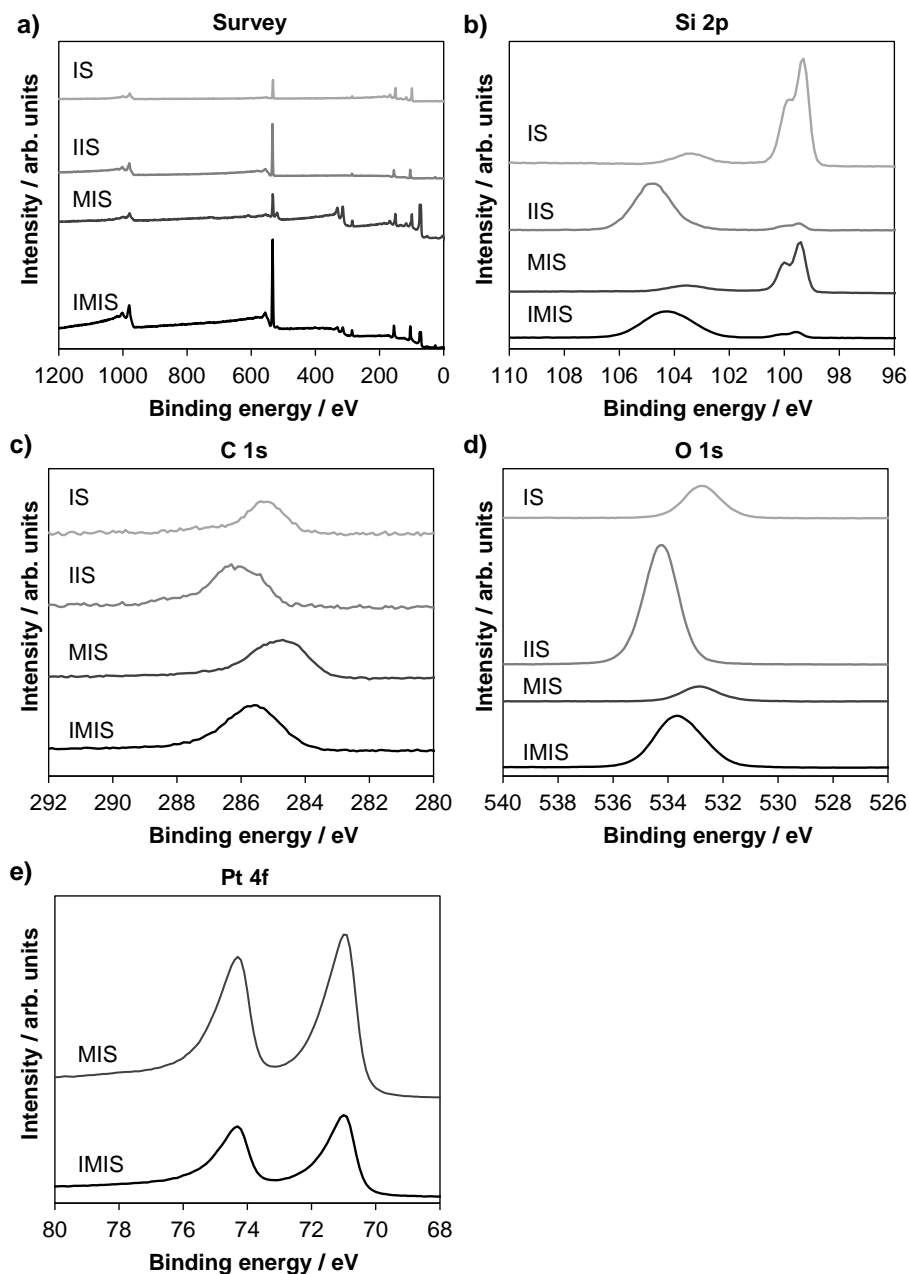


Figure 3.23. XPS results. X-ray photoelectron spectra of 10 nm  $\text{SiO}_x$ /native  $\text{SiO}_2$ /p-Si(100) a) Survey, b) Si 2p, c) C 1s, d) O 1s, and e) Pt 4f. The PDMS was converted into  $\text{SiO}_2$  with trace amounts of carbon remaining. The  $\text{SiO}_x$ /SiO<sub>2</sub>/Si (IIS) contained 50% higher C 1s signal compared to samples containing native  $\text{SiO}_2$  (IS) where the carbon only arises from adventitious carbon compounds.

Table 3.3. Surface composition of samples with and without the SiO<sub>x</sub> overlayer determined by XPS measurements. The SiO<sub>x</sub> thickness of IIS and IMIS samples is 10 nm. The Pt loading for MIS and IMIS samples is 5 µg cm<sup>-2</sup>. All compositions are expressed as atomic percentages as described in the text

	sample	% metallic Si	% Si in SiO <sub>2</sub>	% C	% O	% Pt	O:Si (in SiO <sub>2</sub> ) ratio
IS	SiO <sub>2</sub>  Si	48	7	9	36	0	5.0
IIS	SiO <sub>x</sub>  SiO <sub>2</sub>  Si	2	25	7	66	0	2.6
MIS	Pt SiO <sub>2</sub>  Si	33	9	22	27	9	3.0
IMIS	SiO <sub>x</sub>  Pt SiO <sub>2</sub>  Si	2	26	15	55	2	2.1

### 3.6.3 Summary of Particle Characterization for Electrodes in Figure 3.14

Table 3.4. Summary of Pt structure characterization from SEM image analysis for samples in Figure 3.14.

	SiO <sub>x</sub> thickness (nm)	Particle coverage (%)	Particle density (particle µm <sup>-2</sup> )	Average Pt nanoparticle diameter (nm)	Average distance between particles (nm)	Surface area (cm <sup>2</sup> Pt/geometric area cm <sup>2</sup> )	Pt loading (µg cm <sup>-2</sup> )
MIS	0	31 ± 1.4	71 ± 7	61 ± 43	41 ± 3	1.37 ± 0.05	12 ± 0.9
IMIS	10	29 ± 1.1	82 ± 7	47 ± 47	44 ± 2	1.15 ± 0.06	12 ± 1.5

### 3.6.4 Effective Carrier Diffusion Length

The effective minority carrier diffusion length ( $L_e$ ) was measured to understand differences in carrier collection efficiency between the MIS and IMIS electrodes.  $L_e$  is strongly dependent on both the bulk diffusion length of the semiconductor and the surface recombination velocities associated with interfaces in the devices.<sup>54</sup> In this study, the bulk diffusion lengths of the p-Si(100) substrates are expected to be the identical for all samples, but the surface recombination velocity can be very different based on the nature of the SiO<sub>2</sub>|p-Si(100) interface. No influence of the SiO<sub>x</sub>|native SiO<sub>2</sub>|p-Si interfaces is evident in Figure 3.24, where a plot of  $\ln(J_N)$  versus  $D_L$  for a 3 nm Pt|2 nm Ti|native SiO<sub>2</sub>|p-Si MIS sample is very similar from that of an IMIS sample containing

an additional 10 nm SiO<sub>x</sub> overlayer. From the slopes of these  $\ln(J_N)$  versus  $D_L$  plots, the average values of  $L_e$  were  $103 \mu\text{m} \pm 19 \mu\text{m}$  for the MIS sample and  $103 \mu\text{m} \pm 19 \mu\text{m}$  for the IMIS sample.

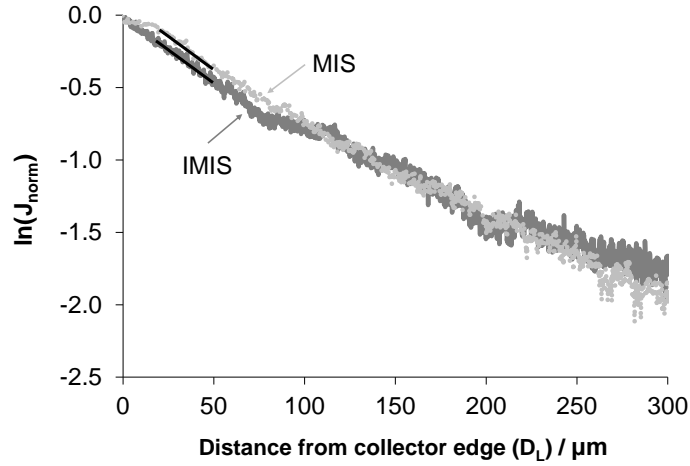


Figure 3.24.  $L_e$  measurements on MIS and 10 nm IMIS. a) Side-view schematic of SPCM measurement set-up used for determining the effective diffusion length in MIS and IMIS control samples in which the metal component, or collector, consisted of e-beam deposited  $500 \mu\text{m}$  bilayer islands with 3 nm Pt on top of 2 nm of Ti. b) Plots of  $\ln(J_N)$  versus  $D_L$ , measured with a 532 nm laser focused to a beam diameter of  $\approx 3 \mu\text{m}$  and with incident power of  $13.3 \mu\text{W}$ .

### 3.6.5 Summary of Particle Characterization for Electrodes in Figure 3.23

Table 3.5. Summary of Pt structure characterization from SEM image analysis for samples in Figure 3.23.

MIS Pt loading	Light intensity test (sun)	Particle coverage (%)	Particle density (particle $\mu\text{m}^{-2}$ )	Average Pt nanoparticle diameter (nm)	Average distance between particles (nm)	Surface area ( $\text{cm}^2$ Pt/geometric area $\text{cm}^2$ )	Pt loading ( $\mu\text{g cm}^{-2}$ )
Low	0.25	$10 \pm 1.1$	$77 \pm 17$	$27 \pm 23$	$79 \pm 10$	$0.32 \pm 0.06$	$2.1 \pm 0.4$
Low	1	$13 \pm 0.6$	$102 \pm 6$	$25 \pm 26$	$60 \pm 3$	$0.46 \pm 0.06$	$3.4 \pm 0.7$
High	0.25	$29 \pm 1.4$	$74 \pm 3$	$38 \pm 39$	$42 \pm 1$	$1.05 \pm 0.06$	$14 \pm 2$
High	1	$31 \pm 1.5$	$22 \pm 2$	$45 \pm 39$	$40 \pm 1$	$1.19 \pm 0.07$	$13 \pm 0.7$



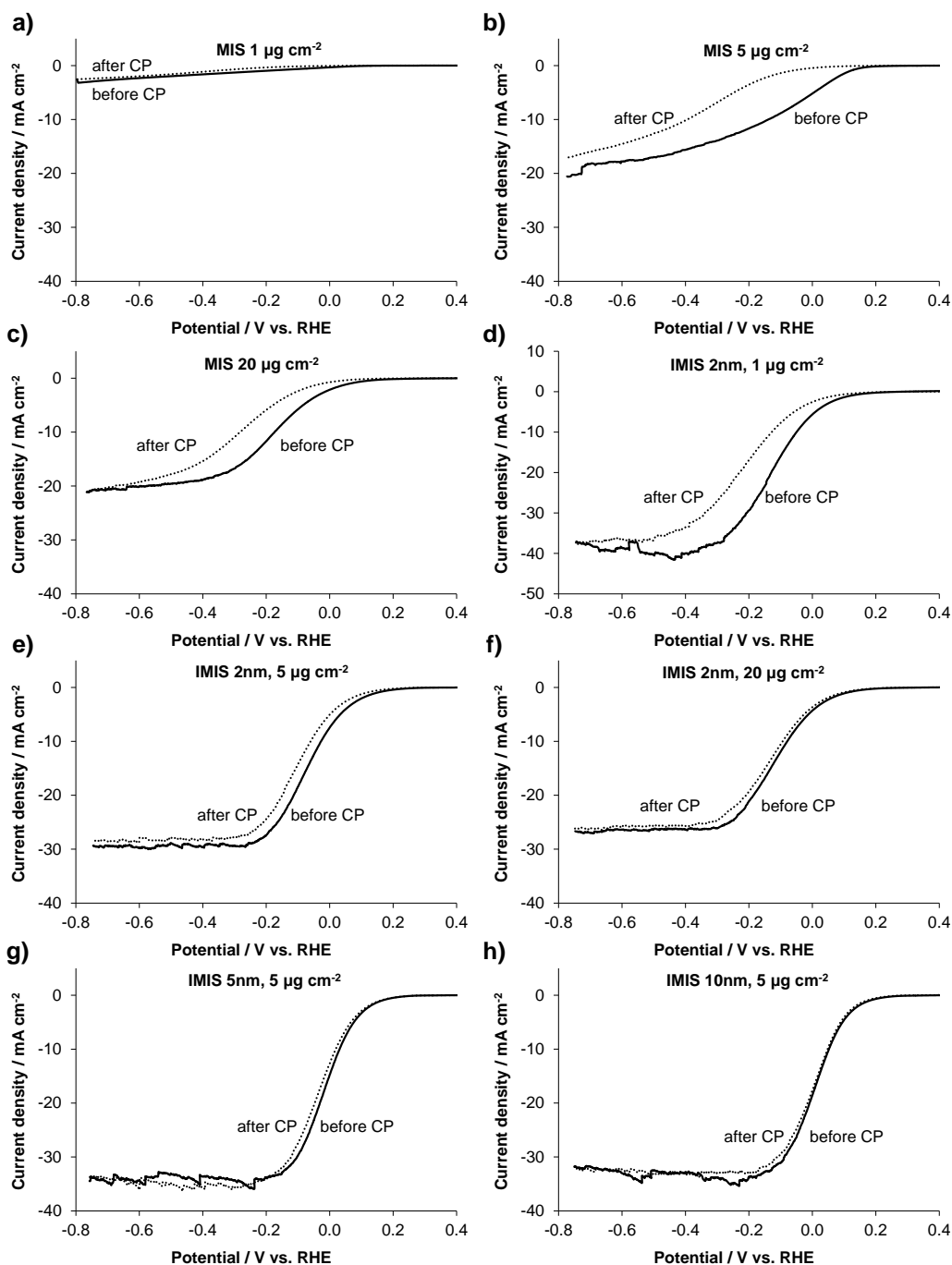


Figure 3.25. LSV before and after stability test. LSV measurements in 0.5 mol L<sup>-1</sup> H<sub>2</sub>SO<sub>4</sub> under 1 sun of AM 1.5G illumination for 'x' nm SiO<sub>x</sub>|'y'  $\mu\text{g cm}^{-2}$  Pt|native SiO<sub>2</sub>|p-Si(100) for various amounts of Pt loading from 1 to 20  $\mu\text{g cm}^{-2}$  and various SiO<sub>x</sub> thicknesses from 0 to 10 nm. a-c) 1, 5, and 20  $\mu\text{g cm}^{-2}$  Pt with 0 nm SiO<sub>x</sub>, d-f) with 2 nm SiO<sub>x</sub>, and g-h) 5  $\mu\text{g cm}^{-2}$  Pt with 5 and 10 nm SiO<sub>x</sub>. The LSV scan rate was 20 mV s<sup>-1</sup>.

### 3.6.6 Cyclic Voltammetry Modelling for Device Series Resistance

The experimental CVs obtained in ferri/ferrocyanide were fit to a standard CV model using EC-lab software V10.40 (Bio-logic). The high-frequency impedance determined series resistance, 11.5  $\Omega$ , determined by electrochemical impedance spectroscopy (EIS) for the control sample lacking an  $\text{SiO}_x$  layer was first used to perform an iR correction on the CV data for all the samples (note: iR correction was only performed for this analysis; the CV shown in Figure 3.19 of the main article contain the raw CV data). The CV for the control sample was first fit assuming no additional uncompensated series resistance, a surface area of 0.246  $\text{cm}^2$ , reductant and oxidant concentrations of 10  $\text{mmol L}^{-1}$ , a scan rate of 100  $\text{mV s}^{-1}$ , room temperature, and the charge transfer coefficient  $\alpha = 0.50$ . The best fit was obtained with  $E_0 \approx 0.27$  vs. Ag/AgCl/sat. KCl electrode,  $k_0 = 0.24 \text{ cm s}^{-1}$ ,<sup>55</sup>  $D_O = 7.1 \times 10^{-6} \text{ cm}^2 \text{ s}^{-1}$ ,  $D_R = 6.1 \times 10^{-6} \text{ cm}^2 \text{ s}^{-1}$ . The values of the diffusion coefficients are similar to those reported by Konopka and McDuffie, who studied millimolar concentrations of ferri/ferrocyanide in 1.0  $\text{mol L}^{-1}$  KCl on platinum and found  $D_O = 7.3 \times 10^{-6} \text{ cm}^2 \text{ s}^{-1}$  and  $D_R = 6.7 \times 10^{-6} \text{ cm}^2 \text{ s}^{-1}$ .<sup>56</sup> The iR-corrected CVs of all  $\text{SiO}_x$ -containing photocathodes were then fit using the parameters obtained from the fit of the CV for the sample lacking the  $\text{SiO}_x$  layer, only varying the uncompensated series resistance, taken here to be the “device resistance” reported in Figure 3.19b. The best fit for the 2 nm, 5 nm, and 10 nm  $\text{SiO}_x$ -containing samples was achieved with device resistance values of 215  $\Omega$ , 225  $\Omega$  and 255  $\Omega$ , respectively. This fitting procedure is adapted from Scheuermann.<sup>19,57</sup> The simulated CV fit and experimental CV of an electrode containing no  $\text{SiO}_x$  overlayer material and an electrode with 2 nm  $\text{SiO}_x$  are shown in Figure 3.26 a and b respectively.

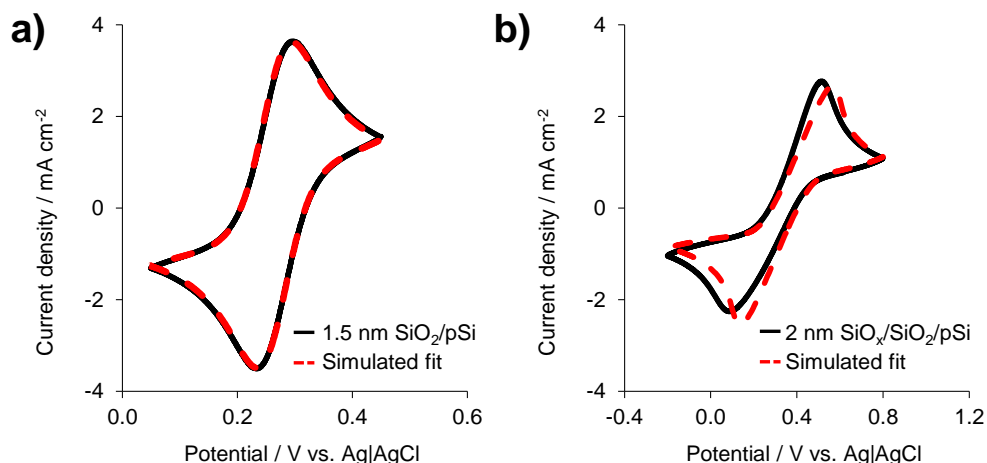


Figure 3.26. Simulated cyclic voltammograms for total series resistance. CV of a) 3 nm Pt|2 nm Ti|1.5 nm SiO<sub>2</sub>|p-Si and b) 3 nm Pt|2 nm Ti|2 nm SiO<sub>x</sub>|1.5 nm SiO<sub>2</sub>|p-Si in ferri/ferrocyanide solution compared to a simulated fit using EC-lab software. CV scan rate was 100 mV s<sup>-1</sup>.

### 3.7 Acknowledgements

I would like to acknowledge Xinxin Li and Yukun Liu for their help preparing electrodes and performing control experiments, Haiyan Tan for performing STEM and analysis, Rongyue Wang for providing cross-sectional SEM images, Jeffery T. Koberstein for insightful conversations and guidance on fabricating the SiO<sub>x</sub> films, and Thomas P. Moffat and Chathuranga De Silva for assistance with XPS measurements and analysis. Dr. Esposito and I acknowledge Columbia University (start-up funds) and the National Science Foundation (NSF) Center for Precision Assembly of Superstratic and Superatomic Solids for funding (DMR-1420634).

### 3.8 References

- (1) Lewis, N. S.; Nocera, D. G. Powering the Planet: Chemical Challenges in Solar Energy Utilization. *Proc. Natl. Acad. Sci.* **2006**, *103* (43), 15729–15735.
- (2) Safaei, H.; Keith, D. W. How Much Bulk Energy Storage Is Needed to Decarbonize Electricity? *Energy Environ. Sci.* **2015**.
- (3) Newman, J.; Hoertz, P. G.; Bonino, C. a.; Trainham, J. A. Review: An Economic

- Perspective on Liquid Solar Fuels. *J. Electrochem. Soc.* **2012**, *159* (10), A1722–A1729.
- (4) Chen, X.; Shen, S.; Guo, L.; Mao, S. S. Semiconductor-Based Photocatalytic Hydrogen Generation. *Chem. Rev.* **2010**, *110* (11), 6503–6570.
  - (5) Walter, M. G.; Warren, E. L.; McKone, J. R.; Boettcher, S. W.; Mi, Q.; Santori, E. A.; Lewis, N. S. Solar Water Splitting Cells. *Chem. Rev.* **2010**, *110* (11), 6446–6473.
  - (6) Gratzel, M. Photoelectrochemical Cells. *Nature* **2001**, *414*, 338–344.
  - (7) Turner, J.; Sverdrup, G.; Mann, M. K.; Maness, P.-C.; Kroposki, B.; Ghirardi, M.; Evans, R. J.; Blake, D. Renewable Hydrogen Production. *Int. J. Energy Res.* **2007**, *32*, 379–407.
  - (8) McKone, J. R.; Lewis, N. S.; Gray, H. B. Will Solar-Driven Water-Splitting Devices See the Light of Day? *Chem. Mater.* **2014**, *26*, 407–414.
  - (9) Lewis, N. S. An Integrated, Systems Approach to the Development of Solar Fuel Generators. *Electrochem. Soc.* **2013**, 43–49.
  - (10) Pinaud, B. A.; Benck, J. D.; Seitz, L. C.; Forman, A. J.; Chen, Z.; Deutsch, T. G.; James, B. D.; Baum, K. N.; Baum, G. N.; Ardo, S.; et al. Technical and Economic Feasibility of Centralized Facilities for Solar Hydrogen Production via Photocatalysis and Photoelectrochemistry. *Energy Environ. Sci.* **2013**, *6* (7), 1983.
  - (11) Zhu, T.; Chong, M. N. Prospects of Metal–insulator–semiconductor (MIS) Nanojunction Structures for Enhanced Hydrogen Evolution in Photoelectrochemical Cells: A Review. *Nano Energy* **2015**, *12*, 347–373.
  - (12) Muñoz, A. G.; Lewerenz, H. J. Advances in Photoelectrocatalysis with Nanotopographical Photoelectrodes. *ChemPhysChem* **2010**, *11* (8), 1603–1615.
  - (13) Lewerenz, H. J.; Skorupska, K.; Muñoz, A. G.; Stempel, T.; Nüsse, N.; Lublow, M.; Vo-Dinh, T.; Kulesza, P. Micro- and Nanotopographies for Photoelectrochemical Energy Conversion. II: Photoelectrocatalysis – Classical and Advanced Systems. *Electrochim. Acta* **2011**, *56*, 10726–10736.
  - (14) Esposito, D. V.; Levin, I.; Moffat, T. P.; Talin, A. A. H<sub>2</sub> Evolution at Si-Based Metal-Insulator-Semiconductor Photoelectrodes Enhanced by Inversion Channel Charge Collection and H Spillover. *Nat. Mater.* **2013**, *12* (6), 562–568.
  - (15) Kenney, M. J.; Gong, M.; Li, Y.; Wu, J. Z.; Feng, J.; Lanza, M.; Dai, H. High-Performance Silicon Photoanodes Passivated with Ultrathin Nickel Films for Water Oxidation. *Science* **2013**, *342* (6160), 836–840.
  - (16) Choi, M. J.; Jung, J.-Y.; Park, M.-J.; Song, J.-W.; Lee, J.-H.; Bang, J. H. Long-Term Durable Silicon Photocathode Protected by a Thin Al<sub>2</sub>O<sub>3</sub>/SiO<sub>x</sub> Layer for Photoelectrochemical Hydrogen Evolution. *J. Mater. Chem. A* **2014**, *2*, 2928.

- (17) Hill, J. C.; Landers, A. T.; Switzer, J. A. An Electrodeposited N-Si/SiO<sub>x</sub>/Co/CoOOH Inhomogeneous Metal-Insulator-Semiconductor Junction for Efficient Photoelectrochemical Water Oxidation. *Nat. Mater.* **2015**, *14*, 6751–6755.
- (18) Chen, Y. W.; Prange, J. D.; Dühnen, S.; Park, Y.; Gunji, M.; Chidsey, C. E. D.; McIntyre, P. C. Atomic Layer-Deposited Tunnel Oxide Stabilizes Silicon Photoanodes for Water Oxidation. *Nat. Mater.* **2011**, *10* (7), 539–544.
- (19) Scheuermann, A. G.; Prange, J. D.; Gunji, M.; Chidsey, C. E. D.; McIntyre, P. C. Effects of Catalyst Material and Atomic Layer Deposited TiO<sub>2</sub> Oxide Thickness on the Water Oxidation Performance of Metal-Insulator-Silicon Anodes. *Energy Environ. Sci.* **2013**, *4* (8), 1166–1169.
- (20) Hu, S.; Shaner, M. R.; Beardslee, J. A.; Lichterman, M.; Brunschwig, B. S.; Lewis, N. S. Amorphous TiO<sub>2</sub> Coatings Stabilize Si, GaAs, and GaP Photoanodes for Efficient Water Oxidation. *Science* **2014**, *344* (6187), 1005–1009.
- (21) Boettcher, S. W.; Warren, E. L.; Putnam, M. C.; Santori, E. A.; Turner-Evans, D.; Kelzenberg, M. D.; Walter, M. G.; McKone, J. R.; Brunschwig, B. S.; Atwater, H. A.; et al. Photoelectrochemical Hydrogen Evolution Using Si Microwire Arrays. *J. Am. Chem. Soc.* **2011**, *133*, 1216–1219.
- (22) Seger, B.; Laursen, A. B.; Vesborg, P. C. K.; Pedersen, T.; Hansen, O.; Dahl, S.; Chorkendorff, I. Hydrogen Production Using a Molybdenum Sulfide Catalyst on a Titanium-Protected n(+)p-Silicon Photocathode. *Angew. Chem. Int. Ed. Engl.* **2012**, *51* (36), 9128–9131.
- (23) Seger, B.; Pedersen, T.; Laursen, A. B.; Vesborg, P. C. K.; Hansen, O.; Chorkendorff, I. Using TiO<sub>2</sub> as a Conductive Protective Layer for Photocathodic H<sub>2</sub> Evolution. *J. Am. Chem. Soc.* **2013**, *135* (3), 1057–1064.
- (24) Laursen, A. B.; Pedersen, T.; Malacrida, P.; Seger, B.; Hansen, O.; Vesborg, P. C. K.; Chorkendorff, I. MoS<sub>2</sub>-an Integrated Protective and Active Layer on n(+)p-Si for Solar H<sub>2</sub> Evolution. *Phys. Chem. Chem. Phys.* **2013**, *15* (46), 20000–20004.
- (25) Ji, L.; McDaniel, M. D.; Wang, S.; Posadas, A. B.; Li, X.; Huang, H.; Lee, J. C.; Demkov, A. A.; Bard, A. J.; Ekerdt, J. G.; et al. A Silicon-Based Photocathode for Water Reduction with an Epitaxial SrTiO<sub>3</sub> Protection Layer and a Nanostructured Catalyst. *Nat. Nanotechnol.* **2014**, *10* (1), 84–90.
- (26) Singh, R.; Green, M. A.; Rajkanan, K. Review of Conductor-Insulator-Semiconductor (CIS) Solar Cells. *Sol. Cells* **1981**, *3* (2), 95–148.
- (27) Dominey, R. N.; Lewis, N. S.; Bruce, J. A.; Bookbinder, D. C.; Wrighton, M. S. Improvement of Photoelectrochemical Hydrogen Generation by Surface Modification of P-Type Silicon Semiconductor Photocathodes. *J. Am. Chem. Soc.* **1982**, *104*, 467–482.
- (28) Szklańczyk, M.; Bockris, J. O. Photoelectrocatalysis and Electrocatalysis on P-Silicon. *J.*

*Phys. Chem.* **1984**, 88, 1808–1815.

- (29) Heller, A. Hydrogen-Evolving Solar Cells. *Science* **1984**, 1141–1148.
- (30) McCrory, C. C. L.; Jung, S.; Ferrer, I. M.; Chatman, S. M.; Peters, J. C.; Jaramillo, T. F. Benchmarking Hydrogen Evolving Reaction and Oxygen Evolving Reaction Electrocatalysts for Solar Water Splitting Devices. *J. Am. Chem. Soc.* **2015**, 137 (13), 4347–4357.
- (31) Shao-Horn, Y.; Sheng, W. C.; Chen, S.; Ferreira, P. J.; Holby, E. F.; Morgan, D. Instability of Supported Platinum Nanoparticles in Low-Temperature Fuel Cells. *Top. Catal.* **2007**, 46 (3–4), 285–305.
- (32) Vesborg, P. C. K.; Jaramillo, T. F. Addressing the Terawatt Challenge: Scalability in the Supply of Chemical Elements for Renewable Energy. *RSC Adv.* **2012**, 2 (21), 7933.
- (33) Heller, A.; Aspnes, D. E.; Porter, J. D.; Sheng, T. T.; Vadimsky, R. G. Transparent Metals Preparation and Characterization of Light-Transmitting Platinum Films. *J. Phys. Chem.* **1985**, 89 (1982), 4444–4452.
- (34) Nakato, Y.; Ueda, K.; Yano, H.; Tsubomura, H. Effect of Microscopic Discontinuity of Metal Overlayers on the Photovoltages in Metal-Coated Semiconductor-Liquid Junction Photoelectrochemical Cells for Efficient Solar Energy. *J. Phys. Chem.* **1988**, 92, 2316–2324.
- (35) Nakato, Y.; Tsubomura, H. Silicon Photoelectrodes Modified with Ultrafine Metal Islands. *Electrochim. Acta* **1992**, 897–907.
- (36) Nakato, Y.; Yano, H.; Nishiura, S.; Ueda, T.; Tsubomura, H. Hydrogen Photoevolution at P-Type Silicon Electrodes Coated with Discontinuous Metal Layers. *J. Electroanal. Chem.* **1987**, 228, 97–108.
- (37) Rossi, R. C.; Tan, M. X.; Lewis, N. S. Size-Dependent Electrical Behavior of Spatially Inhomogeneous Barrier Height Regions on Silicon. *Appl. Phys. Lett.* **2000**, 77, 2698.
- (38) Oskam, G.; Long, J. G.; Natarajan, A.; Searson, P. C. Electrochemical Deposition of Metals onto Silicon. *J. Phys. D. Appl. Phys.* **1998**, 31, 1927–1949.
- (39) Kawamura, Y. L.; Sakka, T.; Ogata, Y. H. Photoassisted Control of Pt Electrodeposition on P-Type Si. *J. Electrochem. Soc.* **2005**, 152, C701.
- (40) Aggour, M.; Skorupska, K.; Stempel Pereira, T.; Jungblut, H.; Grzanna, J.; Lewerenz, H. J. Photoactive Silicon-Based Nanostructure by Self-Organized Electrochemical Processing. *J. Electrochem. Soc.* **2007**, 154 (9), H794–H797.
- (41) Liu, Y. H.; Gokcen, D.; Bertocci, U.; Moffat, T. P. Self-Terminating Growth of Platinum Films by Electrochemical Deposition. *Science* (80-. ). **2012**, 338, 1327–1330.

- (42) Arrington, D.; Curry, M.; Street, S.; Pattanaik, G.; Zangari, G. Copper Electrodeposition onto the Dendrimer-Modified Native Oxide of Silicon Substrates. *Electrochim. Acta* **2008**, *53* (5), 2644–2649.
- (43) Mirley, C.; Koberstein, J. A Room Temperature Method for the Preparation of Ultrathin SiO<sub>x</sub> Films from Langmuir-Blodgett Layers. *Langmuir* **1995**, *11* (4), 1049–1052.
- (44) Gould, T. D.; Izar, A.; Weimer, A. W.; Falconer, J. L.; Medlin, J. W. Stabilizing Ni Catalysts by Molecular Layer Deposition for Harsh, Dry Reforming Conditions. *ACS Catal.* **2014**, *4* (8), 2714–2717.
- (45) Joo, S. H.; Park, J. Y.; Tsung, C.-K.; Yamada, Y.; Yang, P.; Somorjai, G. A. Thermally Stable Pt/Mesoporous Silica Core-Shell Nanocatalysts for High-Temperature Reactions. *Nat. Mater.* **2009**, *8* (2), 126–131.
- (46) Dai, Y.; Lim, B.; Yang, Y.; Cogley, C. M.; Li, W.; Cho, E. C.; Grayson, B.; Fanson, P. T.; Campbell, C. T.; Sun, Y.; et al. A Sinter-Resistant Catalytic System Based on Platinum Nanoparticles Supported on TiO<sub>2</sub> Nanofibers and Covered by Porous Silica. *Angew. Chemie Int. Ed.* **2010**, *49* (44), 8165–8168.
- (47) Takenaka, S.; Miyamoto, H.; Utsunomiya, Y.; Matsune, H.; Kishida, M. Catalytic Activity of Highly Durable Pt/CNT Catalysts Covered with Hydrophobic Silica Layers for the Oxygen Reduction Reaction in PEFCs. *J. Phys. Chem. C* **2014**, *118* (2), 774–783.
- (48) Maeda, K.; Teramura, K.; Lu, D.; Saito, N.; Inoue, Y.; Domen, K. Noble-Metal/Cr<sub>2</sub>O<sub>3</sub> Core/Shell Nanoparticles as a Cocatalyst for Photocatalytic Overall Water Splitting. *Angew. Chemie Int. Ed.* **2006**, *45* (46), 7806–7809.
- (49) Agiral, A.; Soo, H. Sen; Frei, H. Visible Light Induced Hole Transport from Sensitizer to Co<sub>3</sub>O<sub>4</sub> Water Oxidation Catalyst across Nanoscale Silica Barrier with Embedded Molecular Wires. *Chem. Mater.* **2013**, *25* (11), 2264–2273.
- (50) Mirley, C.; Koberstein, J. A Room Temperature Method for the Preparation of Ultrathin SiO<sub>x</sub> Films from Langmuir-Blodgett Layers. *Langmuir* **1995**, *11* (4), 0–3.
- (51) Phely-Bobin, T. S.; Muisener, R. J.; Koberstein, J. T.; Papadimitrakopoulos, F. Site-Specific Self-Assembly of Si/SiO<sub>x</sub> Nanoparticles on Micropatterned Poly(Dimethylsiloxane) Thin Films. *Synth. Met.* **2001**, *116* (1–3), 439–443.
- (52) Ouyang, M.; Yuan, C.; Muisener, R. J.; Boulares, A.; Koberstein, J. T. Conversion of Some Siloxane Polymers to Silicon Oxide by UV/Ozone Photochemical Processes. *Chem. Mater.* **2000**, *12* (29), 1591–1596.
- (53) Ustarroz, J.; Altantzis, T.; Hammons, J. a.; Hubin, A.; Bals, S.; Terryn, H. The Role of Nanocluster Aggregation, Coalescence, and Recrystallization in the Electrochemical Deposition of Platinum Nanostructures. *Chem. Mater.* **2014**, *26* (7), 2396–2406.
- (54) Schroder, D. K. *Semiconductor Material and Device Characterization: Third Edition*; 2005.

- (55) Daum, P. H.; Enke, C. G. Electrochemical Kinetics of the Ferri-Ferrocyanide Couple on Platinum. *Anal. Chem.* **1969**, *41* (4), 653–656.
- (56) Konopka, S. J.; McDuffie, B. Diffusion Coefficients of Ferri- and Ferrocyanide Ions in Aqueous Media, Using Twin-Electrode Thin-Layer Electrochemistry. *Anal. Chem.* **1970**, *42* (14), 1741–1746.
- (57) Scheuermann, A.; Kemp, K.; Tang, K.; Lu, D.; Satterthwaite, P.; Ito, T.; Chidsey, C. E. D.; McIntyre, P. Conductance and Capacitance of Bilayer Protective Oxides for Silicon Water Splitting Anodes. *Energy Environ. Sci.* **2015**.
- (58) Shewchun, J.; Singh, R.; Green, M. A. Theory of Metal-Insulator-Semiconductor Solar Cells. *J. Appl. Phys.* **1977**, *48* (2), 765.
- (59) Ouyang, M.; Muisener, R. .; Boulares, A.; Koberstein, J. . UV–ozone Induced Growth of a SiO<sub>x</sub> Surface Layer on a Cross-Linked Polysiloxane Film: Characterization and Gas Separation Properties. *J. Memb. Sci.* **2000**, *177* (1–2), 177–187.
- (60) Ouyang, M.; Klemchuk, P. P.; Koberstein, J. T. Exploring the Effectiveness of SiO<sub>x</sub> Coatings in Protecting Polymers against Photo-Oxidation. *Polym. Degrad. Stab.* **2000**, *70* (2), 217–228.
- (61) Velmurugan, J.; Zhan, D.; Mirkin, M. V. Electrochemistry through Glass. *Nat. Chem.* **2010**, *2* (6), 498–502.
- (62) Houston, K. S.; Weinkauff, D. H.; Stewart, F. F. Gas Transport Characteristics of Plasma Treated Poly(Dimethylsiloxane) and Polyphosphazene Membrane Materials. *J. Memb. Sci.* **2002**, *205*, 103–112.
- (63) Green, M. A.; King, F. D.; Shewchun, J. Minority Carrier MIS Tunnel Diodes and Their Application to Electron-and Photo-Voltaic Energy Conversion—I. Theory. *Solid. State. Electron.* **1974**, *17*, 551–561.
- (64) Hezel, R. Recent Progress in {MIS} Solar Cells. *Prog. Photovoltaics Res. Appl.* **1997**, *5* (November 1996), 109–120.
- (65) Har-Lavan, R.; Ron, I.; Thieblemont, F.; Cahen, D. Toward Metal-Organic Insulator-Semiconductor Solar Cells, Based on Molecular Monolayer Self-Assembly on n-Si. *Appl. Phys. Lett.* **2009**, *94* (4), 043308.
- (66) Kim, K. H.; Kim, H. J.; Jang, P.; Jung, C.; Seomoon, K. Properties of Low-Temperature Passivation of Silicon with ALD Al<sub>2</sub>O<sub>3</sub> Films and Their PV Applications. *Electron. Mater. Lett.* **2011**, *7* (2), 171–174.
- (67) Jung, Y.; Li, X.; Rajan, N. K.; Taylor, A. D.; Reed, M. a. Record High Efficiency Single-Walled Carbon Nanotube/Silicon p-n Junction Solar Cells. *Nano Lett.* **2013**, *13*, 95–99.
- (68) García De Arquer, F. P.; Mihi, A.; Kufer, D.; Konstantatos, G. Photoelectric Energy



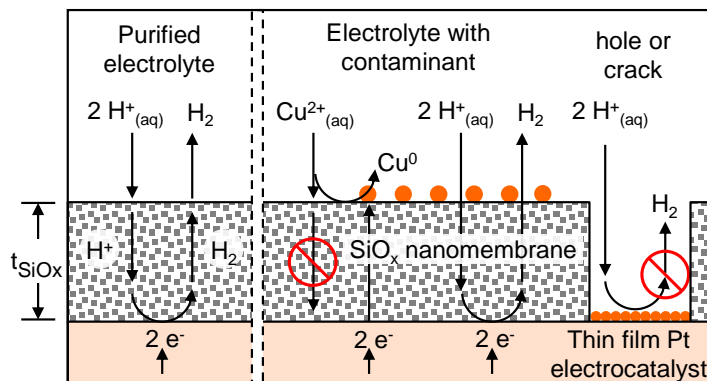
Conversion of Plasmon-Generated Hot Carriers in Metal-Insulator-Semiconductor Structures. *ACS Nano* **2013**, 7 (4), 3581–3588.

- (69) Verwey, J. F.; Amerasekera, E. A.; Bisschop, J. The Physics of SiO<sub>2</sub>. *Rep. Prog. Phys.* **1990**, 53, 1297–1331.
- (70) Lee, J.-Y.; Lee, J. G.; Lee, S.; Seo, M.; Piao, L.; Bae, J. H.; Lim, S. Y.; Park, Y. J.; Chung, T. D. Hydrogen-Atom-Mediated Electrochemistry. *Nat. Commun.* **2013**, 4 (May), 1–8.
- (71) Hattori, T.; Watanabe, K.; Ohashi, M.; Matsuda, M.; Yasutake, M. Electron Tunneling through Chemical Oxide of Silicon. *Appl. Surf. Sci.* **1996**, 102 (96), 86–89.
- (72) Ustarroz, J.; Hammons, J. A.; Altantzis, T.; Hubin, A.; Bals, S.; Terryn, H. A Generalized Electrochemical Aggregative Growth Mechanism. *J. Am. Chem. Soc.* **2013**, 135 (31), 11550–11561.
- (73) Selvarajoo, T. A. L.; Ranjan, R.; Pey, K. L.; Tang, L. J.; Tung, C. H.; Lin, W. Dielectric-Breakdown-Induced Epitaxy: A Universal Breakdown Defect in Ultrathin Gate Dielectrics. In *IEEE Trans. Electron Devices*; 2005; Vol. 5, pp 190–197.
- (74) Pey, K. L.; Tung, C. H.; Radhakrishnan, M. K.; Tang, L. J.; Lin, W. H. Dielectric Breakdown Induced Epitaxy in Ultrathin Gate Oxide - a Reliability Concern. *Int. Electron Devices Meet.* **2002**, 1 (C), 163–166.
- (75) Azizi, N.; Yiannacouras, P. Gate Oxide Breakdown. *ECE1768–Reliability Integr. Circuits* **2003**, 1–33.
- (76) Lombardo, S.; Crupi, F.; La Magna, A.; Spinella, C.; Terrasi, A.; La Mantia, A.; Neri, B. Electrical and Thermal Transient during Dielectric Breakdown of Thin Oxides in Metal-SiO<sub>2</sub>-Silicon Capacitors. *J. Appl. Phys.* **1998**, 84 (1), 472.
- (77) Ranjan, R.; Pey, K. L.; Tung, C. H.; Tang, L. J.; Ang, D. S.; Groeseneken, G.; De Gendt, S.; Bera, L. K. Breakdown-Induced Thermochemical Reactions in HfO<sub>2</sub>/High- $\kappa$ /Polycrystalline Silicon Gate Stacks. *Appl. Phys. Lett.* **2005**, 87 (24), 242907.

## CHAPTER 4

### HYDROGEN EVOLUTION AT THE BURIED INTERFACE BETWEEN PLATINUM THIN FILMS AND SILICON OXIDE NANOMEMBRANES

Chapter 4 builds off of the exciting results from Chapter 3 to better understand the structure-property relationships that underlie the performance of  $\text{SiO}_x$ -coated Pt nanoparticles and to demonstrate selective transport through  $\text{SiO}_x$ . In order to gain a more fundamental understanding of transport through  $\text{SiO}_x$  this study focuses on well-defined and purely (dark) electrocatalytic systems (i.e. PEMEC not PEC) to remove complications associated with nanoparticles and solid-state physics of a semiconducting photoelectrode. Well-defined  $\text{SiO}_x$ -encapsulated Pt thin film electrocatalysts are employed for studying the HER. The selectivity of  $\text{SiO}_x$  is investigated by testing its ability to mitigate poisoning via selective transport of the desired species ( $\text{H}^+$ ) and selective blocking of impurities, such as  $\text{Cu}^{2+}$ , from reaching the catalytically active buried interface. The  $\text{H}^+$  and  $\text{H}_2$  permeability through  $\text{SiO}_x$  is quantified through HER experiments and modeling the concentration overpotentials that result from the  $\text{SiO}_x$  mass transport barrier. The planar Pt thin film electrocatalysts allows for a systematic approach to answering fundamental questions about the properties of the  $\text{SiO}_x$  overlayers that can be tuned to maximize the desired stability benefits without significantly affecting the kinetic or concentration overpotentials for the desired redox chemistry.



## 4.1 Introduction

Electrochemical technologies such as fuel cells, electrolyzers, redox flow batteries, and photoelectrochemical cells are expected to be core technologies in a sustainable energy future because they can facilitate large-scale conversion between electrical energy and storable chemical fuels such as hydrogen.<sup>1–4</sup> However, improvement in the efficiency and lifetime of these technologies is critically important for such a future to be realized.<sup>5–9</sup> Device lifetime can be affected by many factors and involve numerous components, but in many cases it is closely tied to the durability of electrocatalysts, which are typically metallic nanoparticles that serve the essential role of catalyzing the oxidation and reduction reactions of interest. In hydrogen fuel cells and water electrolyzers, two of the most commonly used state-of-the-art catalytic materials are platinum (Pt) and iridium (Ir). Due to the high cost and scarcity of Pt and Ir, the metal loadings are typically kept as low as possible in the form of small nanoparticles (< 5 nm diameter). For example, Pt loading is typically maintained below 0.1 mg Pt cm<sup>-2</sup> for the H<sub>2</sub> evolution and oxidation reactions, and < 0.4 mg Pt cm<sup>-2</sup> for the oxygen reduction reaction (ORR).<sup>10,11</sup> However, minimizing catalyst loading by decreasing particle size often comes at the expense of decreased lifetime and performance that may result from increased rates of particle dissolution, migration, and/or agglomeration.<sup>5,12–14</sup>

To date, efforts to improve the stability of nanoparticle electrocatalysts in fuel cells and electrolyzers have focused on modifying the electrocatalyst itself or the support material to which the nanoparticles are adhered. Researchers who have focused on increasing the stability of the support investigate interactions between the support and Pt NPs and methods to improve the adhesion of electrocatalysts to the support.<sup>15–18</sup> Commonly used approaches to engineer better

support materials are to: i) modify carbon supports with a higher percentage of graphitized carbon<sup>15</sup> nanomaterials such as carbon nanotubes (CNTs)<sup>19,20</sup> and graphene,<sup>21–23</sup> ii) dope carbon, or iii) substitute carbon with non-carbon catalyst supports, including transition metal carbides,<sup>24,25</sup> conductive metal oxides<sup>26,27</sup> or nitrides<sup>28,29</sup>.<sup>30</sup> Efforts to improve the durability of Pt-based cathode catalysts have focused on incorporating another noble metal and/or designing the material structure and morphology with various nanostructures such as core-shell<sup>31</sup> or nanoframe structures.<sup>32</sup> For example, Adzic et al., have shown that the durability of low-dimensional Pt ORR catalysts can be significantly enhanced by utilizing core-shell structures whereby the strong interaction between the Pt and Au core imparts enhanced stability to the Pt.<sup>33,34</sup> The current article is motivated by a different approach to enhance electrocatalyst stability that is based on encapsulating the active electrocatalyst material by an ultrathin, permeable overlayer that can prevent the previously mentioned degradation mechanisms while simultaneously allowing transport of reactants and products between the electrolyte and the surface of the active electrocatalyst.<sup>19,35–40</sup> Similar structures such as core-shell nanoparticles have previously enhanced thermal stability for high temperature heterogeneous catalysis,<sup>41–43</sup> and have been used to suppress undesired back reactions in photoelectrochemical applications.<sup>44–47</sup> Several studies have also demonstrated the benefits of using ultrathin metal oxide layers for stabilizing metallic nanoparticles or molecular catalysts in low-temperature fuel cells<sup>19,48–53</sup> and photoelectrochemical cells,<sup>47,54</sup> including the study presented in Chapter 3.<sup>35</sup> In most of these studies, the encapsulated electrocatalysts exhibited enhanced stability compared to control electrodes lacking protective overlayers, and transport of electroactive species through the overlayers was assumed or implied. However, direct evidence and detailed understanding of transport through the oxide overlayers of encapsulated nanoparticles has been lacking.

Several other studies have reported transport of electroactive species through thin oxide overlayers deposited on electroactive metals,<sup>55–59</sup> although these investigations were not necessarily motivated by electrocatalysis. Velmurugan et al. demonstrated  $\text{H}^+/\text{H}_2\text{O}$  transport through hydrophilic borosilicate glass that was used to encapsulate Pt ultramicroelectrodes.<sup>57</sup> This study investigated voltammetric responses to multiple redox couples to eliminate the possibility of transport through nanoscopic cracks or pinholes. However, a quantitative relationship between proton transport rates,  $\text{SiO}_2$  properties, and  $\text{SiO}_2$  thickness was not obtained in this study, or in the electrocatalysis publications cited above. In all cases, complex or poorly defined electrocatalyst geometries, such as those containing  $\text{SiO}_2$  coatings with varying thickness, have precluded a more detailed understanding of transport through thin oxide layers.

Although these previous studies have provided valuable insights into the viability of using electrocatalytic materials encapsulated by thin, permeable metal oxide overlayers, a number of important questions remain: (i.) How important are pinholes and/or cracks in the overlayers for enabling transport of reactants to the underlying active electrocatalyst? (ii.) If transport primarily occurs through the overlayers, what is the mechanism of transport and can transport properties be tuned to control species transport and catalytic pathways? (iii.) Is transport through ultrathin metal oxide layers facile enough for this architecture to be employed in real-world applications without prohibitively high mass-transport overpotential losses?

We seek to answer these questions by studying well-defined, planar  $\text{SiO}_x$ -coated Pt thin films (Figure 4.1a) that are used as electrocatalysts for the hydrogen evolution reaction (HER). Consistent with previous studies of proton transport through  $\text{SiO}_2$ -based glass,<sup>57,60–63</sup> the zoomed in side-view in Figure 4.1b illustrates proton ( $\text{H}^+$ ) and hydrogen ( $\text{H}_2$ ) transport occurring through the  $\text{SiO}_x$  overlayer, with the HER taking place at the  $\text{SiO}_x|\text{Pt}$  interface. As shown herein, the

transport properties through the overlayer can be selective, meaning that the  $\text{SiO}_x$  layer can be thought of as a “nanomembrane”. In fact, ultrathin layers of  $\text{SiO}_x$  have commonly been used as selective membranes for gas separation<sup>64,65</sup> and in electrochemical systems.<sup>66,67</sup> For this reason, we refer to this electrocatalyst architecture as a membrane-coated electrocatalyst (MCEC). Importantly, the potential benefits of the MCEC architecture can go beyond stabilizing the underlying catalytic particles or films. If the structure-property relationships of the nanomembranes in MCECs can be better understood and controlled, the selective transport of reactants and/or products can be leveraged to control electrocatalytic pathways of complex electrochemical reactions. Similar approaches based on size- and shape-selective transport are commonly used in zeolite catalysis to control reaction pathways in thermal catalysis.<sup>68–70</sup>

In this study, we employ a room-temperature UV ozone synthesis process<sup>35,64</sup> to achieve nanoscale control over the thickness of  $\text{SiO}_x$  films deposited on top of the smooth Pt thin films. By systematically changing the  $\text{SiO}_x$  thickness, we seek to gain deeper understanding of the structure-property relationships that underlie the transport properties of these  $\text{SiO}_x$  nanomembranes. In the first part of this paper, the physical and chemical characteristics of the  $\text{SiO}_x/\text{Pt}$  thin film electrodes are presented, followed by characterization of the electrochemically active surface area (ECSA) of the encapsulated Pt thin films. The HER current-potential behavior of each electrode is then evaluated, allowing for determination of the concentration overpotentials associated with transport of protons through the  $\text{SiO}_x$  overlayers and quantification of the  $\text{H}^+$  and  $\text{H}_2$  permeabilities in the  $\text{SiO}_x$ . Finally, we demonstrate the ability of  $\text{SiO}_x$ -encapsulated Pt to operate as a copper-resistant HER electrocatalyst and discuss the implications of these studies for employing the MCEC architecture in water electrolysis and other electrocatalytic applications.

Overall, we show that the MCEC design holds great promise as a tunable electrocatalyst platform to optimize catalytic properties while minimizing degradation issues.

## 4.2 Experimental Section

### 4.2.1 *SiO<sub>x</sub>/Pt Fabrication*

#### 4.2.1.1 *Electrode Preparation*

Monocrystalline degenerately doped Si(100) wafers ( $p^+Si$ ,  $< 0.005 \Omega \text{ cm}$ , 500-550  $\mu\text{m}$  thick, WRS materials) were used as flat, conductive substrates. 2 nm thick Ti (99.99%) and 3 nm thick Pt (99.99%) layers were then sequentially deposited at  $0.2 \text{ A s}^{-1}$  by electron-beam evaporation without breaking vacuum and without substrate heating in a Angstrom EvoVac evaporator system with a base pressure of  $1.0 \times 10^{-7}$  Torr. Film thicknesses were monitored with quartz crystal thickness monitors.

A low-resistance electrical back contact was made between a copper wire and the back of the  $p^+Si$  substrate with indium solder. Finally, the electrodes were sealed in 3M Electroplater's tape to protect the back contact and create a well-defined  $0.246 \text{ cm}^2$  circular opening on the front of the electrode for electrochemical measurements. 3M Electroplater's tape did not introduce any contaminants into the electrolyte, nor onto the bare Pt electrode surface, as evidenced by the lack of unidentified peaks in cyclic voltammograms (see section 4.3.3.1) and the comparable Tafel slope and exchange current densities to those reported for Pt in literature (see section 4.6.2).

#### 4.2.1.2 *SiO<sub>x</sub> Film Synthesis*

The wafer was cleaved into  $1.5 \times 2 \text{ cm}$  pieces and then ultrasonicated sequentially in acetone, methanol, isopropanol, and DI water. Trimethylsiloxy terminated polydimethylsiloxane (PDMS) was spin coated onto Pt/Ti/ $p^+Si$  substrates at a speed of 2000 rpm for 1 min from a toluene solution.<sup>71,72</sup> The concentration of PMDS/toluene solution of  $1.4 \text{ mg ml}^{-1}$ ,  $2.8 \text{ mg ml}^{-1}$ ,  $4.5 \text{ mg ml}^{-1}$

<sup>1</sup> and 6.9 mg ml<sup>-1</sup> was selected to produce SiO<sub>x</sub> films with thickness of 1.9 nm, 4.6 nm, 9.4 nm, and 19.8 nm respectively. The electrodes were then dried in a vacuum oven at 70 °C for 60 minutes to evaporate the solvent. Afterwards, the PDMS was converted to SiO<sub>x</sub> in a UV ozone cleansing chamber for 2 hours (UVOCS, T10X10/OES).<sup>71,73</sup>

## **4.2.2 Structural Characterization**

### **4.2.2.1 Ellipsometry and Ellipsometric Porosimetry**

The thicknesses of the SiO<sub>x</sub> films, which were fabricated on the Pt film electrodes, were measured with a Woollam alpha-SE ellipsometer and fit with a Cauchy model. Ellipsometry measures the change in polarization of light upon reflection from a sample, which can be described as an amplitude ratio,  $\Psi$ , and a phase difference,  $\delta$ . From these data, the thickness of the porous film and its refractive index can be deduced. The thickness and refractive index of a 9.5 nm and a 107 nm SiO<sub>x</sub> film on p<sup>+</sup>Si were determined by spectroscopic ellipsometry (SE) (Woollam M-2000U ellipsometer (245–1000 nm)) and also fit with a Cauchy model.<sup>74,75</sup> The 107 nm SiO<sub>x</sub> film was fabricated with ten successive SiO<sub>x</sub> layers. The total porosity was calculated based on the SE measured index of refraction. The pore dimension of the SiO<sub>x</sub> films were investigated with ellipsometric porosimetry (EP) measurements, conducted in a home-built vacuum chamber attached to the spectroscopic ellipsometer, with toluene as adsorptive gas. The EP setup used in this study is capable of performing ellipsometry measurements at different relative pressures ( $P/P_0$ ) during adsorption/desorption of toluene in the porous silica film. A detailed description of the EP experiment and the data analysis can be found elsewhere.<sup>74,76,77</sup> After loading the sample in to the vacuum chamber, a spectroscopic ellipsometry (SE) measurement was taken before the introduction of toluene.



#### 4.2.2.2 *Scanning Electron and Atomic Force Microscopy*

The electrodes were imaged with a Zeiss Sigma VP Schottky Thermal Field emission SEM microscope. The morphology of the films was analyzed with atomic force microscopy (AFM) (Bruker Dimension Icon AFM) under ambient conditions. A ScanAsyst silicon tip on a nitride lever silicon cantilever with a 25 nm tip radius, spring force constant of  $0.4 \text{ N m}^{-1}$  and a resonant frequency of 70 kHz was used. All AFM images were acquired with a 0.1 Hz scan rate in peak force quantitative nanomechanical mapping mode. The feedback gain was varied to minimize the peak force error.

#### 4.2.2.3 *X-ray Photoelectron Spectroscopy*

X-ray photoelectron spectroscopy (XPS) measurements were conducted with a Phi XPS system that was operated at a base pressure of  $2 \times 10^{-10}$  Torr using a monochromatic  $\text{Al}_{K\alpha}$  source (X-ray power 15 kV, 20 mA) and a neutralizer. The pass energy was 23.5 eV. XPSpeak software was used to evaluate the peak areas of Si 2p, C 1s, O 1s, Pt 4f, and Cu 2p, spectra based on Shirley's algorithm for background subtraction. The C 1s peaks were shifted and centered to 284.8 eV, and the Si 2p and O 1s peaks associated with the  $\text{SiO}_x$  overlayers were shifted by the same amount. The peak area ratios were calculated after accounting for the atomic sensitivity factors ( $\text{ASF}_i$ ) ( $\text{ASF}_{\text{Si}} = 0.180$ ,  $\text{ASF}_{\text{C}} = 0.296$ ,  $\text{ASF}_{\text{O}} = 0.711$ ,  $\text{ASF}_{\text{Pt}} = 5.575$ , and  $\text{ASF}_{\text{Cu}} = 5.321$ ).<sup>78</sup> The value of the Si atomic sensitivity factor was adjusted (from  $\text{ASF}_{\text{Si}} = 0.339$ ) to account for the difference in atomic density and attenuation lengths between Si in  $\text{SiO}_2$  and Si.

#### 4.2.3 *Electrochemical characterization*

All electrochemical measurements were performed using a SP-200 BioLogic potentiostat controlled by EC-Lab v10.40 software. ECSA and HER experiments were carried out in deaerated 0.1 M sulfuric acid, prepared from concentrated sulfuric acid ( $\text{H}_2\text{SO}_4$ , Fisher Scientific, ACS

grade) and 18 M $\Omega$  deionized water (Millipore, Milli-Q Direct 8). HER experiments were performed in a well stirred electrolyte (1000 rpm) to facilitate bubble removal. Copper stripping voltammetry was performed in 2 mM copper sulfate (CuSO<sub>4</sub>, Sigma Aldrich, ReagentPlus) with 0.1 M H<sub>2</sub>SO<sub>4</sub> as the supporting electrolyte. Copper poisoning experiments were conducted in a 0.2 mM CuSO<sub>4</sub> solution with 0.5 M H<sub>2</sub>SO<sub>4</sub>. A Pt mesh (Alfa Aesar, 99.9%) counter electrode was located in a secondary compartment separated by a glass frit. A commercial Ag|AgCl/sat. 3 M KCl reference electrode (Hach, E21M002) was located in the main compartment.

#### 4.2.3.1 Series Resistance

The series resistance of each electrode immersed in the 0.1 M H<sub>2</sub>SO<sub>4</sub> solution was determined by electrochemical impedance spectroscopy (EIS) at open circuit, and typically found to be  $\approx 16 \Omega$ , independent of SiO<sub>x</sub> thickness ( $t_{\text{SiO}_x}$ ). Although the SiO<sub>x</sub> may be electrically resistive, charge can also be carried across the permeable SiO<sub>x</sub> layer by ion transport through pores and/or interstitial spaces. Given the independence of EIS-measured series resistance on  $t_{\text{SiO}_x}$ , we attribute the majority of the ohmic resistance to ion transport through the bulk solution and contact resistance between the electrical lead and sample substrate. The electrochemical data presented are not  $iR$  corrected, unless stated otherwise. All solutions were bubbled with N<sub>2</sub> gas for 20 minutes to purge dissolved oxygen. During all electrochemical measurements, the head space of the working electrode compartment was continuously purged with nitrogen (N<sub>2</sub>). Current densities are normalized with respect to the geometric area of the exposed electrode.

#### 4.2.3.2 Hydrogen and Copper Underpotential Deposition

The ECSAs of Pt electrodes were calculated from the average of the charge associated with underpotential adsorption and desorption of hydrogen atoms recorded during cyclic voltammetry (CV) between potentials of 0.05 V vs. RHE and 0.45 V vs. RHE. Current due to double layer

capacitance was subtracted during the analysis, and a conversion factor of  $210 \mu\text{C cm}^{-2} \text{Pt}$  was used to compute ECSA from the total  $H_{\text{upd}}$  charge.<sup>79</sup> Before Cu stripping voltammetry, Cu was adsorbed onto exposed Pt by underpotential deposition (upd) at a constant applied potential of +0.36 vs. Ag|AgCl for 50 s. The upd Cu was then stripped from the surface by sweeping the potential from +0.36 V vs. Ag|AgCl to 1.0 V vs. Ag|AgCl at  $100 \text{ mV s}^{-1}$ . The amount of Cu deposited on the surface was quantified from the difference in the Cu stripping LSVs with and without the 2 mM  $\text{CuSO}_4$  in the 0.1 M  $\text{H}_2\text{SO}_4$  supporting electrolyte. A conversion factor of  $420 \mu\text{C cm}^{-2} \text{Pt}$  was used to calculate the ECSA from the integrated  $\text{Cu}_{\text{upd}}$  charge.<sup>80</sup>

### 4.3 Results

#### 4.3.1 Description of $\text{SiO}_x$ -Encapsulated Pt MCEC Electrodes for HER Electrocatalysis

Figure 4.1a shows a schematic side-view of a model MCEC electrode consisting of a silicon oxide ( $\text{SiO}_x$ ) nanomembrane deposited onto a Pt thin film. Figure 4.1b illustrates hydrogen evolution taking place at the buried Pt| $\text{SiO}_x$  interface, and also depicts a hole or crack in the  $\text{SiO}_x$  layer. When the electrode is operated under applied bias, protons transport from the bulk solution to the  $\text{SiO}_x$ |electrolyte interface across a diffusion boundary layer that depends on the hydrodynamics of the bulk electrolyte. After reaching the outer surface of the  $\text{SiO}_x$  layer, protons are transported to the buried Pt| $\text{SiO}_x$  interface by passing through (i.) interstitial spaces and/or micropores ( $< 2 \text{ nm}$ ) in the  $\text{SiO}_x$  overlayer, or (ii.) larger holes in the  $\text{SiO}_x$  overlayer with dimensions exceeding the hydrated radius of the proton, thereby allowing for unimpeded transport from the bulk electrolyte to the exposed Pt surface, or (iii.) non-penetrating holes or cracks in the  $\text{SiO}_x$  in which a permeable barrier film remains at the bottom of the holes.<sup>60,61,63</sup> Protons are then reduced at accessible Pt sites to form the  $\text{H}_2$  product species, which diffuse in the opposite direction until they reach the bulk electrolyte.

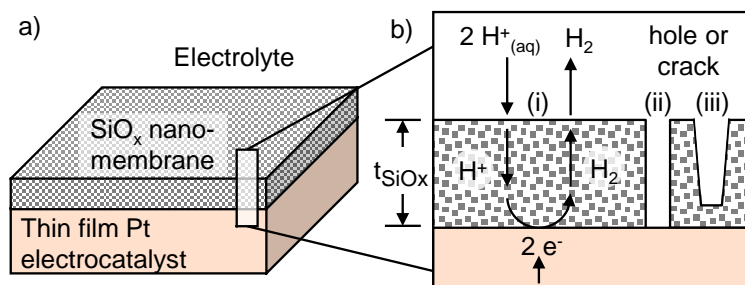


Figure 4.1. a.) Planar electrode platform for studying membrane-coated electrocatalysts (MCECs) in which a thin, permeable  $\text{SiO}_x$  overlayer uniformly coats an electroactive catalyst. b.) Schematic side view illustrating the basic operating process of hydrogen evolution at a planar metallic electrocatalyst (Pt) covered by an ultrathin  $\text{SiO}_x$  overlayer of thickness  $t_{\text{SiO}_x}$  that (i) enables facile transport of reactants and products to and from the electrocatalyst surface. Also shown is a (ii) macroscopic opening in the  $\text{SiO}_x$  through which reactants and products may transport to the electrocatalyst interface unimpeded by the  $\text{SiO}_x$  and (iii) a non-penetrating hole or crack in the  $\text{SiO}_x$  in which a barrier film remains at the bottom of the holes.

### 4.3.2 Characterization of $\text{SiO}_x$ Overlayers

#### 4.3.2.1 $\text{SiO}_x$ Thickness and Surface Topology

A series of  $\text{SiO}_x|\text{Pt}$  MCEC electrodes were fabricated by spin coating PDMS onto Pt thin film substrates, followed by conversion of the PDMS to  $\text{SiO}_x$  by exposure to UV ozone.<sup>71</sup> As measured by ellipsometry, the thicknesses of the  $\text{SiO}_x$  overlayers on each electrode were found to be  $1.9 \pm 0.1$  nm,  $4.6 \pm 0.4$  nm,  $9.4 \pm 0.1$  nm, and  $19.8 \pm 0.5$  nm (Table 4.1). The physical structure of the  $\text{SiO}_x$  overlayers were further characterized by SEM and AFM. In SEM images, nanoscale circular features were observed for all  $\text{SiO}_x$ -encapsulated samples (Figure 4.2).

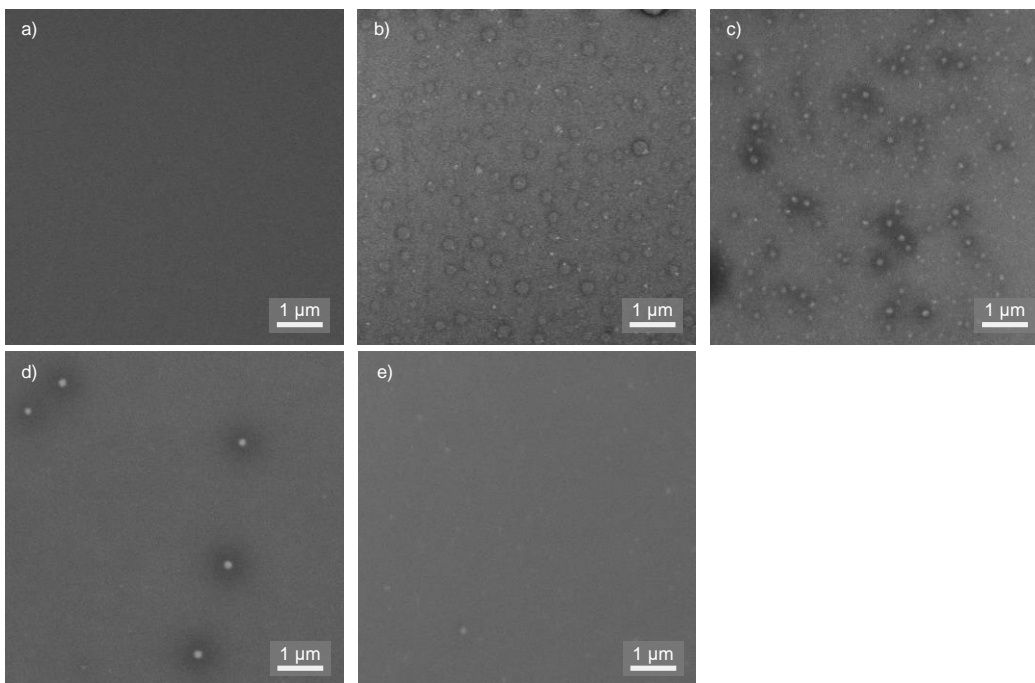


Figure 4.2. Top view SEM images. Representative SEM images of  $\text{SiO}_x/\text{Pt}$  electrodes containing: a.)  $t_{\text{SiO}_x}=0$  nm, b.)  $t_{\text{SiO}_x}=1.9$  nm, c.)  $t_{\text{SiO}_x}=4.6$  nm, d.)  $t_{\text{SiO}_x}=9.4$  nm, and e.)  $t_{\text{SiO}_x}=19.8$  nm  $\text{SiO}_x$  films. Brightness and contrast were increased to see features more clearly.

The topologies of these features were measured by AFM and compared to the bare Pt control sample, which displayed a smooth, uniform surface with root mean squared (rms) surface roughness of  $0.21 \pm 0.01$  nm (Figure 4.3a). By contrast, Figures 4.3b-e show that all of the  $\text{SiO}_x$  coated samples exhibited distinct meso- (2-50 nm) and macroporous (>50 nm) holes in the  $\text{SiO}_x$  overlayer that varied in diameter and density depending on the  $\text{SiO}_x$  thickness. The rms surface roughness for all  $\text{SiO}_x$  films, in areas lacking holes, remained the same as the roughness of the Pt thin film ( $0.21 \pm 0.02$  nm). A trend of decreasing areal hole coverage and hole density with increasing  $\text{SiO}_x$  thickness was observed, as shown by the bar plots in Figure 4.3f. It was found that the percent areal coverage of holes varied from 0.5 % to 8.8 %, while the hole density varied between  $13 \text{ holes } \mu\text{m}^{-2}$  and  $1 \text{ hole } \mu\text{m}^{-2}$ . It was also observed that the average hole diameter decreased monotonically with increasing  $t_{\text{SiO}_x}$ . For all samples, AFM line scans revealed that the

average depths of the holes in the  $\text{SiO}_x$  overlayer were less than the overlayer thickness, as measured by ellipsometry (Figure 4.3f). This observation suggests that many of the holes do not extend all the way through the  $\text{SiO}_x$  overlayer, as illustrated by the non-penetrating hole in Figure 4.1b. Non-penetrating holes are especially common for the thicker  $\text{SiO}_x$  layers, for which the AFM-determined hole depths were only 12-25% of the ellipsometry-determined  $\text{SiO}_x$  thicknesses.

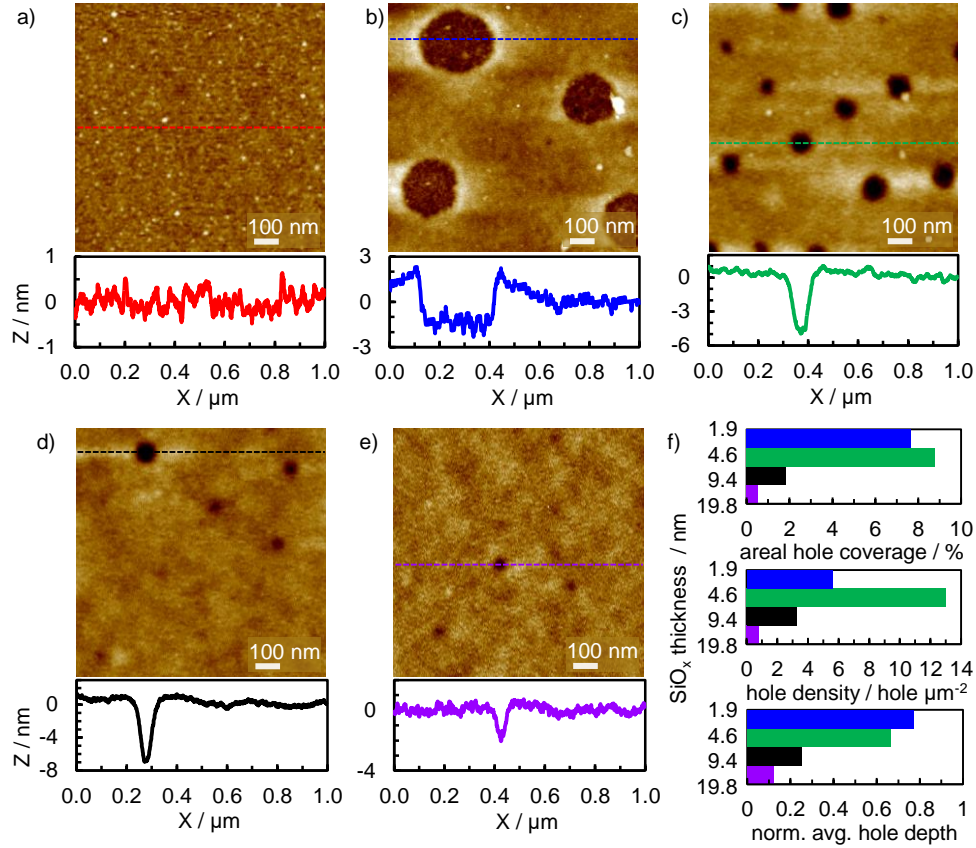


Figure 4.3. Surface topology characterization of  $\text{SiO}_x$  coated Pt thin films. AFM images of as-made  $\text{SiO}_x$ |Pt electrodes and corresponding depth profiles over holes for: a.)  $t_{\text{SiO}_x}=0$  nm, b.)  $t_{\text{SiO}_x}=1.9$  nm, c.)  $t_{\text{SiO}_x}=4.6$  nm, d.)  $t_{\text{SiO}_x}=9.4$  nm, e.)  $t_{\text{SiO}_x}=19.8$  nm  $\text{SiO}_x$  films. f.) Percent areal coverage of holes, hole density, and average hole depth normalized by the ellipsometry measured  $\text{SiO}_x$  thickness for each  $\text{SiO}_x$  film thickness. Characteristics in (f) were calculated from 15  $1 \mu\text{m}^2$  images from each sample.

#### 4.3.2.2 *SiO<sub>x</sub> Porosity*

Spectroscopic ellipsometry (SE) and ellipsometric porosimetry (EP) measurements (described in section 4.2.2.1) were performed to determine the total porosity and pore sizes, respectively, in SiO<sub>x</sub> overlayers deposited on p<sup>+</sup>Si substrates lacking Pt. Spectroscopic ellipsometry yielded a refractive index of 1.40 and 1.43 for a 9.5 nm and 107 nm SiO<sub>x</sub> film, respectively. In comparison, the refractive index for a 100 nm thermally grown SiO<sub>2</sub> was 1.46, consistent with literature.<sup>81</sup> Thus, it was assumed the decrease in measured refractive indices were due to film porosity. The Lorentz-Lorenz effective medium approximation was used to calculate the total porosity<sup>76,77,82–84</sup> in the SiO<sub>x</sub> films, which were 12% and 6% for the t<sub>SiO<sub>x</sub></sub>=9.5 nm and t<sub>SiO<sub>x</sub></sub>=107 nm films, respectively. This porosity was inaccessible for toluene molecule (see Appendix section 4.6.1, Figure 4.12) indicating that pore sizes in the SiO<sub>x</sub> films are smaller than the kinetic diameter of toluene, 5.8 Å.<sup>76,85</sup> These pore sizes are below resolution limit for the AFM measurement and are different from the meso/macroporous holes that were observed in AFM.

#### 4.3.2.3 *SiO<sub>x</sub> Composition*

XPS characterization of the as-synthesized samples revealed that the PDMS precursor was primarily converted to SiO<sub>2</sub>, although trace amounts of residual carbon (C) remained. This finding is consistent with previous studies of SiO<sub>x</sub> films made by the UV ozone process.<sup>71,73</sup> Figure 4.4a shows that the Si 2p peak center is located at 103.5 eV, which corresponds to the Si<sup>4+</sup> oxidation state and is consistent with Si in the form of silicon dioxide (SiO<sub>2</sub>). O 1s and C 1s signals were observed for all SiO<sub>x</sub> films. The excess carbon signal observed for the thicker SiO<sub>x</sub> films can likely be attributed to the self-limiting nature of the UV ozone conversion process. As the PDMS is converted into SiO<sub>x</sub>, newly formed SiO<sub>x</sub> at the top of the overlayer can become a diffusion barrier that suppresses complete conversion of PDMS located closer to the SiO<sub>x</sub>|substrate interface.<sup>64</sup> As

a result, complete or nearly-complete conversion of PDMS to SiO<sub>x</sub> is typically limited to films with thickness less than 20-30 nm.<sup>73</sup> As expected, the sample with the thickest SiO<sub>x</sub> overlayer ( $t_{\text{SiO}_x}$ =19.8 nm) was found to contain the highest carbon content (11 atomic %), while the samples with the thinner SiO<sub>x</sub> overlayers ( $t_{\text{SiO}_x}$ =1.9 nm and 4.6 nm) contained the lowest residual carbon ( $\approx$ 7 atomic %). This residual C may have affected the refracted index in SE measurements and subsequent porosity calculations, however the influence could not be quantified and was not accounted for in the porosity calculation. The binding energies of the Si 2p, O 1s, and C 1s spectra were corrected for sample charging by applying a uniform shift in the binding energy scale to set the C 1s peak center to 284.8 eV. Even after this correction, the Si 2p peak center for the  $t_{\text{SiO}_x}$ =19.8 nm sample is shifted to higher binding energy (+0.4 eV) compared to the  $t_{\text{SiO}_x}$ = 1.9 nm sample. This shift is possibly due to non-uniform charging effects and/or uneven distributions of unconverted carbon in the thicker SiO<sub>x</sub> that could result in the under-correction of the Si 2p signal based on the adjusted C 1s peak center. Pt 4f spectra for the same samples are provided in Figure 4.4b and contain peak locations consistent with metallic Pt.<sup>78</sup> The Pt 4f peak area decreases monotonically with increasing SiO<sub>x</sub> thickness and eventually disappears for the sample with  $t_{\text{SiO}_x}$ =19.8 nm due to screening from the SiO<sub>x</sub> overlayer. The absence of significant Pt 4f signal for the  $t_{\text{SiO}_x}$ = 9.4 nm and  $t_{\text{SiO}_x}$ = 19.8 nm samples corroborates the AFM measurements which showed a low coverage of holes that and holes that did not penetrate down to the Pt surface.



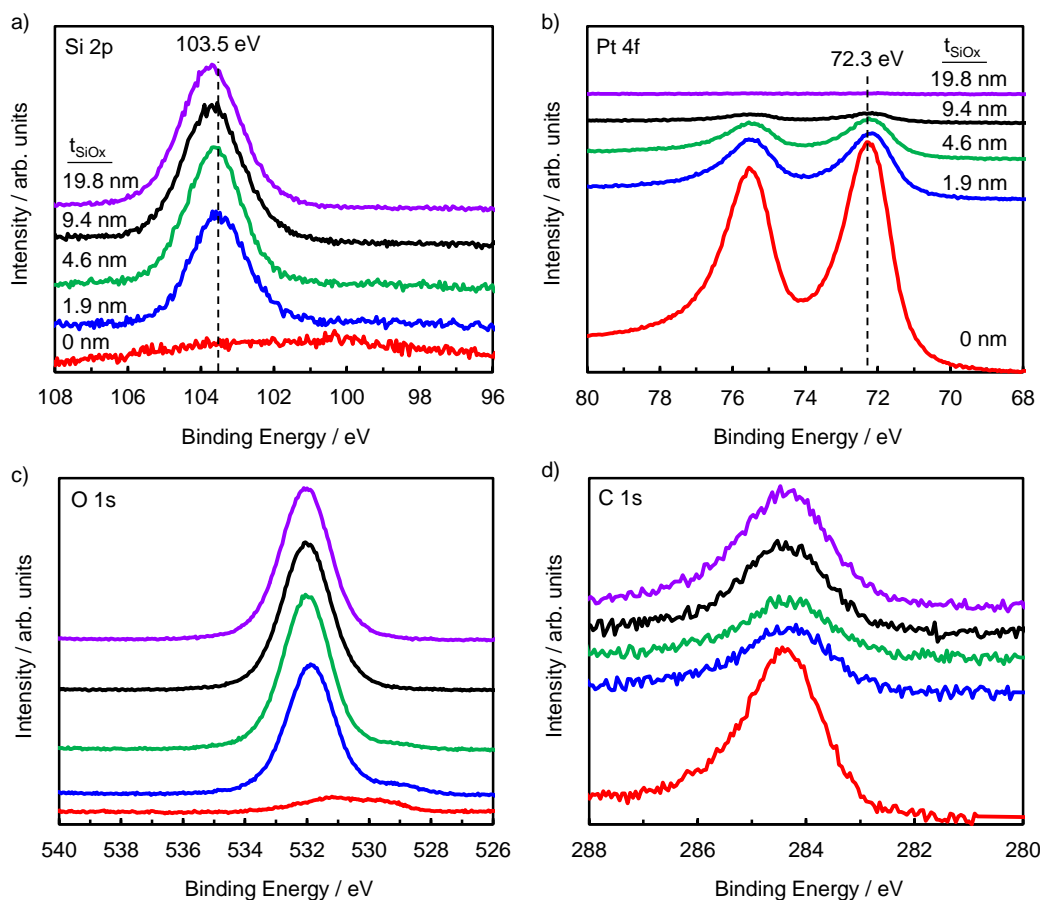


Figure 4.4. XPS characterization of  $\text{SiO}_x$  overlayer. X-ray photoelectron spectra of  $\text{SiO}_x/\text{Pt}$  electrodes a.) Si 2p, b.) Pt 4f, c.) O 1s, and d.) C 1s for various  $\text{SiO}_x$  thicknesses:  $t_{\text{SiO}_x}=0$  nm (red),  $t_{\text{SiO}_x}=1.9$  nm (blue),  $t_{\text{SiO}_x}=4.6$  nm (green),  $t_{\text{SiO}_x}=9.4$  nm (black), and  $t_{\text{SiO}_x}=19.8$  nm (purple). The C 1s peaks were shifted and centered to 284.8 eV and the O 1s peaks associated with the  $\text{SiO}_x$  overlayers were shifted by the same amount.

#### 4.3.3 Electrochemically Active Surface Area of $\text{SiO}_x$ -Encapsulated Pt Thin Films

The electrochemically active surface areas (ECSAs) of all electrodes were characterized in two separate experiments by analyzing the signal associated with hydrogen underpotential deposition ( $\text{H}_{\text{upd}}$ ) and copper underpotential deposition ( $\text{Cu}_{\text{upd}}$ ).

#### 4.3.3.1 Hydrogen Underpotential Deposition

The  $H_{\text{upd}}$  on  $\text{SiO}_x/\text{Pt}$  MCEC electrodes were measured by performing cyclic voltammetry (CV) in 0.1 M  $\text{H}_2\text{SO}_4$  at scan rates between  $1 \text{ mV s}^{-1}$  and  $100 \text{ mV s}^{-1}$ . Figure 4.5a contains the CV curves measured at the fastest scan rate ( $100 \text{ mV s}^{-1}$ ), from which it can be seen that the  $H_{\text{upd}}$  signal decreases monotonically with increasing  $\text{SiO}_x$  thickness. CV curves were also performed at slower scan rates to observe the possible influence of  $\text{H}^+$  diffusion, into and out of the  $\text{SiO}_x$  overlayer, on the integrated  $H_{\text{upd}}$  signal. Diffusion tends to be a much slower process than adsorption and desorption, such that the steady-state coverage of  $H_{\text{upd}}$  at the buried  $\text{Pt}/\text{SiO}_x$  interface might not be achieved during fast scan CV measurements. As a consequence, the integrated  $H_{\text{upd}}$  signal and ECSA of MCEC electrodes can be underestimated at fast scan rates. Consistent with this logic, Figure 4.5b shows that the  $H_{\text{upd}}$  features for the 1.9 nm, 4.6 nm, and 9.4 nm  $\text{SiO}_x/\text{Pt}$  samples become much sharper at a slower scan rate ( $25 \text{ mV s}^{-1}$ ). Concurrently, the integrated  $H_{\text{upd}}$  signal of MCEC samples measured at slower scan rates approach that of the bare Pt control (Figure 4.5c), which exhibits an integrated  $H_{\text{upd}}$  signal with minimal dependency on scan rate. The integrated  $H_{\text{upd}}$  signal at slow scan rates thus provides a more accurate measure of the ECSA for  $\text{SiO}_x/\text{Pt}$  MCEC electrodes. The ECSA of each electrode was determined from the average of the integrated  $H_{\text{upd}}$  adsorption and desorption charges and the resulting values at  $25 \text{ mV s}^{-1}$  are provided in Table 4.1.

Although the CV curves for the 19.8 nm thick  $\text{SiO}_x$  MCEC electrode produced minimal  $H_{\text{upd}}$  signal, Figures 4.5a-c reveal that the electrodes with 1.9 nm, 4.6 nm, and 9.4 nm of  $\text{SiO}_x$  exhibited substantial  $H_{\text{upd}}$  signal. Importantly, the measured ECSA values for these  $\text{SiO}_x$ -encapsulated electrodes are significantly larger than the area that what would be expected if the only ECSA on these samples were the Pt sites located at the bottom of the holes that were observed in AFM measurements. Moreover, the ECSAs determined from CVs at fast scan rates represent

lower limits on the ECSA of the SiO<sub>x</sub>|Pt MCEC samples, and yet the ECSAs are still higher than the coverage of holes. This finding indicates that protons are able to reach a much higher fraction of the Pt surface than what may be directly exposed to the electrolyte through the holes in the SiO<sub>x</sub> overlayer. Stated otherwise, H<sub>upd</sub> characterization suggests that Pt located immediately beneath the SiO<sub>x</sub> overlayers is still electrochemically accessible, and that protons are able to access the buried Pt|SiO<sub>x</sub> interface by diffusing *through* the SiO<sub>x</sub> overlayer.

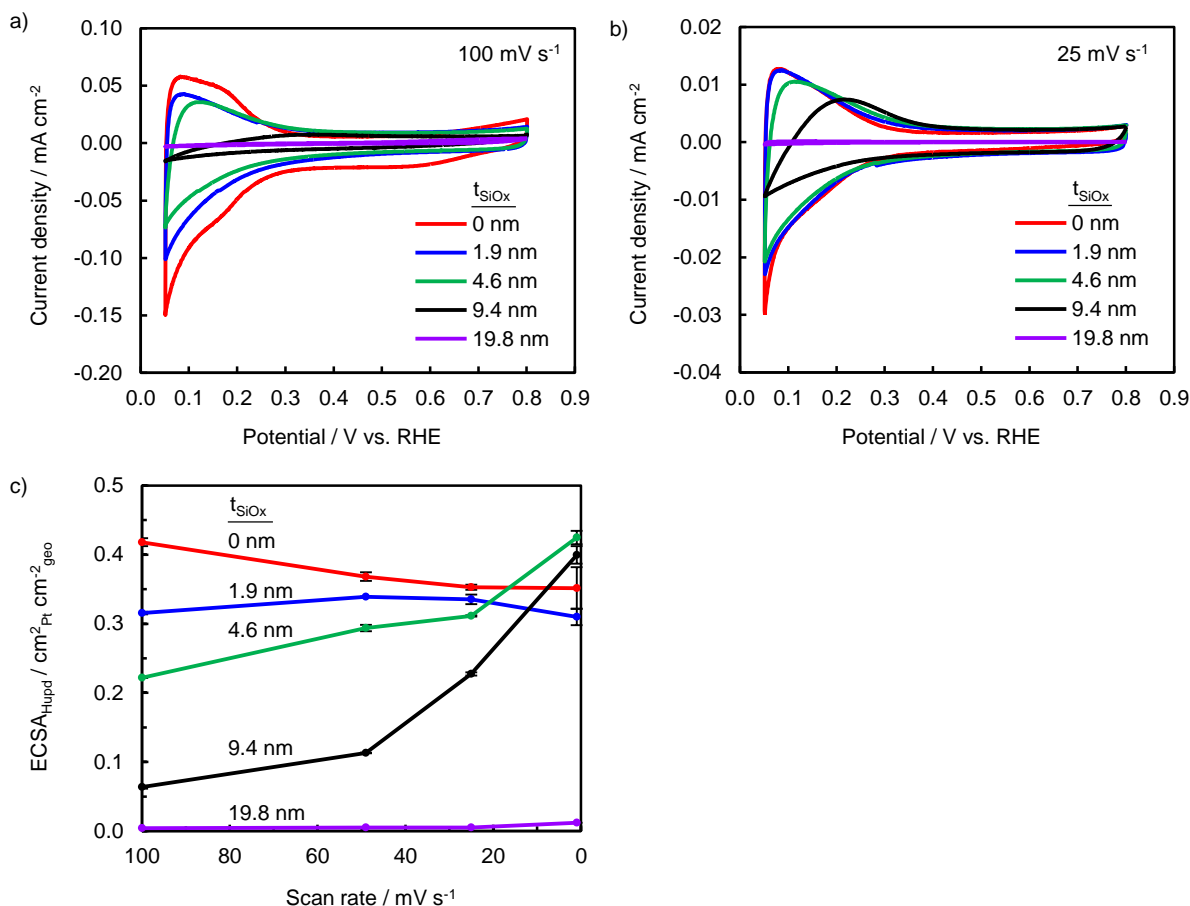


Figure 4.5. Measuring ECSA with H<sub>upd</sub>. a.) CV H<sub>upd</sub> in deaerated 0.1 M H<sub>2</sub>SO<sub>4</sub> for SiO<sub>x</sub>|Pt electrodes containing:  $t_{\text{SiO}_x}$ =0 nm (red),  $t_{\text{SiO}_x}$ =1.9 nm (blue),  $t_{\text{SiO}_x}$ =4.6 nm (green),  $t_{\text{SiO}_x}$ =9.4 nm (black), and  $t_{\text{SiO}_x}$ =19.8 nm (purple) SiO<sub>x</sub> films at 100 mV s<sup>-1</sup> and b.) 25 mV s<sup>-1</sup> in. c.) H<sub>upd</sub> determined ECSAs at different scan rates for SiO<sub>x</sub>|Pt electrodes in (a). Error bars represent 2-sided 95% confidence intervals based on repeated CV measurements.

#### 4.3.3.2 Copper Stripping

The ECSAs of all electrodes were also characterized by analyzing the net charge associated with voltammetric stripping of underpotentially deposited Cu ( $\text{Cu}_{\text{upd}}$ ). In these experiments,  $\text{Cu}^{2+}$  ions are first reduced to form a single layer of adsorbed Cu atoms by underpotential deposition onto electrochemically active Pt during a 50 second potentiostatic pulse at  $E = 0.36 \text{ V vs. RHE}$  ( $E_{\text{Cu/Cu}^{2+}}^0 = 0.32 \text{ V vs. RHE}$ ). Next, adsorbed  $\text{Cu}_{\text{upd}}$  atoms are stripped from the Pt surface when they are oxidized back to  $\text{Cu}^{2+}$  during an LSV scan to a potential of  $E = 1 \text{ V vs. RHE}$ . As in the  $\text{H}_{\text{upd}}$  analysis, the number of  $\text{Cu}_{\text{upd}}$  atoms originally adsorbed onto the Pt surface are then “counted” by analyzing the integrated charge associated with the stripping LSV curve.

In Figure 4.6a, a Cu stripping voltammogram for the bare Pt electrode shows distinct oxidation peaks associated with oxidation of the  $\text{Cu}_{\text{upd}}$ .<sup>80</sup> The ECSAs determined from Cu stripping measurements are summarized in Table 4.1. Based on the literature value of  $420 \mu\text{C cm}^{-2}$  Pt for Cu stripping,<sup>80</sup> integration of the Cu stripping oxidation peak for the Pt control electrode gives a Pt ESCA of  $1 \text{ cm}^2 \text{ Pt per cm}^2$  of geometric area, as expected for a smooth, continuous Pt surface. In sharp contrast to the Cu stripping behavior for the bare Pt electrode, Cu stripping measurements of the  $\text{SiO}_x/\text{Pt}$  MCEC electrodes show that the presence of the  $\text{SiO}_x$  layer significantly suppresses the  $\text{Cu}_{\text{upd}}$  signal that is characteristic of a Pt surface exposed to a Cu-containing electrolyte (Figure 4.6a,b). The fact that the Cu stripping LSV curve for the  $\text{SiO}_x/\text{Pt}$  MCECs are nearly identical to the curve measured in the supporting electrolyte indicates that the  $\text{SiO}_x$  layer blocks transport of  $\text{Cu}^{2+}$  to the underlying Pt. Collectively, the results of the  $\text{H}_{\text{upd}}$  and  $\text{Cu}_{\text{upd}}$  measurements suggest that the  $\text{SiO}_x$  overlayers are permeable to  $\text{H}^+$  but not  $\text{Cu}^{2+}$ .

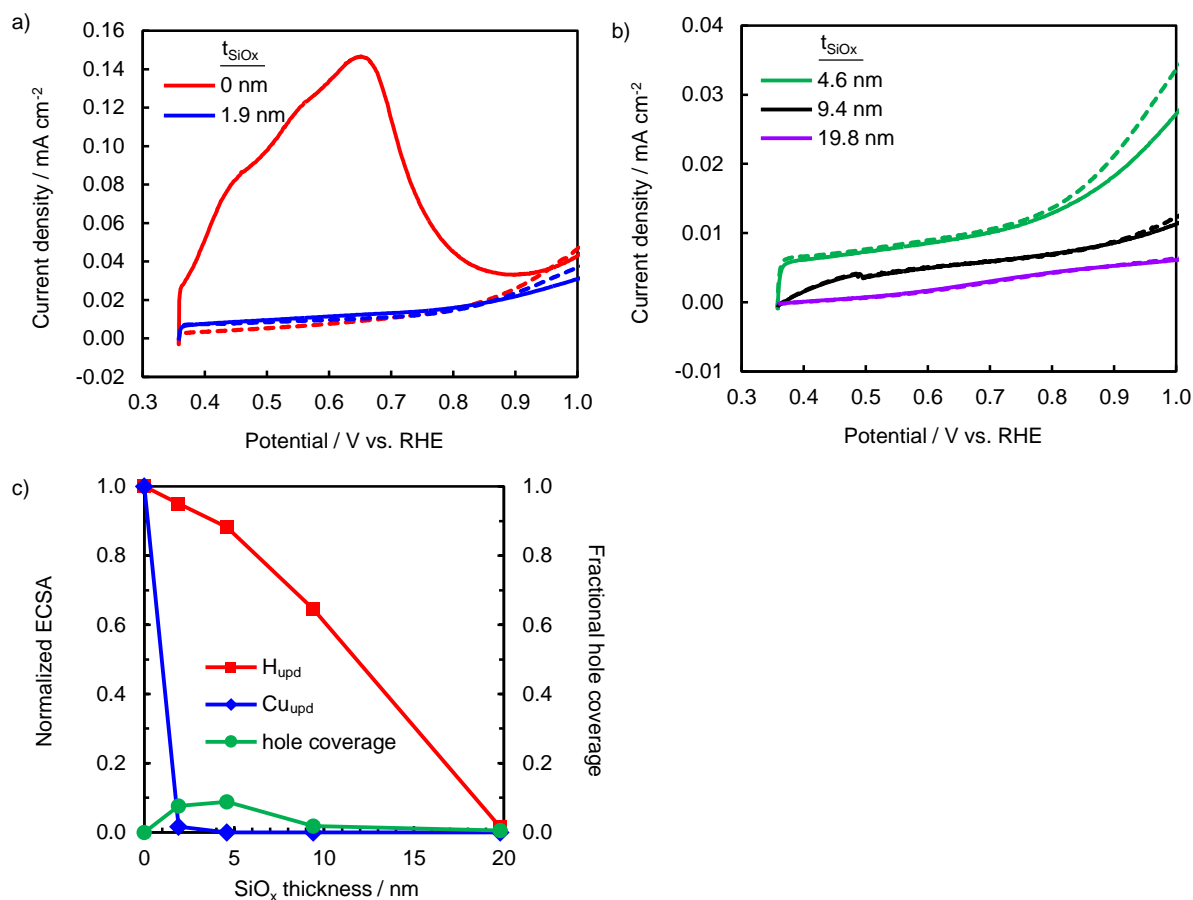


Figure 4.6. Measuring ECSA with  $\text{Cu}_{\text{upd}}$ . Cu stripping in 2 mM  $\text{CuSO}_4$  and 0.1 M  $\text{H}_2\text{SO}_4$  (solid curves) and background current in the 0.1 M  $\text{H}_2\text{SO}_4$  supporting electrolyte (dashed curves) at 100 mV s<sup>-1</sup> for a.)  $t_{\text{SiO}_x}=0$  nm (red) and  $t_{\text{SiO}_x}=1.9$  nm (blue), and b.)  $t_{\text{SiO}_x}=4.6$  nm (green),  $t_{\text{SiO}_x}=9.4$  nm (black), and  $t_{\text{SiO}_x}=19.8$  nm (purple)  $\text{SiO}_x/\text{Pt}$  electrodes. c.)  $H_{\text{upd}}$  (red) and  $\text{Cu}_{\text{upd}}$  (blue) determined ECSAs normalized by the respective  $H_{\text{upd}}$  (at 25 mV s<sup>-1</sup>) and  $\text{Cu}_{\text{upd}}$  determined ECSAs for the bare Pt electrode and the fraction hole coverage from AFM (green) for each  $\text{SiO}_x/\text{Pt}$  electrode. All measurements were performed in deaerated solutions.

Table 4.1 Characterization of  $\text{SiO}_x$  overlayers deposited on Pt thin films, including characterization of  $\text{SiO}_x$  thickness (based on ellipsometry), hole coverage (based on AFM images), and ECSA (based on  $H_{\text{upd}}$  and  $\text{Cu}_{\text{upd}}$  measurements in Figure 4.5 and 4.6).

SiO <sub>x</sub> thickness (nm)	Areal hole coverage (cm <sup>2</sup> holes/ geometric area cm <sup>2</sup> )	H <sub>upd</sub> surface area (cm <sup>2</sup> Pt/ geometric area cm <sup>2</sup> )	Cu <sub>upd</sub> surface area (cm <sup>2</sup> Pt/ geometric area cm <sup>2</sup> )
0	n/a	0.350	1.0
1.9 ± 0.1	0.076	0.340	0.016
4.6 ± 0.4	0.088	0.310	n/a <sup>b</sup>
9.4 ± 0.1	0.018	0.230	n/a <sup>b</sup>
19.8 ± 0.5	0.005	< 0.005 <sup>a</sup>	n/a <sup>b</sup>

<sup>a</sup> H<sub>upd</sub> signal was difficult to deconvolute from capacitance signal

<sup>b</sup> Cu stripping signal was difficult to distinguish from background current measured in the supporting electrolyte.

The combination of the H<sub>upd</sub>, Cu<sub>upd</sub>, and AFM characterization measurements (Table 4.1) can provide useful insights into the nature of the Pt at the bottom of the holes in the SiO<sub>x</sub>. Figure 4.6c summarizes the results of the normalized H<sub>upd</sub>- and Cu<sub>upd</sub>-determined ECSAs, and compares those values to the hole coverages determined from AFM for each SiO<sub>x</sub> thickness. The Cu<sub>upd</sub>-determined Pt ECSAs of the SiO<sub>x</sub>-coated Pt electrodes are much lower than the coverage of holes observed in AFM. The fact that Cu<sup>2+</sup> ions are still unable to adsorb onto Pt, despite the presence of the 20-300 nm diameter holes, suggests that these holes do not penetrate through to the underlying Pt substrate. If the SiO<sub>x</sub> layers are impermeable to Cu<sup>2+</sup> and the Pt sites at the bottom of the holes are directly exposed to the Cu-containing electrolyte, then the areal coverage of the holes should correspond to the ECSA determined from Cu<sub>upd</sub>. However, this is not the case. The hole coverage of the t<sub>SiO<sub>x</sub></sub>=1.9 nm SiO<sub>x</sub> sample was 7.6 %, yet Cu<sub>upd</sub> measurements indicated that only 1.6% of the Pt surface on the electrode was in direct contact with the electrolyte. By contrast, the 4.6 nm, 9.4 nm, and 19.8 nm SiO<sub>x</sub>|Pt electrodes completely suppressed Cu stripping curves, which suggests that ultrathin layers of SiO<sub>x</sub> and/or carbonaceous residue still exist at the bottoms of the holes, as illustrated in Figure 4.1b, preventing Cu<sup>2+</sup> from adsorbing onto Pt. These results are consistent with the average hole depths normalized to the SiO<sub>x</sub> thickness (Figure 4.3f), which is an indicator of the extent of hole propagation through the SiO<sub>x</sub> film. The average hole depth of

the 1.9 nm SiO<sub>x</sub>|Pt electrode penetrated the deepest into the SiO<sub>x</sub> film (77%, 1.5 nm), whereas the holes on the 4.6 nm, 9.4 nm, and 19.8 nm SiO<sub>x</sub>|Pt electrodes were on average only penetrating 65% (3.0 nm), 25% (2.4 nm), and 12% (2.4 nm) into the SiO<sub>x</sub>. Therefore, the combination of H<sub>upd</sub>, Cu<sub>upd</sub>, and AFM measurements indicates that the Pt located beneath the holes in the SiO<sub>x</sub> overlayers is not directly exposed to the electrolyte, and strongly supports the conclusion that protons reaching the Pt surface during H<sub>upd</sub> measurements are primarily transported *through* the SiO<sub>x</sub> overlayer.

#### 4.3.4 Hydrogen Evolution Reaction Performance

The HER performance of the SiO<sub>x</sub>|Pt MCEC electrodes was evaluated by carrying out LSVs in deaerated 0.1 M H<sub>2</sub>SO<sub>4</sub> immediately after completion of the CV measurements in Figure 4.5a (Figure 4.7). For all electrodes, the onset potential for HER is observed around 0.0 V vs. RHE, as expected for Pt HER catalysts. However, the slopes of the LSV curves for the SiO<sub>x</sub>|Pt electrodes decrease with increasing SiO<sub>x</sub> thickness. This is most pronounced for the thicker t<sub>SiO<sub>x</sub></sub> = 9.4 nm and t<sub>SiO<sub>x</sub></sub> = 19.8 nm SiO<sub>x</sub>|Pt electrodes, where the current densities do not exceed -5 mA cm<sup>-2</sup> and -0.4 mA cm<sup>-2</sup>, respectively.

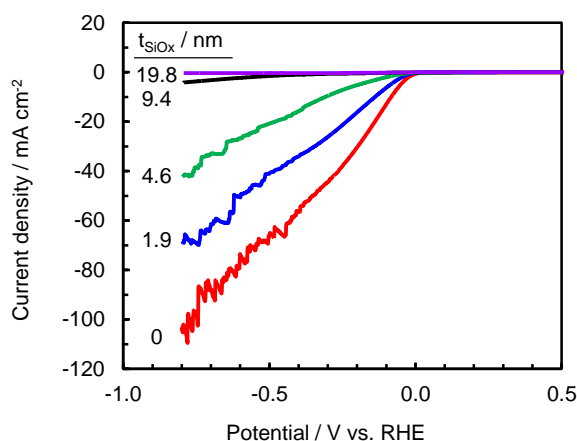


Figure 4.7. H<sub>2</sub> evolution activity of SiO<sub>x</sub>|Pt thin film electrocatalysts. LSV measurements in 0.1 M H<sub>2</sub>SO<sub>4</sub> for “x” nm SiO<sub>x</sub>|Pt for various SiO<sub>x</sub> thicknesses from 0 nm < x < 20 nm. All measurements were performed at 20 mV s<sup>-1</sup> in deaerated solutions.

The LSV curves for the 1.9 nm and 4.6 nm SiO<sub>x</sub>|Pt MCEC electrodes reached relatively large HER current densities, although they did incur additional overpotential losses compared to the bare Pt control. These losses cannot be attributed to a loss in ECSA, since the ECSA for the samples with thin SiO<sub>x</sub> overlayers ( $t_{\text{SiO}_x} < 9.4$  nm) was found to be very similar to that for the bare Pt control sample. Instead, these overpotential losses must be explained by either (i.) a decrease in the intrinsic HER activity at the buried Pt|SiO<sub>x</sub> interface, and/or (ii.) an increase in mass transfer overpotential associated with H<sup>+</sup> and H<sub>2</sub> diffusion through the SiO<sub>x</sub> layer. The strong correlation between HER overpotential and SiO<sub>x</sub> thickness suggests that mass transport through the SiO<sub>x</sub> overlayer is responsible for most of the increased overpotential, since mass transport losses are expected to be highly dependent on the thickness of the layer through which diffusion is taking place. By contrast, it is unlikely that the intrinsic HER activity at the buried Pt|SiO<sub>x</sub> interface would be strongly affected by the thickness of the SiO<sub>x</sub> overlayer. The Tafel slope of 37 mV dec<sup>-1</sup> and exchange current density of  $7.2 \times 10^{-4}$  A cm<sup>-2</sup><sub>Pt</sub> for the bare Pt electrode are comparable to literature values of 30 mV dec<sup>-1</sup> and  $1 \times 10^{-3}$  A cm<sup>-2</sup><sub>Pt</sub> respectively (Appendix section 4.6.2, Figure 4.13).<sup>86–88</sup> If it is assumed that the HER catalytic activity of the buried Pt|SiO<sub>x</sub> interface is comparable to that of bare Pt, then the shift in the operating potential for a MCEC electrode relative to the bare Pt electrode can be considered to be the mass transport overpotential loss associated with H<sup>+</sup> and H<sub>2</sub> diffusion through the SiO<sub>x</sub> film. Despite the presence of additional overpotential losses, Figure 4.7 shows that MCEC electrodes are still able to support relatively high HER currents.



#### **4.3.5 Evaluating the Contribution of Holes in SiO<sub>x</sub> Overlayers to HER Current**

Substantial HER current densities are observed for SiO<sub>x</sub>|Pt MCEC electrodes with ultrathin SiO<sub>x</sub> overlayers, but a crucial issue to address is the extent to which HER takes place at Pt at the buried Pt|SiO<sub>x</sub> interface as compared to HER at Pt that is possibly exposed to the electrolyte at the bottom of the holes in the SiO<sub>x</sub>. Two experiments were carried out to address this question.

##### **4.3.5.1 HER Performance for SiO<sub>x</sub> Bilayer Electrode**

First, a bilayer electrode was fabricated in which two 1.9 nm thick layers of SiO<sub>x</sub> were sequentially deposited onto the Pt thin film electrode (see schematic in Figure 4.8a,b). Figure 4.8c and 4.8d show AFM images after deposition of the first and second SiO<sub>x</sub> layers, respectively. The first SiO<sub>x</sub> layer contains hole features that are similar to those observed on the other electrodes investigated in this study, with hole depths similar to the SiO<sub>x</sub> film thickness as measured by ellipsometry. After the second SiO<sub>x</sub> layer was deposited, holes still remain, but AFM line scans show that the depth of the holes in the bilayer sample are equal to the thickness of the second SiO<sub>x</sub> layer by itself, as opposed to the cumulative thickness of the SiO<sub>x</sub> bilayer. These AFM measurements show that the second SiO<sub>x</sub> layer effectively filled in the holes of the first layer such that few, if any holes in the bilayer penetrate all the way through the SiO<sub>x</sub> to the underlying Pt. Figure 4.8e shows the HER performance of the 3.8 nm bilayer SiO<sub>x</sub>|Pt electrode, for which the LSV curve falls directly between those for the 1.9 nm and 4.6 nm SiO<sub>x</sub>|Pt electrodes (data from Figure 4.7), as expected. The relatively large current densities are comparable to those seen in Figure 4.7 for the 4.6 nm single-layer SiO<sub>x</sub>|Pt electrode, and provide further evidence that a substantial portion of HER taking place on these SiO<sub>x</sub>-coated Pt electrodes involves proton and H<sub>2</sub> transport *through* the SiO<sub>x</sub> layer.

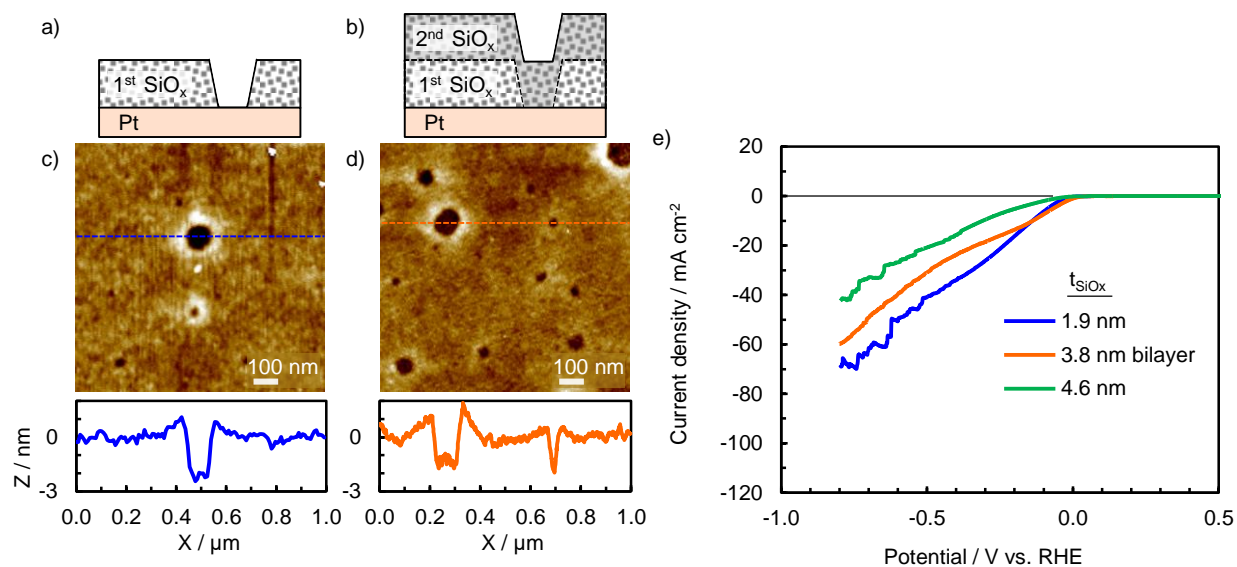


Figure 4.8. H<sub>2</sub> evolution activity of a bilayer SiO<sub>x</sub>|Pt electrode. Schematic side view illustrating the sequential deposition of the a.) first and b.) second SiO<sub>x</sub> layer to create the bilayer SiO<sub>x</sub>|Pt electrode. AFM images of a c.)  $t_{\text{SiO}_x}$ =1.9 nm SiO<sub>x</sub>|Pt electrode and d.) the same electrode after an additional  $t_{\text{SiO}_x}$ =1.9 nm SiO<sub>x</sub> layer. e.) LSV measurement in 0.1 M H<sub>2</sub>SO<sub>4</sub> for the bilayer SiO<sub>x</sub>|Pt MCEC described in (d). All measurements were performed at 20 mV s<sup>-1</sup> in deaerated solutions.

#### 4.3.5.2 HER Performance in the Presence of a Poison

The second experiment used to analyze the contribution of HER taking place through holes in the SiO<sub>x</sub> overlayer was a constant-current (chronopotentiometry (CP)) HER stability measurement carried out in the presence of a catalyst poison. The ideal poison species for this experiment is one that is not able to transport through the SiO<sub>x</sub> overlayer, but can readily deposit onto any Pt that is exposed to the bulk electrolyte and thereby significantly decrease the HER activity. For this study, Cu<sup>2+</sup> was selected as a model poison since it is well-known to suppress HER activity of Pt.<sup>89</sup> Furthermore, the ECSA analysis in Figure 4.6 revealed that Cu<sup>2+</sup> is unable to penetrate through the thin SiO<sub>x</sub> overlayers.

The copper tolerance of the MCEC electrode was evaluated by recording the potential as a function of time at  $-5 \text{ mA cm}^{-2}$  for 1 hour. Figures 4.9a and 4.9b show the CP experiments for a bare Pt control electrode (0 nm  $\text{SiO}_x$ ) and a 4.6 nm  $\text{SiO}_x|\text{Pt}$  MCEC electrode, respectively, in 0.5 M  $\text{H}_2\text{SO}_4$  with and without 0.2 mM  $\text{CuSO}_4$ . First, CP measurements were conducted in pristine 0.5 M  $\text{H}_2\text{SO}_4$ . Both electrodes demonstrated stable performance, although the 4.6 nm  $\text{SiO}_x|\text{Pt}$  MCEC electrode operated at an additional 100 mV overpotential compared to the bare Pt electrode. This can be attributed to mass transport losses through the  $\text{SiO}_x$  layer. Next, CP measurements were repeated in the presence of 0.2 mM  $\text{CuSO}_4$ . The bare Pt control electrode quickly incurred a  $\approx 400$  mV increase in overpotential due to catalysis poisoning whereby metallic Cu deposited on the Pt surface. In contrast, the operating potential of the  $\text{SiO}_x|\text{Pt}$  electrode remained nearly unchanged in the presence of  $\text{Cu}^{2+}$ , with only a  $\approx 20$  mV increase in overpotential. SEM images taken after the poisoning experiment reveal the presence of a continuous copper film on the bare Pt electrode and large Cu particles on the  $\text{SiO}_x|\text{Pt}$  electrode (Figures 4.9c,d). XPS measurements also show that the  $\text{SiO}_x$  overlayer remains intact after the Cu poisoning test, with an O/Si ratio of 2.0 (see Appendix section 4.6.3, Figure 4.14). The presence of Cu particle deposits on the  $\text{SiO}_x$  films can be the result of Cu deposition onto the top of the  $\text{SiO}_x$ .

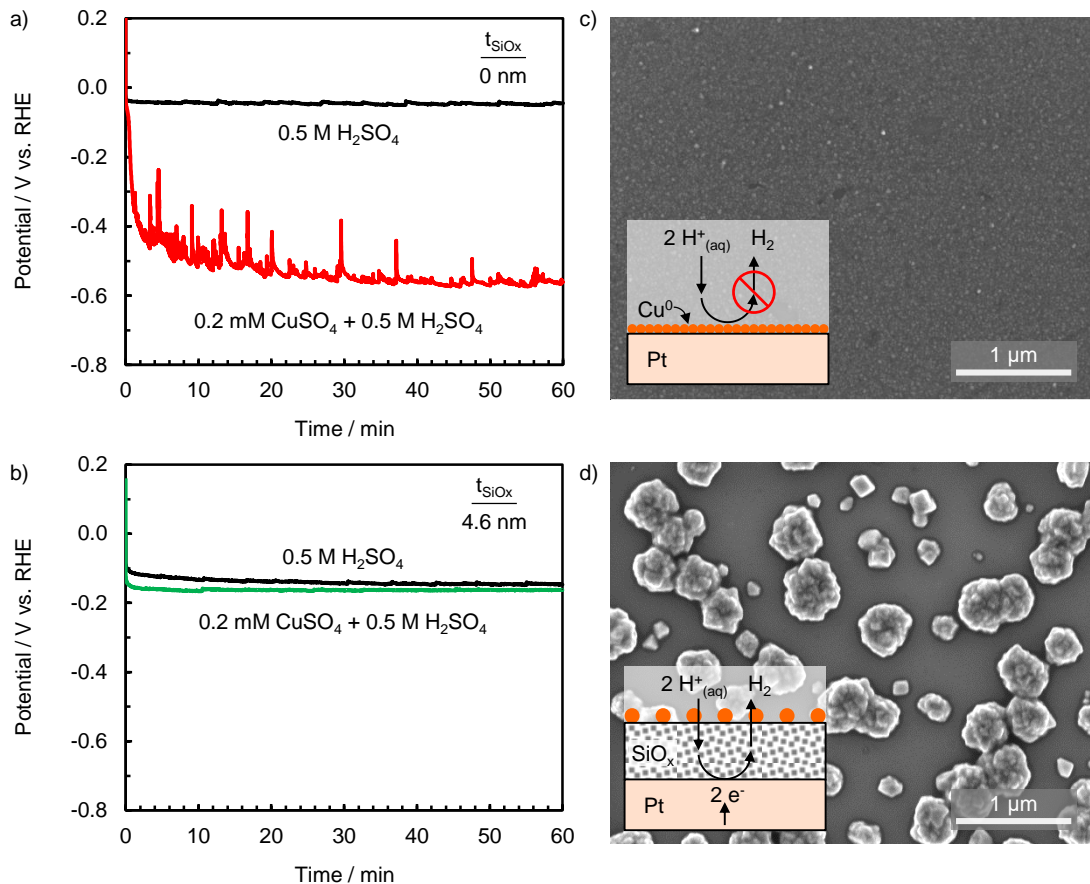


Figure 4.9 Measuring selective proton transport through  $\text{SiO}_x$ . Constant current ( $-5 \text{ mA cm}^{-2}$ ) stability tests conducted on a.)  $t_{\text{SiO}_x} = 0 \text{ nm}$  (red) and b.)  $t_{\text{SiO}_x} = 4.6 \text{ nm}$  (green)  $\text{SiO}_x|\text{Pt}$  electrodes in  $0.5 \text{ M H}_2\text{SO}_4$  with and without (black)  $0.2 \text{ mM CuSO}_4$ . SEM images of Cu deposits on c.)  $t_{\text{SiO}_x} = 0 \text{ nm}$  and d.)  $t_{\text{SiO}_x} = 4.6 \text{ nm}$   $\text{SiO}_x|\text{Pt}$  electrodes after the 1 hour CP experiment in  $0.2 \text{ mM CuSO}_4$  from a) and b).

Electrodeposition on  $\text{SiO}_x$  can be explained by the results in Chapter 3 which showed that  $\text{SiO}_x$  overlayers deposited by the UV ozone method exhibit a small degree of electrical conductivity.<sup>35</sup> However,  $\text{SiO}_x$  itself is not an active HER catalyst (see Appendix section 4.6.4, Figure 4.15), indicating that any Cu deposits at the  $\text{SiO}_x|\text{electrolyte}$  interface should not directly affect the HER overpotential. It is also possible that the locations of Cu particles coincide with a small fraction of holes in the  $\text{SiO}_x$  overlayer that penetrate to the Pt surface. Nonetheless, the presence of the Cu particles on the  $\text{SiO}_x|\text{Pt}$  electrode did not have much of an effect on the HER

performance of the underlying Pt at the buried interface, indicating that the SiO<sub>x</sub> still enables facile transport of protons and H<sub>2</sub> between the bulk electrolyte and encapsulated Pt (Figure 4.8d, inset). This result further demonstrates the ability of the SiO<sub>x</sub> overlayers to function as selective nanomembranes while validating the hypothesis that the HER is occurring primarily at the buried Pt|SiO<sub>x</sub> interface, as opposed to any Pt this may be exposed at the bottom of holes in the SiO<sub>x</sub>. If the HER occurred primarily through the holes, Cu would deposit in those areas of highest activity, quickly decreasing HER activity and thereby increase the required overpotential, as was observed for the bare (unprotected) Pt electrode.

## 4.4 Discussion

This work has employed well-defined, planar SiO<sub>x</sub>|Pt MCECs to better understand their electrochemical properties and evaluate their HER behavior. These MCECs offer exciting opportunities for enhancing electrocatalyst stability<sup>19,35–40</sup> and enabling advanced functionalities.

### 4.4.1 SiO<sub>x</sub> Selectivity

One advanced functionality demonstrated in this study was the resistance of the Pt HER catalysts to poisoning by Cu<sup>2+</sup>, which suggests that the SiO<sub>x</sub> overlayer facilitates selective transport of H<sup>+</sup> while blocking diffusion and/or migration of Cu<sup>2+</sup> ions to the buried Pt|SiO<sub>x</sub> interface. This observation was consistent with Cu<sub>upd</sub> measurements (Figure 4.6), and furthermore provides insight into the factors that affect species permeability, thus transport, through the SiO<sub>x</sub> nanomembrane. The differences in the permeabilities of H<sup>+</sup>, H<sub>2</sub>, and Cu<sup>2+</sup> are most likely tied to differences in their size, charge, and/or chemical interactions with SiO<sub>x</sub>, and furthermore expected to be highly dependent on the structure and surface chemistry of the SiO<sub>x</sub> layer itself. Size-selective transport has been frequently reported for microporous materials such as metal organic frameworks<sup>90</sup> and zeolites,<sup>91</sup> for which transport can be highly sensitive to the relative sizes of the

species being transported compared to the effective pore diameter(s) within these materials. Of the electroactive species investigated in this study, the hydrated radius of  $H^+$  (2.82 Å) is significantly smaller than the hydrated radii of  $Cu^{2+}$  (4.19 Å).<sup>92</sup> The smaller hydrated radius of protons may allow size selective diffusion through the interstitial spaces and/or pores in the  $SiO_x$  layers, which EP measurements indicated have pore sizes less than 5.8 Å (Figure 4.12). Electrostatic and/or chemical interactions of species with the  $SiO_x$  may also play a role in imparting selective transport properties. In strongly acidic solutions such as those used in this work,  $SiO_x$  surface chemistry is usually governed by the polar silanol groups ( $Si-OH$ ),<sup>93</sup> which can lead to electrostatic interactions with other ions in solution. As a result, divalent cations such as  $Cu^{2+}$  are expected to experience a stronger repulsive force than uncharged species or monovalent cations such as  $H_2$  or  $H^+$ , respectively. The formation of silanol groups may also encourage proton transport  $SiO_x$  via ion-exchange or hydrogen bonding interactions.<sup>94,95</sup>

When chemical and/or electronic interactions between the transported species (i.e. “the permeant”) and the membrane dominate the selective uptake and diffusion of the former across the latter, the permeant is often viewed as a solute that has been dissolved inside of the solid phase.<sup>96,97</sup> Under such conditions, permeant transport through a nonporous membrane is often described by solution-diffusion theory.<sup>96,97</sup> Although EP measurements indicated the  $SiO_x$  film is porous, compared to a nonporous bulk  $SiO_2$ , the porosity and pore sizes are very small<sup>96</sup> such that it is still reasonable to describe selective transport across  $SiO_x$  with solution-diffusion theory. According to this theory, the transport of permeant species can be described by Fick’s law, and those species possessing higher solubility within the membrane can achieve larger concentration gradients and therefore higher fluxes.<sup>96,97</sup> Consequently, separation/selectivity arises from differences in species solubility and diffusivity within the  $SiO_x$  membrane.  $H^+$  solubility and

mobility within  $\text{SiO}_x$  may be enhanced, compared to other ions, by a proton hopping mechanism whereby  $\text{H}^+$  diffuses through  $\text{SiO}_2$  by repeatedly associating and dissociating with O atoms in  $\text{SiO}_2$ .<sup>61,62,98</sup> Similar interactions with O atoms are expected to be less energetically favorable with metal ions like  $\text{Cu}^{2+}$ , leading to low solubility and permeability of those ions within the  $\text{SiO}_x$ . Therefore, the poison resistance of  $\text{SiO}_x$ -based MCECs studied in this work may arise from a combination of factors. Future experiments and simulations that systematically explore the effects of molecular-level properties of permeant and  $\text{SiO}_x$  nanomembranes on MCEC performance will be essential for enabling the rational design of MCECs for poison resistance and other advanced functionalities.

#### 4.4.2 $\text{SiO}_x$ Permeability

One important MCEC design consideration is the optimal overlayer thickness that achieves the desired stability/catalysis benefits while minimizing overpotential losses associated with species transport through the nanomembrane. This additional overpotential loss is commonly referred to as a concentration overpotential ( $\eta_{conc}$ ), which results from differences in the concentrations of reactants and products at the buried interface compared to those in the bulk electrolyte. Quantifying these losses in nanoparticle-based electrocatalysts has been elusive due to the heterogeneous nature of those samples, but the well-defined thin film electrodes in this study provide a great opportunity to elucidate the relationship between permeability,  $\text{SiO}_x$  thickness,  $\eta_{conc}$ , and operating current density through a simple, 1D model. To understand this relationship, the LSV measurements in Figure 4.7 were modeled with a combination of ohmic, bulk mass transfer, kinetic, and  $\eta_{conc}$  losses. To account for ohmic  $iR$  losses, the LSVs were  $iR$  corrected based on EIS measured series resistances, which were approximately the same for all electrodes (see section 4.2.3.1). Next, it was assumed that the sum of the mass transfer losses in the bulk

electrolyte,  $\eta_{MT,bulk}$ , and the kinetic overpotential loss incurred by the bare Pt electrode,  $\eta_c$  referred to as “ $\eta_{HER}$ ”, was also the same for the MCEC electrodes on the basis of their identical 1D geometry and similar  $H_{upd}$ -determined ECSAs. Based on this assumption,  $\eta_{conc}$  was estimated as the difference in the MCEC and bare Pt HER LSV curves at a given current density (Figure 4.10).

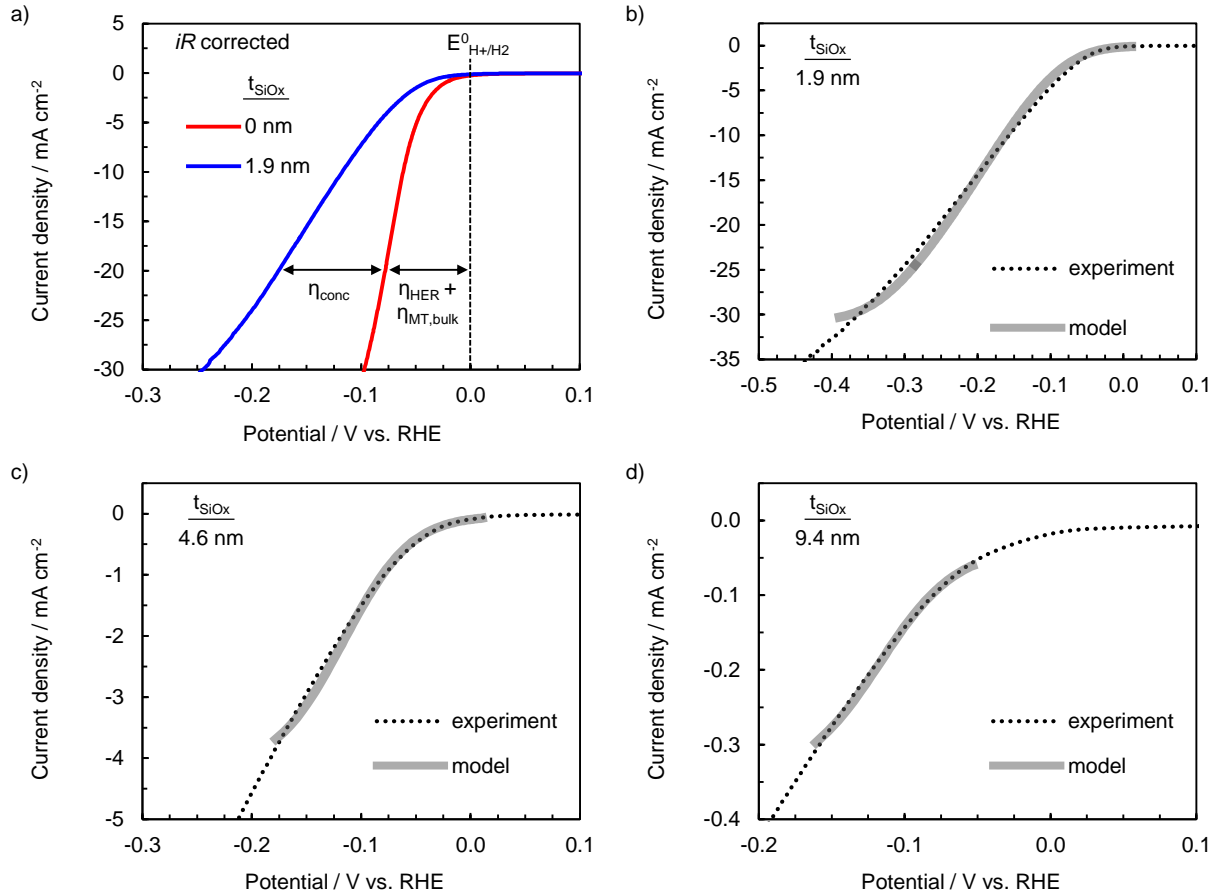


Figure 4.10. a.) Defining kinetic ( $\eta_{HER}$ ) and mass transfer ( $\eta_{MT,bulk}$ ) overpotential versus concentration overpotential ( $\eta_{conc}$ ) losses in LSVs for  $t_{SiOx}$ =0 and  $t_{SiOx}$ =1.9 nm MCEC electrodes. LSVs are *iR* corrected. Comparison of experimental and modeled current density versus potential vs. RHE curves for b.)  $t_{SiOx}$ =1.9 nm, c.)  $t_{SiOx}$ =4.6 nm, and d.)  $t_{SiOx}$ =9.4 nm MCEC electrodes.

An analytical expression for  $\eta_{conc}$  can be derived for 1D diffusive flux across the  $SiO_x$  membrane and is given by Equation (4.1)<sup>99</sup> (see derivation in Appendix section 4.6.5):



$$\eta_{conc} = \frac{RT}{nF} \ln \left( \frac{S_{H^+}^2}{S_{H_2}} \right) + \frac{RT}{nF} \ln \left( \frac{(1-i/i_{lim,H^+})^2}{1+i/i_{lim,H_2}} \right) \quad (4.1)$$

where  $R$  is the gas constant,  $T$  is absolute temperature,  $n$  is the electron transfer number ( $n=2$  for HER),  $F$  is the Faraday constant,  $i$  is the current density, and  $i_{lim,j}$  is the limiting current density for species  $j$ .  $S_j$  is the partition coefficient which describes the solubility of a species in the membrane and is defined as the ratio of the equilibrium concentration of that species inside the  $\text{SiO}_x$  membrane to its concentration in bulk electrolyte. The product of  $S_j$  and the species effective diffusivity,  $D_{e,j}$ , gives the permeability of species  $j$ ,  $P_j$ , which is a useful metric for quantifying the ability of a species to diffuse within a membrane material.

Table 4.2  $\text{H}^+$  and  $\text{H}_2$  permeability through  $\text{SiO}_x$  overlayers deposited on Pt thin films. Analysis is based on modeled LSVs in Figure 4.10.

$\text{SiO}_x$ thickness (nm)	$P_{\text{H}^+}$ ( $\text{cm}^2 \text{s}^{-1}$ )	$P_{\text{H}_2}$ ( $\text{cm}^2 \text{s}^{-1}$ )
$1.9 \pm 0.1$	$3.0 \times 10^{-10}$	$3.4 \times 10^{-10}$
$4.6 \pm 0.4$	$1.0 \times 10^{-10}$	$1.4 \times 10^{-10}$
$9.4 \pm 0.1$	$1.7 \times 10^{-11}$	$4.8 \times 10^{-11}$

$\text{H}^+$  and  $\text{H}_2$  permeabilities through  $\text{SiO}_x$  were obtained by fitting Equation (4.1) to the experimental current density versus concentration overpotential curves (see description on fitting procedure in Appendix section 4.6.6). As seen in Figure 4.10, high quality fits are obtained at low current densities, indicating that 1D transport based on the solution-diffusion theory can accurately describe the performance of these MCEC electrodes.  $\text{H}^+$  and  $\text{H}_2$  permeabilities in the 1.9 nm, 4.6 nm, and 9.4 nm thick  $\text{SiO}_x$  overlayers obtained by fitting Equation (4.1) to experimental data are listed in Table 4.2. Values of  $P_{\text{H}^+}$  and  $P_{\text{H}_2}$  in the range of  $10^{-11} \text{ cm}^2 \text{s}^{-1}$  to  $10^{-10} \text{ cm}^2 \text{s}^{-1}$  were obtained from the nonlinear fitting procedure. From Table 4.2, it is seen that  $P_{\text{H}^+}$  and  $P_{\text{H}_2}$  generally increase

with decreasing  $t_{\text{SiO}_x}$ , which may suggest slight differences in  $\text{SiO}_x$  density, porosity, and/or composition as a function of  $\text{SiO}_x$  thickness.

#### 4.4.3 *SiO<sub>x</sub> Impact on Concentration Overpotential*

From an application standpoint, it is important that  $t_{\text{SiO}_x}$  and/or  $P_j$  is engineered to keep  $\eta_{\text{conc}}$  below acceptable levels. If  $\eta_{\text{conc}}$  becomes too large, device efficiency will be significantly reduced when operated at high current densities. As seen in Figure 4.7, the  $\text{SiO}_x|\text{Pt}$  thin film MCEC electrodes exhibit significantly larger overpotentials than the bare Pt thin film for  $t_{\text{SiO}_x} > 1.9$  nm and current densities larger than  $\approx 10$  mA cm<sup>-2</sup>. At first, this may seem highly problematic because commercial electrolyzers typically operate at current densities in the range of 1-3 A cm<sup>-2</sup> of electrode. However, it is important to recognize the difference in the ECSA of Pt nanoparticles in commercial electrolyzers and fuel cells compared to the ECSAs of the model thin films studied here, for which the ECSA is similar to the geometric area of the electrode. For a polymer electrolyte membrane electrolyzer operating with a current density of 1 A cm<sup>-2</sup> (normalized to the 2D geometric electrode surface area), the current density normalized to the catalyst ECSA (assuming 0.1-1.0 mg cm<sup>-2</sup> Pt loading of spherical, nonporous 5 nm diameter nanoparticles) is only  $\approx 2$ –20 mA cm<sup>-2</sup> of electrocatalyst. At these current densities, the concentration overpotentials incurred by the planar  $t_{\text{SiO}_x}=1.9$  nm and  $t_{\text{SiO}_x}=4.6$  nm  $\text{SiO}_x|\text{Pt}$  MCECs are estimated to be between 14–40 mV and 37–162 mV, respectively, based on the difference in the  $H_{\text{upd}}$  ECSA normalized HER LSV curves (Figure 4.11) for the MCEC and bare Pt electrodes. This analysis indicates that the additional  $\eta_{\text{conc}}$  losses associated mass transport through  $\text{SiO}_x$  in  $\text{SiO}_x|\text{Pt}$  MCECs should not prohibit HER operation at high current densities relevant to commercial electrolyzers. This analysis is consistent with the study by Takenaka, et al.,<sup>19</sup> which showed that the fuel cell IV curves

of high surface area SiO<sub>2</sub>-encapsulated Pt|C ORR electrocatalysts were nearly unaffected by the presence of SiO<sub>x</sub>.

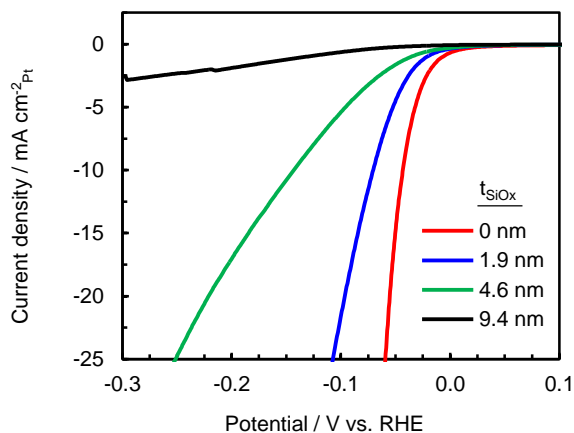


Figure 4.11. *iR* corrected LSVs normalized by ECSA. LSV measurements from Figure 4.7 for various SiO<sub>x</sub> thicknesses from 0 nm < x < 10 nm, zoomed in at relevant ECSA normalized current densities for electrolyzer operation. All LSVs are *iR* corrected ( $R_s = 16 \Omega$ ) and normalized by the  $H_{\text{upd}}$  determined ECSA from CVs performed at 25 mV s<sup>-1</sup>. The LSV for the 19.8 nm SiO<sub>x</sub> film is not included due to the uncertainty in quantification of the  $H_{\text{upd}}$  determined ECSA. The low  $H_{\text{upd}}$  signals complicated the deconvolution from the double layer capacitance. All measurements were performed at 20 mV s<sup>-1</sup> in deaerated solutions.

#### 4.4.4 Inspire Future Studies

While this study has provided some new insights into transport of electroactive species within ultrathin SiO<sub>x</sub> overlayer, many fundamental questions remain. What is the molecular nature of protons within the SiO<sub>x</sub> layer (e.g. H<sup>+</sup> vs. H<sub>3</sub>O<sup>+</sup> vs. Si-OH), and how do the protons interact with counter ions, residual carbon, and/or water molecules as they pass through the overlayer? Is electrostatic repulsion important, and what role, if any, does migration play in describing the transport of protons from the bulk electrolyte to the SiO<sub>x</sub>|Pt surface? Can the buried metal|oxide overlayer interface be manipulated to alter intrinsic catalytic properties such as those observed in electrocatalysis studies involving strong metal-support interaction (SMSI) phenomena?<sup>100,101</sup>

Answering these questions is especially important for applying the  $\text{SiO}_x$  nanomembranes to selectively facilitate the transport of desirable reactants/products, while suppressing transport of poisons and undesirable products. If this knowledge can be harnessed, the MCEC architecture could serve as a powerful new class of tunable electrocatalysts with excellent stability and advanced catalytic functionalities.

## 4.5 Conclusions

This chapter has explored model membrane-coated electrocatalysts (MCECs) based on ultrathin layers of silicon oxide ( $\text{SiO}_x$ ) coated onto Pt thin films, and investigated their performance as hydrogen evolution reaction (HER) electrocatalysts. Through detailed physical and electroanalytical characterization of  $\text{SiO}_x|\text{Pt}$  MCECs with  $\text{SiO}_x$  layers of varied thicknesses, this study has provided compelling evidence that (1.) protons and  $\text{H}_2$  readily transport through the  $\text{SiO}_x$  overlayers, and (2.) significant HER rates occur at the buried  $\text{Pt}|\text{SiO}_x$  interface. Increasing the thickness of the  $\text{SiO}_x$  overlayers results in monotonic increases in the overpotential losses of the MCEC electrodes. These overpotential losses were fit using a one-dimensional diffusion model, from which the  $\text{H}^+$  and  $\text{H}_2$  permeabilities through  $\text{SiO}_x$  were obtained. AFM reveals distinct holes in the  $\text{SiO}_x$  overlayers, but detailed analysis of the Pt ECSA (measured by both  $\text{H}_{\text{upd}}$  and  $\text{Cu}_{\text{upd}}$ ), control experiments based on bilayer  $\text{SiO}_x$  overlayers, and HER poisoning experiments, all indicate that the total HER current is dominated by the reaction occurring at the buried  $\text{Pt}|\text{SiO}_x$  interface in comparison to the very small current contributed by any Pt exposed to the bulk electrolyte at the bottom of these holes. The HER poisoning experiments, performed with  $\text{Cu}^{2+}$  as a model poison, furthermore demonstrate the ability of the  $\text{SiO}_x$  overlayers to serve as nanomembranes that selectively allow for facile  $\text{H}^+/\text{H}_2$  transport while acting as a barrier to the  $\text{Cu}^{2+}$ . This result further validated observations of proton and  $\text{H}_2$  transport occurring *through* the

SiO<sub>x</sub> overlayers, and highlights the potential of the MCECs as a platform for tunable electrocatalysis with advanced functionalities such as poison resistance.

## 4.6 Appendix

### 4.6.1 *Ellipsometric Porosimetry*

A porous film with pore size well above the critical diameter of toluene (5.8 Å) would allow the pores to fill with toluene during adsorption, which results in a change in refractive index of the film. This change in refractive can be converted in to the relative volume of toluene adsorbed by the film, which in turn is a measure of the porosity of the film. For example, Figure 4.12a shows the adsorbed volume of toluene, in a SiO<sub>2</sub> thin film control sample with thickness of  $\approx 164$  nm, and a mean pore radius of  $\approx 9.4$  nm, as a function of relative pressure. The graph shows that the film has an accessible porosity of 77%. Figure 4.12b shows a similar graph for a 9.5 nm and 107 nm thick SiO<sub>x</sub> film synthesized with the UV ozone process. These curves show that there is negligible change in refractive index of the film with change in relative pressure. This could mean that the pore size (2 times pore radius) of the film is below 5.8 Å, which prevent the toluene molecule from entering the pores. While the thicker 107 nm SiO<sub>x</sub> film was not investigated in the electrochemical study, it is presented here because the thickness is comparable to the 164 nm SiO<sub>2</sub> film in Figure 4.12a. The fact that both the 9.5 nm and 107 nm SiO<sub>x</sub> films both show negligible change in refractive index with change in relative pressure indicates the amount of material in 9.5 nm SiO<sub>x</sub> film did not limit the EP measurement.

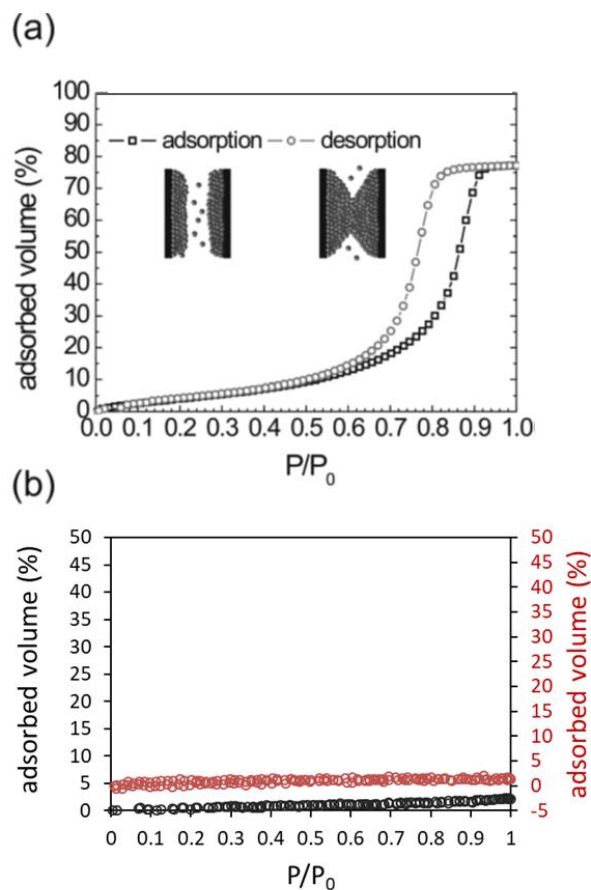


Figure 4.12. Ellipsometric porosimetry results. Adsorbed volume of toluene as a function of relative pressure for a.)  $\approx 164$  nm thick mesoporous silica film with a mean pore radius of  $\approx 9.4$  nm [Adapted from *Langmuir* **2012**, 28 (8), 3852–3859] and b.) 9.5 nm (black) and 107 nm (red)  $\text{SiO}_x$  films made by UV ozone (this work).

#### 4.6.2 Tafel Analysis

The only sample for which Tafel analysis was performed was the bare Pt electrode lacking the  $\text{SiO}_x$  overlayer. Figure 4.13 shows a zoomed in portion of the LSV curve for this sample from Figure 4.11 and a Tafel plot constructed from that LSV curve. From Figure 4.13a, we observe the expected exponential increase in current at low overpotentials and linear relationship between overpotential and  $\log(\text{current density})$  (Figure 4.13b). Tafel analysis was performed at low current densities corresponding to the linear region of the Tafel plot in Figure 4.13b. By fitting the Tafel

equation to the curve in Figure 4.13b between overpotentials of 0 mV and -40 mV, values of the Tafel slope and exchange current density were determined. These values reported in this chapter are slightly off from those commonly reported in literature which is most likely related to the fact that these Pt samples did not undergo CV cycling to positive potentials needed to oxidize, reduce, and restructure the Pt surface and oxidize adventitious species.

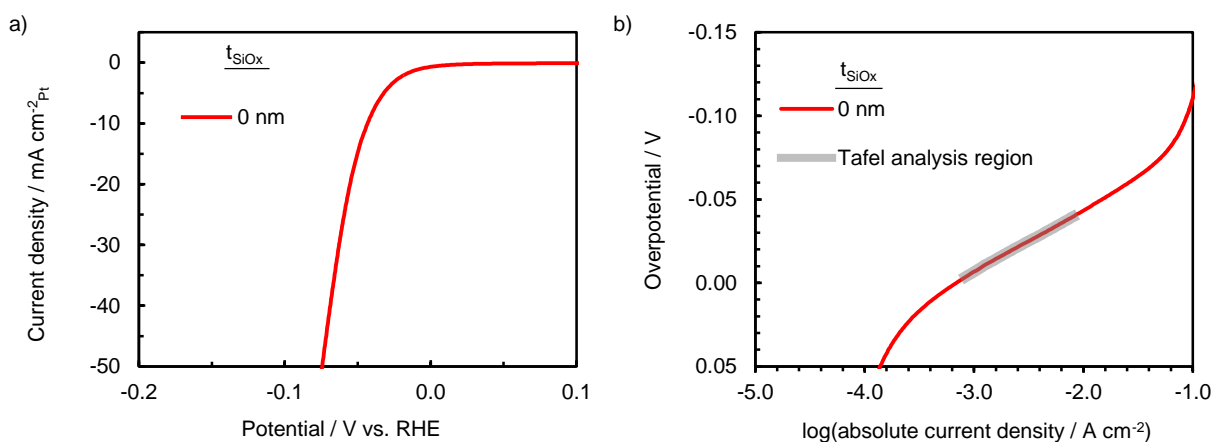


Figure 4.13. a.) Bare Pt LSV from Figure 4.11 and b.) corresponding Tafel plot. LSVs from Figure 4.7 were normalized by ECSA and  $iR$  corrected prior to analysis (Figure 4.11).

### 4.6.3 XPS Characterization of SiO<sub>x</sub> Film after Copper Poisoning Test

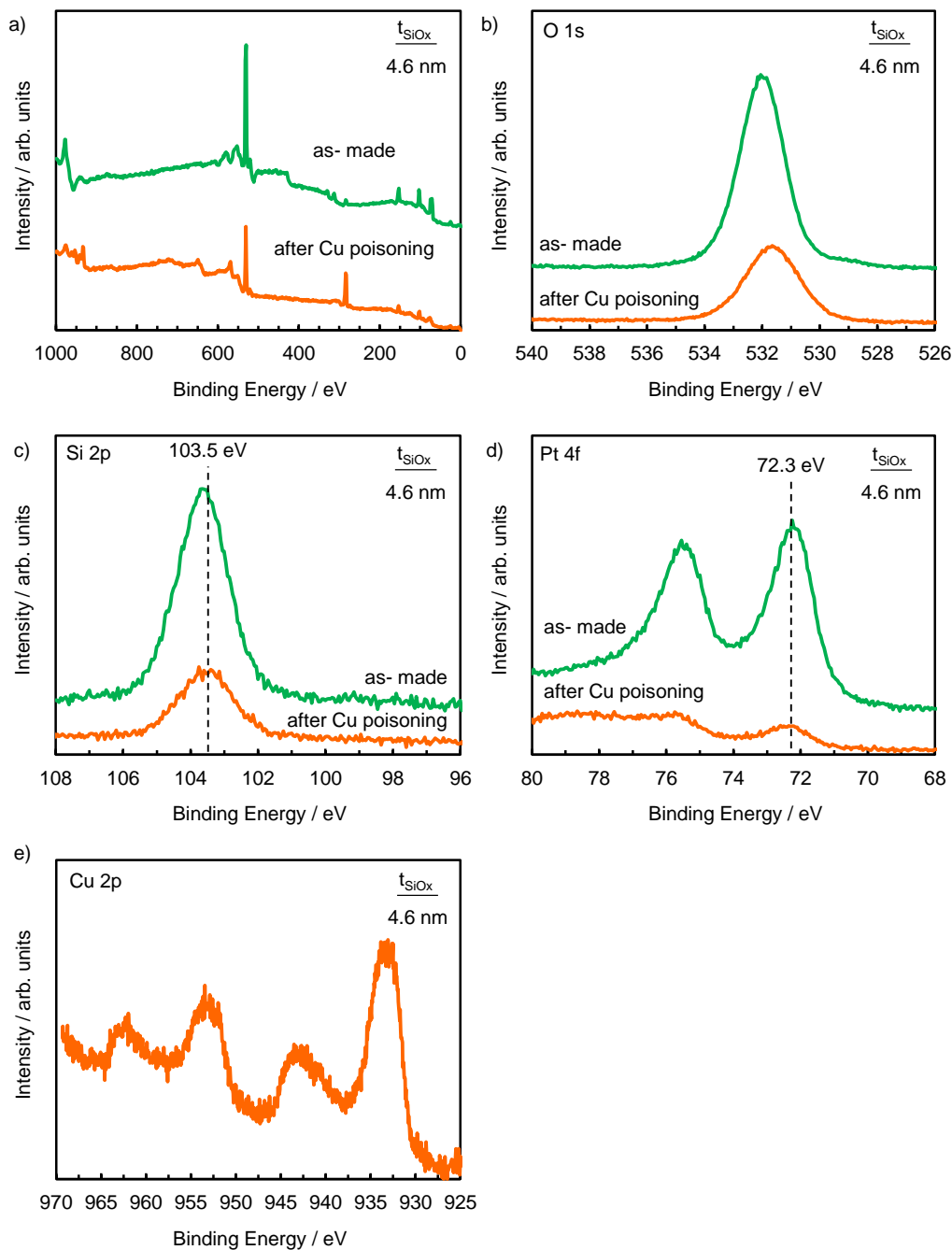


Figure 4.14. XPS results after Cu poisoning test. XPS of 4.6 nm SiO<sub>x</sub>/Pt electrodes before (green) and after operating at  $-5 \text{ mA cm}^{-2}$  for 1 hour in 0.5 M H<sub>2</sub>SO<sub>4</sub> with 0.2 mM CuSO<sub>4</sub> (orange) a.) Survey, b.) Si 2p, c.) O 1s, d.) Pt 4f, and e.) Cu 2p. The C 1s peaks were shifted and centered to 284.8 eV and the O 1s peaks associated with the SiO<sub>x</sub> overlays were shifted by the same amount.



#### 4.6.4 Electrochemical Activity on SiO<sub>x</sub> Only

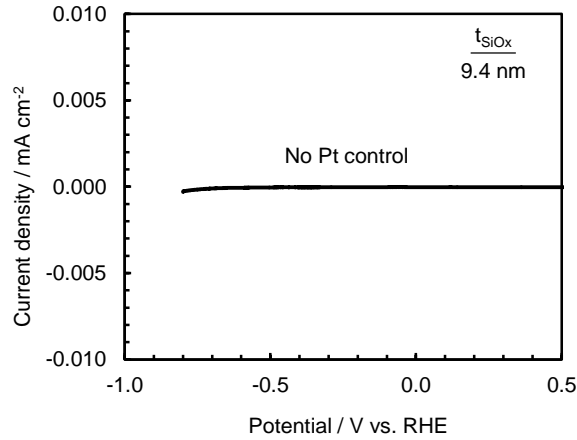


Figure 4.15. H<sub>2</sub> evolution activity of SiO<sub>x</sub> films electrocatalysts. LSV measurements in 0.1 M H<sub>2</sub>SO<sub>4</sub> for a 9.4 nm SiO<sub>x</sub>|p<sup>+</sup>Si electrode to demonstrate lack of HER activity on SiO<sub>x</sub> alone. All LSV measurements were performed at 20 mV s<sup>-1</sup> in deaerated solutions

#### 4.6.5 Derivation of Concentration Overpotential for a 1D Permeable Overlayer

The derivation of the concentration overpotential ( $\eta_{conc}$ ) as a function of current density ( $i$ ) for a SiO<sub>x</sub> membrane-coated electrocatalyst (MCEC) follows the same derivation as in reference<sup>99</sup> for a 1-dimensional (1D) MCEC. The current derivation is applied to the hydrogen evolution reaction (HER),  $2\text{H}^+ + 2\text{e}^- \leftrightarrow \text{H}_2$ , whereas the cited reference provides an expression for  $\eta_{conc}$  for the generic reaction  $\text{O} + \text{ne}^- \leftrightarrow \text{R}$ . Similar assumptions are still valid for the SiO<sub>x</sub>|Pt system studied herein. These assumptions are as follows:

1. The bulk electrolyte is well-stirred such that the:
  - a. overpotential losses due to H<sub>2</sub> bubbles are minimized,
  - b. the concentration gradient across the diffusion boundary layer in the bulk electrolyte is negligible compared to the concentration gradient within the SiO<sub>x</sub> such that the concentration of H<sup>+</sup> and H<sub>2</sub> just outside the SiO<sub>x</sub> is approximately equal to the bulk concentrations, and

- c.  $H^+$  and  $H_2$  bulk concentrations are constant and independent of applied  $i$
2. the  $SiO_x$  overlayer possesses uniform composition and thickness of  $t_{SiO_x}$
3. there is no convection within the pinhole-free overlayer
4. migration effects are neglected within the  $SiO_x$
5.  $H^+$  and  $H_2$  transport through the  $SiO_x$  occurs by diffusion
6.  $H^+$  and  $H_2$  are soluble in the  $SiO_x$  phase such that transport is described by solution diffusion theory.<sup>96,97</sup>

The concentration overpotential in an MCEC may be defined as the potential difference across the membrane between the bulk electrolyte, just outside the  $SiO_x$  membrane ( $x > t_{SiO_x}$ ), and the buried interface ( $x = 0$ ):

$$\eta_{conc} = E(x = 0) - E(x > t_{SiO_x}) \quad (B.4.1)$$

where  $E$  is the potential at distance  $x$  from the Pt| $SiO_x$  buried interface.  $E$  can be calculated from the Nernst Equation:

$$E = E_{H^+/H_2}^{\circ'} + \frac{RT}{nF} \ln \left( \frac{C_{H^+}^2}{C_{H_2}} \right) \quad (B.4.2)$$

where  $R$  is the gas constant,  $T$  is absolute temperature,  $n$  is the electron transfer number ( $n=2$  for HER),  $F$  is Faraday's constant ( $F=96485 \text{ C mol}^{-1}$ ),  $C$  is the concentration of  $H^+$  and  $H_2$  respectively, and  $E_{H^+/H_2}^{\circ'}$  is the formal potential which combines the standard reduction potential  $E_{H^+/H_2}^{\circ}$  with a second term combining activity coefficients for  $H^+$  and  $H_2$ .  $\eta_{conc}$  in MCECs results from a deviation in the ratio of  $C_{H^+}$  to  $C_{H_2}$  at the buried  $SiO_x$ |Pt interface compared to the bulk electrolyte. This deviation is due to  $H^+$  and  $H_2$  diffusion through the overlayer and consumption or generation at the buried interface. According to solution diffusion theory,<sup>96,97</sup> diffusive flux is described by Fick's Law in which a concentration gradient inside the film drives species diffusion across the film:

$$J_{H^+} = - D_{e,H^+} \frac{dC_{H^+}(x)}{dx} \quad (B.4.3)$$

$$J_{H_2} = - D_{e,H_2} \frac{dC_{H_2}(x)}{dx} \quad (B.4.4)$$

where  $J$  is the flux and  $D_e$  is the effective diffusivity of  $H^+$  and  $H_2$  in the  $SiO_x$  film. Discretized, linear approximation of the gradients yields:

$$J_{H^+} = - D_{e,H^+} \frac{C_{H^+}(t_{SiO_x}) - C_{H^+}(0)}{t_{SiO_x}} \quad (B.4.5)$$

$$J_{H_2} = - D_{e,H_2} \frac{C_{H_2}(t_{SiO_x}) - C_{H_2}(0)}{t_{SiO_x}} \quad (B.4.6)$$

The concentration of  $H^+$  and  $H_2$  at the  $SiO_x|electrolyte$  interface ( $x = t_{SiO_x}$ ) is described by the partition coefficient,  $S$ , which describes solubility of a species in the membrane and is defined as the ratio of the concentration of  $H^+$  or  $H_2$  just inside the  $SiO_x$  membrane of thickness  $t_{SiO_x}$  to the concentration in bulk electrolyte,  $C_{H^+,b}$  or  $C_{H_2,b}$ , characterized as:

$$S_{H^+} = \frac{C_{H^+}(t_{SiO_x})}{C_{H^+,b}} \quad (B.4.7)$$

$$S_{H_2} = \frac{C_{H_2}(t_{SiO_x})}{C_{H_2,b}} \quad (B.4.8)$$

where  $C_b$  is the bulk concentration of  $H^+$  and  $H_2$  respectively.  $C_{H_2,b}$  was assumed to the solubility of  $H_2$  in water (0.75 mM).<sup>102</sup> The diffusive flux of electroactive species, given by Equations (B.4.3) and (B.4.4), is related to current density by Faraday's law. Combining Faraday's with Equations (B.4.5) and (B.4.6) and incorporation of Equations (B.4.7) and (B.4.8) we arrive at two expressions for the current density:

$$i_{H^+} = - F D_{e,H^+} \frac{S_{H^+} C_{H^+,b} - C_{H^+}(0)}{t_{SiO_x}} \quad (B.4.9)$$

$$i_{H_2} = - 2 F D_{e,H_2} \frac{S_{H_2} C_{H_2,b} - C_{H_2}(0)}{t_{SiO_x}} \quad (B.4.10)$$

Additionally, the mass transfer limited rates can be defined for the limiting case where  $C_{H^+}(0)$  or  $C_{H_2}(0) = 0$ :

$$i_{lim,H^+} = -F D_{e,H^+} \frac{S_{H^+} C_{H^+,b}}{t_{SiOx}} \quad (B.4.11)$$

$$i_{lim,H_2} = 2 F D_{e,H_2} \frac{S_{H_2} C_{H_2,b}}{t_{SiOx}} \quad (B.4.12)$$

where  $i_{lim,H^+}$  and  $i_{lim,H_2}$  are limiting current density of  $H^+$  reduction (negative current) and  $H_2$  oxidation (positive current). The permeability,  $P$ , of  $H^+$  and  $H_2$  transporting across a membrane is dependent on its solubility and diffusivity in the membrane and is defined as:

$$P_{H^+} = D_{e,H^+} S_{H^+} \quad (B.4.13)$$

$$P_{H_2} = D_{e,H_2} S_{H_2} \quad (B.4.14)$$

For the case of HER at negative overpotentials,  $i_{H_2}$  is negligible and  $i_{H^+}$  dominates  $i$  such that  $i = i_{H^+}$ . Equations (B.4.9) and (B.4.10) are used to solve for expressions of  $C_{H^+}(0)$  and  $C_{H_2}(0)$ :

$$C_{H^+}(0) = S_{H^+} C_{H^+,b} \left( 1 - \frac{i}{i_{lim,H^+}} \right) \quad (B.4.15)$$

$$C_{H_2}(0) = S_{H_2} C_{H_2,b} \left( 1 - \frac{i}{i_{lim,H_2}} \right) \quad (B.4.16)$$

The  $H^+$  and  $H_2$  concentrations at the buried interface, Equations (B.4.15) and (B.4.16), and in the bulk are substituted into Equation (B.4.2) to solve for  $E(x=0)$  and  $E(x > t_{SiOx})$  respectively.

$$E(x=0) = E_{H^+/H_2}^{\circ'} + \frac{RT}{2F} \ln \left( \frac{S_{H^+}^2 C_{H^+,b}^2}{S_{H_2} C_{H_2,b}} \right) + \frac{RT}{2F} \ln \left( \frac{(1-i/i_{lim,H^+})^2}{1-i/i_{lim,H_2}} \right) \quad (B.4.17)$$

$$E(x > t_{SiOx}) = E_{H^+/H_2}^{\circ'} + \frac{RT}{2F} \ln \left( \frac{C_{H^+,b}^2}{C_{H_2,b}} \right) \quad (B.4.18)$$

Finally, Equations (B.4.17) and (B.4.18) are substituted into Equation (B.4.1) to arrive at Equation (B.4.12), the final expression for  $\eta_{conc}$  that appears as Equation (1) in the main article:

$$\eta_{conc} = \frac{RT}{2F} \ln \left( \frac{S_{H^+}^2}{S_{H_2}} \right) + \frac{RT}{2F} \ln \left( \frac{(1-i/i_{lim,H^+})^2}{1-i/i_{lim,H_2}} \right) \quad (B.4.19)$$

#### 4.6.6 Fitting Procedure For Modeling HER LSV Curves

LSV curves were modeled assuming that the total overpotential losses ( $\eta$ ) for MCEC electrodes at a given current density can be described as a summation of ohmic losses ( $\eta_{\Omega}$ ), kinetic losses ( $\eta_{HER}$ ), concentration overpotential ( $\eta_{conc}$ ), and mass transport losses in the bulk electrolyte ( $\eta_{MT,bulk}$ ):

$$\eta = \eta_{\Omega} + \eta_{HER} + \eta_{MT,bulk} + \eta_{conc} \quad (B.4.20)$$

Experimental LSV curves were first  $iR$  corrected based on EIS-measured series resistances to subtract out the ohmic overpotential losses,  $\eta_{\Omega}$ . Next, it was assumed that  $\eta_{MT,bulk}$ , and  $\eta_{HER}$  were the same for bare Pt and MCEC electrodes. These assumptions were made on the basis that the MCEC and bare Pt electrodes have identical planar geometries and similar electrochemically active surface areas (ECSAs). If these assumptions hold, then the difference in HER overpotential of the  $iR$  corrected MCEC and bare Pt LSV curves at a given current density represents the  $\eta_{conc}$  associated with  $H^+$  and  $H_2$  transport through the  $SiO_x$ , as indicated in Figure 4.10a. The experimental  $i$  versus  $\eta_{conc}$  curves were fitted with Equation (B.4.19) using a three parameter nonlinear fitting procedure (Matlab R2015a, nlinfit). The three fitted parameters were  $S_{H_2}^2/S_{H^+}$ ,  $P_{H^+}$ , and  $P_{H_2}$ . Fitting was performed over different ranges of  $i$  in order to establish the maximum range of  $i$  over which the model converged and high quality fits could be obtained. Limitations of this model were evident when the fit was performed over a range that approached the maximum recorded current densities, where it is expected that hydrogen bubbles, convection, and/or migration affect the LSV curve. The model does not converge if fitted to experimental data that is beyond the calculated limiting current densities (B.4.11). No true limiting current is observed as

the applied potential increases to large overpotentials. This may provide evidence for the presence of migration in the SiO<sub>x</sub> overlayers at high current densities, which is not captured by this model. However, it was found that the Equation (B.4.19) fit the data well for low and intermediate current densities, with R<sup>2</sup> values of 0.95, 0.98, and 0.99 obtained for t<sub>SiO<sub>x</sub></sub>=1.9 nm, t<sub>SiO<sub>x</sub></sub>=4.6 nm, and t<sub>SiO<sub>x</sub></sub>=9.4 nm MCEC electrodes. Permeability coefficients of 10<sup>-11</sup> cm<sup>2</sup> s<sup>-1</sup> to 10<sup>-10</sup> cm<sup>2</sup> s<sup>-1</sup> were obtained from these fits and are provided in Table 4.2. Finally,  $\eta_{\Omega}$ ,  $\eta_{MT,bulk}$ , and  $\eta_{HER}$  were added back to the  $i$  versus  $\eta_{conc}$  curves at equivalent  $i$  to reconstruct LSV curves from Figure 4.7, which are shown in Figure 4.10b-d.

#### 4.7 Acknowledgments

I would like to acknowledge Eva L. Songcuan for helping fabricate and conduct experiments, Chathuranga De Silva for performing XPS, Ranjith K. Ramachandran and Christophe Detavernier for their collaboration in performing EP measurements and analysis, Thomas Moffat (NIST) for suggesting the bilayer experiment, Jeffrey Koberstein, Jonathan Davis, and Nicholas Brady for helpful discussions and suggestions, Sebastian Russel for assistance with AFM measurements, Han Chen for fabricating the multilayer SiO<sub>x</sub> for EP measurements, Sophia Kurdziel for assistance in modeling the LSVs in addition to AFM image analysis, in which Bicheng Xu also helped, and Jacob Robinson for assistance with control experiments. I acknowledge Columbia University Columbia Nano Initiative and City University of New York Advanced Science Research Center for use of the physical vapor deposition and SEM equipment. Dr. Esposito and I acknowledge Columbia University (start-up funds) and the National Science Foundation (NSF) Center for Precision Assembly of Superstratic and Superatomic Solids for funding (DMR-1420634). C.D. acknowledge the Flemish Research Foundation (FWO) and the

Special Research Fund BOF of Ghent University (GOA 01G01513). R.K.R. is a postdoctoral fellow of the FWO.

#### 4.8 References

- (1) Gu, S.; Xu, B.; Yan, Y. Electrochemical Energy Engineering: A New Frontier of Chemical Engineering Innovation. *Annu. Rev. Chem. Biomol. Eng.* **2014**, *5* (1), 429–454.
- (2) Greeley, J.; Markovic, N. M. The Road from Animal Electricity to Green Energy: Combining Experiment and Theory in Electrocatalysis. *Energy Environ. Sci.* **2012**, *5* (11), 9246–9256.
- (3) Walter, M. G.; Warren, E. L.; McKone, J. R.; Boettcher, S. W.; Mi, Q.; Santori, E. A.; Lewis, N. S. Solar Water Splitting Cells. *Chem. Rev.* **2010**, *110* (11), 6446–6473.
- (4) Chu, S.; Cui, Y.; Liu, N. The Path towards Sustainable Energy. *Nat. Mater.* **2017**, *16* (1), 16–22.
- (5) Shao-Horn, Y.; Sheng, W. C.; Chen, S.; Ferreira, P. J.; Holby, E. F.; Morgan, D. Instability of Supported Platinum Nanoparticles in Low-Temperature Fuel Cells. *Top. Catal.* **2007**, *46* (3–4), 285–305.
- (6) Wang, Y.; Chen, K. S.; Mishler, J.; Cho, S. C.; Adroher, X. C. A Review of Polymer Electrolyte Membrane Fuel Cells: Technology, Applications, and Needs on Fundamental Research. *Appl. Energy* **2011**, *88* (4), 981–1007.
- (7) Paidar, M.; Fateev, V.; Bouzek, K. Membrane Electrolysis—History, Current Status and Perspective. *Electrochim. Acta* **2016**, *209*, 737–756.
- (8) Debe, M. K. Electrocatalyst Approaches and Challenges for Automotive Fuel Cells. *Nature* **2012**, *486* (7401), 43–51.
- (9) Pinaud, B. A.; Benck, J. D.; Seitz, L. C.; Forman, A. J.; Chen, Z.; Deutsch, T. G.; James, B. D.; Baum, K. N.; Baum, G. N.; Ardo, S.; et al. Technical and Economic Feasibility of Centralized Facilities for Solar Hydrogen Production via Photocatalysis and Photoelectrochemistry. *Energy Environ. Sci.* **2013**, *6* (7), 1983.
- (10) Zalitis, C. M.; Sharman, J.; Wright, E.; Kucernak, A. R. Properties of the Hydrogen Oxidation Reaction on Pt/C Catalysts at Optimised High Mass Transport Conditions and Its Relevance to the Anode Reaction in PEFCs and Cathode Reactions in Electrolysers. *Electrochim. Acta* **2015**, *176*, 763–776.
- (11) Energy, U. S. D. of. *Hydrogen and Fuel Cells Program 2011 Annual Merit Review and Peer Evaluation Report*; 2015.
- (12) Ferreira, P. J.; la O', G. J.; Shao-Horn, Y.; Morgan, D.; Makharia, R.; Kocha, S.; Gasteiger,

- H. A. Instability of Pt/C Electrocatalysts in Proton Exchange Membrane Fuel Cells. *J. Electrochem. Soc.* **2005**, *152* (11), A2256–A2271.
- (13) Pavlišić, A.; Jovanović, P.; Šelih, V. S.; Šala, M.; Hodnik, N.; Hočevar, S.; Gabersček, M. The Influence of Chloride Impurities on Pt/C Fuel Cell Catalyst Corrosion. *Chem. Commun.* **2014**, *50* (28), 3732–3734.
  - (14) Spöri, C.; Kwan, J. T. H.; Bonakdarpour, A.; Wilkinson, D. P.; Strasser, P. The Stability Challenges of Oxygen Evolving Catalysts: Towards a Common Fundamental Understanding and Mitigation of Catalyst Degradation. *Angew. Chemie Int. Ed.* **2017**, *56* (22), 5994–6021.
  - (15) Ashton, S. J.; Arenz, M. Comparative DEMS Study on the Electrochemical Oxidation of Carbon Blacks. *J. Power Sources* **2012**, *217*, 392–399.
  - (16) Feng, C.; Wang, J.; Cheng, Y.; He, P.; Liew, K. M. Diffusion Mechanism of Platinum Nanoclusters on Well-Aligned Carbon Nanotubes. *RSC Adv.* **2014**, *4* (105), 60711–60719.
  - (17) Esposito, D. V.; Hunt, S. T.; Kimmel, Y. C.; Chen, J. G. A New Class of Electrocatalysts for Hydrogen Production from Water Electrolysis: Metal Monolayers Supported on Low-Cost Transition Metal Carbides. *J. Am. Chem. Soc.* **2012**, *134* (6), 3025–3033.
  - (18) Zhang, Z.; Liu, J.; Gu, J.; Su, L.; Cheng, L. An Overview of Metal Oxide Materials as Electrocatalysts and Supports for Polymer Electrolyte Fuel Cells. *Energy Environ. Sci.* **2014**, *7* (8), 2535.
  - (19) Takenaka, S.; Miyamoto, H.; Utsunomiya, Y.; Matsune, H.; Kishida, M. Catalytic Activity of Highly Durable Pt/CNT Catalysts Covered with Hydrophobic Silica Layers for the Oxygen Reduction Reaction in PEFCs. *J. Phys. Chem. C* **2014**, *118* (2), 774–783.
  - (20) Kuo, P. L.; Hsu, C. H.; Wu, H. M.; Hsu, W. S.; Kuo, D. Controllable-Nitrogen Doped Carbon Layer Surrounding Carbon Nanotubes as Novel Carbon Support for Oxygen Reduction Reaction. *Fuel Cells.* **2012**, *12* (4), 649–655.
  - (21) Wang, S.; Zhang, L.; Xia, Z.; Roy, A.; Chang, D. W.; Baek, J. B.; Dai, L. BCN Graphene as Efficient Metal-Free Electrocatalyst for the Oxygen Reduction Reaction. *Angew. Chemie - Int. Ed.* **2012**, *51* (17), 4209–4212.
  - (22) Park, J.; Jang, Y. J.; Kim, Y. J.; Song, M.; Yoon, S.; Kim, D. H.; Kim, S.-J. Sulfur-Doped Graphene as a Potential Alternative Metal-Free Electrocatalyst and Pt-Catalyst Supporting Material for Oxygen Reduction Reaction. *Phys. Chem. Chem. Phys.* **2014**, *16* (1), 103–109.
  - (23) Zhou, X.; Qiao, J.; Yang, L.; Zhang, J. A Review of Graphene-Based Nanostructural Materials for Both Catalyst Supports and Metal-Free Catalysts in PEM Fuel Cell Oxygen Reduction Reactions. *Advanced Energy Materials.* 2014.
  - (24) Esposito, D. V.; Hunt, S. T.; Kimmel, Y. C.; Chen, J. G. A New Class of Electrocatalysts for Hydrogen Production from Water Electrolysis: Metal Monolayers Supported on Low-



Cost Transition Metal Carbides. *J. Am. Chem. Soc.* **2012**, *134* (6), 3025–3033.

- (25) Esposito, D. V.; Hunt, S. T.; Stottlemeyer, A. L.; Dobson, K. D.; McCandless, B. E.; Birkmire, R. W.; Chen, J. G. Low-Cost Hydrogen-Evolution Catalysts Based on Monolayer Platinum on Tungsten Monocarbide Substrates. *Angew. Chemie Int. Ed.* **2010**, *49* (51), 9859–9862.
- (26) Tripković, V.; Abild-Pedersen, F.; Studt, F.; Cerri, I.; Nagami, T.; Bligaard, T.; Rossmeisl, J. Metal Oxide-Supported Platinum Overlayers as Proton-Exchange Membrane Fuel Cell Cathodes. *ChemCatChem* **2012**, *4* (2), 228–235.
- (27) Danilovic, N.; Subbaraman, R.; Chang, K. C.; Chang, S. H.; Kang, Y. J.; Snyder, J.; Paulikas, A. P.; Strmcnik, D.; Kim, Y. T.; Myers, D.; et al. Activity-Stability Trends for the Oxygen Evolution Reaction on Monometallic Oxides in Acidic Environments. *J. Phys. Chem. Lett.* **2014**, *5* (14), 2474–2478.
- (28) Pan, Z.; Xiao, Y.; Fu, Z.; Zhan, G.; Wu, S.; Xiao, C.; Hu, G.; Wei, Z. Hollow and Porous Titanium Nitride Nanotubes as High-Performance Catalyst Supports for Oxygen Reduction Reaction. *J. Mater. Chem. A* **2014**, *2* (34), 13966–13975.
- (29) Pylypenko, S.; Borisevich, A.; More, K. L.; Corpuz, A. R.; Holme, T.; Dameron, A. A.; Olson, T. S.; Dinh, H. N.; Gennett, T.; O’Hayre, R. Nitrogen: Unraveling the Secret to Stable Carbon-Supported Pt-Alloy Electrocatalysts. *Energy Environ. Sci.* **2013**, *6* (10), 2957–2964.
- (30) Shao, Y.; Liu, J.; Wang, Y.; Lin, Y. Novel Catalyst Support Materials for PEMfuelcells: Current Status and Future Prospects. *J. Mater. Chem.* **2009**, *19* (1), 46–59.
- (31) Sun, X.; Li, D.; Ding, Y.; Zhu, W.; Guo, S.; Wang, Z. L.; Sun, S. Core/Shell Au/CuPt Nanoparticles and Their Dual Electrocatalysis for Both Reduction and Oxidation Reactions. *J. Am. Chem. Soc.* **2014**, *136* (15), 5745–5749.
- (32) Liu, X.; Fu, G.; Chen, Y.; Tang, Y.; She, P.; Lu, T. Pt-Pd-Co Trimetallic Alloy Network Nanostructures with Superior Electrocatalytic Activity towards the Oxygen Reduction Reaction. *Chem. - A Eur. J.* **2014**, *20* (2), 585–590.
- (33) Zhang, J.; Lima, F. H. B.; Shao, M. H.; Sasaki, K.; Wang, J. X.; Hanson, J.; Adzic, R. R. Platinum Monolayer on Nonnoble Metal–Noble Metal Core–Shell Nanoparticle Electrocatalysts for O<sub>2</sub> Reduction. *J. Phys. Chem. B* **2005**, *109* (48), 22701–22704.
- (34) Sasaki, K.; Naohara, H.; Choi, Y.; Cai, Y.; Chen, W.-F.; Liu, P.; Adzic, R. R. Highly Stable Pt Monolayer on PdAu Nanoparticle Electrocatalysts for the Oxygen Reduction Reaction. *Nat. Commun.* **2012**, *3*, 1–9.
- (35) Labrador, N. Y.; Li, X.; Liu, Y.; Tan, H.; Wang, R.; Koberstein, J. T.; Moffat, T. P.; Esposito, D. V. Enhanced Performance of Si MIS Photocathodes Containing Oxide-Coated Nanoparticle Electrocatalysts. *Nano Lett.* **2016**, *16* (10), 6452–6459.

- (36) Chung, D. Y.; Jun, S. W.; Yoon, G.; Kwon, S. G.; Shin, D. Y.; Seo, P.; Yoo, J. M.; Shin, H.; Chung, Y.-H.; Kim, H.; et al. Highly Durable and Active PtFe Nanocatalyst for Electrochemical Oxygen Reduction Reaction. *J. Am. Chem. Soc.* **2015**, *137* (49), 15478–15485.
- (37) Baldizzone, C.; Mezzavilla, S.; Carvalho, H. W. P.; Meier, J. C.; Schuppert, A. K.; Heggen, M.; Galeano, C.; Grunwaldt, J.-D.; Schüth, F.; Mayrhofer, K. J. J. Confined-Space Alloying of Nanoparticles for the Synthesis of Efficient PtNi Fuel-Cell Catalysts. *Angew. Chemie Int. Ed.* **2014**, *53* (51), 14250–14254.
- (38) Galeano, C.; Meier, J. C.; Peinecke, V.; Bongard, H.; Katsounaros, I.; Topalov, A. A.; Lu, A.; Mayrhofer, K. J. J.; Schüth, F. Toward Highly Stable Electrocatalysts via Nanoparticle Pore Confinement. *J. Am. Chem. Soc.* **2012**, *134* (50), 20457–20465.
- (39) Guo, L.; Jiang, W.-J.; Zhang, Y.; Hu, J.-S.; Wei, Z.-D.; Wan, L.-J. Embedding Pt Nanocrystals in N-Doped Porous Carbon/Carbon Nanotubes toward Highly Stable Electrocatalysts for the Oxygen Reduction Reaction. *ACS Catal.* **2015**, *5* (5), 2903–2909.
- (40) Wadsworth, B. L.; Beiler, A. M.; Khusnutdinova, D.; Jacob, S. I.; Moore, G. F. Electrocatalytic and Optical Properties of Cobaloxime Catalysts Immobilized at a Surface-Grafted Polymer Interface. *ACS Catal.* **2016**, *6* (12), 8048–8057.
- (41) Gould, T. D.; Izar, A.; Weimer, A. W.; Falconer, J. L.; Medlin, J. W. Stabilizing Ni Catalysts by Molecular Layer Deposition for Harsh, Dry Reforming Conditions. *ACS Catal.* **2014**, *4* (8), 2714–2717.
- (42) Joo, S. H.; Park, J. Y.; Tsung, C.-K.; Yamada, Y.; Yang, P.; Somorjai, G. A. Thermally Stable Pt/Mesoporous Silica Core-shell Nanocatalysts for High-Temperature Reactions. *Nat. Mater.* **2009**, *8* (2), 126–131.
- (43) Dai, Y.; Lim, B.; Yang, Y.; Cogley, C. M.; Li, W.; Cho, E. C.; Grayson, B.; Fanson, P. T.; Campbell, C. T.; Sun, Y.; et al. A Sinter-Resistant Catalytic System Based on Platinum Nanoparticles Supported on TiO<sub>2</sub> Nanofibers and Covered by Porous Silica. *Angew. Chemie Int. Ed.* **2010**, *49* (44), 8165–8168.
- (44) Maeda, K.; Teramura, K.; Lu, D.; Saito, N.; Inoue, Y.; Domen, K. Noble-Metal/Cr<sub>2</sub>O<sub>3</sub> Core/Shell Nanoparticles as a Cocatalyst for Photocatalytic Overall Water Splitting. *Angew. Chemie Int. Ed.* **2006**, *45* (46), 7806–7809.
- (45) Agiral, A.; Soo, H. Sen; Frei, H. Visible Light Induced Hole Transport from Sensitizer to Co<sub>3</sub>O<sub>4</sub> Water Oxidation Catalyst across Nanoscale Silica Barrier with Embedded Molecular Wires. *Chem. Mater.* **2013**, *25* (11), 2264–2273.
- (46) Wang, Q.; Hisatomi, T.; Jia, Q.; Tokudome, H.; Zhong, M.; Wang, C.; Pan, Z.; Takata, T.; Nakabayashi, M.; Shibata, N.; et al. Scalable Water Splitting on Particulate Photocatalyst Sheets with a Solar-to-Hydrogen Energy Conversion Efficiency Exceeding 1%. *Nat. Mater.* **2016**, *15* (6), 611–615.

- (47) Garcia-Esparza, A. T.; Shinagawa, T.; Ould-Chikh, S.; Qureshi, M.; Peng, X.; Wei, N.; Anjum, D. H.; Clo, A.; Weng, T.-C.; Nordlund, D.; et al. An Oxygen-Insensitive Hydrogen Evolution Catalyst Coated by a Molybdenum-Based Layer for Overall Water Splitting. *Angew. Chemie Int. Ed.* **2017**, *56* (21), 5780–5784.
- (48) Takenaka, S.; Matsumori, H.; Arike, T.; Matsune, H.; Kishida, M. Preparation of Carbon Nanotube-Supported Pt Metal Particles Covered with Silica Layers and Their Application to Electrocatalysts for PEMFC. *Top. Catal.* **2009**, *52* (6–7), 731–738.
- (49) Matsumori, H.; Takenaka, S.; Matsune, H.; Kishida, M. Preparation of Carbon Nanotube-Supported Pt Catalysts Covered with Silica Layers; Application to Cathode Catalysts for PEFC. *Appl. Catal. A Gen.* **2010**, *373* (1–2), 176–185.
- (50) Takenaka, S.; Susuki, N.; Miyamoto, H.; Tanabe, E.; Matsune, H.; Kishida, M. Highly Durable Pd Metal Catalysts for the Oxygen Reduction Reaction in Fuel Cells; Coverage of Pd Metal with Silica. *Chem. Commun.* **2010**, *46* (47), 8950–8952.
- (51) Takenaka, S.; Susuki, N.; Miyamoto, H.; Tanabe, E.; Matsune, H.; Kishida, M. Highly Durable Carbon Nanotube-Supported Pd Catalysts Covered with Silica Layers for the Oxygen Reduction Reaction. *J. Catal.* **2011**, *279* (2), 381–388.
- (52) Takenaka, S.; Matsumori, H.; Matsune, H.; Kishida, M. Highly Durable Pt Cathode Catalysts for Polymer Electrolyte Fuel Cells; Coverage of Carbon Black-Supported Pt Catalysts with Silica Layers. *Appl. Catal. A Gen.* **2011**, *409–410*, 248–256.
- (53) Takenaka, S.; Miyazaki, T.; Matsune, H.; Kishida, M. Highly Active and Durable Silica-Coated Pt Cathode Catalysts for Polymer Electrolyte Fuel Cells: Control of Micropore Structures in Silica Layers. *Catal. Sci. Technol.* **2015**, *5* (2), 1133–1142.
- (54) Gu, J.; Yan, Y.; Young, J. L.; Steirer, K. X.; Neale, N. R.; Turner, J. A. Water Reduction by a P-GaInP<sub>2</sub> Photoelectrode Stabilized by an Amorphous TiO<sub>2</sub> Coating and a Molecular Cobalt Catalyst. *Nat. Mater.* **2015**, *15* (4), 456–460.
- (55) Ito, T.; Audi, A. A.; Dible, G. P. Electrochemical Characterization of Recessed Nanodisk-Array Electrodes Prepared from Track-Etched Membranes. *Anal. Chem.* **2006**, *78* (19), 7048–7053.
- (56) Williams, M. E.; Stevenson, K. J.; Massari, A. M.; Hupp, J. T. Imaging Size-Selective Permeation through Micropatterned Thin Films Using Scanning Electrochemical Microscopy. *Anal. Chem.* **2000**, *72* (14), 3122–3128.
- (57) Velmurugan, J.; Zhan, D.; Mirkin, M. V. Electrochemistry through Glass. *Nat. Chem.* **2010**, *2* (6), 498–502.
- (58) Szunerits, S.; Kirchner, C. N.; Wittstock, G.; Boukherroub, R.; Gondran, C. Electrochemical Investigation of the Influence of Thin SiO<sub>x</sub> Films Deposited on Gold on Charge Transfer Characteristics. *Electrochim. Acta* **2008**, *53* (27), 7908–7914.

- (59) Lu, J.; Fan, Y.; Howard, M. D.; Vaughan, J. C.; Zhang, B. Single-Molecule Electrochemistry on a Porous Silica-Coated Electrode. *J. Am. Chem. Soc.* **2017**, *139* (8), 2964–2971.
- (60) Smets, B. M. J.; Tholen, M. G. W.; Lommen, T. P. A. The Effect of Divalent Cations on the Leaching Kinetics of Glass. *J. Non. Cryst. Solids* **1984**, *65* (2–3), 319–332.
- (61) Godet, J.; Pasquarello, A. Proton Diffusion Mechanism in Amorphous SiO<sub>2</sub>. *Phys. Rev. Lett.* **2006**, *97* (15), 155901.
- (62) Godet, J.; Pasquarello, A. Proton Diffusion in Amorphous SiO<sub>2</sub> and Hafnium Silicate by Ab Initio Molecular Dynamics. In *AIP Conference Proceedings*; AIP, 2007; Vol. 893, pp 195–196.
- (63) Bousse, L.; Bergveld, P. The Role of Buried OH Sites in the Response Mechanism of Inorganic-Gate PH-Sensitive ISFETs. *Sensors and Actuators* **1984**, *6* (1), 65–78.
- (64) Ouyang, M.; Muisener, R. .; Boulares, A.; Koberstein, J. . UV–ozone Induced Growth of a SiO<sub>x</sub> Surface Layer on a Cross-Linked Polysiloxane Film: Characterization and Gas Separation Properties. *J. Memb. Sci.* **2000**, *177* (1–2), 177–187.
- (65) Fu, Y.-J.; Qui, H.; Liao, K.-S.; Lue, S. J.; Hu, C.-C.; Lee, K.-R.; Lai, J.-Y. Effect of UV-Ozone Treatment on Poly(Dimethylsiloxane) Membranes: Surface Characterization and Gas Separation Performance. *Langmuir* **2010**, *26* (6), 4392–4399.
- (66) Yuan, G.; Agiral, A.; Pellet, N.; Kim, W.; Frei, H. Inorganic Core–shell Assemblies for Closing the Artificial Photosynthetic Cycle. *Faraday Discuss.* **2014**, *176*, 233–249.
- (67) Kim, W.; Edri, E.; Frei, H. Hierarchical Inorganic Assemblies for Artificial Photosynthesis. *Acc. Chem. Res.* **2016**, *49* (9), 1634–1645.
- (68) Banerjee, R.; Phan, A.; Wang, B.; Knobler, C.; Furukawa, H.; O’Keeffe, M.; Yaghi, O. M. High-Throughput Synthesis of Zeolitic Imidazolate Frameworks and Application to CO<sub>2</sub> Capture. *Science* **2008**, *319* (5865), 939–943.
- (69) de Jong, K. P.; Zečević, J. Porous Catalysts: The Platinum Rush. *Nat. Mater.* **2016**, *16* (1), 7–8.
- (70) Liu, L.; Díaz, U.; Arenal, R.; Agostini, G.; Concepción, P.; Corma, A. Generation of Subnanometric Platinum with High Stability during Transformation of a 2D Zeolite into 3D. *Nat. Mater.* **2016**, *16* (January), 1–28.
- (71) Mirley, C.; Koberstein, J. A Room Temperature Method for the Preparation of Ultrathin SiO<sub>x</sub> Films from Langmuir-Blodgett Layers. *Langmuir* **1995**, *11* (4), 0–3.
- (72) Phely-Bobin, T. S.; Muisener, R. J.; Koberstein, J. T.; Papadimitrakopoulos, F. Site-Specific Self-Assembly of Si/SiO<sub>x</sub> Nanoparticles on Micropatterned Poly(Dimethylsiloxane) Thin Films. *Synth. Met.* **2001**, *116* (1–3), 439–443.

- (73) Ouyang, M.; Yuan, C.; Muisener, R. J.; Boulares, A.; Koberstein, J. T. Conversion of Some Siloxane Polymers to Silicon Oxide by UV/Ozone Photochemical Processes. *Chem. Mater.* **2000**, *12* (29), 1591–1596.
- (74) Dendooven, J.; Devloo-Casier, K.; Levrau, E.; Van Hove, R.; Pulinthanathu Sree, S.; Baklanov, M. R.; Martens, J. A.; Detavernier, C. In Situ Monitoring of Atomic Layer Deposition in Nanoporous Thin Films Using Ellipsometric Porosimetry. *Langmuir* **2012**, *28* (8), 3852–3859.
- (75) Langereis, E.; Heil, S. B. S.; Knoops, H. C. M.; Keuning, W.; van de Sanden, M. C. M.; Kessels, W. M. M. In Situ Spectroscopic Ellipsometry as a Versatile Tool for Studying Atomic Layer Deposition. *J. Phys. D. Appl. Phys.* **2009**, *42* (7), 073001.
- (76) Dendooven, J.; Devloo-Casier, K.; Ide, M.; Grandfield, K.; Kurttepel, M.; Ludwig, K. F.; Bals, S.; Van Der Voort, P.; Detavernier, C. Atomic Layer Deposition-Based Tuning of the Pore Size in Mesoporous Thin Films Studied by in Situ Grazing Incidence Small Angle X-Ray Scattering. *Nanoscale* **2014**, *6* (24), 14991–14998.
- (77) Baklanov, M. R.; Mogilnikov, K. P.; Polovinkin, V. G.; Dultsev, F. N. Determination of Pore Size Distribution in Thin Films by Ellipsometric Porosimetry. *J. Vac. Sci. Technol. B Microelectron. Nanom. Struct.* **2000**, *18* (3), 1385–1391.
- (78) Moulder, J. F.; Stickle, W. F.; Sobol, P. E.; Bomben, K. D. *Handbook of X-Ray Photoelectron Spectroscopy*; Chastain, J., King, R. C. J., Eds.; Physical Electronics, Inc.: Eden Prairie, MN, 1995.
- (79) Biegler, T.; Rand, D. A. J.; Woods, R. Limiting Oxygen Coverage on Platinized Platinum; Relevance to Determination of Real Platinum Area by Hydrogen Adsorption. *J. Electroanal. Chem. Interfacial Electrochem.* **1971**, *29* (2), 269–277.
- (80) Green, C. L.; Kucernak, A. Determination of the Platinum and Ruthenium Surface Areas in Platinum–Ruthenium Alloy Electrocatalysts by Underpotential Deposition of Copper. I. Unsupported Catalysts. *J. Phys. Chem. B* **2002**, *106* (5), 1036–1047.
- (81) Lide, D. R. *CRC Handbook of Chemistry and Physics*, 84th ed.; CRC Press: Boca Raton, FL, 2003.
- (82) Garahan, A.; Pilon, L.; Yin, J.; Saxena, I. Effective Optical Properties of Absorbing Nanoporous and Nanocomposite Thin Films. *J. Appl. Phys.* **2007**, *101* (1), 014320.
- (83) Himcinschi, C.; Friedrich, M.; Fruhauf, S.; Streiter, I.; Shulz, S. E.; Gessner, T.; Baklanov, M. R.; Mogilnikov, K. P.; Zahn, D. R. T. Ellipsometric Study of the Change in the Porosity of Silica Xerogels after Chemical Modification of the Surface with Hexamethyldisilazane. *Anal. Bioanal. Chem.* **2002**, *374* (4), 654–657.
- (84) Hutchinson, N. J.; Coquil, T.; Navid, A.; Pilon, L. Effective Optical Properties of Highly Ordered Mesoporous Thin Films. *Thin Solid Films* **2010**, *518* (8), 2141–2146.

- (85) Roque-Malherbe, R.; Wendelbo, R.; Mifsud, A.; Corma, A. Diffusion of Aromatic Hydrocarbons in H-ZSM-5, H-Beta, and H-MCM-22 Zeolites. *J. Phys. Chem.* **1995**, *99* (38), 14064–14071.
- (86) Bockris, J. O.; Reddy, A. K. N. *Modern Electrochemistry*, Vol. 2.; Press, Plenum: New York, 1970.
- (87) Greeley, J.; Jaramillo, T. F.; Bonde, J.; Chorkendorff, I. B.; Norskov, J. K. Computational High-Throughput Screening of Electrocatalytic Materials for Hydrogen Evolution. *Nat. Mater.* **2006**, *5* (11), 909–913.
- (88) Appleby, A.; Chemla, M.; Kita, H.; Bronoel, G.; Bard, A. J. *Encyclopedia of Electrochemistry of the Elements*, A.; Dekker, Marcel: New York, 1982.
- (89) Tavares, M. .; Machado, S. A. .; Mazo, L. . Study of Hydrogen Evolution Reaction in Acid Medium on Pt Microelectrodes. *Electrochim. Acta* **2001**, *46* (28), 4359–4369.
- (90) Kuznicki, S. M.; Bell, V. a; Nair, S.; Hillhouse, H. W.; Jacubinas, R. M.; Braunbarth, C. M.; Toby, B. H.; Tsapatsis, M. A Titanosilicate Molecular Sieve with Adjustable Pores for Size-Selective Adsorption of Molecules. *Nature* **2001**, *412* (6848), 720–724.
- (91) Xu, Z.; Michos, I.; Cao, Z.; Jing, W.; Gu, X.; Hinkle, K.; Murad, S.; Dong, J. Proton-Selective Ion Transport in ZSM-5 Zeolite Membrane. *J. Phys. Chem. C* **2016**, *120* (46), 26386–26392.
- (92) Nightingale, E. R. Phenomenological Theory of Ion Solvation. Effective Radii of Hydrated Ions. *J. Phys. Chem.* **1959**, *63* (9), 1381–1387.
- (93) West, R.; Baney, R. H. Hydrogen Bonding Studies. II. 1 The Acidity and Basicity of Silanols Compared to Alcohols 2. *J. Am. Chem. Soc.* **1959**, *81* (23), 6145–6148.
- (94) Nawrocki, J. The Silanol Group and Its Role in Liquid Chromatography. *J. Chromatogr. A* **1997**, *779* (1–2), 29–71.
- (95) Basila, M. R. Hydrogen Bonding Interaction between Adsorbate Molecules and Surface Hydroxyl Groups on Silica. *J. Chem. Phys.* **1961**, *35* (4), 1151–1158.
- (96) Wijmans, J. G.; Baker, R. W. The Solution-Diffusion Model: A Review. *J. Memb. Sci.* **1995**, *107*, 1–21.
- (97) Geise, G. M.; Paul, D. R.; Freeman, B. D. Fundamental Water and Salt Transport Properties of Polymeric Materials. *Prog. Polym. Sci.* **2014**, *39* (1), 1–42.
- (98) Fogarty, J. C.; Aktulga, H. M.; Grama, A. Y.; van Duin, A. C. T.; Pandit, S. A. A Reactive Molecular Dynamics Simulation of the Silica-Water Interface. *J. Chem. Phys.* **2010**, *132* (17), 174704.
- (99) Esposito, D. V. Membrane-Coated Electrocatalysts—An Alternative Approach To

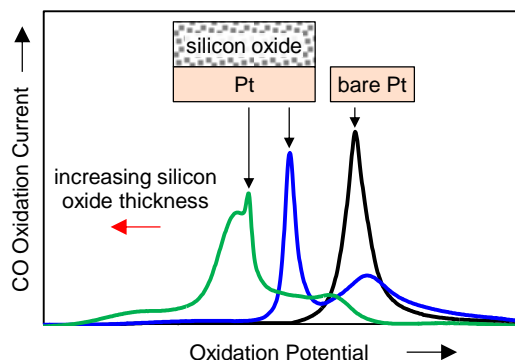
Achieving Stable and Tunable Electrocatalysis. *ACS Catal.* **2018**, 8 (1), 457–465.

- (100) Krstajic, N. V.; Vracar, L. M.; Radmilovic, V. R.; Neophytides, S. G.; Labou, M.; Jaksic, J. M.; Tunold, R.; Falaras, P.; Jaksic, M. M. Advances in Interactive Supported Electrocatalysts for Hydrogen and Oxygen Electrode Reactions. *Surf. Sci.* **2007**, 601 (9), 1949–1966.
- (101) SHI, X. Y.; ZHANG, W.; ZHANG, C.; ZHENG, W. T.; CHEN, H.; Qi, J. G. Real-Space Observation of Strong Metal-Support Interaction: State-of-the-Art and What's the Next. *J. Microsc.* **2016**, 262 (3), 203–215.
- (102) Crozier, T. E.; Yamamoto, S. Solubility of Hydrogen in Water, Sea Water, and Sodium Chloride Solutions. *J. Chem. Eng. Data* **1974**, 19 (3), 242–244.

## CHAPTER 5

### SILICON OXIDE-ENCAPSULATED PLATINUM THIN FILMS AS HIGHLY ACTIVE ELECTROCATALYSTS FOR CARBON MONOXIDE AND ALCOHOL OXIDATION

Chapter 5 also utilizes the well-defined  $\text{SiO}_x$ -encapsulated Pt thin film architecture to investigate the ability of  $\text{SiO}_x$  to affect catalytic pathways through unique energetics at buried interfaces and/or direct participation in the electrooxidation of CO, methanol, and ethanol. As previously mentioned in section 1.6.3 hydroxyl groups within or on oxide materials have been shown to facilitate the removal of CO-intermediates from the surface of the metallic catalysts such as Pt.<sup>1-3</sup> Among various oxides,  $\text{SiO}_2$  is acid-stable and forms hydroxyl species in acidic solution making it a good candidate for MOR and EOR electrocatalyst in PEM based DAFCs. To efficiently promote the bifunctional mechanism and oxidize CO intermediates, it is critically important that catalytic materials are designed with architectures that minimize the distance between the active sites for alcohol decomposition and CO oxidation while also maximizing the density of these neighboring sites. The oxide-encapsulated electrocatalyst design it leverages the high density of metal/oxide interfacial sites at the buried interface, compared to conventional oxide-supported nanoparticles, to achieve unique kinetics. Overall, these demonstrations highlight the potential of using  $\text{SiO}_x$ -based MCECs for CO tolerant and highly active alcohol oxidation electrocatalysts.





## 5.1 Introduction

Small alcohol fuels, such as methanol and ethanol, are attractive energy carriers for a sustainable energy future because of their high energy densities, ease of storage as liquids, and the ability to produce them electrochemically from carbon dioxide ( $\text{CO}_2$ ) and water ( $\text{H}_2\text{O}$ ) using electricity from renewable resources.<sup>4–7</sup> These alcohol fuels can be converted back into electricity for various applications using direct alcohol fuel cells (DAFCs), where alcohol oxidation at the anode is coupled with the oxygen reduction reaction (ORR) at the cathode.<sup>8,9</sup> Despite recent advances in the performance of DAFCs,<sup>8</sup> their power densities ( $\approx 0.01\text{--}10\text{ W cm}^{-2}$ ) are still significantly lower than hydrogen fuel cells (HFCs), which typically achieve power densities of  $\approx 10\text{--}100\text{ W cm}^{-2}$ .<sup>10</sup> Major reasons for the performance gap between DAFCs and HFCs are voltage losses that originate from (i) fuel cross-over to the cathode, and (ii) sluggish reaction kinetics associated with alcohol oxidation at the DAFC anode.<sup>11,12</sup> The state-of-the-art anode catalysts in acidic medium are based on nanoparticles of platinum (Pt) or Pt alloys that are supported on high surface area carbon (Pt/C).<sup>13–15</sup> The performance of DAFC anodes can also suffer from degradation of the electrocatalyst and carbon support, which can lead to dissolution, detachment, migration, and/or agglomeration of the catalytic nanoparticles.<sup>16–18</sup>

In order to reduce kinetic overpotential losses associated with the methanol oxidation reaction (MOR) and ethanol oxidation reaction (EOR), significant research efforts have been made to better understand the mechanisms that underlie these reactions. It is now well understood that the MOR and EOR are complex multistep reactions that require catalytic sites for alcohol adsorption and dehydrogenation, as well as sites that facilitate oxidation of carbonaceous intermediates to the desired end product, carbon dioxide ( $\text{CO}_2$ ).<sup>5,19–23</sup> Many studies have highlighted the importance of efficiently oxidizing carbon monoxide (CO), a commonly observed

intermediate in alcohol oxidation that can “poison” active sites if they bind to this molecule too strongly.<sup>8,24</sup> Others have found that CO oxidation is more favorable when oxygen-containing co-reactants such as adsorbed hydroxyl groups ( $\text{OH}_{\text{ad}}$ ) are located in close proximity to the adsorbed CO.<sup>25–27</sup> The two most common methods to introduce oxygen-containing species near active sites, and thereby improve CO tolerance, are (i) to alloy Pt-based catalysts with a second metal that has a higher affinity for oxygen (more oxophilic), such as ruthenium (Ru)<sup>28,29</sup> or tin (Sn),<sup>30,31</sup> and (ii) to support metal nanoparticles on metal oxide supports that contain hydroxyl groups.<sup>2,31–38</sup> The enhanced electrocatalytic activity of Pt electrocatalysts to the MOR and EOR by these two modifications is attributed to the so-called bifunctional mechanism whereby metallic Pt provides sites to initially adsorb and dehydrogenate the alcohol while the oxophilic material supplies oxygen-containing species that subsequently oxidize the adsorbed carbonaceous intermediates to  $\text{CO}_2$ .<sup>39</sup> Alloying Pt with Ru or Sn has proven to be effective for alleviating CO poisoning issues,<sup>28–31</sup> but it does not address the issue of carbon support oxidation. As a result, oxide supports have attracted considerable attention for MOR and EOR due to their: (i) higher corrosion resistance than carbon<sup>40,41</sup> (ii) abundance of hydroxyl groups to facilitate CO removal, and (iii) their potential to suppress catalyst particle migration thanks to partial encapsulation and/or stronger bonding between the oxide material and the metal nanoparticles.<sup>41–43</sup> In particular, metal oxide supports, such as  $\text{CeO}_2$ ,<sup>44,45</sup>  $\text{MgO}$ ,<sup>46</sup>  $\text{WO}_3$ ,<sup>47</sup>  $\text{SnO}_2$ ,<sup>31</sup> and  $\text{TiO}_2$ ,<sup>33–35</sup> have demonstrated enhanced electrocatalytic MOR and EOR when paired with Pt nanoparticles.

Motivated by prior studies on metal oxide supports for alcohol oxidation, the current paper investigates oxide|metal electrocatalysts for alcohol oxidation that are composites of silicon oxide ( $\text{SiO}_x$ ) and Pt.<sup>48–53</sup> Similar to many other oxides supports,  $\text{SiO}_x$  contains hydroxyl groups, in the form of silanols ( $\text{Si-OH}$ ),<sup>54–56</sup> which have been shown to promote CO oxidation on Pt

electrocatalysts. Additionally, silica ( $\text{SiO}_2$ ) is known to have excellent chemical stability in acidic and neutral pHs.<sup>57</sup> Many studies have demonstrated improved MOR activity and stability with  $\text{SiO}_2$  supported Pt catalysts, with most suggesting that silanol groups suppress CO poisoning and thereby enhance MOR activity through the bifunctional mechanism.<sup>48–52</sup> Pt/ $\text{SiO}_2$  catalysts have also shown enhanced EOR activity compared to Pt/graphite.<sup>58</sup>

Despite the promising reports of high alcohol oxidation activity with Pt/oxide composite electrocatalysts, two common concerns are the lower surface areas and electrical conductivities of oxides such as silica compared to conventional carbon supports.<sup>52</sup> Consequently, studies that involve oxide supports typically require intricate modifications to improve their low electrical conductivity and surface area. To improve the electrical conductivity,  $\text{TiO}_2$  is commonly doped with Nb,<sup>3,59</sup> C,<sup>60</sup> or N.<sup>61</sup> For  $\text{SiO}_2$  supports, unique architectures have been employed to increase conductivity and surface area such as incorporating Pt/silica into mesoporous conductive carbon supports<sup>62</sup> and functionalizing hollow  $\text{SiO}_2$  spheres with amino acids to help anchor Pt onto  $\text{SiO}_2$  and  $\text{SiO}_2$  onto conductive supports.<sup>52</sup> Although these approaches can effectively improve CO tolerance, they often require complex, high temperature synthesis methods to produce the precise composition, structure, and loading. Moreover, methods that involve high temperature treatment could ultimately decrease specific surface area of the support and catalyst.

In order to compensate for the low surface areas of oxide supports and minimize catalyst loading, researchers have also tried to minimize catalyst nanoparticle size, albeit at the expense of accelerated dissolution of the smaller nanoparticles.<sup>1,63</sup> If smaller ( $< 5$  nm) Pt nanoparticles could be stabilized on oxide supports, Chao-Cheng et. al suggested that they could better take advantage of the bifunctional mechanism compared to larger particles because a higher percentage of the Pt sites would be located in close proximity to the hydroxyl-containing oxide support.<sup>63</sup> Extending

this logic further, we hypothesize that the most active alcohol oxidation electrocatalysts are those that are designed to maximize the number of active sites for alcohol adsorption/dehydrogenation that are in close proximity to hydroxyl sites for CO oxidation.

Towards this end, we explore  $\text{SiO}_x|\text{Pt}$  alcohol oxidation electrocatalysts based on the membrane-coated electrocatalyst (MCEC) architecture,<sup>64</sup> in which the active metal electrocatalyst (Pt) is encapsulated by an ultrathin ( $<10$  nm thick) oxide layer ( $\text{SiO}_x$ ) that can exhibit membrane-like transport properties.<sup>65</sup> The  $\text{SiO}_x$  overlayers used in this study are fabricated with a room-temperature ultraviolet ozone (UV ozone) synthesis procedure to deposit ultrathin ( $< 10$  nm), permeable silicon oxide ( $\text{SiO}_x$ ) nanomembranes over well-defined Pt thin film electrocatalysts ( $\text{SiO}_x|\text{Pt}$ ), as depicted schematically in Figure 5.1. The underlying motivations for investigating these  $\text{SiO}_x|\text{Pt}$  MCECs are their potential to (i) maximize interfacial contact between the Pt catalyst and hydroxyl-containing  $\text{SiO}_x$  overlayer, (ii) suppress corrosion of the metal nanoparticles and the underlying conductive support, and (iii) create unique active sites at the metal/oxide buried interface through confinement effects.<sup>66–68</sup>

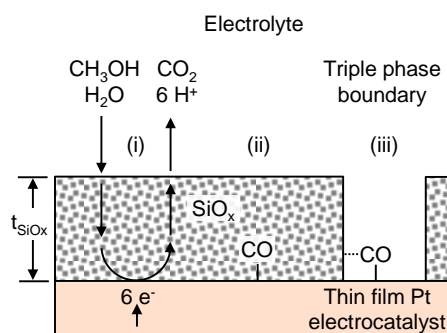


Figure 5.1. Schematic side view illustrating methanol oxidation at a planar Pt electrocatalyst covered by an ultrathin, permeable  $\text{SiO}_x$  overlayer with thickness  $t_{\text{SiO}_x}$ . The overlayer enables (i) transport of reactants and products to and from the electrocatalytic  $\text{Pt}|\text{SiO}_x$  buried interface. Also shown are adsorbed CO intermediates located at (ii) the buried interface and (iii) an opening in the  $\text{SiO}_x$  film which can create a triple phase boundary site

MCEC-type architectures have been previously employed for stabilizing metallic nanoparticles or molecular catalysts in low-temperature fuel cells<sup>69–77</sup> and photoelectrochemical cells.<sup>78–80</sup> Takenaka et. al. demonstrated that silica coatings on Pt nanoparticle catalysts improved durability and minimized particle agglomeration and dissolution for the ORR, but found that the same electrodes exhibited poor activity for the MOR and EOR compared to uncoated Pt/C nanoparticle catalysts.<sup>74</sup> The poor alcohol oxidation activity was attributed to suppressed transport of small polar alcohols across the hydrophobic silica used in that study. By contrast, we report herein on the use of hydrophilic SiO<sub>x</sub>|Pt MCECs that enhance alcohol oxidation. We have recently shown that SiO<sub>x</sub> overlayers, fabricated with the UV ozone method, are effective at suppressing Pt nanoparticle migration<sup>80</sup> and facilitating facile transport of protons (H<sup>+</sup>) and hydrogen (H<sub>2</sub>) between the bulk electrolyte and buried SiO<sub>2</sub>|Pt interface.<sup>65</sup> In the current paper, we extend the use of these hydrophilic SiO<sub>x</sub> overlayers, deposited on planar Pt films, to study CO oxidation, MOR, EOR, and formic acid oxidation reactions (FAOR) at Pt|SiO<sub>x</sub> interfaces (Figure 5.1). These model thin film electrodes are an attractive platform for studying these reactions because they have very well-defined catalyst surface areas, avoid complexities/non-uniformities associated with nanoparticles, and allow for detailed characterization of the buried oxide/metal interface. The thin film SiO<sub>x</sub>|Pt electrodes in this study demonstrate that the MCEC design leverages the high density of reaction sites at Pt|SiO<sub>x</sub> interfaces to readily oxidize intermediates and increase MOR, EOR, and FAOR activity. Furthermore, the impact of varied potential and pH conditions on Pt-OH<sub>ad</sub>, PtO<sub>x</sub> and Si-OH formation are evaluated to elucidate the role of hydroxyl groups on Pt and SiO<sub>x</sub> during the MOR. Overall, this study shows that the SiO<sub>x</sub>-encapsulated Pt electrocatalysts can enhance alcohol oxidation reactions with minimal diffusion barrier against alcohol transport to Pt|SiO<sub>x</sub> interfaces.

## 5.2 Experimental Methods

### 5.2.1 Electrode Preparation

A detailed description of the procedure for synthesizing Pt and SiO<sub>x</sub>/Pt thin film electrodes can be found in Chapter 4.<sup>65</sup> Briefly, a 4.5 nm thick Ti adhesion layer and 50 nm thick Pt film were sequentially deposited by electron-beam evaporation onto degeneratively doped Si(100) conductive substrates (p<sup>+</sup>Si, WRS materials). For SiO<sub>x</sub>/Pt electrodes, a mixture of the trimethylsiloxy terminated polydimethylsiloxane (PDMS) precursor in toluene<sup>81,82</sup> was spin coated onto Pt/Ti/p<sup>+</sup>Si substrates at a speed of 4000 rpm for 2.5 min. PDMS/toluene solution concentrations of 1.2 mg ml<sup>-1</sup> and 3.0 mg ml<sup>-1</sup> were selected to produce SiO<sub>x</sub> films with thicknesses of  $\approx 2$  nm and  $\approx 5$  nm, respectively. The films were dried in a vacuum oven and converted to SiO<sub>x</sub> under UV light in air for 2 hours within an UV ozone cleaning system (UVOCS, T10X10/OES).<sup>81,83</sup> Electrical contacts were made by soldering a Cu wire to the back side of the electrode substrate. Electrodes were then sealed with vinyl 3M<sup>TM</sup> Electroplating Tape 470, leaving a well-defined 0.246 cm<sup>2</sup> circular opening on the front of the electrode for electrochemical measurements.

### 5.2.2 Structural Characterization

The thickness of the SiO<sub>x</sub> film was measured with a Woollam alpha-SE ellipsometer and fit with a Cauchy model. A standard error in thickness was determined from measurements on all the  $\approx 2$  nm (sample size N=2) and  $\approx 5$  nm (N=6) thick samples used in this study. The morphology of the SiO<sub>x</sub> thin films was analyzed with a Bruker Dimension Icon atomic force microscopy (AFM). A ScanAsyst silicon tip on a nitride lever silicon cantilever with a 25 nm tip radius, spring force constant of 0.4 N m<sup>-1</sup> and a resonant frequency of 70 kHz was used to acquire images with a 0.1 Hz scan rate in peak force quantitative nanomechanical mapping mode. X-ray photoelectron

spectroscopy (XPS) measurements were performed with a Phi XPS system that was operated at a base pressure of  $2 \times 10^{-10}$  Torr using a monochromatic aluminum K $\alpha$  source (X-ray power 15 kV, 20 mA), a pass energy of 23.5 eV, and a charge neutralizer. The charge neutralizer was calibrated to give a C 1s peak center was of 284.5 eV; the Si 2p, O 1s, and Pt 4f peaks were consequently shifted by the same amount. The peak area ratios were calculated after accounting for the atomic sensitivity factors (ASF<sub>i</sub>) (ASF<sub>Si</sub> = 0.180, ASF<sub>C</sub> = 0.296, ASF<sub>O</sub> = 0.711, ASF<sub>Pt</sub> = 5.575).<sup>84</sup> The value of the Si ASF for SiO<sub>2</sub> was adjusted from ASF<sub>Si</sub> = 0.339 for pure Si to account for the difference in atomic density and attenuation lengths between Si in SiO<sub>2</sub> and pure Si.

***Electrochemical Characterization***

All electrochemical measurements were performed with a SP-200 BioLogic potentiostat controlled by EC-Lab v11.18 software. A carbon rod (Saturn Industries) counter electrode and a Ag|AgCl/sat. 3 M KCl reference electrode ( $E^\circ = 0.21$  V vs. NHE, Hach, E21M002) were used in a standard three electrode configuration. Cyclic voltammetry (CV) measurements used to determine the electrochemically active surface areas (ECSA) from hydrogen underpotential deposition ( $H_{\text{upd}}$ ) signal were carried out in deaerated 0.5 M sulfuric acid that was prepared from concentrated sulfuric acid (H<sub>2</sub>SO<sub>4</sub>, Fisher Scientific, ACS grade) and 18 M $\Omega$  deionized water (Millipore, Milli-Q Direct 8). All H<sub>2</sub>SO<sub>4</sub> solutions were bubbled with nitrogen (N<sub>2</sub>) gas for 20 minutes to purge dissolved oxygen prior to measurements. During all electrochemical measurements, the head space of the electrochemical cell was continuously purged N<sub>2</sub>. Current densities are normalized with respect to the geometric area of the exposed electrode unless stated otherwise. The ECSAs of Pt electrodes were calculated from the average of the net charge associated with underpotential adsorption and desorption of hydrogen atoms that was recorded between potentials of 0.05 V and 0.45 V vs. RHE during CV measurements. Current due to double

layer capacitance was subtracted during the analysis, and a conversion factor of  $210 \mu\text{C cm}^{-2} \text{Pt}$  was used to compute ECSA from the  $H_{\text{upd}}$  charge.<sup>85</sup> Before CO stripping voltammetry, CO was adsorbed onto Pt at a constant applied potential of 0.05 V vs. RHE for 3 min in a CO saturated solution. While the electrode was held at this potential, excess CO in solution was subsequently removed by purging the solution with  $\text{N}_2$  gas for 20 min. The CO was then stripped from the surface by sweeping the potential from 0.22 V to 0.0 V to 1.2 V vs. RHE at  $20 \text{ mV s}^{-1}$ . Upon reaching the positive scan vertex, the scan direction was reversed to complete the first CV cycle. A second CV cycle was subsequently recorded over the same potential range to verify that no CO remained adsorbed on the electrode after the first cycle. The amount of CO deposited on the surface was quantified from the difference in current measured during the positive scans of the first and second CV cycles. A conversion factor of  $420 \mu\text{C cm}^{-2} \text{Pt}$  was used to calculate the ECSA from the integrated CO stripping charge.<sup>86</sup> The alcohol and formic acid oxidation experiments were performed in 0.5 M  $\text{H}_2\text{SO}_4$  with 0.5 M methanol ( $\text{CH}_3\text{OH}$ , Fisher Chemical, ACS grade), 0.5 M ethanol ( $\text{C}_2\text{H}_5\text{OH}$ , Sigma Aldrich, ACS reagent), or 0.5 M formic acid ( $\text{HCOOH}$ , Decon Laboratories, USP grade). CVs were performed for 100 cycles and typically reached a steady state by cycle 15. In examining the effect of the CV vertex on electrochemical activity, the upper vertex potential was increased from 0.8 V to 1.2 V vs. RHE in 100 mV increments. Each upper vertex was maintained for 15 cycles to allow the sample to reach a steady state. Following the last cycle with an upper vertex potential of 1.2 V vs. RHE, the vertex was decreased back to 0.8 V vs. RHE to evaluate any discrepancy from the beginning of cycling. Potassium hydroxide (KOH, Sigma Aldrich, ACS reagent) was used to remove  $\text{SiO}_x$  from Pt for control experiments, in which samples were exposed to  $\text{SiO}_x$  synthesis conditions. KOH etching was performed in 20 wt% KOH with 3 v/v% isopropyl alcohol ( $\text{C}_3\text{H}_8\text{OH}$ , Fisher Chemical, ACS reagent) for 10 minutes at  $75^\circ\text{C}$ .



Experiments in neutral pH electrolytes were performed in a 0.1 M sodium phosphate buffer solution ( $\text{Na}_2\text{HPO}_4/\text{NaH}_2\text{PO}_4$ , Sigma Aldrich, Reagent Plus).

## 5.3 Results

### 5.3.1 Characterization

#### 5.3.1.1 Physical and Chemical Characterization

As-made  $\text{SiO}_x/\text{Pt}$  and Pt thin films were first characterized by ellipsometry, AFM, and XPS to evaluate their composition and structure. The thickness of  $\text{SiO}_x$  overlayers were determined by ellipsometry and found to be  $2.4 \pm 0.2$  nm and  $5.4 \pm 0.3$  nm. For simplicity, these samples are referred to herein as 2 nm  $\text{SiO}_x/\text{Pt}$  and 5 nm  $\text{SiO}_x/\text{Pt}$ . The topologies of these  $\text{SiO}_x$  films were measured by AFM and compared to the bare Pt control sample. The Pt thin film exhibited a uniform surface with root mean squared (rms) surface roughness of 0.95 nm, while the 2 nm and 5 nm  $\text{SiO}_x$  films exhibited a more smooth surface with increasing  $\text{SiO}_x$  thickness, rms of 0.55 nm and 0.41 nm respectively (Figure 5.2). No microscopic holes in the  $\text{SiO}_x$  overlayers were observed.

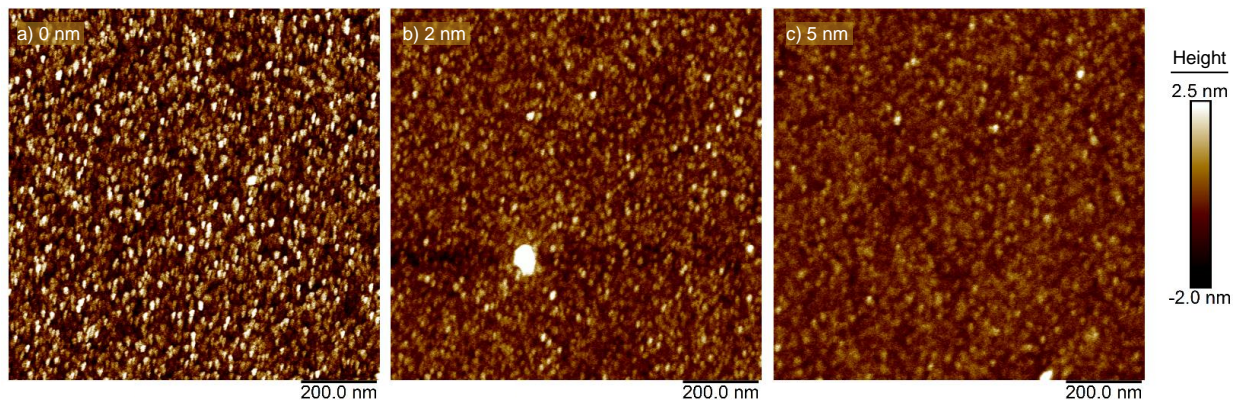


Figure 5.2. AFM images of as-made a) 0 nm, b) 2 nm, and c) 5 nm  $\text{SiO}_x/\text{Pt}$  electrodes.

XPS characterization of the as-synthesized  $\text{SiO}_x$  films revealed that the PDMS precursor was primarily converted to  $\text{SiO}_2$ , although  $\approx 8$  atomic % carbon (C) remained (Figure 5.3). These findings are consistent with previous studies of  $\text{SiO}_x$  films made by the UV ozone process.<sup>81,83</sup> The

Si 2p peak center was located at 103.5 eV, which corresponds to the  $\text{Si}^{4+}$  oxidation state and is consistent with most of the Si in the form of silicon dioxide ( $\text{SiO}_2$ ).

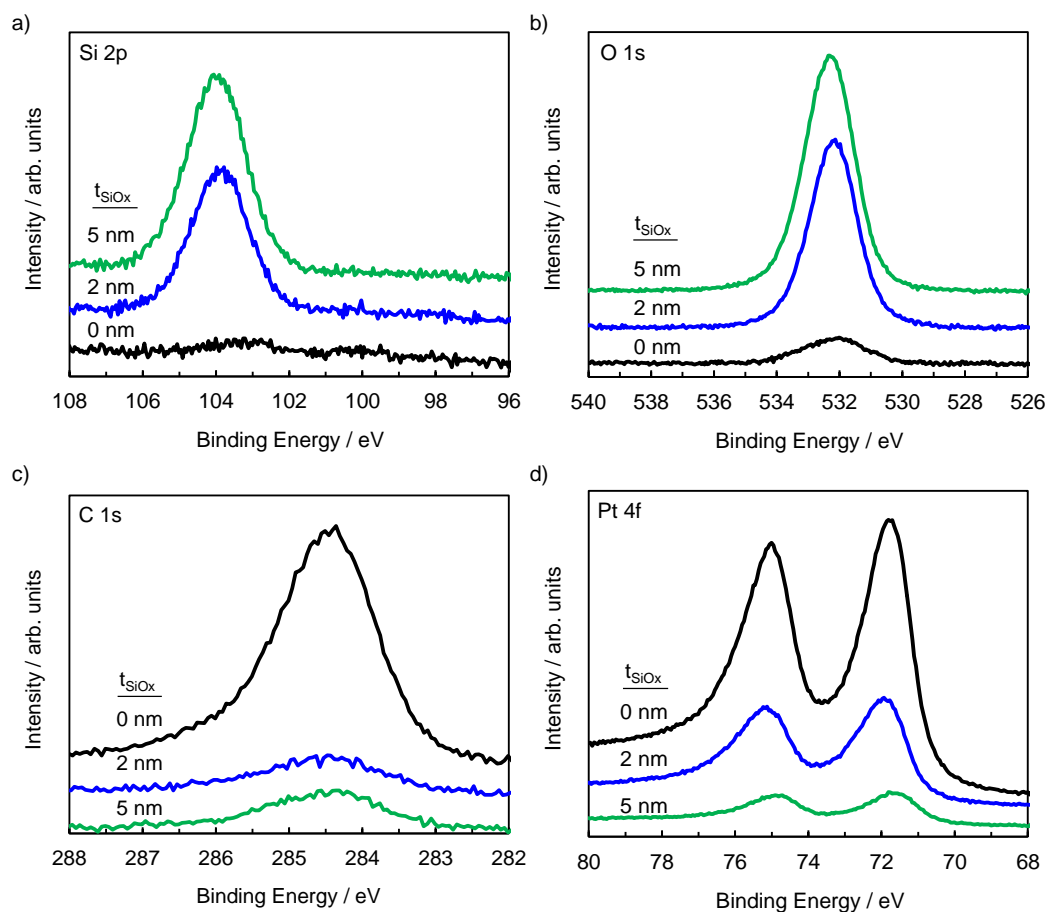


Figure 5.3. a.) Si 2p, b.) O 1s, c.) C 1s and d) Pt 4f XPS spectras for 0 nm (black), 2 nm (blue), and 5 nm  $\text{SiO}_x$ |Pt electrodes. The C 1s peaks were shifted and centered to 284.8 eV and the O 1s peaks associated with the  $\text{SiO}_x$  overlays were shifted by the same amount.

### 5.3.1.2 Electrochemically Active Surface Area

The electrochemically active surface areas (ECSAs) of all electrodes were characterized by analyzing the signal associated with  $\text{H}_{\text{upd}}$  during CV cycling in 0.5 M  $\text{H}_2\text{SO}_4$ . The steady state voltammograms for the 0 nm (bare Pt), 2 nm, and 5 nm  $\text{SiO}_x$ |Pt samples are provided in Figure 5.4. All samples exhibit  $\text{H}_{\text{upd}}$  signal and Pt-oxide formation/reduction peaks that are characteristic of polycrystalline Pt electrodes in sulfuric acid.<sup>87,88</sup> Analysis of the integrated  $\text{H}_{\text{upd}}$  signal gives

ECSA values of 1.09, 1.12, and 1.23 cm<sup>2</sup> Pt per cm<sup>2</sup> geometric area for the 0 nm, 2 nm, and 5 nm samples, respectively. Similar to other publications,<sup>65,74,89</sup> the fact that the ECSA does not decrease for SiO<sub>x</sub>|Pt electrodes attests to the ability of protons to transport through the SiO<sub>x</sub> overlayer and confirms that the buried interface between the SiO<sub>x</sub> and Pt thin film is electrochemically active. Despite having a similar H<sub>upd</sub>-determined ECSA to the bare Pt control, the CV curve for the 5 nm SiO<sub>x</sub>|Pt sample shows some key differences from bare Pt. In addition to slight shifts in the H<sub>upd</sub> peak locations, Figure 5.4 reveals significant differences in the features at more positive potentials associated with (i) formation of adsorbed oxygen species such as O<sub>ad</sub> and OH<sub>ad</sub>, (ii) their subsequent oxidation to form Pt-oxides, and (iii) reduction of these species during the negative scan. Notably, the onset of Pt oxidation shifts to slightly less positive potentials with increasing SiO<sub>x</sub> thickness.

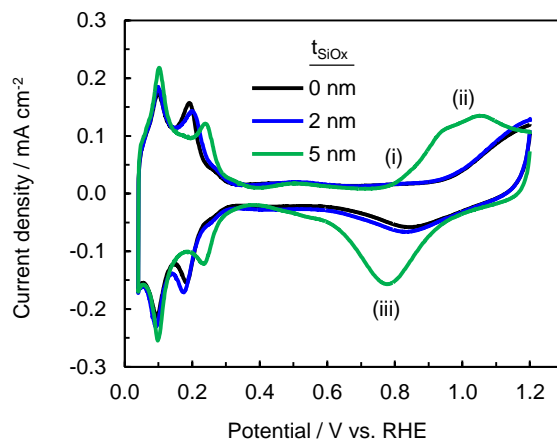


Figure 5.4. CV curves (30<sup>th</sup> cycle) recorded at 100 mV s<sup>-1</sup> in deaerated 0.5 M H<sub>2</sub>SO<sub>4</sub> for SiO<sub>x</sub>|Pt electrodes containing: t<sub>SiO<sub>x</sub></sub>=0 nm (black), t<sub>SiO<sub>x</sub></sub>=2 nm (blue), t<sub>SiO<sub>x</sub></sub>=5 nm (green) SiO<sub>x</sub> films

### 5.3.2 CO stripping voltammetry

Carbon monoxide (CO) stripping voltammetry was performed on SiO<sub>x</sub>|Pt and bare Pt to simultaneously measure their ECSA and evaluate their ability to oxidize CO. Figure 5.5 compares

the CO stripping curves for 0 nm (bare Pt), 2 nm SiO<sub>x</sub>|Pt, and 5 nm SiO<sub>x</sub>|Pt electrodes. For all the electrodes, no H<sub>upd</sub> signal is observed in the first cycle (solid curves), indicating that almost all electroactive sites are occupied by adsorbed CO. As the potential is scanned to more positive potentials, distinct peaks associated with CO oxidation are observed for all electrodes. The second cycle (dashed curves) shows only H<sub>upd</sub> peaks and minor features associated with Pt-oxide formation and reduction, indicating that all of the adsorbed CO was fully oxidized and stripped from the electrode surface during the first cycle. The ECSAs determined from CO stripping are 1.04, 0.86, and 1.16 cm<sup>2</sup> Pt per cm<sup>2</sup> of geometric area for the electrodes coated with 0 nm, 2 nm, and 5 nm silicon oxide, respectively.

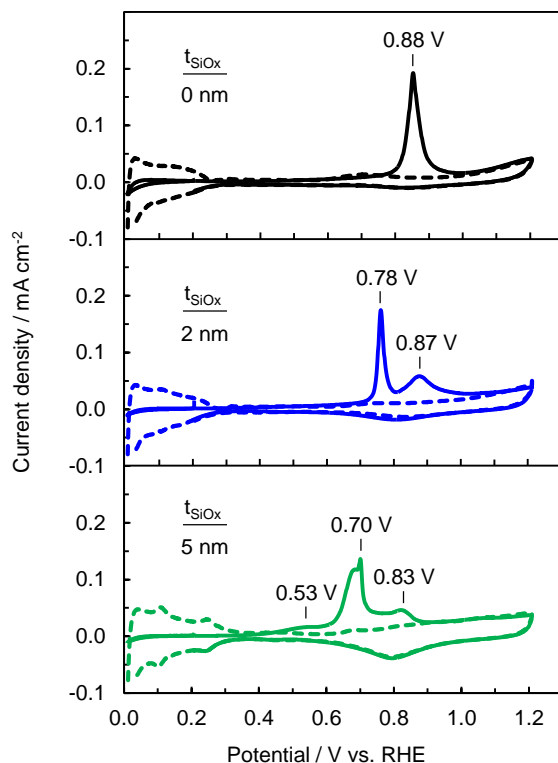


Figure 5.5. CO stripping voltammetry curves measured in 0.5 M H<sub>2</sub>SO<sub>4</sub> at a scan rate of 20 mV s<sup>-1</sup> for Pt (black), 2 nm SiO<sub>x</sub>|Pt (blue), and 5 nm SiO<sub>x</sub>|Pt (green). Solid curves represent the first CV cycle that was

carried out with CO adsorbed on the electrode surface, while dashed curves represent the second CV cycle that was performed after CO was stripped from the electrode surface during the first cycle.

Although the integrated CO oxidation charge was similar for each sample, the location and number of peaks observed for each sample varied substantially. The peak centers of the main CO oxidation peak for the bare Pt and UV ozone treated bare Pt control samples (Appendix section 5.6.1, Figure 5.13) are located at 0.88 V and 0.87 V vs. RHE, respectively. These values are in good agreement with those reported in literature,<sup>33,36</sup> and are consistent with the fact that Pt has a strong binding energy for CO. The 2 nm SiO<sub>x</sub>|Pt and 5 nm SiO<sub>x</sub>|Pt electrodes exhibit CO oxidation peaks that are shifted to more negative potentials, with peak centers located at 0.78 V and 0.72 V vs. RHE, respectively. Catalysts that require smaller overpotentials for CO oxidation are commonly described as “CO tolerant” because they require a smaller driving force to remove CO intermediates.<sup>23,38</sup> This enhanced ability to oxidize CO is often associated with the bifunctional mechanism of methanol oxidation, especially for composite electrocatalysts in which Pt is combined with oxophilic materials.<sup>29,36,48</sup>

In addition to the primary CO oxidation peaks observed in Figure 5.5, smaller but distinct oxidation peaks are also observed at more positive potentials for the 2 nm and 5 nm SiO<sub>x</sub>|Pt electrodes at 0.87 V and 0.83 V vs. RHE, respectively. These peak locations are similar to those observed for CO oxidation on bare Pt and may suggest that a small fraction of the Pt on the SiO<sub>x</sub>|Pt electrodes still exhibit bare Pt-like behavior for CO-oxidation. Another minor peak, shifted even more negative than the primary CO oxidation peaks for the SiO<sub>x</sub>|Pt electrodes, is present at  $\approx 0.53$  V vs. RHE. Importantly, the presence of this peak and the negative shift of the primary CO oxidation peaks strongly suggest that the reactive environments at the buried SiO<sub>x</sub>|Pt interface and/or SiO<sub>x</sub>|Pt|electrolyte triple phase boundary sites are very different from that at the

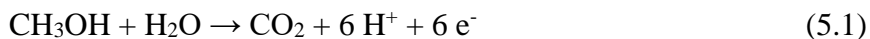
electrolyte/bare Pt interface. The negative shifts in the CO oxidation features of the SiO<sub>x</sub>|Pt electrodes with respect to those of the bare Pt control samples indicates that the SiO<sub>x</sub>|Pt is able to more easily oxidize adsorbed CO than Pt. Numerous studies on MOR electrocatalysts have connected a negative shift in the CO oxidation features to enhanced MOR activity, hypothesizing that the high activity is explained by lower CO binding energy, and therefore lower susceptibility to CO poisoning.<sup>36,38,48</sup>

### 5.3.3 *Cyclic voltammetry in methanol, ethanol, and formic acid*

The electrocatalytic activity of Pt and SiO<sub>x</sub>|Pt electrodes towards the electrooxidation of methanol, ethanol, and formic acid was evaluated by performing 100 CV cycles in a deaerated 0.5 M H<sub>2</sub>SO<sub>4</sub> supporting electrolyte.

#### 5.3.3.1 *Methanol Oxidation*

Figure 5.6 compares the CVs for 0 nm, 2 nm, and 5 nm SiO<sub>x</sub>|Pt electrodes in 0.5 M methanol, for which the methanol oxidation half reaction is:<sup>90</sup>



The MOR CV curves for all samples possess two primary oxidation peaks, which occur in the positive and negative scan directions and are centered at 0.84 V and 0.65 V vs. RHE, respectively. Recent studies have demonstrated that both of these peaks can be attributed to direct oxidation of methanol, as opposed to oxidation of intermediates, with the hysteresis in the MOR peaks arising from differences in Pt surface oxidation state during the positive and negative scan directions.<sup>91,92</sup> In the positive (forward) scan, methanol oxidation occurs on Pt before it is suppressed by the formation of a high coverage of Pt-hydroxides (Pt-OH<sub>ad</sub>) and/or Pt oxides (PtO<sub>x</sub>) at more positive potentials.<sup>91</sup> After the scan direction is reversed at the positive scan vertex, methanol oxidation gradually increases again as Pt-OH<sub>ad</sub> and PtO<sub>x</sub> species are reduced to free up metallic Pt sites that

are known to be more active for methanol decomposition. By this means, the extent of Pt oxidation that occurs during the scan to positive potentials greatly impacts the peak MOR current density that occurs during the negative (backward) scan ( $I_b$ ) as well as the ratio of the forward peak current ( $I_f$ ) to  $I_b$ . Due to the important role of Pt-oxides, the ratio of MOR peak current densities ( $I_f/I_b$ ) can be used as an indicator of the catalyst oxophilicity, which is described as the metallic (M) catalyst's susceptibility to form M-OH or  $MO_x$  species.<sup>91,93</sup> Electrocatalysts with large  $I_f/I_b$  are those with a high affinity for oxygen (oxophilic), while those with small  $I_f/I_b$  are less readily oxidized or are more easily reactivated by reducing the oxidized form back to the metallic state.<sup>91,93</sup> From Figure 5.6,  $I_f/I_b$  ratios of 1.4, 1.05 and 1.00 are computed for the 0 nm, 2 nm and 5 nm  $SiO_x|Pt$  electrodes, respectively. The relationship between the  $I_f/I_b$  ratios, catalyst oxophilicity, and Pt-OH<sub>ad</sub> and PtO<sub>x</sub> coverage are discussed further below. Overall, Figure 5.6 demonstrates the superior MOR activity of  $SiO_x|Pt$  MCECs compared to bare Pt.

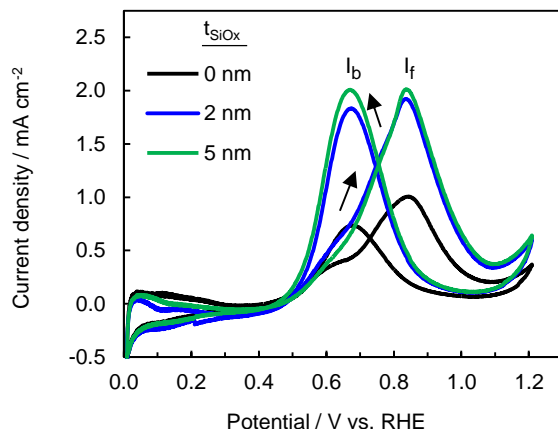


Figure 5.6. Methanol oxidation CV curves (cycle 30) measured at a scan rate of  $100\ mV\ s^{-1}$  for bare Pt (black), 2 nm  $SiO_x|Pt$  (blue), and 5 nm  $SiO_x|Pt$  (green) in deaerated 0.5 M  $H_2SO_4$  solution containing 0.5 M  $CH_3OH$ .

### 5.3.3.2 Ethanol Oxidation

The electrooxidation activity of the SiO<sub>x</sub>|Pt electrodes was further investigated for the EOR (Figure 5.7), for which the half reaction is:<sup>7</sup>



The key difference between the EOR and MOR is that the former requires breaking a carbon-carbon bond, which leads to larger overpotentials and smaller current densities.<sup>94,95</sup> Comparing Figures 5.6 (MOR) and 4b (EOR), the EOR onset potential in the positive scan direction is shifted by  $\approx +200$  mV with respect to the MOR onset potentials for both bare Pt and 5 nm SiO<sub>x</sub>|Pt. As with the MOR CVs, the EOR CVs show that the SiO<sub>x</sub>|Pt electrode achieves significantly higher  $I_f$  compared to the bare Pt control sample, but the values of  $I_f$  are greatly suppressed compared to those measured in methanol. Another major difference between the MOR and EOR CVs is the change in the ratio  $I_f/I_b$ . This difference can be primarily explained by incomplete oxidation of ethanol during the positive scan. Previous studies have shown that  $I_f$  and  $I_b$  in EOR CVs are primarily associated with ethanol oxidation and subsequent oxidation of intermediates, respectively.<sup>94</sup> Consistent with previous studies of Pt-based EOR electrocatalysts, we compute values of  $I_f/I_b$  of 0.26 and 0.31 for the bare Pt and SiO<sub>x</sub>|Pt samples, respectively. Additionally, similar to the MOR results, the SiO<sub>x</sub>|Pt electrode exhibits an approximate twofold increase in current densities compared to Pt, during both the positive and negative scans.



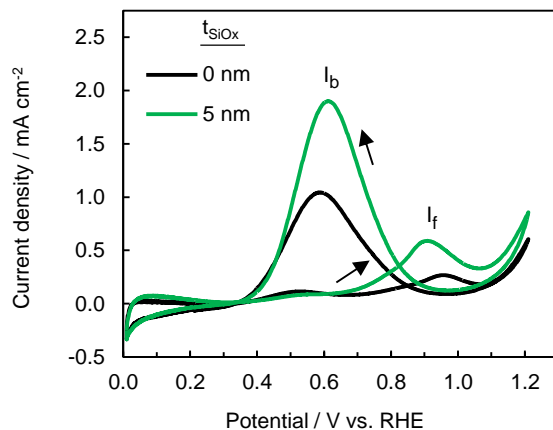
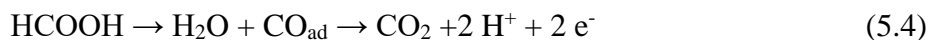


Figure 5.7. Ethanol oxidation CV curves (cycle 30) measured at a scan rate of 100 mV s<sup>-1</sup> for bare Pt (black) and 5 nm SiO<sub>x</sub>|Pt (green) in deaerated 0.5 M H<sub>2</sub>SO<sub>4</sub> solution containing 0.5 M C<sub>2</sub>H<sub>5</sub>OH.

### 5.3.3.3 Formic Acid Oxidation

Figure 5.8 compares the FAOR for bare Pt and 5 nm SiO<sub>x</sub>|Pt electrodes. Formic acid is of interest, not only as a liquid fuel, but also because it has been reported as an intermediate species produced during the MOR and EOR.<sup>96</sup> The FAOR is commonly considered to occur through two parallel reaction paths: the direct (Equation 5.3) and indirect (Equation 5.4) mechanisms:<sup>97</sup>



In the direct mechanism, formic acid is rapidly converted into the CO<sub>2</sub> end product, while the indirect mechanism proceeds through an adsorbed CO intermediate (CO<sub>ad</sub>). Ideally, an efficient electrocatalyst will promote the direct FAOR to avoid adsorbed CO poisoning that can result from the indirect oxidation pathway. As seen in Figure 5.8, two oxidation peaks are observed in the forward scan and are centered at  $\approx 0.60$  V and  $\approx 0.95$  V (labeled I<sub>f1</sub> and I<sub>f2</sub>). The first peak, I<sub>f1</sub>, and second peak, I<sub>f2</sub>, in the positive scans are primarily associated with the direct and indirect FAOR, respectively, in which I<sub>f2</sub> arises at more positive potentials where CO<sub>ad</sub> can be more easily oxidized.<sup>96,97</sup> The broad peak in the negative scan, I<sub>b</sub>, is commonly associated with the oxidation

of residual intermediates.<sup>96,97</sup> As with the methanol and ethanol CVs, the formic acid CV curves in Figure 5.8 show that the 5 nm SiO<sub>x</sub>|Pt exhibits higher FAOR activity than bare Pt. Both 5 nm SiO<sub>x</sub>|Pt and bare Pt electrode show two peaks in the forward scan, indicating both samples catalyze direct and indirect FAOR. In addition, the 5 nm SiO<sub>x</sub>|Pt I<sub>f2</sub> peak center is shifted to a less positive potential by 25 mV with respect to I<sub>f2</sub> for bare Pt, consistent with the negative shift in CO oxidation peaks for the SiO<sub>x</sub>|Pt compared to bare Pt (Figure 5.5).

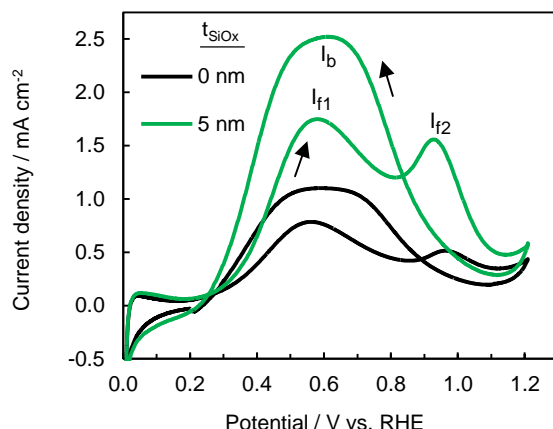


Figure 5.8. Formic acid oxidation CV curves (cycle 30) measured at a scan rate of 100 mV s<sup>-1</sup> for bare Pt (black) and 5 nm SiO<sub>x</sub>|Pt (green) in deaerated 0.5 M H<sub>2</sub>SO<sub>4</sub> solution containing 0.5 M HCOOH.

#### 5.3.4 Role of Pt-OH<sub>ad</sub> and PtO<sub>x</sub> on methanol oxidation

Several studies have shown that the extent of Pt oxidation can influence CO oxidation and MOR activity. While the formation of Pt-oxides (PtO<sub>x</sub>, x=1 or 2)<sup>98</sup> has a prohibitive effect on MOR activity,<sup>91,93,99</sup> the presence of intermediate coverages of Pt hydroxides, Pt-OH<sub>ad</sub>, is believed to assist in CO removal to allow continual MOR.<sup>91</sup> To investigate the role of Pt oxides on the MOR for bare Pt and SiO<sub>x</sub>|Pt electrodes, MOR CVs were carried out where the upper vertex potential was incrementally increased. Upper scan vertices ranging between 0.8 V and 1.2 V were chosen

to transition between conditions where Pt oxidation would be avoided or favored, based on the Pt-OH<sub>ad</sub> and PtO<sub>x</sub> features observed in the control CV curves performed in 0.5 M H<sub>2</sub>SO<sub>4</sub> without methanol (Figure 5.4). Figure 5.9 shows MOR CVs for bare Pt and 5 nm SiO<sub>x</sub>|Pt electrodes with upper vertices of 0.8 V, 1.0 V, and 1.2 V vs. RHE. The effect of the positive vertex potential on the forward and backward scan peak currents are summarized in Figure 5.9c, with the complete set of CV curves provided in Appendix section 5.6.2, Figure 5.14. Figure 5.9a shows that the bare Pt electrode exhibits very low MOR activity for CVs with positive vertex potentials less than 1.1 V vs. RHE, but that a sudden jump in MOR activity is achieved once the scan vertex is more positive than 1.1 V vs. RHE. In contrast, Figure 5.9b shows the SiO<sub>x</sub>|Pt electrode achieves high MOR activity regardless of upper vertex potential. Interestingly, when the potential vertex was changed back to 0.8 V vs. RHE (Figure 5.14) the bare Pt showed an increased MOR activity similar to the CV performed to 1.2 V vs. RHE, while the MOR activity of the SiO<sub>x</sub>|Pt remained high for all CV scans. These results demonstrate the formation of Pt-OH<sub>ad</sub> and PtO<sub>x</sub>, specifically at more oxidizing potentials, has a strong effect on initiating MOR activity for bare Pt but has essentially no effect for SiO<sub>x</sub>|Pt. For bare Pt, the upper potential vertex that leads to an increase in MOR activity approximately coincides with the onset potential for Pt oxidation, as observed in Figure 5.4. This result is consistent with many previous studies on Pt-based MOR electrocatalysts that have shown the importance of having some Pt-OH<sub>ad</sub> species in order to facilitate removal of adsorbed CO intermediates.<sup>91,100</sup> Meanwhile, for SiO<sub>x</sub>|Pt, the lack of dependency of the MOR peak currents on the upper scan rate suggests that the formation of Pt-OH<sub>ad</sub>, may not be necessary to accelerate methanol oxidation.

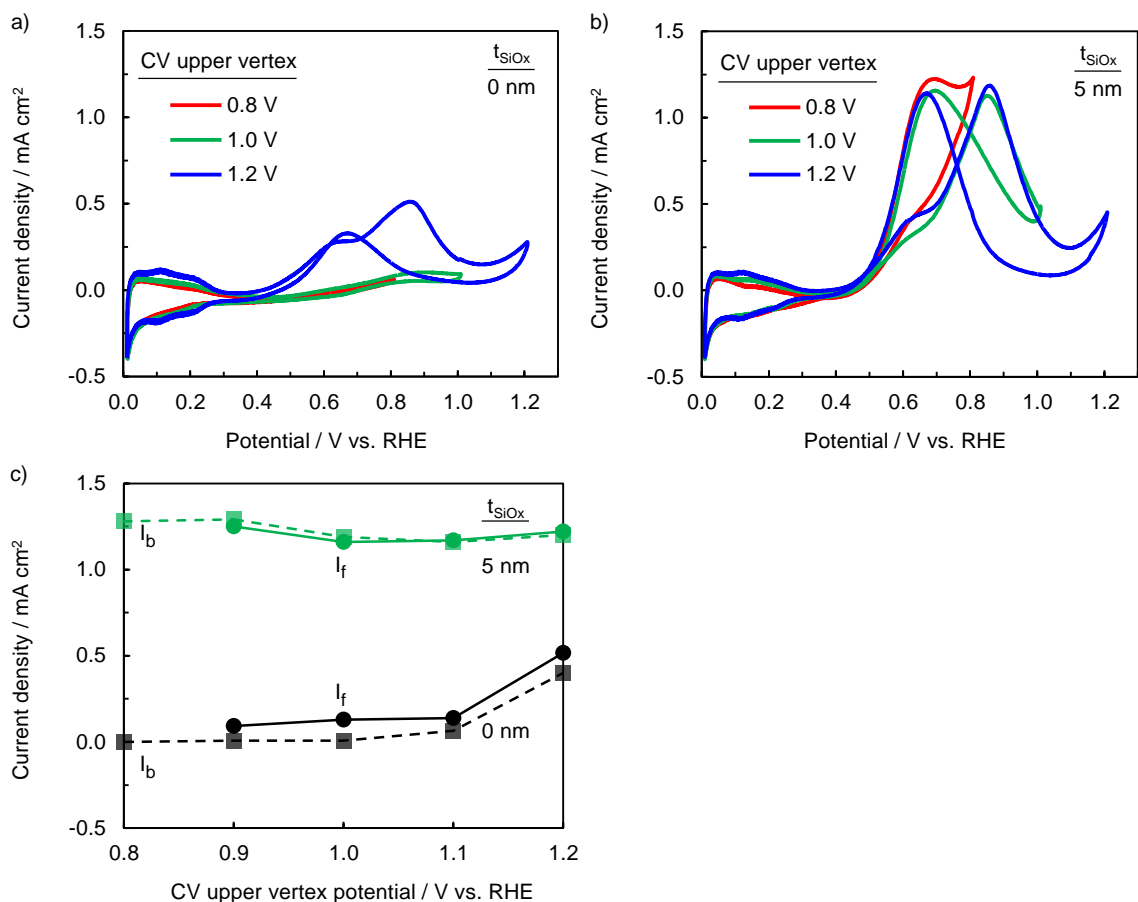


Figure 5.9. Methanol oxidation CVs (steady state cycle 15) with different upper scan vertices for a)  $t_{\text{SiO}_x} = 0 \text{ nm}$  and b)  $t_{\text{SiO}_x} = 5 \text{ nm}$  SiO<sub>x</sub>|Pt MCEC. c) Peak MOR current densities recorded during the forward ( $I_f$ ) and backward ( $I_b$ ) scan segments as a function of upper vertex potential. CVs were performed in 0.5 M H<sub>2</sub>SO<sub>4</sub> containing 0.5 M CH<sub>3</sub>OH and measured at 100 mV s<sup>-1</sup>.

### 5.3.5 Electrocatalyst stability

Figure 5.10 contains the 1<sup>st</sup>, 10<sup>th</sup>, 50<sup>th</sup>, and 100<sup>th</sup> CV cycles for bare Pt and 5 nm SiO<sub>x</sub>|Pt electrodes during MOR. The MOR peak currents for bare Pt rapidly increase for the first 10 cycles before reaching maximum values between 10 and 50 cycles. Some decline in MOR peak current is observed towards the end of CV cycling, possibly due to the gradual depletion of methanol from the bulk electrolyte caused by slow evaporation of methanol into the headspace. The transient nature of the MOR peak current densities during CV cycling was very different for the SiO<sub>x</sub>|Pt

electrodes, which show very high initial MOR peak current densities that gradually decrease with cycle number (Figure 5.10b).

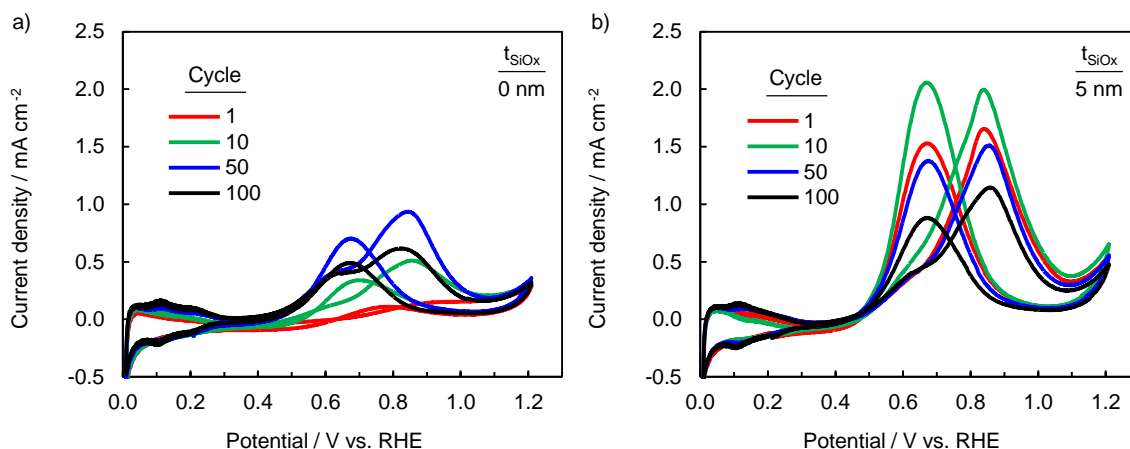


Figure 5.10. 1<sup>st</sup> (red), 10<sup>th</sup> (green), 50<sup>th</sup> (blue), and 100<sup>th</sup> (black) CV cycles for a) bare Pt and b) 5 nm SiO<sub>x</sub>|Pt in 0.5 M H<sub>2</sub>SO<sub>4</sub> containing 0.5 M CH<sub>3</sub>OH and measured at 100 mV s<sup>-1</sup>.

Despite the decreasing MOR current densities, the peak current densities of the SiO<sub>x</sub>|Pt electrodes still exceeded those of the bare Pt electrode at the end of CV cycling. Control MOR experiments on KOH etched bare Pt and 5 nm SiO<sub>x</sub>|Pt, in which no SiO<sub>x</sub> remained after the KOH etch, show no difference in MOR activity, confirming that the presence of the SiO<sub>x</sub> film is necessary for enhanced MOR current densities, relative to bare Pt (Figure 5.11). This result suggests that (some) SiO<sub>x</sub> must still be present on the electrode at the end of CV cycling to maintain higher currents than Pt.

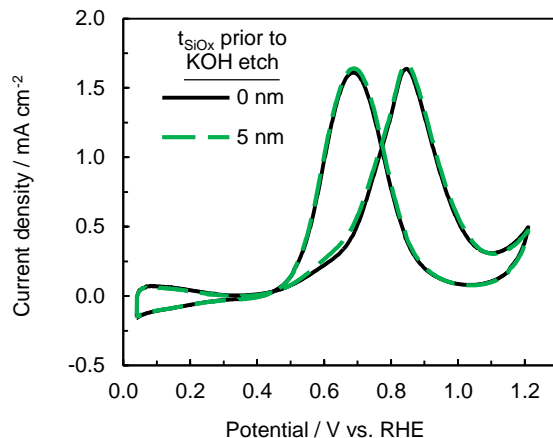


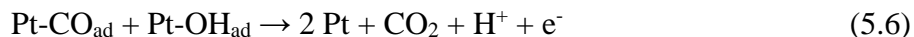
Figure 5.11 Methanol oxidation CVs after a KOH etch on bare Pt (black) and 5 nm  $\text{SiO}_x/\text{Pt}$  (no  $\text{SiO}_x$  remaining after KOH etch) CVs were performed in deaerated 0.5 M  $\text{H}_2\text{SO}_4$  with 0.5 M  $\text{CH}_3\text{OH}$  and at 100  $\text{mV s}^{-1}$ .

In addition to methanol depletion, the gradual decrease in  $\text{SiO}_x/\text{Pt}$  activity may be related to changes in the  $\text{SiO}_x$  structure, as evidenced by AFM and XPS analysis of MCEC samples after CV cycling (Appendix section 5.6.3, Figures 5.15 and 5.16) that show possible  $\text{SiO}_x$  delamination and/or  $\text{SiO}_x$  “island” formation. Although the  $\text{SiO}_x/\text{Pt}$  electrocatalysts appear to be susceptible to degradation during extended cycling, the repeated oxidation/reduction of  $\text{Pt}/\text{PtO}_x$  during CV cycling is likely to cause stress at the  $\text{Pt}/\text{SiO}_x$  interface. The repeated restructuring of the  $\text{Pt}/\text{SiO}_x$  interface may lead to gradual delamination, especially for these thin film electrodes where the  $\text{SiO}_x$  is only anchored to Pt. In fuel cell-relevant nanoparticle/support systems, delamination between  $\text{SiO}_x$  and the inert support should be less of a concern due to the lack of significant electrochemistry at those interfaces.

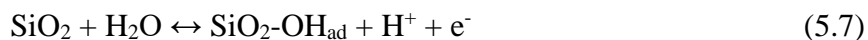
## 5.4 Discussion

### 5.4.1 Role of SiO<sub>x</sub> in Bifunctional Mechanism

The results in Figures 5.5–5.8 demonstrate that deposition of SiO<sub>x</sub> onto Pt thin films significantly enhances CO, methanol, ethanol, and formic acid oxidation activity compared to bare Pt. Similar observations have been made in prior studies of silicon oxide supported Pt nanoparticle electrocatalysts, with the improved performance most commonly attributed to hydroxyl-facilitated removal of CO-intermediates through the aforementioned bifunctional mechanism.<sup>48–53</sup> In order to design catalysts that are more CO tolerant, it is important to understand the source of the hydroxyl groups that are responsible for aiding in the removal of adsorbed CO intermediates on Pt (Pt-CO<sub>ad</sub>). As expressed in Equations 5.5 and 5.6, CO oxidation may be achieved through reaction with silanol groups attached to SiO<sub>x</sub> (SiO<sub>x</sub>-OH) or hydroxyls on Pt (Pt-OH):<sup>1,11,15,101</sup>



where in both cases, hydroxyls must be regenerated through an additional oxidation step:



Prior studies on SiO<sub>2</sub>-supported MOR catalysts have suggested that silanol groups may enhance MOR activity by accelerating CO oxidation as a part of the bifunctional (2-site) mechanism.<sup>48–53</sup> In this study, Figure 5.4 shows that the presence of SiO<sub>x</sub> overlayers can also affect Pt oxophilicity, and likely, the coverage of Pt-OH<sub>ad</sub> at a given applied potential. If CO and methanol oxidation occur at the buried interface of MCECs, it is expected that the presence of the SiO<sub>x</sub> may also indirectly influence reaction energetics at the buried interface through confinement (steric) effects, varying concentrations of reactants and spectator ions near active sites, and

alteration of electric fields caused by disruption of the electrochemical double layer. A density functional theory study investigating confined catalysis determined the adsorption energy of CO on Pt was lowered due to the presence of a graphene overlayer which destabilized the CO<sub>ad</sub> molecule.<sup>68</sup> This result suggests the ability of overlayers on catalysts to create confined environments and alter the interactions and energetics between molecules and catalysts. Thus, the SiO<sub>x</sub> overlayer may directly and/or indirectly influence alcohol oxidation kinetics. Here, we focus on better understanding the role of SiO<sub>x</sub> in the bifunctional mechanism, information that is expected to be important for guiding the design of MCECs with even better CO tolerance and alcohol oxidation activity.

The CO stripping results in Figure 5.5 showed that the presence of 5 nm of SiO<sub>x</sub> on Pt shifts CO oxidation features by 100 mV and 200 mV relative to those for the 2 nm SiO<sub>x</sub>|Pt and bare Pt electrodes, respectively. Despite the very positive oxidation potential required to form hydroxyls on Pt (>0.85 V vs. RHE),<sup>102,103</sup> SiO<sub>x</sub>|Pt is still able to achieve high MOR currents at moderate oxidation potentials (Figure 5.9b), which suggests hydroxyls are readily available at lower oxidation potentials for the bifunctional mechanism. The silanol groups on SiO<sub>x</sub>, in acidic environments<sup>54–56</sup> may serve as an abundant source of hydroxyl groups that are in close proximity to Pt-CO<sub>ad</sub> at the Pt|SiO<sub>x</sub> interface. We also hypothesize that the SiO<sub>x</sub> may change the Pt oxophilicity to make Pt-OH formation more energetically favorable at lower overpotentials, as suggested by the negative shift in the onset potential of Pt oxidation with increasing SiO<sub>x</sub> thickness (1 V to 0.8 V vs. RHE for 2 nm to 5 nm SiO<sub>x</sub> respectively). This trend in the Pt oxidation onset potential may be related to the negative shift in the CO oxidation onset potentials for the 2 nm and 5 nm SiO<sub>x</sub>|Pt samples (0.70 V to 0.60 V vs. RHE respectively). However, it must also be noted that the onset for CO oxidation for the 5 nm SiO<sub>x</sub>|Pt occurs 200 mV more negative than the onset



of Pt-oxidation features, meaning that it is unlikely Pt-OH alone can explain the enhanced CO oxidation activity more negative than 0.8 V vs. RHE.

#### 5.4.2 *Oxophilicity and Reactivation Efficiency*

Hydroxyl species formed on Pt surfaces can enhance the MOR by promoting the bifunctional mechanism, as suggested by the initiation of MOR activity only after Pt oxide (Pt-OH<sub>ad</sub> and PtO<sub>x</sub>) formation (Figure 5.9). Additional insights into the role of Pt-OH species can be obtained by analyzing the ratio of the peak current densities during methanol oxidation CVs ( $I_f/I_b$ ), as mentioned in section 5.3.3.1. In studies on PtRu MOR electrocatalysts, a high  $I_f/I_b$  ratio greater than 1 is commonly associated with a catalyst that is oxophilic.<sup>28,42</sup> A study focused on the origin of the low  $I_b$  concluded that the propensity for PtRu catalysts to more easily form oxygenated species during CV excursions to the positive scan vertex inhibits the MOR during the negative (backward) scan segment because the high OH<sub>ad</sub> and oxide coverage blocks catalytic sites and thereby lowers  $I_b$ .<sup>91</sup> In other words, hydroxyls are necessary for the promotion of MOR, but excessive OH<sub>ad</sub> and/or oxide coverage on catalytic sites hinders further MOR due to the low abundance of metallic active sites. As a result, electrocatalysts that are more oxophilic tend to achieve high MOR activity in the positive (forward) scan,  $I_f$ , but lower MOR activity in the negative (backward) scan,  $I_b$ . This is why PtRu catalysts often have high  $I_f/I_b$ , especially compared to Pt. By contrast, SiO<sub>x</sub>|Pt electrodes showed higher  $I_f$  and lower  $I_f/I_b$  than Pt in Figure 5.6 ( $I_f/I_b$  of 1.0 and 1.4 respectively). Extending the interpretation of the role of PtRu oxophilicity on MOR kinetics to SiO<sub>x</sub>|Pt electrocatalysts, the low  $I_f/I_b$  for SiO<sub>x</sub>|Pt electrodes suggests these electrodes are less oxophilic than bare Pt. However, this statement contradicts the observations of more facile Pt-OH<sub>ad</sub>/PtO<sub>x</sub> formation for 5 nm SiO<sub>x</sub>|Pt in the CV curves in the 0.5 M H<sub>2</sub>SO<sub>4</sub> supporting electrolyte (Figure 5.4).

The different relationships between metal oxophilicity and MOR  $I_f/I_b$  peak ratios for  $\text{SiO}_x/\text{Pt}$  electrocatalysts compared to PtRu electrocatalysts suggests that metal oxophilicity plays different roles in promoting MOR in these two types of electrocatalysts. Despite the higher oxophilicity, the high  $I_b$  suggests that the  $\text{SiO}_x/\text{Pt}$  electrodes have a relatively moderate coverage of  $\text{OH}_{\text{ad}}$  and/or oxide species during the backward scan, which allow for high MOR currents. Furthermore, the onset of  $I_b$  has been shown to coincide with the reduction of  $\text{Pt-OH}_{\text{ad}}$  and  $\text{PtO}_x$ .<sup>93</sup> Consistent with these observations, this study on  $\text{SiO}_x/\text{Pt}$  electrocatalysts suggests that oxophilic electrocatalysts may still exhibit high  $I_f$  and  $I_b$  so long as the kinetics of  $\text{Pt-OH}$  and  $\text{PtO}_x$  reduction are fast enough to reactivate enough active sites for methanol decomposition during the backward scan. In other words, the  $I_f/I_b$  ratio correlates strongly with the ability of the metallic catalyst to regenerate hydroxyl species and/or metallic Pt sites, which can be referred to as a reactivation efficiency. Following this logic, the  $\text{SiO}_x/\text{Pt}$  catalysts are oxophilic but also have a relatively high reactivation efficiency compared to bare Pt.

We hypothesize that the high oxophilicity and reactivation efficiency of the  $\text{SiO}_x/\text{Pt}$  catalysts is due to hydroxyls from Si-OH that are not actually adsorbed onto the Pt surface, but only share a proximity. Such proximal hydroxyls would not block Pt sites from methanol decomposition, but instead would still be available to facilitate oxidation of CO intermediates through the bifunctional mechanism. Furthermore, proximal hydroxyls provided by Si-OH would allow for all of the Pt sites to be utilized for methanol decomposition, as opposed to conventional Pt electrocatalysts, where some fraction of the Pt surface must be occupied by  $\text{Pt-OH}_{\text{ad}}$  (or  $\text{Ru-OH}_{\text{ad}}$  in the case of PtRu alloy). This difference in available catalytic Pt sites may help explain the twofold increase in alcohol oxidation current of  $\text{SiO}_x/\text{Pt}$  compared to Pt (Figures 5.6-5.8). Accordingly, the bifunctional mechanism is expected to proceed predominantly through silanol-

mediated CO removal (Equation 5.5) rather than CO oxidation by Pt-OH<sub>ad</sub> (Equation 5.6). Therefore, the change in Pt oxophilicity observed for 5 nm SiO<sub>x</sub>|Pt (Figure 5.4) may be a secondary effect of SiO<sub>x</sub> encapsulation that does not play a key role in determining MOR activity.

### 5.4.3 Role of Silanol Groups in CO and Methanol Oxidation

To better understand the role of silanol groups in facilitating the electrocatalytic properties of the SiO<sub>x</sub>|Pt thin films, CO and methanol oxidation experiments were performed in a pH 7 sodium phosphate buffer solution in which silanol groups may become deprotonated. Silica is known to have two different types of silanol groups, each with a different pK<sub>a</sub>.<sup>54–56,104</sup> Silanol groups form when the solution pH is below the pK<sub>a</sub> of Si-OH (pK<sub>a1</sub>≈4 and pK<sub>a2</sub>≈9).<sup>54,55</sup> Figure 5.11 shows CO stripping CVs for the bare Pt and 5 nm SiO<sub>x</sub>|Pt at pH 7, for which the low-pK<sub>a</sub> silanol groups should be deprotonated. Both electrodes exhibit multiple CO oxidation peaks with similar onset potentials (0.40 V and 0.54 V vs. RHE) that are shifted more negative than in acidic media (Figure 5.5). These features and differences between acidic and neutral pH are consistent with CO oxidation on multifaceted Pt in alkaline electrolytes.<sup>105,106</sup> Importantly, the CO stripping curves are nearly identical for the SiO<sub>x</sub>|Pt and Pt electrodes. If SiO<sub>x</sub>|Pt were more active than Pt in neutral pH, we would expect to observe a higher fraction of CO oxidation charge (i.e. a larger peak) at lower overpotentials.<sup>106,107</sup> In Figure 5.11, the extent of CO oxidation at lower overpotentials (< 0.6 V vs. RHE) is nearly equivalent for both the SiO<sub>x</sub>|Pt and Pt electrodes, indicating the CO oxidation activity is similar for both electrocatalysts. This result at neutral pH provides strong evidence that silanol groups, not just the presence of SiO<sub>x</sub>, are needed to enhance the CO oxidation compared to bare Pt.

Methanol oxidation was also performed in the pH 7 electrolyte (Figure 5.11b) for bare Pt and 5 nm SiO<sub>x</sub>|Pt. These measurements show that the SiO<sub>x</sub>|Pt electrode still maintains enhanced

MOR activity compared to bare Pt. It should also be noted that the ratio of peak currents,  $I_f/I_b$ , also increased for both electrodes compared to in acid, from 1.4 to 2.3 for bare Pt and 1.0 to 2.5 for 5 nm  $\text{SiO}_x/\text{Pt}$ , consistent with observations of methanol oxidation in more alkaline media.<sup>108–110</sup> The increase in  $I_f/I_b$  for  $\text{SiO}_x/\text{Pt}$  in neutral pH lends support to the hypothesis that proximal silanols were responsible for the low  $I_f/I_b$  in the acidic electrolyte. However, it does not explain why  $\text{SiO}_x/\text{Pt}$  electrodes still maintain a higher MOR activity than bare Pt at neutral pH. One explanation is local acidification at the buried  $\text{SiO}_x/\text{Pt}$  interface, which might arise from suppressed diffusion of protons, generated by methanol oxidation (Equation 5.1), through  $\text{SiO}_x$  and back to the bulk electrolyte. Local acidification could help to keep silanol groups protonated even though the pH of the bulk electrolyte is above the silanol  $\text{pK}_{a1}$ . It is also possible that silanol groups associated with  $\text{pK}_{a2}$  of  $\text{SiO}_2$  are still present and participate in the MOR, at higher oxidation potentials, even though they do not appear to influence CO oxidation (Figure 5.11a), which occurs at lower potentials between 0.4 and 0.8 V vs. RHE. However, the enhanced MOR current for  $\text{SiO}_x/\text{Pt}$  compared to bare Pt at the neutral pH might also result from the aforementioned “indirect” mechanisms by which the  $\text{SiO}_x$  overlayer can alter reaction energetics without directly being involved as an active site as in the bifunctional mechanism. Although these questions are beyond the scope of the current study, they will be important to address in future studies aimed at a deeper molecular understanding of electrocatalysis at buried interfaces.

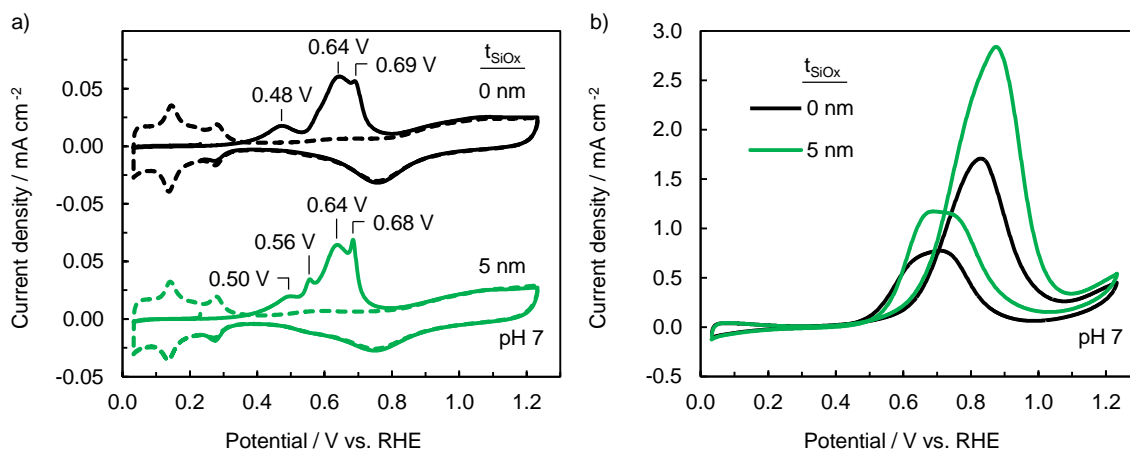


Figure 5.12. a) CO stripping and b) methanol oxidation CVs (cycle 30) in pH neutral electrolyte, 0.1 M sodium phosphate (buffered), with 0.5 M methanol for (b), for bare Pt (black) and 5 nm SiO<sub>x</sub>|Pt (green) electrodes at a scan rate of 100 mV s<sup>-1</sup>.

## 5.5 Conclusions

The planar MCEC architecture investigated in this work provided a well-defined platform to investigate the unique electrocatalytic properties of the oxide-encapsulated metal electrocatalyst. In this study, we examined the effect of 2-5 nm thick SiO<sub>x</sub> overlayers on Pt catalyst films for alcohol oxidation in acidic media. These SiO<sub>x</sub> MCECs demonstrated lower CO oxidation onset potentials during CO stripping voltammetry than Pt in an acidic supporting electrolyte. The increased CO tolerance is likely due to the ability of silanol groups on SiO<sub>x</sub> to promote oxidation of adsorbed CO on Pt. Furthermore, the SiO<sub>x</sub>|Pt MCECs exhibit a twofold increase in the maximum peak current densities for alcohol oxidation compared to Pt. The enhanced performance towards alcohol oxidation, in acidic electrolyte, is largely attributed to the interactions between proximal hydroxyls from silanol groups and adsorbed intermediates on Pt. These interfacial regions are maximized with the MCEC design, such that an abundance of hydroxyl groups are readily provided at Pt|SiO<sub>x</sub> interfaces where they can accelerate alcohol oxidation by the bifunctional mechanism. Varied CV vertex potential and pH measurements indicate that silanol

groups, which are present at all relevant potentials in acidic pH, are active participants in CO and methanol oxidation. Although the MOR activity of  $\text{SiO}_x/\text{Pt}$  electrodes decreases during long-time cycling, this study demonstrates the MCEC design is promising approach for CO tolerant and highly active alcohol oxidation electrocatalysts.

## 5.6 Appendix

### 5.6.1 CO Stripping on UV Ozone Treated Platinum

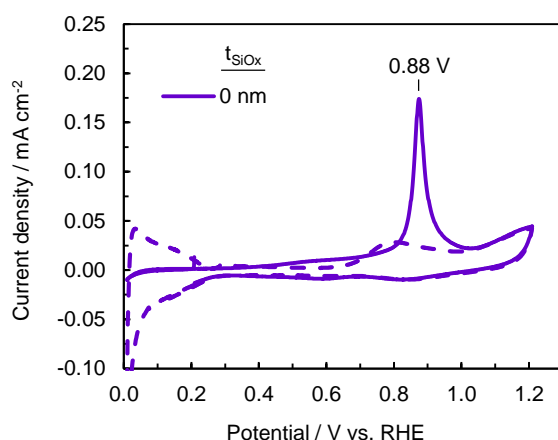


Figure 5.13. CO stripping voltammetry curves measured in 0.5 M  $\text{H}_2\text{SO}_4$  at  $20 \text{ mV s}^{-1}$  scan rate for bare Pt electrode that underwent two hours of UV ozone exposure. Solid curves represent the first CV cycle that was carried out with CO adsorbed on the electrode surface, while and dashed curves represent the second CV cycle that was performed after CO was stripped from the electrode surface during the first cycle.

### 5.6.2 Methanol Oxidation Behavior for Varied CV Upper Vertex Potentials

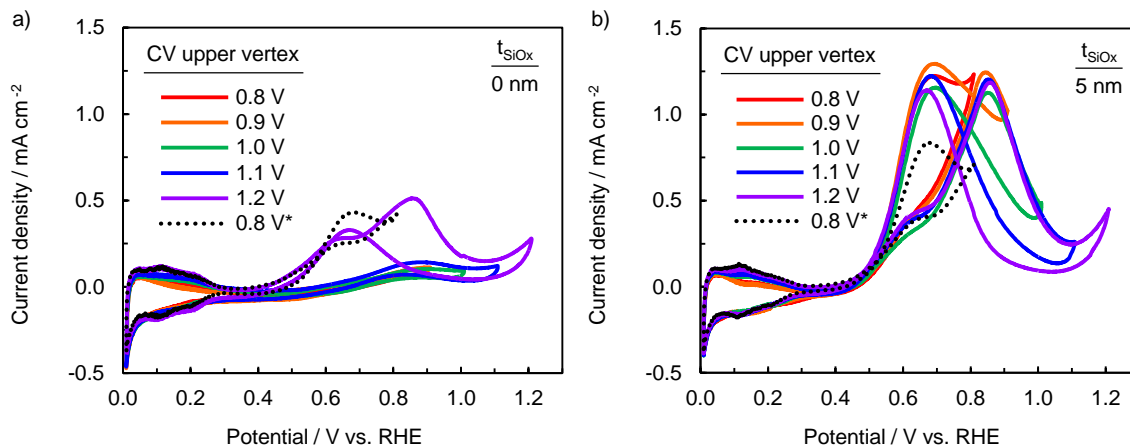


Figure 5.14. Methanol oxidation CVs with different anodic voltage limits for a)  $t_{\text{SiO}_x} = 0 \text{ nm}$  and b)  $t_{\text{SiO}_x} = 5 \text{ nm}$  SiO<sub>x</sub>|Pt MCEC. Upper limit voltages of 0.8 V (red), 0.9 V (blue), 1.0V (green), 1.1 V (black), and 1.2 V (orange) vs. RHE are shown. The CV was returned to an upper limit of 0.8 V vs. RHE (purple). Peak forward and backward current densities as a function of upper potential limit. CVs were performed in deaerated 0.5 M H<sub>2</sub>SO<sub>4</sub> with 0.5 M CH<sub>3</sub>OH and measured within a potential range of 0.0 V to 1.2 V vs. RHE at 100 mV s<sup>-1</sup>.

### 5.6.3 AFM and XPS Characterization of SiO<sub>x</sub> Films Post Methanol CV Measurements

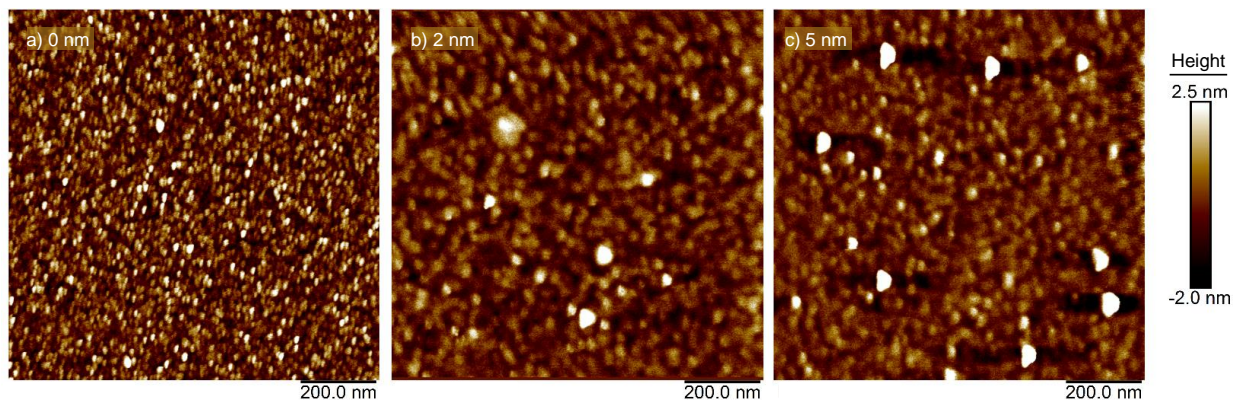


Figure 5.15. AFM images of as made a) 0 nm, b) 2 nm, and c) 5 nm SiO<sub>x</sub>|Pt electrodes following 100 methanol oxidation CV cycles.

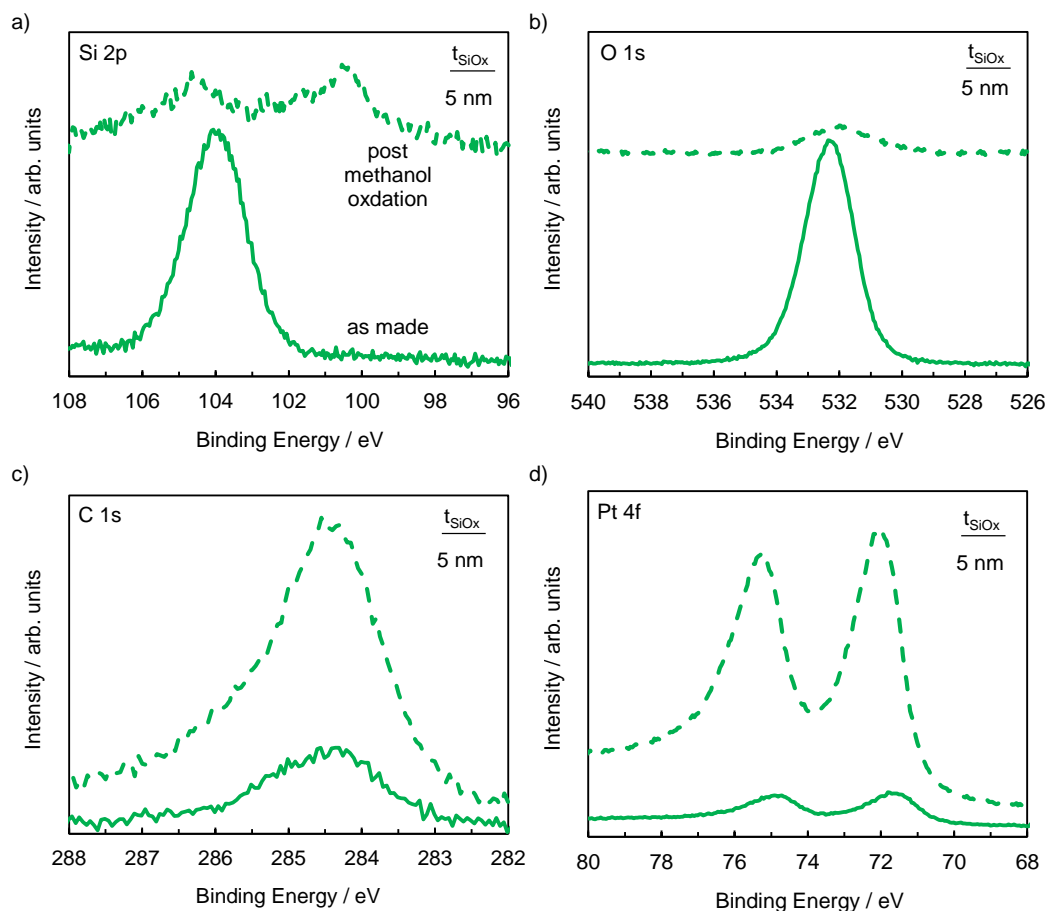


Figure 5.16. a) Si 2p, b) O 1s, c) C 1s and d) Pt 4f XPS spectra of the 5 nm  $\text{SiO}_x|\text{Pt}$  electrodes before (solid) and after (dashed) 100 CV cycles at  $100 \text{ mV s}^{-1}$  between potentials of 0.02 and 1.2 V RHE in 0.5 M  $\text{CH}_3\text{OH}$  containing 0.5 M  $\text{H}_2\text{SO}_4$ . Upon completion of CV measurements, electrodes were rinsed with DI water, dried with compressed  $\text{N}_2$ , and loaded into the XPS loading chamber.

## 5.7 Acknowledgments

I would like to acknowledge Jacob E. Robinson for the numerous contributions to the content in this chapter and for performing CO stripping, methanol, ethanol, and formic acid oxidation, and varying CV vertex experiments, Han Chen for his assistance with characterizing the films with ellipsometry, AFM, and  $H_{\text{upd}}$  CVs, Ed Sartor for assisting Han Chen with the KOH etch experiment, and Xiangye Liu for helpful discussions and suggestions. Dr. Esposito and I



acknowledge Columbia University Columbia Nano Initiative and City University of New York Advanced Science Research Center for use of the physical vapor deposition and SEM equipment. DVE and NYL acknowledge Columbia University (start-up funds) and the National Science Foundation (NSF) (CBET-1752340).

## 5.8 References

- (1) Ting, C.-C.; Liu, C.-H.; Tai, C.-Y.; Hsu, S.-C.; Chao, C.-S.; Pan, F.-M. The Size Effect of Titania-Supported Pt Nanoparticles on the Electrocatalytic Activity towards Methanol Oxidation Reaction Primarily via the Bifunctional Mechanism. *J. Power Sources* **2015**, *280*, 166–172.
- (2) Ranga Rao, G.; Justin, P.; Meher, S. K. Metal Oxide Promoted Electrocatalysts for Methanol Oxidation. *Catal. Surv. from Asia* **2011**, *15* (4), 221–229.
- (3) Rigdon, W. A.; Huang, X. Carbon Monoxide Tolerant Platinum Electrocatalysts on Niobium Doped Titania and Carbon Nanotube Composite Supports. *J. Power Sources* **2014**, *272*, 845–859.
- (4) Moura, A.; Fajín, J.; Mandado, M.; Cordeiro, M. Ruthenium–Platinum Catalysts and Direct Methanol Fuel Cells (DMFC): A Review of Theoretical and Experimental Breakthroughs. *Catalysts* **2017**, *7* (2), 47.
- (5) Antolini, E. *Electrocatalysis of Direct Methanol Fuel Cells: From Fundamentals to Applications*; Liu, H., Zhang, J., Eds.; Wiley-VCH: Weinheim, Germany, 2009.
- (6) Léger, J.-M.; Rousseau, S.; Coutanceau, C.; Hahn, F.; Lamy, C.; Kamarudin, M. Z. F.; Kamarudin, S. K.; Masdar, M. S.; Daud, W. R. W.; Akhairi, M. A. F.; et al. Review: Direct Ethanol Fuel Cells. *Int. J. Hydrogen Energy* **2015**, *50* (7), 4214–4228.
- (7) Kamarudin, M. Z. F.; Kamarudin, S. K.; Masdar, M. S.; Daud, W. R. W. Review: Direct Ethanol Fuel Cells. *Int. J. Hydrogen Energy* **2013**, *38* (22), 9438–9453.
- (8) Chen, Y.; Bellini, M.; Bevilacqua, M.; Fornasiero, P.; Lavacchi, A.; Miller, H. A.; Wang, L.; Vizza, F. Direct Alcohol Fuel Cells: Toward the Power Densities of Hydrogen-Fed Proton Exchange Membrane Fuel Cells. *ChemSusChem* **2015**, *8* (3), 524–533.
- (9) Badwal, S. P. S.; Giddey, S.; Kulkarni, A.; Goel, J.; Basu, S. Direct Ethanol Fuel Cells for Transport and Stationary Applications – A Comprehensive Review. *Appl. Energy* **2015**, *145*, 80–103.
- (10) Coutanceau, C.; Baranton, S. Electrochemical Conversion of Alcohols for Hydrogen Production: A Short Overview. *Wiley Interdiscip. Rev. Energy Environ.* **2016**, *5* (4), 388–400.

- (11) Li, Q.; He, R.; Gao, J.-A.; Jensen, J. O.; Bjerrum, N. J. The CO Poisoning Effect in PEMFCs Operational at Temperatures up to 200°C. *J. Electrochem. Soc.* **2003**, *150* (12), A1599.
- (12) Camara, G. A.; Ticianelli, E. A.; Mukerjee, S.; Lee, S. J.; McBreen, J. The CO Poisoning Mechanism of the Hydrogen Oxidation Reaction in Proton Exchange Membrane Fuel Cells. *J. Electrochem. Soc.* **2002**, *149* (6), A748.
- (13) McCabe, R. W.; McCready, D. F. Kinetics and Reaction Pathways of Methanol Oxidation on Platinum. *J. Phys. Chem.* **1986**, *90* (7), 1428–1435.
- (14) Miller, A. V.; Kaichev, V. V.; Prosvirin, I. P.; Bukhtiyarov, V. I. Mechanistic Study of Methanol Decomposition and Oxidation on Pt(111). *J. Phys. Chem. C* **2013**, *117* (16), 8189–8197.
- (15) Rednyk, A.; Johánek, V.; Khalakhan, I.; Dubau, M.; Vorokhta, M.; Matolín, V. Methanol Oxidation on Sputter-Coated Platinum Oxide Catalysts. *Int. J. Hydrogen Energy* **2016**, *41* (1), 265–275.
- (16) He, Q.; Joy, D. C.; Keffer, D. J. Impact of Oxidation on Nanoparticle Adhesion to Carbon Substrates. *RSC Adv.* **2013**, *3* (36), 15792.
- (17) Dam, V. A. T.; de Bruijn, F. A. The Stability of PEMFC Electrodes. *J. Electrochem. Soc.* **2007**, *154* (5), B494.
- (18) Li, L.; Hu, L.; Li, J.; Wei, Z. Enhanced Stability of Pt Nanoparticle Electrocatalysts for Fuel Cells. *Nano Res.* **2015**, *8* (2), 418–440.
- (19) Iwasita, T. *Handbook of Fuel Cells*, Vol. 2.; Gasteiger, H. A., Kocha, S. S., Sompali, B., Wagner, F. T., Eds.; John Wiley & Sons, Ltd: London, 2010.
- (20) Iwasita, T. Electrocatalysis of Methanol Oxidation. *Electrochim. Acta* **2002**, *47* (22–23), 3663–3674.
- (21) Nassr, A. B. A. A.; Sinev, I.; Pohl, M.-M.; Grünert, W.; Bron, M. Rapid Microwave-Assisted Polyol Reduction for the Preparation of Highly Active PtNi/CNT Electrocatalysts for Methanol Oxidation. *ACS Catal.* **2014**, *4* (8), 2449–2462.
- (22) Wasmus, S.; Küver, A. Methanol Oxidation and Direct Methanol Fuel Cells: A Selective Review. *J. Electroanal. Chem.* **1999**, *461* (1–2), 14–31.
- (23) Léger, J. M. Mechanistic Aspects of Methanol Oxidation on Platinum-Based Electrocatalysts. *J. Appl. Electrochem.* **2001**, *31* (7), 767–771.
- (24) Tong, Kim, H. S.; Babu, P. K.; Waszczuk, P.; Wieckowski, A.; Oldfield, E. An NMR Investigation of CO Tolerance in a Pt/Ru Fuel Cell Catalyst. *J. Am. Chem. Soc.* **2002**, *124* (3), 468–473.
- (25) Zhang, K.; Yang, W.; Ma, C.; Wang, Y.; Sun, C.; Chen, Y.; Duchesne, P.; Zhou, J.; Wang,

- J.; Hu, Y.; et al. A Highly Active, Stable and Synergistic Pt Nanoparticles/Mo<sub>2</sub>C Nanotube Catalyst for Methanol Electro-Oxidation. *NPG Asia Mater.* **2015**, 7 (1), e153.
- (26) Scofield, M. E.; Koenigsmann, C.; Bobb-Semple, D.; Tao, J.; Tong, X.; Wang, L.; Lewis, C. S.; Vukmirovic, M. B.; Zhu, Y.; Adzic, R. R.; et al. Correlating the Chemical Composition and Size of Various Metal Oxide Substrates with the Catalytic Activity and Stability of As-Deposited Pt Nanoparticles for the Methanol Oxidation Reaction. *Catal. Sci. Technol.* **2016**, 6 (7), 2435–2450.
  - (27) Du, P.; Wu, P.; Cai, C. Mechanistic Insight into the Facet-Dependent Adsorption of Methanol on a Pt<sub>3</sub>Ni Nanocatalyst. *J. Phys. Chem. C* **2015**, 119 (32), 18352–18363.
  - (28) Liu, Z.; Ling, X. Y.; Su, X.; Lee, J. Y. Carbon-Supported Pt and PtRu Nanoparticles as Catalysts for a Direct Methanol Fuel Cell. *J. Phys. Chem. B* **2004**, 108 (24), 8234–8240.
  - (29) Selvaraj, V.; Alagar, M. Pt and Pt-Ru Nanoparticles Decorated Polypyrrole/Multiwalled Carbon Nanotubes and Their Catalytic Activity towards Methanol Oxidation. *Electrochem. commun.* **2007**, 9 (5), 1145–1153.
  - (30) Antolini, E.; Gonzalez, E. R. Effect of Synthesis Method and Structural Characteristics of Pt–Sn Fuel Cell Catalysts on the Electro-Oxidation of CH<sub>3</sub>OH and CH<sub>3</sub>CH<sub>2</sub>OH in Acid Medium☆. *Catal. Today* **2011**, 160 (1), 28–38.
  - (31) Merati, Z.; Basiri Parsa, J. Enhancement of the Catalytic Activity of Pt Nanoparticles toward Methanol Electro-Oxidation Using Doped-SnO<sub>2</sub> Supporting Materials. *Appl. Surf. Sci.* **2018**, 435, 535–542.
  - (32) Sharma, S.; Pollet, B. G. Support Materials for PEMFC and DMFC Electrocatalysts—A Review. *J. Power Sources* **2012**, 208, 96–119.
  - (33) Qin, Y.-H.; Li, Y.; Lv, R.-L.; Wang, T.-L.; Wang, W.-G.; Wang, C.-W. Enhanced Methanol Oxidation Activity and Stability of Pt Particles Anchored on Carbon-Doped TiO<sub>2</sub> Nanocoating Support. *J. Power Sources* **2015**, 278, 639–644.
  - (34) Xing, L.; Jia, J.; Wang, Y.; Zhang, B.; Dong, S. Pt Modified TiO<sub>2</sub> Nanotubes Electrode: Preparation and Electrocatalytic Application for Methanol Oxidation. *Int. J. Hydrogen Energy* **2010**, 35 (22), 12169–12173.
  - (35) Wu, X.; Zhuang, W.; Lu, L.; Li, L.; Zhu, J.; Mu, L.; Li, W.; Zhu, Y.; Lu, X. Excellent Performance of Pt-C/TiO<sub>2</sub> for Methanol Oxidation: Contribution of Mesopores and Partially Coated Carbon. *Appl. Surf. Sci.* **2017**, 426, 890–896.
  - (36) Zhuang, Y.; Ding, W.; Liu, Y.; Mou, Z.; Sun, J.; Guan, M. Reduced Nanostructured Titanium Oxide Coating as an Electrocatalyst Support for Methanol Oxidation. *J. Mater. Sci.* **2015**, 50 (11), 3875–3882.
  - (37) Su, N.; Hu, X.; Zhang, J.; Huang, H.; Cheng, J.; Yu, J.; Ge, C. Plasma-Induced Synthesis of Pt Nanoparticles Supported on TiO<sub>2</sub> Nanotubes for Enhanced Methanol Electro-

Oxidation. *Appl. Surf. Sci.* **2017**, 399, 403–410.

- (38) Cui, G.; Shen, P. K.; Meng, H.; Zhao, J.; Wu, G. Tungsten Carbide as Supports for Pt Electrocatalysts with Improved CO Tolerance in Methanol Oxidation. *J. Power Sources* **2011**, 196 (15), 6125–6130.
- (39) Watanabe, M.; Motoo, S. Electrocatalysis by Ad-Atoms. *J. Electroanal. Chem. Interfacial Electrochem.* **1975**, 60 (3), 267–273.
- (40) Mancharan, R.; Goodenough, J. B. Methanol Oxidation in Acid on Ordered NiTi. *J. Mater. Chem.* **1992**, 2 (8), 875.
- (41) Pan, C.-J.; Tsai, M.-C.; Su, W.-N.; Rick, J.; Akalework, N. G.; Agegnehu, A. K.; Cheng, S.-Y.; Hwang, B.-J. Tuning/Exploiting Strong Metal-Support Interaction (SMSI) in Heterogeneous Catalysis. *J. Taiwan Inst. Chem. Eng.* **2017**, 74, 154–186.
- (42) Liu, S.; Yu, W.; Chen, C.; Lo, A.; Hwang, B.; Chien, S.-H.; Liu, S.-B. Fabrication and Characterization of Well-Dispersed and Highly Stable PtRu Nanoparticles on Carbon Mesoporous Material for Applications in Direct Methanol Fuel Cell. *Chem. Mater.* **2008**, 20 (4), 1622–1628.
- (43) Kumar, A.; Ramani, V. Strong Metal–Support Interactions Enhance the Activity and Durability of Platinum Supported on Tantalum-Modified Titanium Dioxide Electrocatalysts. *ACS Catal.* **2014**, 4 (5), 1516–1525.
- (44) Xu, C.; Shen, P. K. Novel Pt/CeO<sub>2</sub>/C Catalysts for Electrooxidation of Alcohols in Alkaline Media. *Chem. Commun.* **2004**, No. 19, 2238.
- (45) Xu, C.; Shen, P. K. Electrochemical Oxidation of Ethanol on Pt-CeO<sub>2</sub>/C Catalysts. *J. Power Sources* **2005**, 142 (1–2), 27–29.
- (46) Xu, C.; Shen, P. K.; Ji, X.; Zeng, R.; Liu, Y. Enhanced Activity for Ethanol Electrooxidation on Pt–MgO/C Catalysts. *Electrochem. commun.* **2005**, 7 (12), 1305–1308.
- (47) Jayaraman, S.; Jaramillo, T. F.; Baeck, S.-H.; McFarland, E. W. Synthesis and Characterization of Pt-WO<sub>3</sub> as Methanol Oxidation Catalysts for Fuel Cells. *J. Phys. Chem. B* **2005**, 109, 22958–22966.
- (48) Tiwari, J. N.; Pan, F.-M.; . Tiwari, R. N.; . Nandi, S. . Facile Synthesis of Continuous Pt Island Networks and Their Electrochemical Properties for Methanol Electrooxidation. *Chem. Commun.* **2008**, No. 48, 6516.
- (49) Permyakova, A. A.; Han, B.; Jensen, J. O.; Bjerrum, N. J.; Shao-Horn, Y. Pt—Si Bifunctional Surfaces for CO and Methanol Electro-Oxidation. *J. Phys. Chem. C* **2015**, 119 (15), 8023–8031.
- (50) Tiwari, J. N.; Pan, F.-M.; Chen, T.-M.; Tiwari, R. N.; Lin, K.-L. Electrocatalytic Activity of Pt Nanoparticles Electrodeposited on Amorphous Carbon-Coated Silicon Nanocones. *J.*

- (51) Vu, T. H. T.; Tran, T. T. T.; Le, H. N. T.; Tran, L. T.; Nguyen, P. H. T.; Nguyen, H. T.; Bui, N. Q. Solvothermal Synthesis of Pt-SiO<sub>2</sub>/Graphene Nanocomposites as Efficient Electrocatalyst for Methanol Oxidation. *Electrochim. Acta* **2015**, 161, 335–342.
- (52) Melvin, A. A.; Joshi, V. S.; Poudyal, D. C.; Khushalani, D.; Haram, S. K. Electrocatalyst on Insulating Support?: Hollow Silica Spheres Loaded with Pt Nanoparticles for Methanol Oxidation. *ACS Appl. Mater. Interfaces* **2015**, 7 (12), 6590–6595.
- (53) Nam, K.; Lim, S.; Kim, S. K.; Yoon, S. H.; Jung, D. H. Application of Silica as a Catalyst Support at High Concentrations of Methanol for Direct Methanol Fuel Cells. *Int. J. Hydrogen Energy* **2012**, 37 (5), 4619–4626.
- (54) Azam, M. S.; Weeraman, C. N.; Gibbs-Davis, J. M. Specific Cation Effects on the Bimodal Acid–Base Behavior of the Silica/Water Interface. *J. Phys. Chem. Lett.* **2012**, 3 (10), 1269–1274.
- (55) Ong, S.; Zhao, X.; Eissenthal, K. B. Polarization of Water Molecules at a Charged Interface: Second Harmonic Studies of the Silica/Water Interface. *Chem. Phys. Lett.* **1992**, 191 (3–4), 327–335.
- (56) Leung, K.; Nielsen, I. M. B.; Criscenti, L. J. Elucidating the Bimodal Acid–Base Behavior of the Water–Silica Interface from First Principles. *J. Am. Chem. Soc.* **2009**, 131 (51), 18358–18365.
- (57) Pourbaix, M. *Atlas of Electrochemical Equilibria in Aqueous Solutions*; Oxford: Pergamon Press: New York, 1974.
- (58) Liu, B.; Chen, J. H.; Zhong, X. X.; Cui, K. Z.; Zhou, H. H.; Kuang, Y. F. Preparation and Electrocatalytic Properties of Pt–SiO<sub>2</sub> Nanocatalysts for Ethanol Electrooxidation. *J. Colloid Interface Sci.* **2007**, 307 (1), 139–144.
- (59) Huang, S.-Y.; Ganesan, P.; Popov, B. N. Electrocatalytic Activity and Stability of Niobium-Doped Titanium Oxide Supported Platinum Catalyst for Polymer Electrolyte Membrane Fuel Cells. *Appl. Catal. B Environ.* **2011**, 102 (1–2), 71–77.
- (60) Hahn, R.; Schmidt-Stein, F.; Salonen, J.; Thiemann, S.; Song, Y.; Kunze, J.; Lehto, V.-P.; Schmuki, P. Semimetallic TiO<sub>2</sub> Nanotubes. *Angew. Chemie Int. Ed.* **2009**, 48 (39), 7236–7239.
- (61) Zhu, J.; Zhao, X.; Xiao, M.; Liang, L.; Liu, C.; Liao, J.; Xing, W. The Construction of Nitrogen-Doped Graphitized Carbon–TiO<sub>2</sub> Composite to Improve the Electrocatalyst for Methanol Oxidation. *Carbon N. Y.* **2014**, 72, 114–124.
- (62) Tang, H.; Jiang, S. P. Self-Assembled Pt/Mesoporous Silica–Carbon Electrocatalysts for Elevated-Temperature Polymer Electrolyte Membrane Fuel Cells. *J. Phys. Chem. C* **2008**, 112 (49), 19748–19755.

- (63) Ting, C.-C.; Chao, C.-H.; Tsai, C. Y.; Cheng, I.-K.; Pan, F.-M. Electrocatalytic Performance of Pt Nanoparticles Sputter-Deposited on Indium Tin Oxide toward Methanol Oxidation Reaction: The Particle Size Effect. *Appl. Surf. Sci.* **2017**, *416*, 365–370.
- (64) Esposito, D. V. Membrane-Coated Electrocatalysts—An Alternative Approach To Achieving Stable and Tunable Electrocatalysis. *ACS Catal.* **2018**, *8* (1), 457–465.
- (65) Labrador, N. Y.; Songcuan, E. L.; De Silva, C.; Chen, H.; Kurdziel, S. J.; Ramachandran, R. K.; Detavernier, C.; Esposito, D. V. Hydrogen Evolution at the Buried Interface between Pt Thin Films and Silicon Oxide Nanomembranes. *ACS Catal.* **2018**, *8*, 1767–1778.
- (66) Doyle, A. D.; Montoya, J. H.; Vojvodic, A. Improving Oxygen Electrochemistry through Nanoscopic Confinement. *ChemCatChem* **2015**, *7* (5), 738–742.
- (67) Fu, Y.; Rudnev, A. V.; Wiberg, G. K. H.; Arenz, M. Single Graphene Layer on Pt(111) Creates Confined Electrochemical Environment via Selective Ion Transport. *Angew. Chemie - Int. Ed.* **2017**, *56* (42), 12883–12887.
- (68) Li, H.; Xiao, J.; Fu, Q.; Bao, X. Confined Catalysis under Two-Dimensional Materials. *Proc. Natl. Acad. Sci.* **2017**, *114* (23), 5930–5934.
- (69) Takenaka, S.; Matsumori, H.; Arike, T.; Matsune, H.; Kishida, M. Preparation of Carbon Nanotube-Supported Pt Metal Particles Covered with Silica Layers and Their Application to Electrocatalysts for PEMFC. *Top. Catal.* **2009**, *52* (6–7), 731–738.
- (70) Matsumori, H.; Takenaka, S.; Matsune, H.; Kishida, M. Preparation of Carbon Nanotube-Supported Pt Catalysts Covered with Silica Layers; Application to Cathode Catalysts for PEFC. *Appl. Catal. A Gen.* **2010**, *373* (1–2), 176–185.
- (71) Takenaka, S.; Susuki, N.; Miyamoto, H.; Tanabe, E.; Matsune, H.; Kishida, M. Highly Durable Pd Metal Catalysts for the Oxygen Reduction Reaction in Fuel Cells; Coverage of Pd Metal with Silica. *Chem. Commun.* **2010**, *46* (47), 8950–8952.
- (72) Takenaka, S.; Susuki, N.; Miyamoto, H.; Tanabe, E.; Matsune, H.; Kishida, M. Highly Durable Carbon Nanotube-Supported Pd Catalysts Covered with Silica Layers for the Oxygen Reduction Reaction. *J. Catal.* **2011**, *279* (2), 381–388.
- (73) Takenaka, S.; Matsumori, H.; Matsune, H.; Kishida, M. Highly Durable Pt Cathode Catalysts for Polymer Electrolyte Fuel Cells; Coverage of Carbon Black-Supported Pt Catalysts with Silica Layers. *Appl. Catal. A Gen.* **2011**, *409–410*, 248–256.
- (74) Takenaka, S.; Miyamoto, H.; Utsunomiya, Y.; Matsune, H.; Kishida, M. Catalytic Activity of Highly Durable Pt/CNT Catalysts Covered with Hydrophobic Silica Layers for the Oxygen Reduction Reaction in PEFCs. *J. Phys. Chem. C* **2014**, *118* (2), 774–783.
- (75) Takenaka, S.; Miyazaki, T.; Matsune, H.; Kishida, M. Highly Active and Durable Silica-Coated Pt Cathode Catalysts for Polymer Electrolyte Fuel Cells: Control of Micropore Structures in Silica Layers. *Catal. Sci. Technol.* **2015**, *5* (2), 1133–1142.

- (76) Yaowarat, W.; Li, O. L.; Saito, N. Highly Durable Silica Coated Pt/Cs with Different Surfactant Types for Proton Exchange Membrane Fuel Cell Applications. *RSC Adv.* **2015**, 5 (55), 44258–44262.
- (77) Yaowarat, W.; Li, O. L. H.; Saito, N. Highly Durable Silica-Coated Pt/Carbon Nanotubes for Proton-Exchange Membrane Fuel Cells Application. *Jpn. J. Appl. Phys.* **2016**, 55 (1S), 01AE23.
- (78) Gu, J.; Yan, Y.; Young, J. L.; Steirer, K. X.; Neale, N. R.; Turner, J. A. Water Reduction by a P-GaInP<sub>2</sub> Photoelectrode Stabilized by an Amorphous TiO<sub>2</sub> Coating and a Molecular Cobalt Catalyst. *Nat. Mater.* **2015**, 15 (4), 456–460.
- (79) Garcia-Esparza, A. T.; Shinagawa, T.; Ould-Chikh, S.; Qureshi, M.; Peng, X.; Wei, N.; Anjum, D. H.; Clo, A.; Weng, T.-C.; Nordlund, D.; et al. An Oxygen-Insensitive Hydrogen Evolution Catalyst Coated by a Molybdenum-Based Layer for Overall Water Splitting. *Angew. Chemie Int. Ed.* **2017**, 56 (21), 5780–5784.
- (80) Labrador, N. Y.; Li, X.; Liu, Y.; Tan, H.; Wang, R.; Koberstein, J. T.; Moffat, T. P.; Esposito, D. V. Enhanced Performance of Si MIS Photocathodes Containing Oxide-Coated Nanoparticle Electrocatalysts. *Nano Lett.* **2016**, 16 (10), 6452–6459.
- (81) Mirley, C.; Koberstein, J. A Room Temperature Method for the Preparation of Ultrathin SiO<sub>x</sub> Films from Langmuir-Blodgett Layers. *Langmuir* **1995**, 11 (4), 0–3.
- (82) Phely-Bobin, T. S.; Muisener, R. J.; Koberstein, J. T.; Papadimitrakopoulos, F. Site-Specific Self-Assembly of Si/SiO<sub>x</sub> Nanoparticles on Micropatterned Poly(Dimethylsiloxane) Thin Films. *Synth. Met.* **2001**, 116 (1–3), 439–443.
- (83) Ouyang, M.; Yuan, C.; Muisener, R. J.; Boulares, A.; Koberstein, J. T. Conversion of Some Siloxane Polymers to Silicon Oxide by UV/Ozone Photochemical Processes. *Chem. Mater.* **2000**, 12 (29), 1591–1596.
- (84) Moulder, J. F.; Stickle, W. F.; Sobol, P. E.; Bomben, K. D. *Handbook of X-Ray Photoelectron Spectroscopy*; Chastain, J., King, R. C. J., Eds.; Physical Electronics, Inc.: Eden Prairie, MN, 1995.
- (85) Biegler, T.; Rand, D. A. J.; Woods, R. Limiting Oxygen Coverage on Platinized Platinum; Relevance to Determination of Real Platinum Area by Hydrogen Adsorption. *J. Electroanal. Chem. Interfacial Electrochem.* **1971**, 29 (2), 269–277.
- (86) Binniger, T.; Fabbri, E.; Kotz, R.; Schmidt, T. J. Determination of the Electrochemically Active Surface Area of Metal-Oxide Supported Platinum Catalyst. *J. Electrochem. Soc.* **2013**, 161 (3), H121–H128.
- (87) Angerstein-Kozłowska, H.; Conway, B. E.; Sharp, W. B. A. The Real Condition of Electrochemically Oxidized Platinum Surfaces. Part I. Resolution of Component Processes. *J. Electroanal. Chem.* **1973**, 43 (1), 9–36.

- (88) Conway, B. E. Electrochemical At Noble Metals Oxide Film Formation As a Surface-Chemical Process. *Prog. Surf. Sci.* **1995**, 49 (95), 331–452.
- (89) Yuan, G.; Agiral, A.; Pellet, N.; Kim, W.; Frei, H. Inorganic Core–shell Assemblies for Closing the Artificial Photosynthetic Cycle. *Faraday Discuss.* **2014**, 176, 233–249.
- (90) Lamy, C.; Guenot, B.; Cretin, M.; Pourcelly, G. (Invited) A Kinetics Analysis of Methanol Oxidation under Electrolysis/Fuel Cell Working Conditions. *ECS Trans.* **2015**, 66 (29), 1–12.
- (91) Chung, D. Y.; Lee, K.-J.; Sung, Y.-E. Methanol Electro-Oxidation on the Pt Surface: Revisiting the Cyclic Voltammetry Interpretation. *J. Phys. Chem. C* **2016**, 120 (17), 9028–9035.
- (92) Hofstead-Duffy, A. M.; Chen, D.-J.; Sun, S.-G.; Tong, Y. J. Origin of the Current Peak of Negative Scan in the Cyclic Voltammetry of Methanol Electro-Oxidation on Pt-Based Electrocatalysts: A Revisit to the Current Ratio Criterion. *J. Mater. Chem.* **2012**, 22 (11), 5205.
- (93) Zhao, Y.; Li, X.; Schechter, J. M.; Yang, Y. Revisiting the Oxidation Peak in the Cathodic Scan of the Cyclic Voltammogram of Alcohol Oxidation on Noble Metal Electrodes. *RSC Adv.* **2016**, 6 (7), 5384–5390.
- (94) Cantane, D. A.; Ambrosio, W. F.; Chatenet, M.; Lima, F. H. B. Electro-Oxidation of Ethanol on Pt/C, Rh/C, and Pt/Rh/C-Based Electrocatalysts Investigated by on-Line DEMS. *J. Electroanal. Chem.* **2012**, 681, 56–65.
- (95) Akhairi, M. A. F.; Kamarudin, S. K. Catalysts in Direct Ethanol Fuel Cell (DEFC): An Overview. *Int. J. Hydrogen Energy* **2016**, 41 (7), 4214–4228.
- (96) El-Deab, M. S. Electrocatalysis by Nanoparticles: Oxidation of Formic Acid at Manganese Oxide Nanorods-Modified Pt Planar and Nanohole-Arrays. *J. Adv. Res.* **2010**, 1 (1), 87–93.
- (97) Li, C.; Wang, J.; Wen, Y.; Ning, Y.; Wen, Y.; Yuan, X.; Li, M.; Yang, D. Polyaniline/CeO<sub>2</sub> Nanofiber Composite Membrane as a Promoter of Pt for Formic Acid Electro-Oxidation. *ECS Electrochem. Lett.* **2012**, 2 (1), H1–H4.
- (98) Redmond, E. L.; Setzler, B. P.; Alamgir, F. M.; Fuller, T. F. Elucidating the Oxide Growth Mechanism on Platinum at the Cathode in PEM Fuel Cells. *Phys. Chem. Chem. Phys.* **2014**, 16 (11), 5301.
- (99) Eickes, C.; Piela, P.; Davey, J.; Zelenay, P. Recoverable Cathode Performance Loss in Direct Methanol Fuel Cells. *J. Electrochem. Soc.* **2006**, 153 (1), A171.
- (100) Tripković, A. V.; Popović, K. Đ.; Momčilović, J. D.; Dražić, D. M. Kinetic and Mechanistic Study of Methanol Oxidation on a Pt(110) Surface in Alkaline Media. *Electrochim. Acta* **1998**, 44 (6–7), 1135–1145.



- (101) Markovic, N. Surface Science Studies of Model Fuel Cell Electrocatalysts. *Surf. Sci. Rep.* **2002**, *45* (4–6), 117–229.
- (102) Conway, B. E. Electrochemical Oxide Film Formation at Noble Metals as a Surface-Chemical Process. *Prog. Surf. Sci.* **1995**, *49* (4), 331–452.
- (103) Jerkiewicz, G.; Vatankhah, G.; Lessard, J.; Soriaga, M. P.; Park, Y.-S. Surface-Oxide Growth at Platinum Electrodes in Aqueous H<sub>2</sub>SO<sub>4</sub>. *Electrochim. Acta* **2004**, *49* (9–10), 1451–1459.
- (104) Pfeiffer-Laplaud, M.; Costa, D.; Tielens, F.; Gaigeot, M.-P.; Sulpizi, M. Bimodal Acidity at the Amorphous Silica/Water Interface. *J. Phys. Chem. C* **2015**, *119* (49), 27354–27362.
- (105) Spendelow, J. S.; Goodpaster, J. D.; Kenis, P. J. A.; Wieckowski, A. Mechanism of CO Oxidation on Pt(111) in Alkaline Media. *J. Phys. Chem. B* **2006**, *110* (19), 9545–9555.
- (106) Spendelow, J. S.; Lu, G. Q.; Kenis, P. J. A.; Wieckowski, A. Electrooxidation of Adsorbed CO on Pt(111) and Pt(111)/Ru in Alkaline Media and Comparison with Results from Acidic Media. *J. Electroanal. Chem.* **2004**, *568* (1–2), 215–224.
- (107) Wang, Y.; Wang, G.; Li, G.; Huang, B.; Pan, J.; Liu, Q.; Han, J.; Xiao, L.; Lu, J.; Zhuang, L. Pt–Ru Catalyzed Hydrogen Oxidation in Alkaline Media: Oxophilic Effect or Electronic Effect? *Energy Environ. Sci.* **2015**, *8* (1), 177–181.
- (108) Tripković, A. ; Popović, K. ; Grgur, B. ; Blizanac, B.; Ross, P. ; Marković, N. . Methanol Electrooxidation on Supported Pt and PtRu Catalysts in Acid and Alkaline Solutions. *Electrochim. Acta* **2002**, *47* (22–23), 3707–3714.
- (109) Cohen, J. L.; Volpe, D. J.; Abruña, H. D. Electrochemical Determination of Activation Energies for Methanol Oxidation on Polycrystalline Platinum in Acidic and Alkaline Electrolytes. *Phys. Chem. Chem. Phys.* **2007**, *9* (1), 49–77.
- (110) Spendelow, J. S.; Goodpaster, J. D.; Kenis, P. J. A.; Wieckowski, A. Methanol Dehydrogenation and Oxidation on Pt(111) in Alkaline Solutions. *Langmuir* **2006**, *22* (25), 10457–10464.

## CHAPTER 6

### CONCLUSIONS AND FUTURE DIRECTIONS

This dissertation demonstrated four advanced electrocatalytic functionalities of oxide-encapsulated electrocatalysts: i) stabilize nanoparticles, ii) improve electron transfer between a semiconducting substrate and metal nanoparticle, iii) control reaction pathways through selective transport, and iv) alter reaction energetics associated with catalysis at the buried interface. The materials platform investigated herein transitioned from heterogeneous Pt nanoparticles to ideal, well-defined Pt thin films that were partially or fully encapsulated by ultra-thin overlayers of silicon oxide, respectively. The silicon oxide films were synthesized by a room temperature UV ozone process, a technique that allowed for nanometer level control over the oxide thickness. Chapter 3 established the ability of the silicon oxide overlayers to promote nanoparticle adhesion to the support surface and mitigate nanoparticle detachment, migration, and coalescence. Chapter 4 employed SiO<sub>x</sub> as a membrane that permitted transport of the desired redox species while selectively blocking the transport of contaminants to the underlying electrocatalyst. Chapter 5 exploited unique catalytic properties at the buried interface to improve alcohol oxidation performance. Overall, this dissertation showcased oxide-encapsulated electrocatalysts as highly versatile and potentially tunable structures for various electrochemical technologies for solar fuels production and conversion.

This dissertation sought to develop a broad knowledge base that would allow the tunable oxide-encapsulated electrocatalyst architecture to be applied to a wide range of materials and electrocatalytic applications. However, to fully realize this potential, additional insights on the transport and kinetic mechanisms that influence reaction pathways are needed. This knowledge

can be harnessed to develop design rules for the rational design of stable oxide-encapsulated electrocatalysts capable of highly efficient and selective solar fuels production and conversion.

## **6.1 Future Directions of Oxide-Encapsulated Electrocatalysts**

In order to lay the groundwork for the rational design of this multifunctional electrocatalyst architecture, it will be crucial that future studies also focus on model planar electrodes to more clearly establish processing-structure-property-performance relationships. As presented in this dissertation, the oxide thickness and surface chemistry can be tuned to impact stability, control selective transport, and modify reaction sites at the buried interface. Additionally, it was shown that studying different electrochemical systems (e.g. DAFC in Chapter 5) can provide valuable information on overlayer/catalysis interactions. This section suggests future directions and opportunities of oxide-encapsulated electrocatalysts that should be explored to help gain a fundamental understanding of electrical, transport, and kinetic properties that impact its operation.

### **6.1.1 *Modification of Oxide Overlayers***

One important aspect of oxide-encapsulated electrocatalysts is the potential to tune their structure and/or composition to select desired properties for a given application. Incorporating dopants, changing the oxide precursor, and/or altering the oxide synthesis procedure may modify several key properties of the oxide. However, potential tradeoffs between conductivity, stability, and kinetic activity must be taken into consideration when modifying the oxide. Furthermore, modifications to the oxide must still allow for transport of desired reactants and products. Through these rational design studies, one should gain a detailed understanding of the structure-property relationships that govern the performance of the oxide-encapsulated electrocatalysts to establish design guidelines that may be broadly applied to other systems.

#### 6.1.1.1 *Incorporate Dopants*

Doping the oxide overlayer with impurities or inducing charged defects can lead to improved electrical conductivity or modified selective transport properties. Chapter 3 investigated the electronic resistance as a function of thickness and observed that the  $\text{SiO}_x$  did not behave like a typical tunneling oxide. Instead, the  $\text{SiO}_x$  was moderately conductive and could thereby enhance electron transport from the semiconducting substrate to the electrocatalyst. It was suggested that this conductivity could have resulted from defects and/or residual carbon from the UV ozone synthesis process. Intentionally doping the oxide with a dopant that is well-known to improve electrical conductivity (e.g. niobium)<sup>1,2</sup> would provide better control over the electronic properties of the oxide layers to more easily study their implications for photoelectrocatalysis.

In Chapter 4 it was shown that the  $\text{SiO}_x$  would selectively transport  $\text{H}^+$  and  $\text{H}_2$ , but not  $\text{Cu}^{2+}$ . It was suggested that the positive charge on impurity species could experience electrostatic repulsion when they interact with the partially positive silanol groups ( $\text{Si-OH}$ ) that form when  $\text{SiO}_x$  is exposed to an acidic environment. As a result, large positive ions may not easily dissolve into  $\text{SiO}_x$ , thereby slowing the diffusion through  $\text{SiO}_x$ . By contrast, uncharged organic species or monovalent cations may be able to more easily dissolve into and diffuse through  $\text{SiO}_x$ . Doping the oxide with charged species could affect electrostatic repulsion between charged impurity species and dopants within the oxide to further improve the resistance to a variety of charged poison species. However, the material would need to be designed properly such that the dopants do not adversely affect facile  $\text{H}^+$  permeability and selectivity through  $\text{SiO}_x$ .

#### 6.1.1.2 *Change Oxide Precursor*

Other oxide materials with different electrical, chemical, and structural properties should be explored to broaden the knowledge library of structure-property-performance relationships.

Changing the  $\text{SiO}_x$  precursor material from polydimethylsiloxane (PDMS) to other silicon containing polymers are expected to alter the final oxide structure and composition. For example, Takenaka et al. investigated how different silica precursors and sol-gel synthesis modifications impacted the ECSA and ORR performance of thin  $\text{SiO}_2$  coatings.<sup>3,4</sup> These studies demonstrated that precursors containing more methyl groups ( $-\text{CH}_3$ ) produced silica with larger, more hydrophobic pores (with  $\text{Si}-\text{CH}_3$  groups) which promoted the diffusion of some reactants and products ( $\text{O}_2$  and  $\text{H}_2\text{O}$ ), whereas the other silica structure that contained hydrophilic  $\text{Si}-\text{OH}$  groups inhibited diffusion of  $\text{H}_2\text{O}$  products out of the pores.<sup>3,4</sup>

It is anticipated that changing the  $\text{SiO}_x$  precursor for the UV ozone process will also produce significant changes in structure and electrocatalytic performance of  $\text{SiO}_x$ -encapsulated electrocatalysts. Ouyang et al. characterized various siloxane precursors, for the UV ozone process, containing differing alkyl groups and varying degrees of silicon coordination with oxygen atoms.<sup>5</sup> For reference, silicon atoms in polydimethylsiloxane (PDMS) are coordinated to two oxygen atoms and two methyl groups, whereas silicon atoms within the other polymers investigated in Ouyang's study were coordinated to one to four oxygen atoms. After UV ozone exposure, Ouyang observed that the siloxane polymers containing a higher density of silicon-oxygen bonds were more readily converted to  $\text{SiO}_2$  and contained lowered amounts of residual carbon. However, neither the nature of the residual carbon (i.e. atomic carbon, methyl, etc.) nor the effect of the precursor on the final structure (e.g. pore size) was elucidated in that study.

The UV ozone conversion process could also be applied to titanium alkoxide precursors (e.g. titanium isopropoxide) to produce titanium dioxide.  $\text{TiO}_2$  is very relevant for PEC, PEMEC, PEMFC, and DAFC applications because it is very stable over a wide pH range, relatively conductive (compared to other oxides) and is known to influence catalytic activity through SMSI<sup>6</sup>

and bifunctional mechanisms.<sup>7,8</sup> Therefore, TiO<sub>2</sub> encapsulated electrocatalysts may be more practical in systems where conductivity and/or stability (at alkaline pH) tend to limit performance.

#### *6.1.1.3 Alter Synthesis Technique*

Common methods for synthesizing oxide thin films include sol-gel processes and chemical vapor deposition (CVD).<sup>9,10</sup> Both processes have been previously used to fabricate oxide-encapsulated electrocatalysts for improving stability<sup>3</sup> and preventing undesired back reactions,<sup>11</sup> but a fundamental understanding of transport and kinetic mechanisms were not developed. Each technique provides advantages and disadvantages for creating unique structures for specific applications.

Both techniques usually involve the use of toxic precursor materials that release alcohols during the conversion process and can cause undesired cracking of the films.<sup>12</sup> Furthermore, sol-gel processing typically requires high-temperature annealing to remove residual alkyl groups from precursor materials, although alkyl groups were still apparent in the Takenaka studies despite the high temperature annealing (see previous section 6.1.1.2).<sup>3</sup> Despite this challenge, the sol-gel synthesis method can produce stable structures for applications in which a hydrophobic oxide coating is tolerable or even desirable. For example, a hydrophobic coating can be expected to be beneficial for preventing alcohol crossover to the ORR anode in a DAFC. CVD synthesis of SiO<sub>2</sub> requires a vacuum environment, therefore presenting challenges for large-scale fabrication. Atomic layer deposition (ALD), a type of CVD, is particularly interesting as an approach to fabricate oxide-encapsulated electrocatalysts due to the ability to precisely control film thickness. Using this technique, Yuan et al. were able to fabricate a dense silica that allowed HER (H<sup>+</sup> and H<sub>2</sub> transport) but prevented ORR (O<sub>2</sub> transport).<sup>13</sup> The dense silica synthesized by Yuan et al. starkly contrasts the more porous silica used by Takenaka et al., which emphasizes the impact that

different processing procedures have on the structure and performance of oxide-encapsulated electrocatalysts.

The UV ozone process is advantageous compared to sol-gel and CVD techniques in that it does not require toxic precursors nor a high temperature or vacuum environment.<sup>14–17</sup> Moreover, the conversion of PDMS to SiO<sub>x</sub> produces smaller byproducts (H<sub>2</sub>O and CO<sub>2</sub>) than the other processes which could suppress non-uniformities. However a comparative study of sol-gel, CVD, and UV ozone synthesis techniques could provide further insight into process-structure-performance relationships to understand how properties can be tuned to maximize desired stability and selectivity benefits without significantly affecting the kinetic or mass transport overpotentials for the desired redox chemistry.

### ***6.1.2 Preventing Dissolution of Electrocatalyst Materials***

In order to reduce the cost and loading of precious rare earth metal electrocatalysts, researchers have developed electrocatalysts based on inexpensive and more earth abundant materials. Unfortunately, these electrocatalysts materials are typically unstable in acidic environments needed for PEM technologies (e.g. Ni and Fe composites for HER and OER<sup>18</sup>). As mentioned in the Introduction (section 1.7.1), Takenaka et al. demonstrated silica layers could prevent Pd dissolution during ORR operation.<sup>19,20</sup> If SiO<sub>x</sub> can also prevent dissolution of less noble, less stable Ni and Fe HER catalysts, while still allowing for transport of the desired reactants and products, this strategy could apply to other types of metal catalysts and electrocatalytic reactions. For example, IrO<sub>x</sub> is the only known stable, active OER electrocatalyst for operation in acidic electrolytes.<sup>18</sup> Therefore, oxide-encapsulated electrocatalysts would be a major contribution to the field if oxide overlayers could be tuned to protect other OER catalysts, while maintaining high activity and allowing H<sub>2</sub>O and O<sub>2</sub> transport.

### 6.1.2.1 Apply to Overlayers to Smaller Nanoparticles

Nanoparticles (NP) that are smaller than those investigated in Chapter 3, are expected to degrade at accelerated rates compared to larger particles ( $\approx 10$  nm versus  $\approx 40$  nm). To evaluate the role of  $\text{SiO}_x$  in preventing the degradation mechanisms discussed in section 1.6.1, Pt NPs, electrodeposited on photoelectrodes ( $\text{SiO}_2|\text{p-Si}$ ), were characterized before and after a 7 hr constant current (chronopotentiometry (CP)) stability measurement. Figure 6.1a shows the operating potentials required to maintain  $-10 \text{ mA cm}^{-2}$  for a bare Pt NP (0 nm  $\text{SiO}_x$ ) and a 10 nm  $\text{SiO}_x$ -encapsulated Pt NPs. Consistent with the results in Chapter 3, the 10 nm  $\text{SiO}_x|\text{Pt}$  NP photoelectrode performance remained constant over the 7 hr test, whereas the bare Pt NP (0 nm) performance varied. LSVs conducted before and after CP experiments clearly show a significant decrease in performance for the bare Pt NPs but not for the 10 nm  $\text{SiO}_x|\text{Pt}$  NPs (Figure 6.1b).

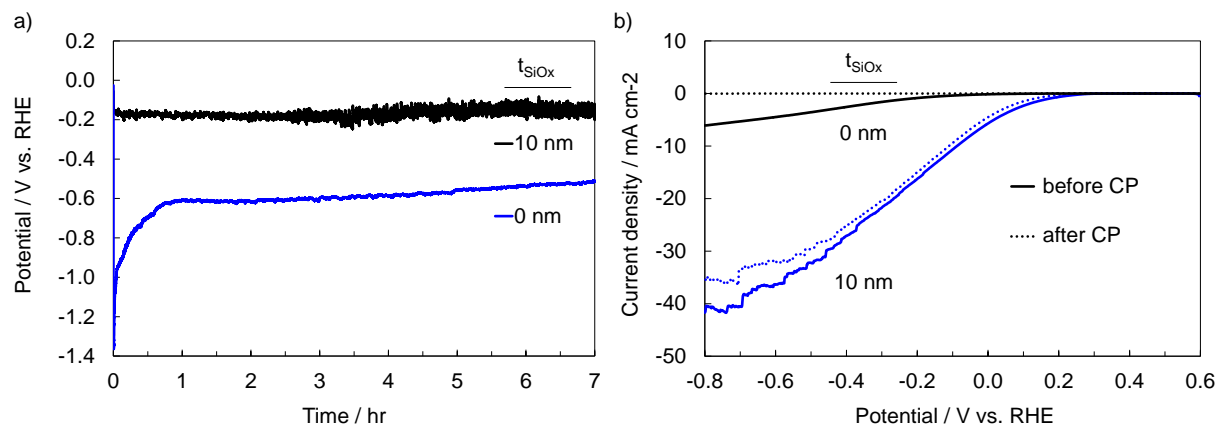


Figure 6.1. a) CP stability measurements for 0 nm  $\text{SiO}_x|\text{Pt}$  NP and 10 nm  $\text{SiO}_x|\text{Pt}$  NP photoelectrode operating at  $-10 \text{ mA cm}^{-2}$  for 7 hrs under AM 1.5G illumination. b) LSV measurements ( $20 \text{ mV s}^{-1}$ ) before and after the CP in (a). Experiments were performed under AM 1.5G illumination in 0.5 M  $\text{H}_2\text{SO}_4$  that was stirred at 1000 rpm to facilitate bubble removal.



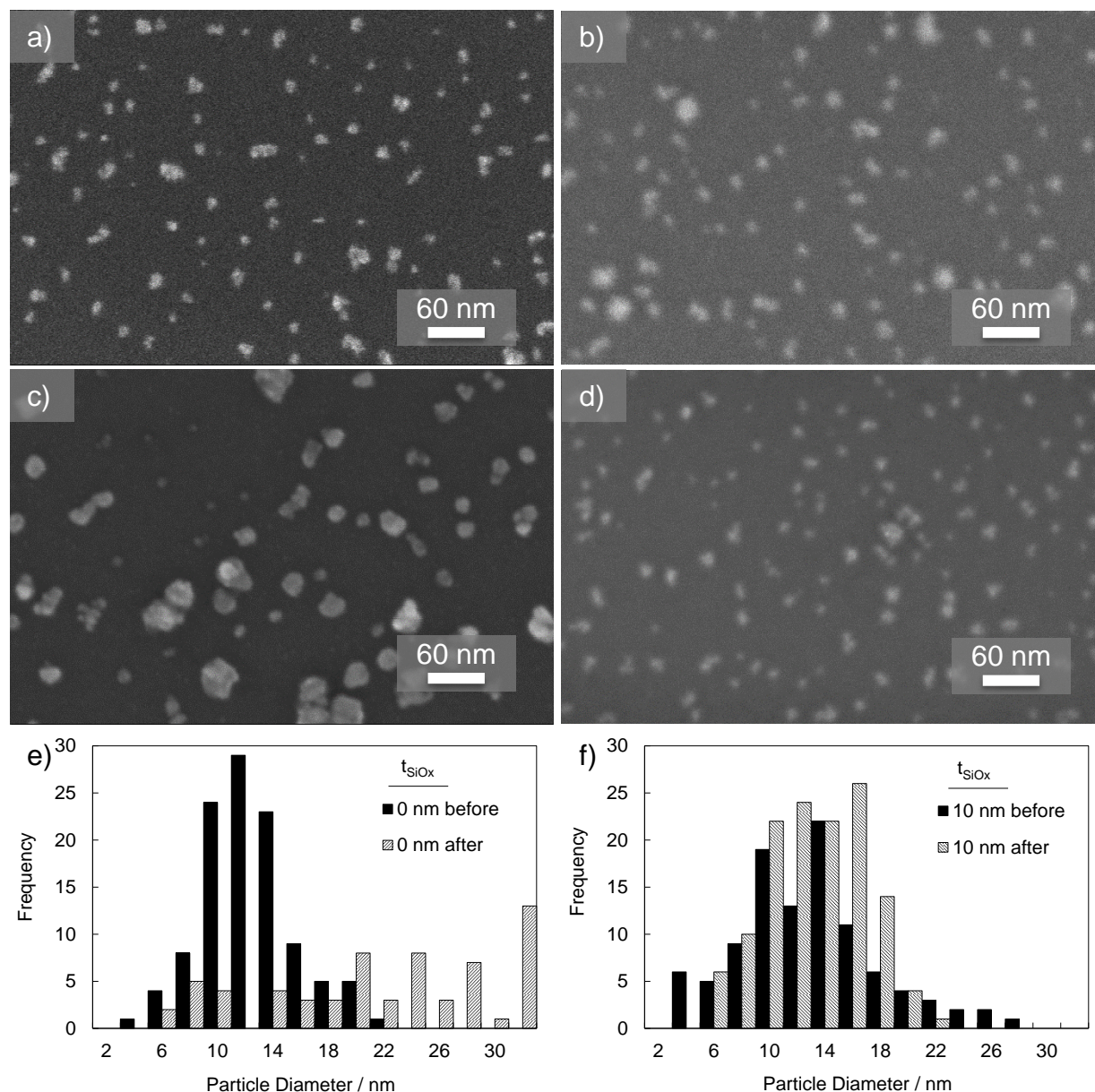


Figure 6.2. SEM images taken at x200.00k magnification of a) 0 nm SiO<sub>x</sub>|Pt NP and b) 10 nm SiO<sub>x</sub>|Pt NP before and c) d) after stability measurements in Figure 6.1, respectively. Histograms of particle diameters before and after the 7 hr CP for e) 0 nm SiO<sub>x</sub>|Pt NP and f) 10 nm SiO<sub>x</sub>|Pt NP.

Figure 6.2 shows SEM images obtained before and after the 7 hr CP stability test. SEM images for the 0 nm SiO<sub>x</sub>|Pt NP photoelectrode (Figure 6.2a and 6.2c) demonstrate visible agglomeration of Pt nanoparticles, whereas the particles structures on the 10 nm SiO<sub>x</sub>|Pt NP

photoelectrode (Figure 6.2b and 6.2d) remained similar before and after the CP. Particle diameter histograms (Figure 6.2e and 6.2f) reveal the distribution of nanoparticles on the bare Pt sample shift to larger diameters after the CP stability test from  $11.4 \pm 3.4$  nm to  $21.4 \pm 9.1$  nm average particle diameter. By contrast, the distribution and average particle diameter for 10 nm SiO<sub>x</sub>/Pt remains relatively constant ( $12.1 \pm 5.1$  nm before to  $12.2 \pm 3.5$  nm after CP). These SEM images are consistent with LSV curves in Figure 6.1b in which the 10 nm SiO<sub>x</sub>/Pt NP photoelectrode was stable and the 0 nm SiO<sub>x</sub>/Pt NP was not stable. These results demonstrate the stability advantages of the SiO<sub>x</sub> overlayer, as it clearly prevents agglomeration/migration and possibly dissolution of Pt nanoparticles. If this architecture could be successfully applied to thermodynamically unstable nanoparticles, a new class of stable and efficient inexpensive catalysts can be developed.

### **6.1.3 Extend Poison Resistance**

Chapter 4 provided an example of poison resistance against a model poison species, Cu<sup>2+</sup>. Copper is a relevant poison for real world applications because Cu<sup>2+</sup> is a well-known Pt poison and can exist in tap water and or leach from pipes, fittings, and/or electronics.<sup>21</sup> However, other poisons may exist in untreated water such as sulfur containing species that strongly adsorb onto Pt, and dissolved metals that can readily electrodeposit onto HER catalysts. Developing trends between species properties (e.g. size, charge, charge density, and shape) and transport through SiO<sub>x</sub> will require studies with other electroactive metal species that are not necessarily common poisons. Understanding how differences in species size and charge (e.g. Fe<sup>3+</sup>, Ni<sup>2+</sup>, Au<sup>2+</sup>, Ag<sup>+</sup>, Pb<sup>2+</sup>, and S<sup>2-</sup>) impact transport will provide valuable insights on the origin of selectivity.

#### **6.1.3.1 Operation in Hudson River Water**

In order to test the ability of oxide-encapsulated electrocatalysts to withstand the detrimental effects of a larger range of impurities that may be encountered in electrolysis

applications, HER durability tests of the  $\text{SiO}_x/\text{Pt}$  and bare Pt electrodes were conducted in water obtained from the Hudson River adjacent to New York City. Before experiments, the pH of the river water was adjusted with concentrated sulfuric acid to be equivalent to that measured for 0.5 M  $\text{H}_2\text{SO}_4$ . Analysis of dissolved metals in water and sediment samples from the Hudson River have previously indicated the presence of Ag, Cd, Cu, Pb, and Zn.<sup>22–24</sup> At HER operating potentials, Ag, Cu, and Pb can easily deposit onto Pt and thereby decrease the Pt HER activity. The poison tolerance of the  $\text{SiO}_x/\text{Pt}$  electrode was evaluated by recording the potential as a function of time at  $-5 \text{ mA cm}^{-2}$  for 1 hour. Figure 6.3a and 6.3b show the CP experiments for a bare Pt control electrode (0 nm  $\text{SiO}_x$ ) and a 4.6 nm  $\text{SiO}_x/\text{Pt}$  electrode, respectively, in 0.5 M  $\text{H}_2\text{SO}_4$  with and without Hudson River water.

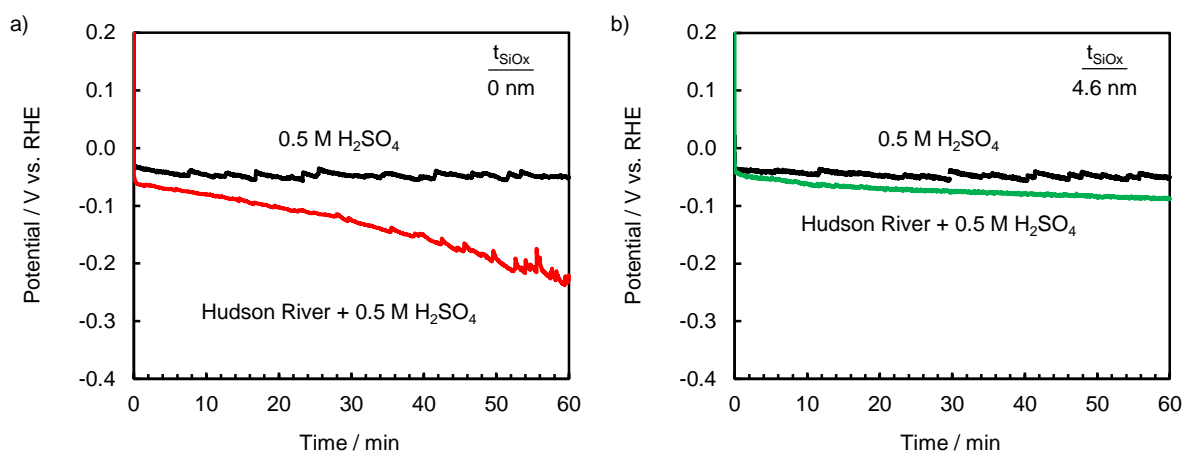


Figure 6.3. Electrocatalysis poisoning test performed in Hudson River water. Constant current density ( $-5 \text{ mA cm}^{-2}$ ) stability tests conducted on a)  $t_{\text{SiO}_x}=0 \text{ nm}$  (red) and b)  $t_{\text{SiO}_x}=4.6 \text{ nm}$  (green)  $\text{SiO}_x/\text{Pt}$  electrodes in 0.5 M  $\text{H}_2\text{SO}_4$  with and without (black) unfiltered water obtained directly from the Hudson River.

As demonstrated in Chapter 4, both electrodes were stable in 0.5 M  $\text{H}_2\text{SO}_4$ . However, the bare Pt control electrode incurred 190 mV additional overpotential after operation in the presence of the Hudson River water for 1 hour. Although some additional overpotential was also incurred for the MCEC electrode in the river water (38 mV), it was substantially less than the bare Pt

control. Post XPS analysis of a bare Pt control electrode tested over three hours revealed that significant amounts of Cu, Ag, sulfates and organic species had deposited onto the Pt surface (Figure 6.4). This result demonstrates the poisoning tolerance of SiO<sub>x</sub>|Pt electrodes in the presence of multiple water contaminants. However, additional control experiments are needed to understand how different S<sup>-2</sup> and Ag<sup>+</sup> impurities individually impact HER stability.

The concentration of copper contaminants (0.2 mM) investigated in Chapter 4 is several orders of magnitude larger than the 20 nM concentration expected in untreated Hudson River water samples. Due to these high concentrations the 1 hour chronopotentiometry test can be viewed as an accelerated stability test and provide good platform for studying selectivity against individual poisons.

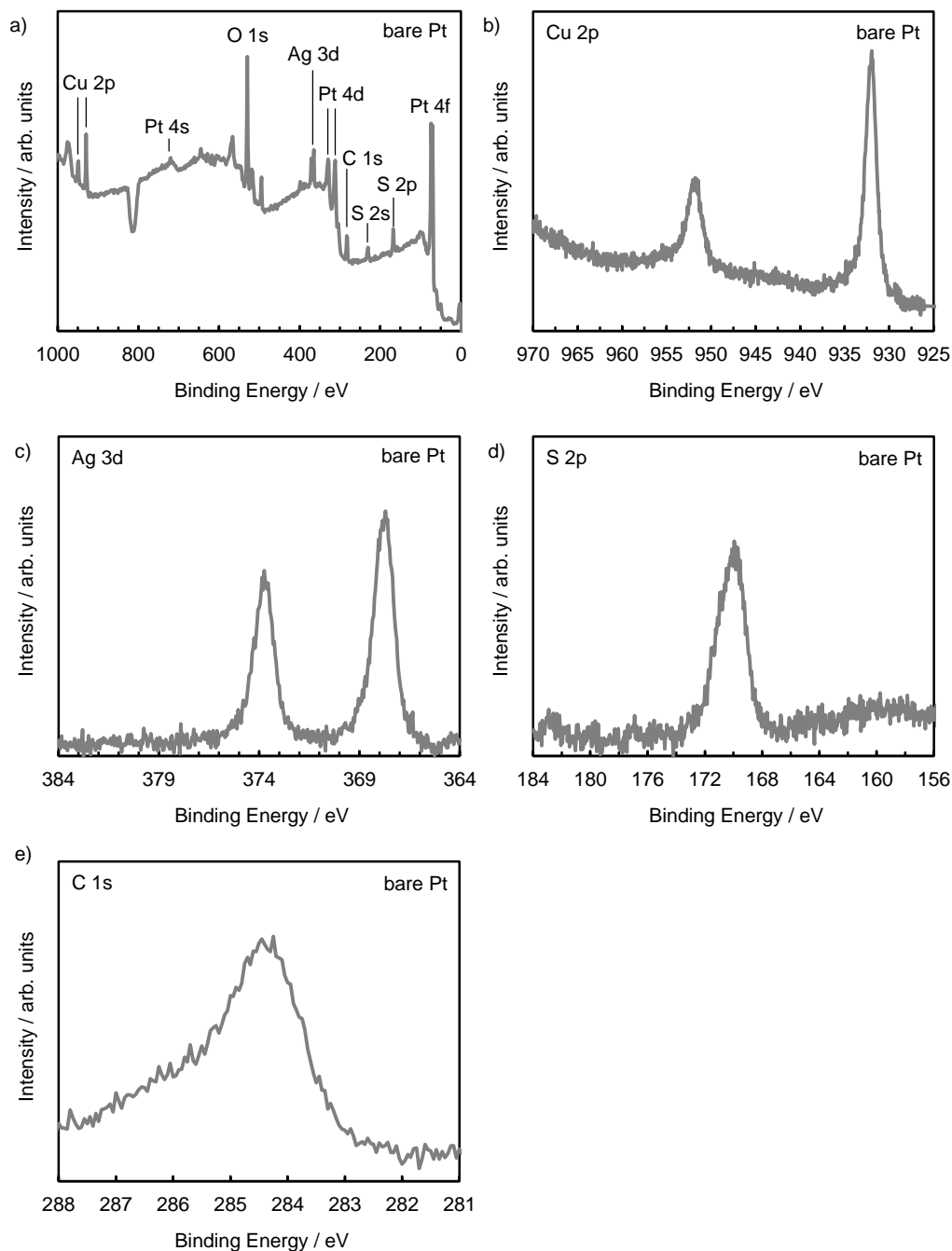


Figure 6.4. XPS results after Hudson River water poisoning test. XPS spectra of a bare Pt electrode: a) Survey, b) Cu 2p, c) Ag 3d, d) S 2p, and e) C 1s, after operating at  $-5 \text{ mA cm}^{-2}$  for 3 hours in Hudson River water modified with 0.5 M  $\text{H}_2\text{SO}_4$  to concentrate deposited contaminants onto Pt surface to a detectable level. Atomic percent of each were 6 %, 3%, 1%, and 23% respectively, while the Pt and O were 15 % and 50 % respectively.

### 6.1.3.2 *Other Design Considerations that Influence Species Transport Through Overlayers*

The size of pores and/or interstitial spaces within the  $\text{SiO}_x$  overlayers synthesized by UV ozone are sufficiently small such that the size and charge of the permeant species are expected to have a strong effect on the interactions with the  $\text{SiO}_x$  in a way that enables selective diffusion through nanopores.<sup>25</sup> The hydrated radii may be considered an appropriate upper limit of the size of ionic species as it diffuses through the  $\text{SiO}_x$  since the energy of solvation/desolvation can be significant for many electroactive species. While the exact nature of the ions within the  $\text{SiO}_x$  is not known, it has been shown that water molecules can diffuse through nanometer-thick borosilicate glass on ultramicroelectrodes,<sup>26</sup> suggesting that ionic species can also exist within a hydrated  $\text{SiO}_x$ . Another important consideration for ionic reactants is that their charge must always be balanced by nearby counterions, charge from the  $\text{SiO}_x$  matrix, or electrode surface in order to maintain electroneutrality. Stated otherwise, it is likely that  $\text{HSO}_4^-$  counterion species are simultaneously transported with  $\text{H}^+$ . Thus, the hydrated radius of the counterion might be a more important parameter for describing transport through thin overlayers. Furthermore, the role of the counterion species should also be considered when designing studies to better understand selective transport, since counterions can preferentially complex with some electroactive species but not others.

Although the hydrated radii of some species may be smaller than the interstitial dimensions of  $\text{SiO}_2$ , the positive charge on these species can cause an electrostatic repulsion between the partially positive silanol groups (detailed in Chapter 4). As a result, divalent cations such as  $\text{Cu}^{2+}$  are expected to experience a stronger repulsive force than uncharged species or monovalent cations such as  $\text{H}^+$  or  $\text{Ag}^+$ . Furthermore, the  $\text{H}^+$  diffusion into  $\text{SiO}_x$  may be enhanced, compared to other ions, from the  $\text{H}^+$  interactions with O atoms in  $\text{SiO}_2$ , as described by the proton hopping mechanisms whereby  $\text{H}^+$  diffuses through  $\text{SiO}_2$  by associating and dissociating with O atoms in

SiO<sub>x</sub>.<sup>27–29</sup> These types of interactions with O atoms are expected to be less energetically favorable with metal ions like Cu<sup>2+</sup> and Ag<sup>+</sup>, leading to slow transport rates of those ions within the SiO<sub>x</sub>.

Consequently, efforts to improve the rate at which H<sup>+</sup> dissolves in and interacts with O atoms in SiO<sub>x</sub> should also be considered. This might be achieved by changing the chemical environment surrounding O atoms by replacing some Si atoms with an element that decreases the activation energy to form and break O-H<sup>+</sup> bonds in the lattice. Many factors such as carbon content and hydrophobic character of the SiO<sub>x</sub> may alter these interactions and thereby modify its transport properties. The model thin film electrode design provides a great opportunity to alter synthesis procedures to control these properties and thereby tune the catalytic pathways for oxide-encapsulated electrocatalysts.

It is anticipated that the additional HER overpotential losses tied to the presence of the SiO<sub>x</sub> overlayer would become prohibitive if the oxide-encapsulated architecture were applied to applications for which electroactive species of interest have significantly smaller effective diffusivities than H<sup>+</sup> and H<sub>2</sub> in SiO<sub>x</sub>. In these cases, it is necessary to develop a deeper knowledge of the transport mechanisms through the SiO<sub>x</sub> and understand how those transport properties are affected by changes to the SiO<sub>x</sub> structure and/or chemical composition. Although there are still complex open questions relating to the molecular-level structure-property relationships that dictate transport mechanisms, this dissertation is intended to inspire additional studies that: i) involve more advanced experimental and modeling techniques, ii) explore tuning the membrane properties for desirable selectivity and permeability, and iii) lay the groundwork for rational design oxide-encapsulated electrocatalysts.

## 6.2 Integrating Oxide-Encapsulated Electrocatalysts into Electrochemical Technologies

On a more practical level, the poisoning experiments conducted in Chapter 4 highlighted the ability to use oxide-encapsulated electrocatalysts for poison-resistant electrocatalysis in an electrolyte containing undesirable impurities. For applications such as water electrolysis, the poison-resistance of oxide-encapsulated electrocatalysts may extend the operating life of the device, reducing risks of catastrophic failure if an impurity is suddenly introduced into the system. Device lifetime is one of the most sensitive parameters in technoeconomic analyses of water splitting systems.<sup>30,31</sup> Additionally, impurity tolerant catalysts may reduce capital and operating costs associated with purification of the aqueous feed and fabrication of electrolyzer stacks with expensive compatible materials. Normally, unpurified water or non-compatible system components (e.g. tubing, gasket materials, etc.), would introduce impurities within the electrolyzer system and degrade the electrocatalyst and/or membrane. An electrolyzer system without these stringent requirements would be highly complementary to emerging membraneless electrolyzer designs.<sup>32</sup> Membranes are also known to be susceptible to degraded performance in the presence of impurities, thus employing poison-resistant electrocatalysts with membraneless electrolyzers would, in principle, enable highly robust water electrolysis in highly impure water.

More generally, the oxide-encapsulated electrocatalyst architecture may be of interest to any application (including fuel cells) for which electrocatalytic nanoparticles are susceptible to dissolution, agglomeration, and/or detachment. Takenaka et al. demonstrated the viability of oxide-encapsulated electrocatalyst in fuel cells in which the catalyst layer is in contact with a gas-phase environment.<sup>4</sup> Contaminants could also arise from the air feed at the ORR electrode and can create similar electrocatalyst and/or membrane degradation problems as in electrolyzers.



Therefore, oxide-encapsulated electrocatalysts could also extend fuel cell device lifetime by preventing all four catalyst degradation mechanisms (section 1.6.1).

To ensure renewable energies continue to penetrate the energy market, large-scale energy storage and conversion technologies, such as electrolyzers and fuel cells, respectively, must become more efficient, durable, and economical for renewables to remain competitive. Oxide-encapsulated electrocatalysts have the potential to have a direct impact on each of these requirements and significantly reduce capital and operating costs associated with solar fuels production and conversion.

### 6.3 References

- (1) Yan, L.; Huang, K.; Chen, Y.; Xing, Y. High Content Niobium in Rutile Titania as Catalyst Support to Promote Methanol Electro-Oxidation. *ECS Electrochem. Lett.* **2014**, *3* (5), F27–F29.
- (2) Huang, S.-Y.; Ganesan, P.; Popov, B. N. Electrocatalytic Activity and Stability of Niobium-Doped Titanium Oxide Supported Platinum Catalyst for Polymer Electrolyte Membrane Fuel Cells. *Appl. Catal. B Environ.* **2011**, *102* (1–2), 71–77.
- (3) Takenaka, S.; Miyamoto, H.; Utsunomiya, Y.; Matsune, H.; Kishida, M. Catalytic Activity of Highly Durable Pt/CNT Catalysts Covered with Hydrophobic Silica Layers for the Oxygen Reduction Reaction in PEFCs. *J. Phys. Chem. C* **2014**, *118* (2), 774–783.
- (4) Takenaka, S.; Miyazaki, T.; Matsune, H.; Kishida, M. Highly Active and Durable Silica-Coated Pt Cathode Catalysts for Polymer Electrolyte Fuel Cells: Control of Micropore Structures in Silica Layers. *Catal. Sci. Technol.* **2015**, *5* (2), 1133–1142.
- (5) Ouyang, M.; Yuan, C.; Muisener, R. J.; Boulares, A.; Koberstein, J. T. Conversion of Some Siloxane Polymers to Silicon Oxide by UV/Ozone Photochemical Processes. *Chem. Mater.* **2000**, *12* (29), 1591–1596.
- (6) Kumar, A.; Ramani, V. Strong Metal–Support Interactions Enhance the Activity and Durability of Platinum Supported on Tantalum-Modified Titanium Dioxide Electrocatalysts. *ACS Catal.* **2014**, *4* (5), 1516–1525.
- (7) Zhuang, Y.; Ding, W.; Liu, Y.; Mou, Z.; Sun, J.; Guan, M. Reduced Nanostructured Titanium Oxide Coating as an Electrocatalyst Support for Methanol Oxidation. *J. Mater. Sci.* **2015**, *50* (11), 3875–3882.
- (8) Rigdon, W. A.; Huang, X. Carbon Monoxide Tolerant Platinum Electrocatalysts on

- Niobium Doped Titania and Carbon Nanotube Composite Supports. *J. Power Sources* **2014**, 272, 845–859.
- (9) Brinker, C. J.; Scherer, G. W. *Sol-Gel Science: The Physics and Chemistry of Sol-Gel Processing*; Academic Press London: San Diego, CA, 1990; Vol. 8.
  - (10) Pierson, H. O. *Handbook of Chemical Vapor Deposition: Principles, Technology and Applications*, 2nd ed.; Noyes Publication: Park Ridge, NJ, 1999.
  - (11) Edri, E.; Frei, H. Charge Transport through Organic Molecular Wires Embedded in Ultrathin Insulating Inorganic Layer. *J. Phys. Chem. C* **2015**, 119 (51), 28326–28334.
  - (12) Sakka, S. *In Sol-Gel Processing of Advanced Materials*; The American Chemical Society: Westerville, OH, 1991.
  - (13) Yuan, G.; Agiral, A.; Pellet, N.; Kim, W.; Frei, H. Inorganic Core–shell Assemblies for Closing the Artificial Photosynthetic Cycle. *Faraday Discuss.* **2014**, 176, 233–249.
  - (14) Egitto, F. D.; Matienzo, L. J. Transformation of Poly(Dimethylsiloxane) into Thin Surface Films of SiO<sub>x</sub> by UV/Ozone Treatment. Part I: Factors Affecting Modification. *J. Mater. Sci.* **2006**, 41 (19), 6362–6373.
  - (15) Ouyang, M.; Klemchuk, P. P.; Koberstein, J. T. Exploring the Effectiveness of SiO<sub>x</sub> Coatings in Protecting Polymers against Photo-Oxidation. *Polym. Degrad. Stab.* **2000**, 70 (2), 217–228.
  - (16) Wu, C.-K.; Hultman, K. L.; O'Brien, S.; Koberstein, J. T. Functional Oligomers for the Control and Fixation of Spatial Organization in Nanoparticle Assemblies. *J. Am. Chem. Soc.* **2008**, 130 (11), 3516–3520.
  - (17) Dölle, C.; Pappmeyer, M.; Ott, M.; Vissing, K. Gradual Photochemical-Induced Conversion of Liquid Polydimethylsiloxane Layers to Carbon Containing Silica Coatings by VUV Irradiation at 172 Nm. *Langmuir* **2009**, 25 (12), 7129–7134.
  - (18) McCrory, C. C. L.; Jung, S.; Ferrer, I. M.; Chatman, S. M.; Peters, J. C.; Jaramillo, T. F. Benchmarking Hydrogen Evolving Reaction and Oxygen Evolving Reaction Electrocatalysts for Solar Water Splitting Devices. *J. Am. Chem. Soc.* **2015**, 137 (13), 4347–4357.
  - (19) Takenaka, S.; Susuki, N.; Miyamoto, H.; Tanabe, E.; Matsune, H.; Kishida, M. Highly Durable Carbon Nanotube-Supported Pd Catalysts Covered with Silica Layers for the Oxygen Reduction Reaction. *J. Catal.* **2011**, 279 (2), 381–388.
  - (20) Takenaka, S.; Kishida, M. Functionalization of Carbon Nanotube-Supported Precious Metal Catalysts by Coverage with Metal Oxide Layers. *Catal. Surv. from Asia* **2013**, 17 (2), 71–84.
  - (21) Tavares, M. .; Machado, S. A. .; Mazo, L. . Study of Hydrogen Evolution Reaction in Acid

- Medium on Pt Microelectrodes. *Electrochim. Acta* **2001**, 46 (28), 4359–4369.
- (22) Feng, H.; Kirk Cochran, J.; Lwiza, H.; Brownawell, B. J.; Hirschberg, D. J. Distribution of Heavy Metal and PCB Contaminants in the Sediments of an Urban Estuary: The Hudson River. *Mar. Environ. Res.* **1998**, 45 (1), 69–88.
  - (23) Sañudo-Wilhelmy, S. A.; Gill, G. A. Impact of the Clean Water Act on the Levels of Toxic Metals in Urban Estuaries: The Hudson River Estuary Revisited. *Environ. Sci. Technol.* **1999**, 33 (20), 3477–3481.
  - (24) Feng, H.; Kirk Cochran, J.; J. Hirschberg, D. Transport and Sources of Metal Contaminants over the Course of Tidal Cycle in the Turbidity Maximum Zone of the Hudson River Estuary. *Water Res.* **2002**, 36 (3), 733–743.
  - (25) Cervera, J.; Ramírez, P.; Manzanares, J. A.; Mafé, S. Incorporating Ionic Size in the Transport Equations for Charged Nanopores. *Microfluid. Nanofluidics* **2010**, 9 (1), 41–53.
  - (26) Velmurugan, J.; Zhan, D.; Mirkin, M. V. Electrochemistry through Glass. *Nat. Chem.* **2010**, 2 (6), 498–502.
  - (27) Godet, J.; Pasquarello, A. Proton Diffusion Mechanism in Amorphous SiO<sub>2</sub>. *Phys. Rev. Lett.* **2006**, 97 (15), 155901.
  - (28) Godet, J.; Pasquarello, A. Proton Diffusion in Amorphous SiO<sub>2</sub> and Hafnium Silicate by Ab Initio Molecular Dynamics. In *AIP Conference Proceedings*; AIP, 2007; Vol. 893, pp 195–196.
  - (29) Fogarty, J. C.; Aktulga, H. M.; Grama, A. Y.; van Duin, A. C. T.; Pandit, S. A. A Reactive Molecular Dynamics Simulation of the Silica-Water Interface. *J. Chem. Phys.* **2010**, 132 (17), 174704.
  - (30) Pinaud, B. A.; Benck, J. D.; Seitz, L. C.; Forman, A. J.; Chen, Z.; Deutsch, T. G.; James, B. D.; Baum, K. N.; Baum, G. N.; Ardo, S.; et al. Technical and Economic Feasibility of Centralized Facilities for Solar Hydrogen Production via Photocatalysis and Photoelectrochemistry. *Energy Environ. Sci.* **2013**, 6 (7), 1983.
  - (31) Colella, W. G.; James, B. D.; Moton, J. M.; Saur, G.; Ramsden, T. Techno-Economic Analysis of PEM Electrolysis for Hydrogen Production. In *Electrolytic Hydrogen Production Workshop*; 2014.
  - (32) Esposito, D. V. Membraneless Electrolyzers for Low-Cost Hydrogen Production in a Renewable Energy Future. *Joule* **2017**, 1 (4), 651–658.